Sapthagireesh Subbarayan

Fabrication of a Novel Al/Mg Composite:

Processing and Characterization of Pure Aluminium, Al/AZ31 Alloy Bi-Metal and Aluminium based Sheet Composites by Severe Plastic Deformation

Thesis for the degree of Philosophiae Doctor

Trondheim, November 2013

Norwegian University of Science and Technology
Faculty of Natural Sciences and Technology
Department of Materials Science and Engineering

NTNU – Trondheim
Norwegian University of
Science and Technology

NTNU
Norwegian University of Science and Technology

Thesis for the degree of Philosophiae Doctor

Faculty of Natural Sciences and Technology
Department of Materials Science and Engineering

© Sapthagireesh Subbarayan

ISBN 978-82-471-4773-3 (printed ver.)
ISBN 978-82-471-4774-0 (electronic ver.)
ISSN 1503-8181

Doctoral theses at NTNU, 2013:318

Printed by NTNU-trykk

Preface

The present work is submitted in partial fulfilment of the requirements for the degree of philosophiae doctor (PhD) at the Norwegian University of Science and Technology (NTNU). The work presented as a thesis was carried out at the Department of Materials Science and Engineering, NTNU at the Gløshaugen campus. The work was supervised by Professor dr. techn. Hans Jørgen Roven between September 2008 and October 2012.

The main results presented in this thesis have been published or are in the process of being published, in peer reviewed international journals. As part of the PhD program, some of these results have been presented at International conferences such as the TMS annual meeting and NANOSPD series.

Trondheim, June 2013

Sapthagireesh Subbarayan

Acknowledgements

First of all, I would like to express my sincere thanks to my supervisor, Professor dr. techn. Hans Jørgen Roven for his guidance, motivation and valuable assistance during the entire four years. His assistance and support without any restrictions on my ideas and valuable discussions when most needed are greatly acknowledged. He has been a very kind and very helpful supervisor, all one could ask for.

Many thanks to Pål Christian Skaret, who has been of immense help to me throughout my PhD study and provided with technical assistance during the ECAP experiments. It would be an understatement to say that without him, the experiments and the results of various trials on different new materials would not have been possible. I can never forget the ECAP sessions we had together, especially when trying new configurations. I am very thankful to Mr. Robert Karlsen at the NT Faculty workshop, for his assistance regarding the machining of the samples for different experiments and help in delivering them on time. Thanks are due to Dr. Yongjun Chen, Dr. Rajiv Giri and Dr. Yingda Yu for their interesting tea sessions and Chinese language lessons. I am thankful to Prof. Jarle Hjelen and Wilhelm Dall for their discussions and assistance in EBSD experiments. It has been a pleasure to work with them. Thanks are also due to Ms.Torild Krogstad for her help in obtaining and mixing chemicals and assistance with XRD goniometer for texture measurements. Valuable discussions with Dr. Bjørn Holmedal on the texture measurements are greatly acknowledged. I am extremely grateful to my colleagues here at NTNU and my friends in Trondheim. It is not possible to list them all, but to name a few, Mr. Sindre Bunkholt, Mr. Ning Wang, Mr. Qinglong Zhao, Ms. Sarina Bao, Mr. Anotine Autruffe, Ms. Chiara Modanese, Ms. Elena Dal Martello, Dr. Martin Bellmann and Ms. Irina Semeshka, Dr. Erlend Nordstrand, Dr. Ralf Beck, Dr. Pierre Delaleau, Dr. Julien Degoulange, Dr. Michal Kolar and Ms. Aurora Chirstiansen, Dr. Mohseni Peymann, Dr. Christopher Nwakuo, Dr. Katharina Teichmann, Dr. Emmanuel Hersent, Mr. Tomas Manik, Dr. Jirang Cui, Mr. Terje Hals, Dr. Frederik Widerøe and Dr.

Harald Vestøl. Thanks are due to my friends in Moholt for the awesome parties we had every Saturday. To name a few, Thanks to Asi, Fannar, Karol, Honza, Zuzana, Marketa, Lada, Luber, Alex Costa, Andre and Marcus.

Special thanks to Prof. Zhihong Jia and Ms. Min Zha with whom I have shared my office during the past four years. Also thanks are due to the Indian community friends here in Trondheim who have reminded me every now then of the other enjoyable things and social life in Trondheim. To name a few, Thanks to, Mr.Nagaraj Govindaraj Vinayagam, Mr. Vinothkumar Palanisamy, Dr. Navaneethan Muthuswamy, Mr. Valamburi Ganesan and Mrs. Sathya Valamburi, Dr. Kaushik Jayasayee, and Mrs. Kamakshi Bharathan, Mr. Mayilvahanan Alagan Chella and his family, Mr. Rengarajan Soundararajan, Mr. Balamurugan Loganathan, Mr. Rajesh Raju, Mr. S.M Ganesan, Dr. Ramprasad Yelchuru and his family, Mr. Giri Gunnu Rajsekhar and Mr. Phani Kumar Manne. I am also grateful to my ex-housemates, Dr. Dhandapani Kannan and his family, Mr. Nishaharan Varatharajah, Mr. Gnanam Vettivel and his family, Mr. Håken, Mr. Anders Lund and Mr. Eirik Holgernes for the great time we had at Kornblomstveien 12B, during my first year in Norway.

Very special thanks goes to my parents, Mrs. Janaki Subbarayan and Mr. Subbarayan Ranganatha Rao, my sister, Ms. Lakshmi and her family for supporting me all these years in my life and my friends (DAAD mates, schoolmates and Techians and IITians) for their moral support and fun we had together all these years.

Finally I thank my sweetest and dearest wife, Aishwarya, without whom I would not have completed my PhD in time and for being there, loving and supporting me in good and bad times and for her patience to bear with me all these years.

கண்ணுடையர் என்பவர் கற்றோர் முகத்திரண்டு
புண்ணுடையர் கல்லா தவர்.

திருவள்ளுவர்

The learned alone have eyes on face
The ignorant, two sores of disgrace.
Thiruvalluvar

Dedicated to my parents, my wife and Sachin Ramesh Tendulkar- The God of Cricket

Abstract

The main objective of this study is to develop a high strength Al/Mg based composites at a reduced cost as compared to high strength Al-Mg binary alloys produced by equal channel angular pressing (ECAP). Typical high strength Al-Mg solid solution alloys are difficult to process due to low ductility and a high strain hardening rate. Hence, the study was aimed at processing such a composite by mixing pure aluminium and AZ31 Mg alloy chips, followed by further processing by ECAP. This would not only ease the processing of such material owing to pure Al in the system, but also demonstrate high strength due to the presence of magnesium. The entire study was divided into four parts.

The first part involved investigations on the effect of temperature and strain on the microstructural evolution of pure aluminium. Here, pure Al samples were processed by ECAP route Bc up to 8 passes at room temperature (RT), 150°C, 250°C and 350°C. The microstructure evolution was studied using the electron back scattered diffraction (EBSD) technique. EBSD scans were used to investigate grain shape, grain size distribution, grain size evolution and their related mechanisms. Stored energy calculations were performed using the mean grain size and grain boundary fractions from the EBSD data. The calculations were used to identify the evolution of geometrically necessary boundaries (GNBs) and statistically stored dislocations (SSDs) with respect to increasing strain. Recovery and recrystallization mechanisms were also investigated in relation to temperature and strain. Microhardness investigations were performed and correlated to the microstructure evolution. Finally, texture evolution was studied using the x-ray goniometer. The texture development corresponded to the different mechanisms involved in the microstructure evolution of pure Al. These investigations were conducted to understand the behaviour of

pure Al with increasing strain and temperature with the purpose to obtain significant grain refinement even at high temperature when co-deformed with the less deformable AZ31 alloy.

The second part concerned fabrication of an ECAP'ed Al/AZ31 core-shell structure at elevated temperatures. One intended to understand the interfacial characteristics when Al and the AZ31 alloy were co-deformed. Accordingly, the interface characteristics were studied using SEM equipped with an energy dispersive spectrometry (EDS) system, but also applying the electron probe microanalysis (EPMA) technique. The samples were initially deformed at 250°C for 1 pass. However, since AZ31 cracked at that temperature, samples were processed at 350°C. Effects of increasing strain up to 6 passes by ECAP route Bc was investigated, and mechanisms were laid out for different constituents formed at the interface. Tensile tests and microhardness measurements were also performed and correlated to the influence of the interface. The microstructure evolution was also investigated using EBSD scans and linked to the interface effect.

Thirdly, a macrocomposite was prepared using the knowledge obtained from the above results on pure Al and Al/AZ31 rod type structure. It was concluded that at least 350°C was necessary to co-deform AZ31 and Al without premature cracking. Also, only a limited strength could be achieved with a single brittle interface owing to the thick intermetallic phases. Hence multiple interfaces containing intermetallics was foreseen as necessary along with a high deformation temperature ($T \geq 350°C$). A high strength composite was thus prepared using screw extrusion of a mixture of Al and AZ31 chips at ~ 400°C. The as-extruded sample was further processed by ECAP at 200°C for 1 pass. The microstructure of the Al/Mg macrocomposite was then studied using optical and electron microscopy techniques. Tensile tests were performed on both as-screw extruded and the ECAPed samples to demonstrate the increase in yield strength and ultimate

tensile strength (UTS). In addition, the ECAPed specimen was further rolled to ~2.7 von Mises strain for comparison. The macrocomposite was also compared to existing alloys, and the advantages and limitations of the same were also discussed. The potential of the Al/Mg macrocomposite prepared from chips was explained accordingly based on the microstructure, presence of intermetallics, solid solution of Mg in Al and their dislocation interactions.

A crude physical model was developed from the results obtained for the Al/Mg macrocomposite and the possible importance of this new genre of material was explained. Potential applications of such a material were also suggested.

The final and fourth part consisted of a study of Al/Al and Al/3103 sheet composites. This study was aimed at a better understanding of the interface characteristics. Al/Al composites were used to study the experimental parameters and the Al/3103 composites were used to study the effect of interface on material behaviour at constant experimental parameters. Al/Al samples were subjected to ECAP by placing three sheets on top of each other and then ECAPed at RT. Different parameters such as, effect of specimen length, effect of back pressure, effect of pressing speed and the effect of surface roughness were studied. Microstructure was also investigated using EBSD data. Al/3103 samples were processed at constant optimised experimental parameters obtained from the Al/Al study. The microstructure evolution was studied using EBSD and transmission electron microscopy (TEM) images. Finally, the microstructure evolution in the Al/3103 composite was correlated to the Al/Mg macrocomposite processed by ECAP.

TABLE OF CONTENTS

Chapter 1 Introduction

The demand for aluminium products in the automotive sector is continuously increasing owing to the technology development and global focus on emissions and CO2 energy reduction. Figure 1.1 reveals the evolution of Al usage in a car since 1980 as reported by European aluminium association (EAA) [1].

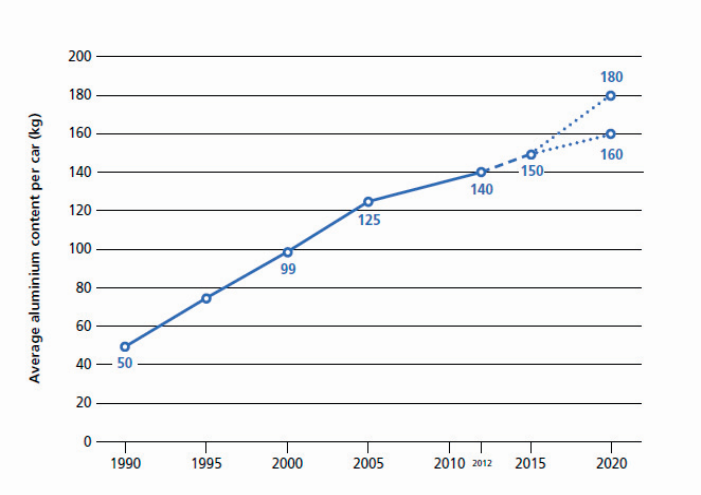

Figure 1.1. Evolution of aluminium content in a car [1].

A clear increase in the amount of Al used per car can be observed. Aluminium is a light metal and hence reduces the amount of fuel spent by automobiles thus reducing the emission of greenhouse gases. Further, recycling of aluminium is increasingly emphasized and represents a sustainable development. It is believed that about 95% of the energy can be saved by recycling Al. Further, 95% of the Al can be recovered by recycling within transportation and especially for cars [1]. Currently, efforts are being taken to reduce the usage of steel and iron alloys in order to save energy. Al and Mg alloys and their composites are emerging as the alternative materials to replace steels. The potential applications of Al based materials in a car are numerous and they are normally part of new technological

developments. Figure 1.2 gives an account of potential applications of Al in a car [1].

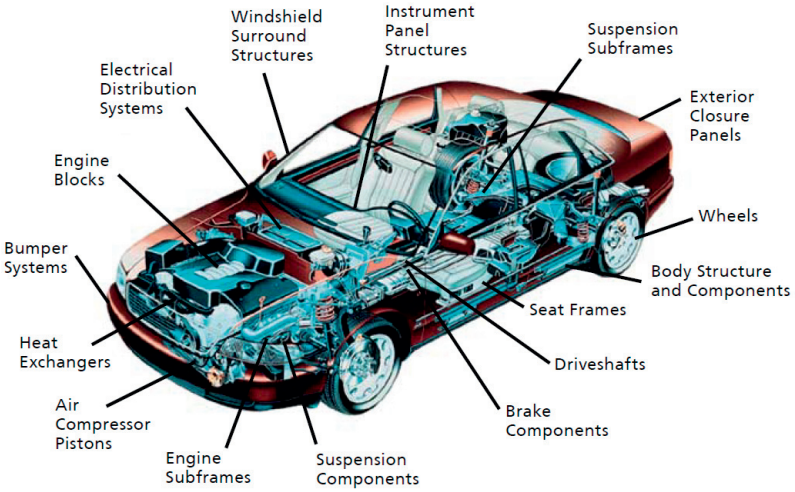

Figure 1.2. Potential applications of aluminium in a car [1].

Moderate to high strength Al alloys are widely used in automotive, construction, electronics and space sectors. Most of these conventional alloys are cast, shaped and heat treated before entering the market.

Recently, the application of severely plastically deformed Al-Mg alloys has gained importance owing to their light weight. In addition, high solubility of Mg in Al leads to high strengthening potentials. However, the cost of these alloys can be relatively high. Hence, in order to increase both the strength-to-weight ratio, as compared to conventional Al alloys, and at the same time reduce the energy consumption, fabrication of a novel Al/Mg composite processed from laboratory made chips was initiated. The approach can be extended further to replace chips with industrial scrap. The present study is therefore a preliminary stage in the development of a new genre of bi-metal composites.

Detailed and systematic investigations were recently carried out on the energy reduction and the feasibility of processing Al alloy scrap by equal channel

angular pressing (ECAP) [2]. It was found that processing scrap by SPD would lead to a maximum of 93% energy reduction.

In order to develop the bi-metal composite, pure aluminium and an Mg-3wt% Al alloy (AZ31) was considered. The magnesium alloy was primarily selected due to the difficulty in machining pure Mg into fine chips/turnings, i.e. pyrophoric nature. However, the AZ31 alloy is difficult to extrude in the as-cast condition and hence pure Al was added in order to facilitate successful plastic deformation of the bi-metal.

Accordingly, the entire study was divided into four parts. The first part involved a systematic study aiming to understand the behaviour of pure aluminium with regard to deformation temperature and strain. A series of samples of pure Al were processed at room temperature (RT), 150°C, 250°C and 350°C by ECAP route Bc up to 8 passes. The pure Al study was intended to gain knowledge on the evolution of the microstructure in Al at higher temperatures as compared to RT, in particular, exploring whether the possible grain refinement could be achieved at elevated temperatures. The higher temperature was considered necessary for compensating for the deformation difficulty of the AZ31 alloy used.

In the second part, co-deformation of Al/AZ31 by ECAP was carried out as a core-shell structure at the lowest possible elevated temperature in order to obtain both grain refinement and also avoid premature cracking in the Mg alloy. This part also intended to examine the interface characteristics that can be achieved by combining pure Al with the AZ31 alloy. These investigations were primarily focussed on the composition at interfaces, bonding mechanisms and further the effect of interfaces on the surrounding microstructure evolution.

The work was then, in the third part concentrated on the development of the desired composite containing Al and AZ31 machined chips. It involved high temperature co-extrusion of the chips into a composite containing Mg and Al islands. Subsequently, further processing of the composite by ECAP at a relative lower temperature was carried out. In addition, the composite was subsequently deformed at RT by cold-rolling. Finally, all these samples were subjected to tensile tests for estimating the yield strength, ultimate tensile strength (UTS) and the

elongation to fracture. The mechanical test results were promising as compared to the existing conventional counterparts.

Finally, the fourth part involved investigations of layered laminates processed by ECAP. These investigations were aimed at optimising the process itself by understanding the mechanisms and the evolution of interfaces upon ECAP processing, and also revealing the behaviour of such laminates subjected to optimised experimental parameters.

In summary, the present study provides an insight into fabricating a new genre of bi-metal composites that contain Al and Mg and how to improve their properties by controlling the processing parameters. For instance, the strain hardening rate can be influenced by controlling the amount of dissolution of Mg in Al by lowering the deformation temperature and strain. Hence, these types of materials provide a wide choice of alternate alloys for specialized applications challenging the currently used conventional light alloys. However, the present work is probably the first work of its kind and should be considered as such. Nevertheless, it is believed that the originality of the work is present and could open doors for more investigations on these types of bi-metal composites.

Chapter 2 Literature background

2.1 Equal channel angular pressing (ECAP)

2.1.1 General introduction to ECAP

Professor Richard Feynman's famous lecture titled "*There is a plenty of room at the bottom*" in the late 1950's has inspired many scientists around the globe to study "Nanotechnology" [3]. Both the top-down approach involving the breakup of macro entities into small nano-entities and the bottom-up approach involving the aggregation of atoms and molecules and their subsequent build up into nano-entities have been developed. ECAP is one of the techniques used in the top down approach to fabricate ultrafine grained and nano grained metals, alloys and composites. ECAP was first developed in the former Soviet Union by V.M.Segal [4]. Although this technique has been well proven to introduce high shear in the material leading to better properties, it did not capture the interest of the west and the development was much limited to within the then USSR. It is the enhanced superplasticity at high strain rates at relatively low temperatures observed in these materials that led to the now commendable NANOSPD organization [5] and wide research efforts around the world (NanoSPD conferences, Bulk Nano Materials (BNM) conferences, private communications between eminent research experts, collaborations etc.).

ECAP involves pressing the material through an intersection of two equal channels at an angle to each other. In common practice, most of the dies have a right angled intersection. A typical schematic illustration of a right angled ECAP die is shown in Fig 2.1 [6].

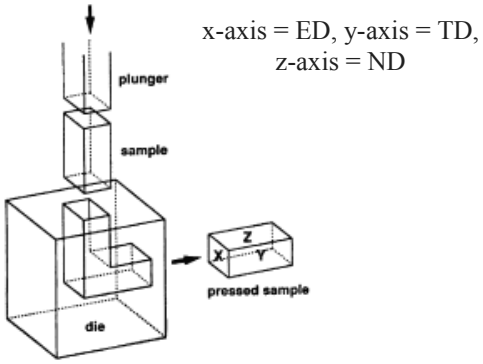

Figure 2.1. Schematic representation of typical ECAP process [6].

The principle of ECAP is based upon "simple shear" type deformation. When a billet is pressed through the channel, the material undergoes simple shear at the intersection of the two channels. As the two intersecting channels are equal in dimensions, the sample does not undergo a change in the shape and hence it is possible to induct more strain into the sample without any change in the cross section. The geometry of the die determines the direction in which simple shear occurs and the amount of shear. The total amount of accumulated shear deformation is proportional to the number of pressings. Hence, very large strains can be achieved even at room temperature for most of the Al alloys.

2.1.2 Physical characteristics

Geometry of the die

The geometry of the die is a very important physical characteristic that determines the macro shear plane and the amount of shear that can be imparted during each pass. The die geometry can be represented by three parameters, angle Φ between the intersecting channels, the arc of curvature, ψ, and the cross section area. Among these parameters, arc of curvature is a parameter representing the practicality of the processing and is defined as the arc of curvature of the outer edge of the ECAP die. A schematic diagram representing the flow of a unit cubic element during the course of the various ECAP routes is shown in Fig 2.2 [7] .

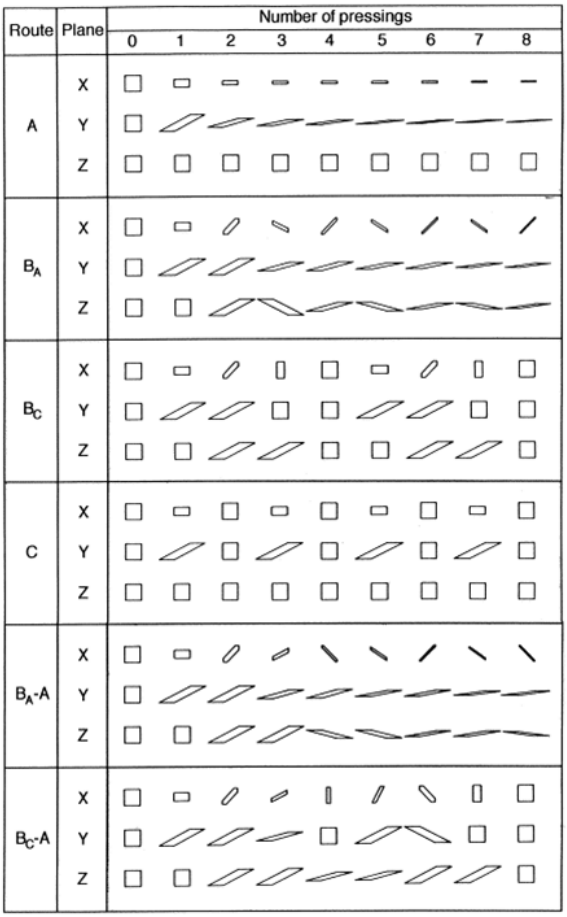

Figure 2.2. Schematic representation of shearing of a cubic element during each ECAP pass up to 8 passes for the six standard deformation routes [7].

Iwahashi et al. [8] derived an equation to calculate the shear strain (γ) imposed on the material during each pass and is given by

$$\gamma = 2\cot\left(\frac{\Phi}{2}+\frac{\psi}{2}\right) + \psi\,\mathrm{cosec}\left(\frac{\Phi}{2}+\frac{\psi}{2}\right) \qquad (2.1)$$

It can be seen that the above equation reduces to $\gamma = 2\cot\frac{\phi}{2}$, when ψ=0. The accumulated equivalent strain after a number of passes, N, was expressed as,

$$\varepsilon_n = \frac{N}{\sqrt{3}}.\gamma \tag{2.2}$$

Figure 2.3 shows the variation of equivalent strain as a function of intersecting angle, Φ, and the arc of curvature, ψ [9]. It can be seen that the effect of ψ is insignificant when the channel angle is greater than 90°. Also the strain decreases linearly with increase in the channel angle beyond 90°. For acute angles, the increase in strain is exponential with a decrease in the angle (Φ) and increasing ψ has a small negative effect on the equivalent strain.

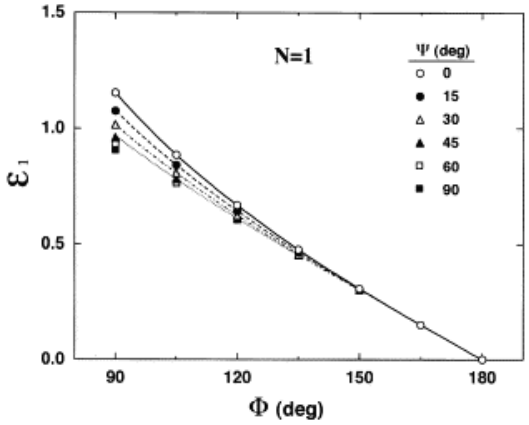

Figure 2.3. Equivalent strain as a function of angle of intersection and angle of curvature for 1 pass ECAP [9].

Effect of pressing speed

The effect of pressing speed on the material processing is limited. The present results so far show that there is minor influence of the pressing speed on the microstructure evolution. Yamaguchi et al. [10] showed that adiabatic heating during high pressing speeds is important only for high strength materials processing. However, Berbon et al. [11] reported that for pure Al and an Al-1% Mg

alloy, recovery occurs at lower pressing speeds and hence the microstructure becomes more equiaxed at lower speeds.

Effect of processing route

There are four basic processing routes which are mostly used in ECAP [12], e.g. shown in Fig 2.4. Processing routes influence the activation of different slip systems during pressing by different shearing patterns. This leads to the evolution of significantly different microstructures for different processing routes.

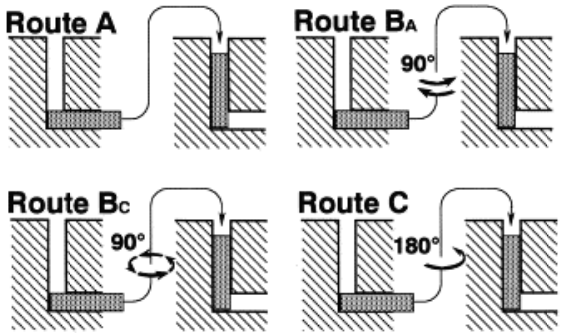

Figure 2.4. Schematic representation the most commonly used processing routes in ECAP [12].

The shearing patterns for the three basic routes A, B and C are shown schematically in Fig 2.5 [13].

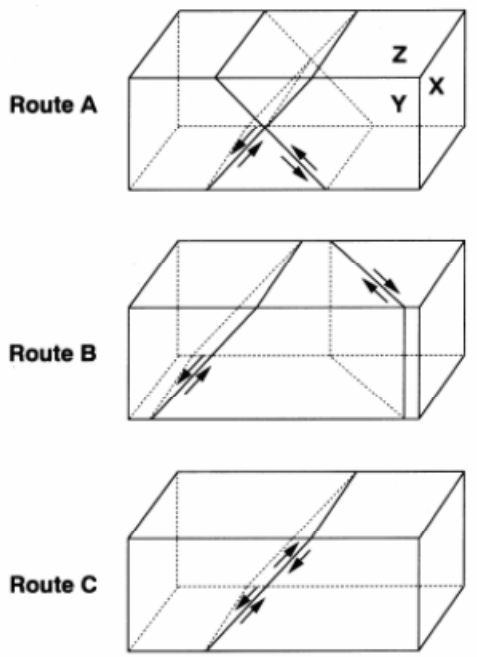

Figure 2.5. Schematic representation of the shearing patterns for different basic processing routes in ECAP [13].

Route A involves repeatedly pressing with no rotation of the sample during subsequent pressings. In route B_A, the sample is rotated 90° in alternate directions between consecutive passes. Route C is carried out by rotating the sample 180° between the passes, whereas route B_C involves rotating the sample 90° in the counter clockwise (CCW) direction after each pass. Figure 2.2 above shows a schematic representation of the shear patterns in all the three planes up to 8 passes of ECAP. Firstly, it is obvious that the routes A and B_A have similar shear characteristics, while route B and route C are similar. Strain is redundant in route B_C after every fourth pass and after every second pass for route C. Also route A and route C do not show any deformation along the z-plane. Hence, for a better grain refinement, imposed by successive shear, route B_C can be preferred over route A and B_A because the strain is reversed in route B_C and allows imparting of more strain than either of them. Route B_C is also better than route C because route

C does not undergo deformation along the z-plane. However, the selection of a particular route or combination of routes, tailor-made to suit the desired application of the material and a combination of the basic routes can also be used to enhance the properties.

Effect of back pressure

Back pressure (BP) is another value added parameter that could enhance the grain refinement mechanism in ECAP processing. The back pressure has lot of influence in the ECAP process itself and also in the grain refinement. Figure 2.6 shows a schematic representation of the BP die [14]. BP majorly prevents cracking in samples that are less ductile. Valiev et al. [15] showed that copper samples, which cracked after 12 passes, revealed no cracking even after 16 passes in the presence of back pressure. It is believed that back pressure also influences the grain size evolution. McKenzie et al. [16] reported that an AA6016 alloy showed smaller average grain size after pressing with an increase in back pressure. Back pressure can also be used to provide more uniform metal flow during ECAP. Without the BP, there can be a possible dead zone where the metal is not sheared and also formation of a wide fan shape zone instead of a narrow shear line type zone. BP can be applied either by a separate punch on the exit of the channel (Fig 2.6) [17] or a viscous medium, put in front of the sample can also be used [6].

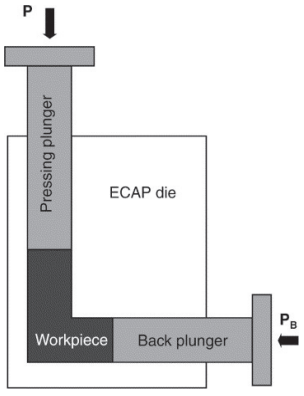

Figure 2.6 Schematic representation of the BP die [14].

2.1.3 Material characteristics

Grain refinement

Grain refinement in materials processed at room temperature (RT) by ECAP is one of the most striking features of ECAP and the most studied area of interest. The ability of the ECAP in fabricating extremely fine grains down to few tens of nanometres makes it a very attractive technique both to research and commercial applications. Pure metals generally show a relatively larger grain size compared to their alloys. Iwahashi et al. studied the microstructure of polycrystalline pure aluminium after ECAP [13]. They found that with one pass, the material obtained a similar behaviour as that in a single crystal, e.g. with the formation of sub-grains with low angle misorientation between them. With an increase in strain ~4, say four passes, the sub-grains evolve themselves into high angle grain boundaries. Pure Cu and Ti also showed similar results wherein the initial sub-grain structure evolves into a more homogeneous equiaxed structure with the increase in number of passes [18]. The grain size after 6 passes for pure Al by route B at room temperature was found to be close to 1 μm, whereas the grains were refined close to 400 nm after 6 passes in an Al-1 wt% Mg alloy [19].

Homogeneity of the evolved grain structure depends on many parameters such as processing route, effective deformation temperature, size of the processing die channel, stacking fault energy of the material, etc. The presence of second phase particles also affects the grain structure homogeneity. It has been shown that route Bc is the most suited for obtaining homogeneous microstructures as compared to other routes [20, 21]. The size of the processing die channel, to some extent affects the homogeneity. Smaller dimensions mean that the shear zone is close to the ideal narrow shear zone and hence the material undergoes more uniform shear. Larger dimensions would result in a wider shearing zone, thus increasing the area of the fan shaped zone. The area of the dead zone located at the bottom of the channel intersection is also higher with increased dimensions. This leads to a non-homogeneous structure of the material. Further, the stacking fault energy (SFE) of the material also affects the homogeneity condition [22]. In previous studies, Al had larger grain size and a much more homogeneous structure

than Cu, which showed a very fine grain size but an inhomogeneous structure [23, 24]. Ni, which has an SFE between Cu and Al, showed finer grain size than Al and also a reasonably homogeneous grain structure. Materials with high stacking fault energy tend to form more homogeneous structures but at the expense of grain refinement.

Mechanical properties

Materials subjected to ECAP generally demonstrate high strength at the expense of loss of ductility. A significant increase in the yield strength (YS) and the ultimate tensile strength (UTS) can be expected when materials are pressed at room temperature. Although a decrease in ductility is observed even after post-ECAP treatment. ECAP usually shows higher ductility than the conventional cold working processes. For example, Horita et al. showed that an ECAP'ed 3004 alloy is more ductile than cold rolled 3004 alloy [25]. Processing of pure Cu also yielded similar results [15]. Deformation mechanisms such as grain boundary sliding and grain rotation have been proposed as an explanation for the observation of increased ductility. Wang et al. [26] reported that pure Cu processed by ECAP followed by rolling at liquid nitrogen temperature and then heating to 450 K, produced a bi-modal grain size distribution, leading to increased strength along with increased ductility. The engineering stress-strain curves in Fig 2.7 show that curve E (93% cold worked and annealed at 200°C for 3 min) has a significant higher combination of strength and ductility than curve A (annealed, coarse grained Cu).

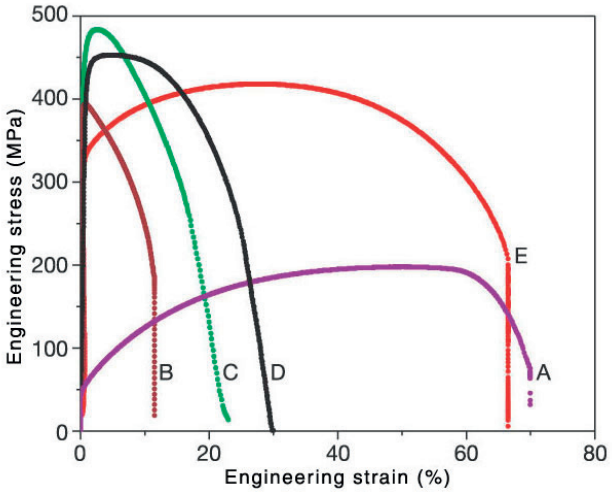

Figure 2.7. Engineering stress-strain curves of nanostructured Cu. Curve A, annealed, coarse-grained Cu; B, room temperature rolling to 95% cold work (CW); C, liquid-nitrogen-temperature rolling to 93% CW; D, 93% CW + 180 °C, 3 min.; and E, 93% CW + 200 °C, 3 min [26].

Alternatively, thermo-mechanical treatments after ECAP can also lead to an increase in ductility. Pre-ECAP solid-solution treatment combined with post-ECAP precipitation hardening in a 6061 Al alloy lead to an increase in about 40% of the UTS and yield stress [27]. ECAP of the 2024 Al alloy in solutionised condition followed by low temperature ageing also showed excellent enhancement in yield strength coupled with good ductility [28].

Texture evolution

Plastic anisotropy of a polycrystalline material makes the evolution of texture an important issue, especially when combined with the investigations of the microstructural evolution. Texture evolution is very important as the deformation kinetics and mechanisms represent a tool for understanding ECAP'ed materials. As the material deforms, the arrangement of the active slip systems determines how the microstructure evolves. The microstructure evolution depends on various factors such as initial texture and composition of the material, die geometry (ψ and die angle) and other processing parameters such as temperature, pressing speed and

the processing route. There have been a number of reports on the texture evolution of FCC metals and alloys during ECAP [29-34]. The texture evolution in ECAP is explained by the simple shear model. The simple shear model was first proposed by Segal et al. [35] and assumes a simple shear occurring along the intersection of the die channel. However, the die angle is assumed to be a sharp right angle i.e. ψ is 0, and that there is no superimposed friction. The ideal orientations during ECAP for FCC materials for a 90° die [1], are shown in pole figures (Fig 2.8) and tabulated below (Table 2.1).

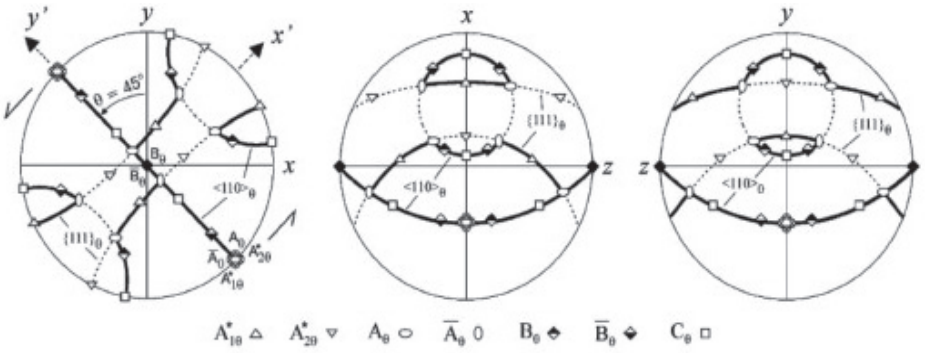

Figure 2.8. Typical texture (1 1 1) pole figures of textures with the main ideal orientations ($A^*_{1\theta}$, $A^*_{2\theta}$, $A_\theta/\bar{A}_\theta$, $B_0/\bar{B}_0$, C_θ) and fiber textures (<1 1 0>$_\theta$ and {1 1 1}$_\theta$) of FCC materials after ECAP with $\Phi = 90°$. The textures are derived for negative simple shear by a 45° CCW-rotation around the *z*-axis. The arrows indicate the sense of shear. Here x, y, z axes are ED, ND, TD respectively [36].

Table 2.1 Main ideal orientations in simple shear deformation of FCC materials. Given in the $\Phi_2 = 0°$, 45° and 90° sections with $\Phi_1 = 0–270°$ only [36].

Notation	{hkl}<uvw>	Euler angles (°)		
		Φ1	Φ	Φ2
*A1**	(111) [-1-12]	35.26/215.26	45	0/90
		125.26	90	45

*A2**	(111) [11-2]	144.74	45	0/90
		54.74/234.74	90	45
A	(1-11) [110]	0	35.26	45
$\bar{A}$	(-11-1) [-1-10]	180	35.26	45
B	(1-11) [110]	0/120/240	54.74	45
$\bar{B}$	(-11-1) [-1-10]	60/180	54.74	45
C	{001}<110>	90/270	45	0/90
		0/180	90	45

The ideal orientations for different crystal structures are determined by their respective simple shear textures except that in ECAP the shear direction is 45º in the XY plane (see Fig 2.1). However, the experimental observations of the textures show that there is a deviation of about 20º from the ideal orientations and this 'tilt', as referred to by Beyerlein et al. [36], is due to a variety of reasons. These authors argue that the tilt is very similar to the effect of axial stresses as in fixed end torsion or from the lengthening/shortening of the specimen in ECAP.

The effect of the broad deformation fan-zone originating from the round corners of the die was also discussed as to the deviation of ideal orientations. Apart from the above mentioned experimental effects, the polycrystal model itself could be a source of error. While the model used by Beyerlein et al., i.e. the so called visco plastic self-consistent (VPSC) model, showed some tilting around TD, the effect of the latent hardening coefficient cannot be neglected. The texture evolution gets even more complicated when using route C and route Bc as the sample is rotated 180º and 90º respectively every turn. This leads to some ambiguity in this present model. The most important fact is that the simple shear model cannot explain the increase in texture intensity with increasing number of passes up to 4 by route Bc. The saturation of texture after a large number of passes has so far not been clearly explained. However, Gholinia et al. [37] proposed that a disproportionate effect of the plane strain component existing in the deformation zone during ECAP, may lead to rotation of a primary 'B' fibre around TD.

Material characteristics also affect the evolution of texture during ECAP. Stacking fault energy (SFE) is one such material property that leads to different textures. Low SFE FCC materials show a {112} <110> instead of a strong C component [38]. However, SFE can only be effective at higher strains when there is a transition in deformation mechanisms such as from twinning to more dominant dislocation glide and a corresponding sub-structure evolution etc. Also sub-structure by itself, affects the evolution of texture. Deformation bands formed within the grains may use different slip systems and hence alter the slip activity. Each deformation band evolves during subsequent passes leading to a change in the overall texture components. Xue et al. [39] studied Cu subjected to ECAP and found that the boundaries formed along the primary ECAP shear plane in the first pass add an intersecting set of boundaries after second pass. This leads to the refinement by recovery of intersecting junctions and equiaxed grains are being formed.

Deformation twinning is a more important mechanism in HCP materials than in FCC materials with low SFE. In FCC metals, twinning assists in grain refinement. However, twinning in HCP materials has a greater effect in the evolution of deformation texture. The texture thus evolved depends on alloying content, c/a ratio, strain rate, initial orientation and temperature [36, 40-43]. Most of the research in the texture evolution in HCP materials has been restricted to Mg and Ti alloys [44-48]. Different twinning modes and twins were observed in different HCP materials. For example, in Ti alloys and pure Ti subjected to ECAP, $\{10\bar{1}1\}$ twinning is more prominent [48, 49]. In ECAP of Zr $\{10\bar{1}2\}$ twinning seems important to the texture evolution in addition to crystallographic slip [50]. $\{10\bar{1}2\} < 10\bar{1}1 >$ twins are the most commonly observed twinning mechanisms for ECAP of Mg and its alloys [44-46, 51]. Interestingly, Be did not undergo twinning at all at high temperatures [52, 53] after ECAP. This could be the effect of changing the operating mechanism from twinning to dislocation glide.

Reports on texture evolution of high stacking fault metals at room temperature show that a typical torsion texture with a partial 'B' fibre {hkl}<110> along with a less strong partial 'A' fibre {111}<uvw> are present [36]. Further, Li

et al. [54] reported a comparative study between Cu and Al (Fig 2.9). Cu showed uniform orientation density along these fibres but Al showed orientation distributions highly concentrated around C_θ. This was attributed to the difference in SFE of the metals. El Danaf [55] studied the texture evolution of commercially pure Al after 16 passes at RT and showed that the texture was similar to that observed by Li et al. and a weakening of texture occurred with increasing passes.

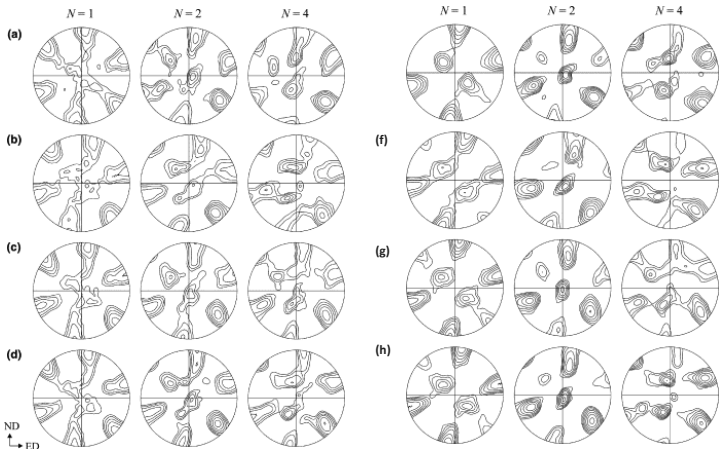

Figure 2.9. (1 1 1) pole figures showing textures in Cu samples after 1, 2 and 4 passes: (a) measured; (b)–(d) simulated by the VPSC model using deformation history from the (b) simple shear, (c) fan and (d) FE models, respectively. Pole figures (e)-(h) are similar to (a)-(d) but are for Al [54].

The initial texture is also an important factor for the final textures evolved. The ECAP processing route may also have a large influence on twinning in HCP materials. For example, Shin et al. [49] showed that different deformation textures evolved with different processing routes for an initial basal texture along the billet axis of CP-Ti. Although the first pass introduced $\{10\bar{1}1\}$ compressive twins, further processing lead to different textures. Route A led to secondary twinning, however no twinning was observed by route Bc and C.

2.1.4 Other material properties

Fatigue

Fatigue is an important material property for metals processed by ECAP. Fatigue can be divided into two regimes viz. low cycle fatigue (LCF) and high cycle fatigue (HCF) with regard to the subjected strain amplitudes. HCF involves resistance to crack initiation and in LCF crack propagation occurs easily. Ideally, a material should have high strength and high ductility to sustain a high fatigue endurance in both LCF and HCF regimes. Fortunately, UFG materials have a high strength combined with sufficient ductility, and thus are expected to fit into both these regimes as good fatigue resistant materials.

Under stress controlled loading, the UFG materials exhibit very good fatigue resistance. For instance, Hanlon et al. [56] studied fatigue in both nanocrystalline (NC) Ni and a cryorolled Al-Mg alloy and stated that UFG Ni produced by electrodeposition exhibits substantially higher resistance to stress-controlled fatigue compared to conventional polycrystalline Ni. However, strain controlled fatigue life of the UFG materials has shown disappointing results for Al alloys and Cu. The fatigue life was found to be shorter than conventional coarse-grained Cu and Al alloys counterparts [57, 58]. The reason for such behaviour was attributed to low thermal and mechanical stability and a strong tendency to recover the highly-deformed UFG structure [6]. Crack initiation upon localization of strain by cyclic loading, subsequently leading to failure by shear bands (SBs) is an important damage mechanism in UFG materials [6]. The formed SBs were ‘‘persistent’’ as they reappeared on the surface after re-polishing [59]. However Vinogadrov et al. [60] studied the SPD Ti under fatigue and found that even under strain controlled testing, the same material showed an improved behaviour. This was attributed to a synergistic effect due to work hardening and grain refinement. Thermally active processes such as recrystallization and grain growth also seemed to occur due to cyclic plasticity. Hashimoto et al. [61] showed that lamellar grains undergo recrystallization whereas equiaxed grains do not undergo recrystallization in SPD commercially pure Cu during fatigue at room temperature.

Efforts to optimise the fatigue performance of UFG metals and alloys by ECAP have been going on. For instance, increasing the number of passes leads to a high monotonic strength and thereby improvement in the fatigue limit [62]. Thermo-mechanical treatments have also been found to assist the fatigue performance of ECAP'ed metals and alloys. Susceptibility of shear banding can be reduced in Cu and the fatigue life in LCF can be improved by an order of magnitude by annealing for 10 min at 523 K after ECAP [63]. Also post ECAP rolling of CP-Ti can lead to a significant increase in the fatigue limit [64]. Similar results have been observed for Al-Mg alloys [65].

Valiev and Langdon [6] suggested three approaches for fatigue life improvement. "*The first is the achievement of a compromise between strength and ductility in a minimum number of passes of ECAP, where only a single pass is used, whenever possible, since this is a cost-effective procedure employing relatively small imposed strains. The second is the achievement of the maximum possible strength leading to high cycle fatigue life. The third is the achievement of both high strength and ductility through multipass ECAP leading to enhanced low and high cycle fatigue lives*."

Superplasticity

Superplasticity is a phenomenon where materials plastically deform to very large strains without any geometrical instability under tension at low stresses. This was first demonstrated by Jenkins [66] in 1928. Superplasticity can be achieved only under certain conditions [67], here directly referring:

- The material must have fine grains which are equiaxed ($\leq$10 μm) and must be thermally stable at high temperatures. This makes eutectic and eutectoid compositions quite suitable for producing finely dispersed phases. However with the advent of severe plastic deformation where the grain size can be reduced to a few hundreds of nanometres even in pure metals, superplasticity can be achieved in a wide variety of metals and alloys at a strain rates greater than 10^{-3} s^{-1}.

- The strain rate sensitivity factor of the material must be high (m ≥ 0.3) as compared to ~0.1 seen in conventional deformation. The strain rate sensitivity 'm' is not a constant parameter and varies with temperature, strain rate and grain size. It increases with increasing temperature and strain rate but decreases with increasing grain size. This sensitivity is also influenced by solid solution contents such as in the Al-Mg alloys.
- The processing temperature typical for superplastic materials is quite high (T≥0.5Tm) where, Tm is the melting temperature of the material.

Grain boundary sliding (GBS) has been widely accepted as the most important mechanism for superplasticity in such metals and alloys [68-72]. However, GBS is often accompanied by several other mechanisms such as diffusion creep, a combination of GBS and GB migration and a combination of all the mechanisms [73, 74]. The steady state deformation rate which determines the rate of grain boundary sliding, is given by

$$\dot{\varepsilon} = \frac{ADGb}{kT}\left(\frac{b}{d}\right)^{p}\left(\frac{\sigma}{G}\right)^{n} \qquad (2.3)$$

where, $\dot{\varepsilon}$ is the steady state deformation rate, A is a dimensionless constant, D is the diffusion coefficient, G is the shear modulus, b is the Burgers vector, k is the Boltzmann's constant and T is the absolute temperature. Further, σ is the applied stress, d is the grain size, p is the inverse grain size exponent and n is the stress exponent. The diffusion coefficient D is defined by,

$$D = D_o \cdot e^{-\left(\frac{Q}{RT}\right)} \qquad (2.4)$$

Here, D_o is a material constant, Q is the activation energy for the process, R is the gas constant and T is the absolute temperature. Although grain refinement in SPD treated materials has been of interest for researchers per se, superplasticity has been a particular motivation for the processing of materials by ECAP and other SPD techniques.

Superplasticity in UFG materials processed by ECAP and other SPD techniques involves a material with grain size of ~200 nm with a lot of strain induced into the material. This leads to superplasticity at lower temperatures and higher strain rates [75-77]. This facilitates superplastic forming at shorter time

intervals, hence making the process viable for commercial low cost and high volume components rather than the present application being restricted to high end components for the defence sector and space sector [78].

Valiev et al. [79] showed that it was possible to achieve superplasticity in Al-Cu-Zr and Al-Mg-Li-Zr alloys at a strain rate of 10^{-2} s^{-1} with a failure strain of 1180% at 623 K. Superplasticity at temperatures as low as 433K for Al-Mg alloys was also reported by ECAP [78]. The following figure, Figure 2.10 shows superplasticity as a function of ECAP strain for the Al 7034 alloy processed at different temperatures [80]. It can be seen that with an increase in the number of passes, the material can be strained at higher strain rates as compared to that of materials subjected lower number of passes.

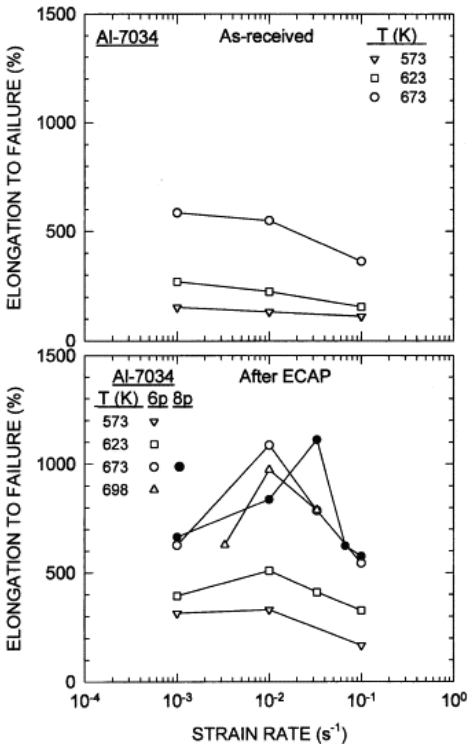

Figure 2.10. Failure strain as a function of uniaxial strain rate at various temperatures for 7034 Al alloy subjected to ECAP [80].

Islamgaliev et al. [81] also reported a shift in the peak values of failure strain vs. strain rate to the higher strain rate regime for an Al-Mg-Li-Zr alloy. Although significant elongation has been observed in Al alloys, superplasticity is of more expediency to the difficult-to-deform brittle materials, such as Mg alloys which cannot be deformed at room temperature due to the limited number of active slip systems in the HCP crystal structure. Mg alloys are lighter than Al alloys and hence could lead to a greater range of materials to be used in the automotive, aeronautics and defence sectors. However, magnesium and its alloys are much difficult to deform by ECAP especially at room temperature and grain refinement is limited. Yamashita et al. [82] showed that there was no significant refinement even after 3 passes ECAP at 673 K in pure Mg.

Further Horita et al. [83] showed that extrusion of Mg alloys before ECAP can lead to significant improvements in superplastic properties. They reported superplastic behaviour of Mg-Al alloys by such combined processing up to an elongation of about 800% at 473 K at a strain rate of 10^{-4} s^{-1}.

Functional properties

Severely plastically deformed materials are not only strong and potentially robust for structural applications but also exhibit enhanced functional properties. The most interesting and the most widely studied of these materials are Ti and its alloys for biomedical applications. Commercially pure Ti (CP Ti) and Ti-6Al-4V alloys are attractive for bio-medical applications mainly for their bio-compatibility, excellent corrosion resistance and high strength [84]. However, applications of pure Ti are limited owing to relatively low strength compared to other Ti alloys.

On the contrary, second generation Ti based bio-materials containing alloying elements such as Nb, Mo, Ta, Zr etc. are not only very expensive but also increase the weight and toxicity of the material. Hence SPD treatment of CP Ti and Ti-6Al-4V alloys seems promising owing to a significant increase in strength and bio-compatibility. For instance, Park et al. [85] demonstrated that UFG CP Ti and Ti-6Al-4V showed enhanced osteoblasts response compared to conventional coarse grained material. The increase in the surface energy by reducing the grain size has been attributed to the increased bio compatibility.

Another important aspect of the bio-materials is the elastic modulus (E). Humans demand an E value close to that of the bone whereas surgeons demand an E value higher than bone to avoid spring back during and after the operation procedure [86]. One way to increase strength without increasing the modulus is to increase the number and density of dislocations. This means that processing of these materials by SPD will make them more compatible for both patients and surgeons.

Shape memory alloys (SMAs) such as NiTi alloys exhibit enhanced shape memory effect and high strength by ECAP and other SPD techniques [6]. Pushin et al. [87] investigated $Ti_{49.8}Ni_{50.2}$ SMA by ECAP at 450°C up to 12 passes. It was found that the yield strength increases up to 100% and the UTS increases ~30% after ECAP. Also, the ductility of the SMA was increased by annealing the alloy at 500 °C after ECAP. The grain size was reduced from 80 μm to 250 nm after 8 passes. All the transformation temperatures decreased with increasing number of ECAP passes and were much lower than in the quenched state. The grains were also found to be thermally stable up to 500°C. The maximum recoverable strain, which is another important shape memory parameter, also increased with increasing number of ECAP passes. Stolyarov et al. [88] observed a record 9% maximum recoverable strain for the same material after four ECAP passes which could not be obtained by conventional processing and thermo-mechanical treatments.

SPD treated materials also show enhanced magnetic properties. A comparative study of anisotropic ($(Nd_{0.55}Ho_{0.45})_2(Fe_{0.8}Co_{0.2})_{14}B$) and isotropic ($Y_2(Fe_{0.8}Co_{0.2})_{14}B$) magnetic materials on the hysteresis magnetic properties, showed that both anisotropic and isotropic materials exhibit high coercive fields compared to conventional bulk materials [89]. Suehiro et al. [90] also observed a change in the magnetic property of the Cu - 6.5 wt% Co magnetic alloy. They found that the coercive force increased almost twice with one pass ECAP. They attributed this to the fragmentation of Co particles in the matrix by ECAP shear.

2.2 ECAP of aluminium and its alloys

2.2.1 ECAP of pure aluminium

Aluminium and its alloys are one of the widely studied materials by severe plastic deformation. This is because of high deformability and the ease of processing. Pure aluminium with its distinct material characteristics such as high SFE, high ductility, high recovery rates etc., is particularly interesting to study as it can be useful both for examining processing behaviour and material behaviour during ECAP. Extensive studies have been conducted on ECAP of pure Al at room temperature [13, 91-101].

Early works by Iwahashi et al. [101] and [13] showed that pure Al can be refined to 1 μm after 4 passes at room temperature and attributed the grain refinement due to the sub-grain evolution into high angle grain boundaries. Skrotzki et al. [102] investigated the microstructure evolution of ultra-high purity Al subjected to ECAP at room temperature and found that 5N Al (99.999% pure) undergoes discontinuous dynamic recrystallization at RT. Horita et al. compared the grain refinement behaviour of pure Al, pure Au and pure Cu [103]. They found that with increase in the number of passes, both 4N Al and 5N Al decrease in hardness after increasing up to 2 passes. However, 5N Al showed a more significant decrease as compared to 4N Al.

On the contrary, the hardness values of 3N Cu and 7N Cu increased with increase in the number of passes and showed similar hardness values. In other words, purity did not affect the microstructure evolution in Cu as much as it did in Al. 5N Au showed that no difference in hardness values were observed between RT processing and processing at 427 K. It was concluded that the difference in SFE of the Al, Cu and Au contributed to the difference in their grain refining behaviour.

2.2.2 ECAP of Al alloys

Al alloys can be broadly classified into two groups based on their precipitation behaviour viz. non heat treatable alloys and heat treatable alloys.

Non heat treatable alloys

Non heat treatable Al alloys are strengthened from the solid solution, i.e. of solute elements dissolved in Al. Although some precipitation may occur, principal strengthening mechanisms are due to solute hardening. Some of the alloys that fall into this category are commercial purity Al (1xxx series), Al-Mg alloys (5xxx series), and Al-Mn alloys (3xxx series). For these alloys, the effect of alloying has a very significant role to play in microstructure evolution and regarding mechanical properties. Figure 2.11 shows the UTS versus different conditions and elements for non-heat treatable alloys [21]. The 'O' temper refers to annealed condition, H18 refers to the cold rolled condition and H38 refers to the cold rolled and stabilized condition. Al-Mg alloys are very interesting among the non-heat treatable Al alloys. This is because, Mg is the most preferred solid solution strengthening element owing to its high solubility and high atomic size misfit (13%).

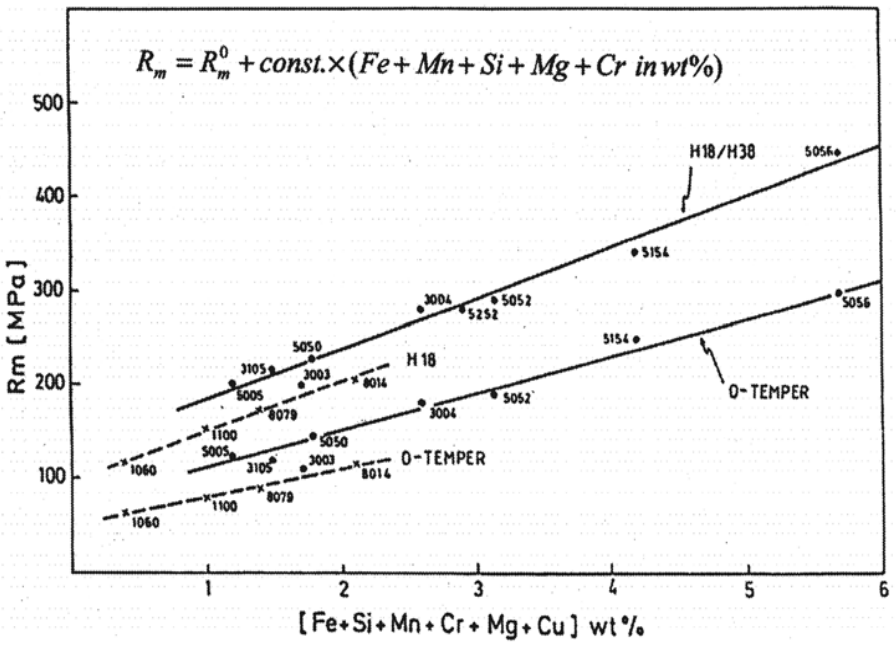

Figure 2.11 UTS as a function of alloying additions in aluminium for various non-heat treatable alloys under O-temper and as-rolled conditions [21].

A lot of research is being carried out in Al-Mg alloys by SPD [104-110]. Murashkin et al. [111] showed that the 1570 Al-Mg alloy can demonstrate a "super strength" of 950 MPa and with a reasonable 4.5% ductility after high pressure torsion (HPT). ECAP of Al-2.7 Mg showed that the strength can be increased to 400 MPa after only 4 passes [112]. Annealing of a 5083 Al alloy deformed at cryogenic temperature has been reported to show a good combination of uniform elongation and high strength [113]. This is due to the suppression of recovery when processed at cryogenic temperatures.

Thermal stability studies in Al-3 wt% Mg showed that non-equilibrium grain boundaries were formed during ECAP and this led to a microstructure instability and recrystallization of the alloy at 500-550 K [114]. Recently, Chen et al. [105] observed ultrafine grained twins in an Al-Mg alloy processed by ECAP at cryogenic temperatures. Furthermore, studies on a UFG Al-1 wt% Mg alloy showed that in compression, stage III work hardening decreased and vanished at a grain size of about 350 nm. They attributed this to the effect of grain size on kinetics of substructure evolution during the initial deformation [115]. The deformation behaviour of an Al-1.5 wt% Mg alloy subjected to ECAP at room temperature revealed an increase in strain rate sensitivity compared to the coarse grained counterpart [116]. It was also reported that the peak strain rate sensitivity shifted to lower temperature after ECAP.

Heat treatable alloys

Heat treatable alloys are generally stronger than the non-heat treatable counterparts as they gain strength from precipitation of one or more elements dissolved in the matrix. The most common heat treatable Al alloys are Al-Cu alloys (2XXX series) and Al-Mg-Si (6XXX) alloys. A large number of studies were carried out on ECAP of Al heat treatable alloys, e.g. both to increase strength and for studying the precipitation behaviour under high strain [117-134]. Precipitation in these alloys can occur at room temperature (age hardening) as in Al-Cu alloys, or at elevated temperature (precipitation hardening) as in AA6082 alloys or during deformation (dynamic precipitation). Precipitation during ECAP has not yet been fully understood. For instance, Roven et al. [135] observed dynamic precipitation

during ECAP of an Al-Mg-Si alloy even at room temperature, however Cabbibo et al. [136] reported that during ECAP of the 6082 Al alloy, Mg_2Si precipitates were cut and fragmented by dislocations while Si particles dissolved into the matrix. A similar dissolution of theta prime and theta particles were observed in an Al-Cu alloy [137]. Another study on the 2024 Al-Cu alloy showed that grain growth was limited even after annealing at 300°C [138].

Microstructure evolution of Al and Al alloys

The primary aim of most of the research on pure Al and its alloys is to study the effective grain refinement that can be achieved by ECAP. Aluminium has a high SFE of about 160 mJm^{-2} [139] and undergoes a high rate of recovery [140]. In general, deformation involves the formation of geometrically necessary boundaries (GNBs) and incidental dislocation boundaries (IDBs) or statistically stored dislocations (SSDs). With increase in strain, GNBs evolve into deformation bands and increase the misorientation of boundaries with progressive strain. IDBs on the other hand, arrange themselves to a low energy configuration into cell structures [140]. However, certain alloy systems such as the Al-Mg alloys, do not form cells, instead, classical Taylor lattices are created [141].

The evolution of these structures has been reported in the literature [141-145]. Bay et al. [142] suggested a list of deformation structures for pure Al, e.g. cell blocks (CBs) which contain dislocation cells sharing same operating glide systems, dense dislocation walls (DDWs) separating cell blocks and contain high density of dislocations compared to the cells, microbands (MBs) which are similar to CBs but have smaller dislocation cells and higher misorientations than CBs.

The theory explaining the microstructure evolution depends on low energy dislocation structures (LEDS), as formulated by Kuhlmann-Wilsdorf [146-150]. This theory also postulates the grain refinement mechanism.

The LEDS hypothesis states that "*among all microstructures that are in equilibrium with the applied stresses and are in principal accessible to dislocations, those are formed which minimize the energy of the system composed of the deforming material and the applied tractions"* [150]. During the initial stages of deformation involving small strains to intermediate strains, grains deform

to form an array of CBs separated by DDWs thus collectively fulfilling the Taylor assumption for strain accommodation. However, the different CBs formed as separate volume elements is due to the fact that not all the regions within the grain have five independent operating slip systems as predicted by the Taylor theory owing to the energy criterion. GNBs are thus formed to accommodate the strain imposed to the material. These GNBs arrange themselves into DDWs which subsequently evolve into laminar boundaries (LBs) separating CBs at large strains.

Figure 2.12 gives a schematic representation of these deformation structures [142]. The IDBs are formed by statistical trapping of mobile and stored dislocations with in a cell. At large strains, layers of elongated cells or sub-grains are formed in bands as a lamellar structure parallel to the deformation direction and are separated by LBs.

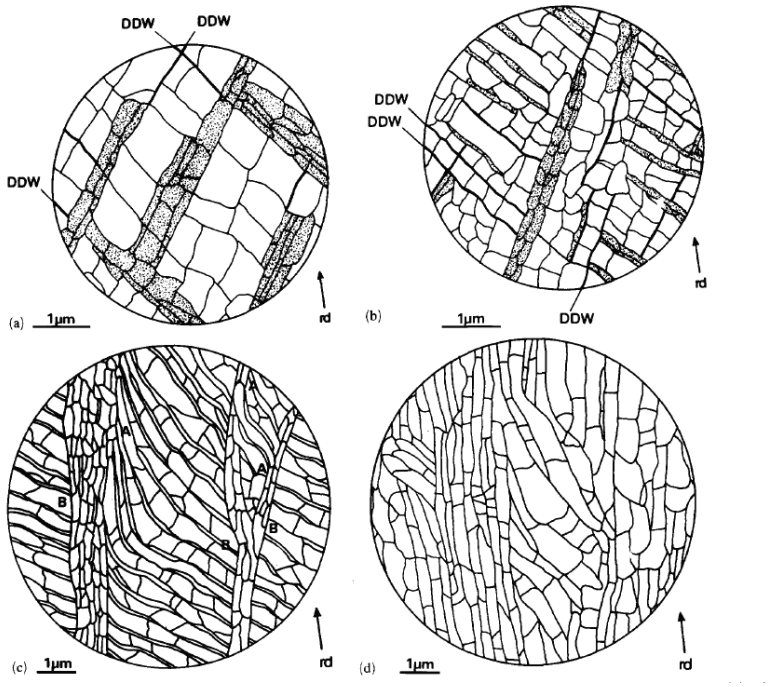

Figure 2.12. Schematic illustrations of the changes in microstructure during cold rolling of pure aluminium. (a) 30% rolled, (b) 50% rolled, (c) 70% rolled, (d) 90% rolled In (a)and (b) the DDWs are drawn as thick lines and sub-grains in MBs are dotted [142]. Markings A and B represent the two types of DDW-MB structures.

Furthermore, the spacing of GNBs and IDBs decreases with increasing strain or decreasing processing temperature. GNBs gradually increase their misorientation with increasing strain more rapidly up to ~20° as compared to the IDBs which increase slowly and reach a maximum at ~3° (see Fig 2.13 for the case of room temperature of nickel) [151].

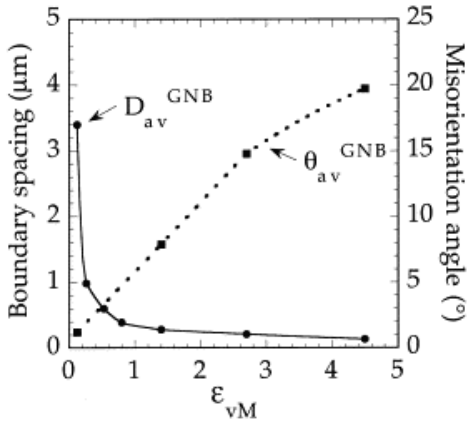

Figure 2.13. Boundary spacing (D) and misorientation angle (θ) as a function of strain in cold-rolled Ni [151].

All the above explanations have been based on rolling pure Al and those alloys forming cell structures on deformation. However, for SPD treated materials, the microstructure evolution is very similar except that the kinetics of deformation is altered. With increase in number of ECAP passes, the misorientation increases and the sub-grains accumulate additional dislocations thus resulting in sub-grain rotation forming high angle grain boundaries (HAGBs). By this, grains are formed from pre-existing sub-grains [6, 18].

A typical Al-Mg binary phase diagram [152] is shown in Fig 2.14. The maximum solubility of Al in Mg is 11.8 at% at a eutectic temperature of 437°C according to the above phase diagram. Apart from the solid solution of Al in Mg and vice versa, different intermetallic phases can be identified from the phase

diagram. The compound with an approximate stoichiometry of Al_3Mg_2, is the β phase and is within the range of 38.5 to 43.3 at% Mg, however, pure Al_3Mg_2 has a complex crystal structure and melting point of about (refer). The line compound R is at the composition of 42 at% Mg. The compound γ, with α Mn structure, at 45 to 60 at% Mg has the stoichiometry $Mg_{17}Al_{12}$ (58.6 at% Mg) [152]. This phase was found to occur at the grain boundaries either as narrow bands or octagonal precipitates inside grains [153]. The maximum solid solubility of Mg in Al is 18.9 at % at the eutectic temperature of 450°C but above ~5.5% of Al, intermetallics such as Mg_5Al_3, Mg_5Al_8, Al_3Mg_2 etc. [154, 155] are formed at the grain boundaries making the material brittle. A table ontaining properties different phases in Al-Mg phse duiagram is shown as table by Ignat et al. [156]

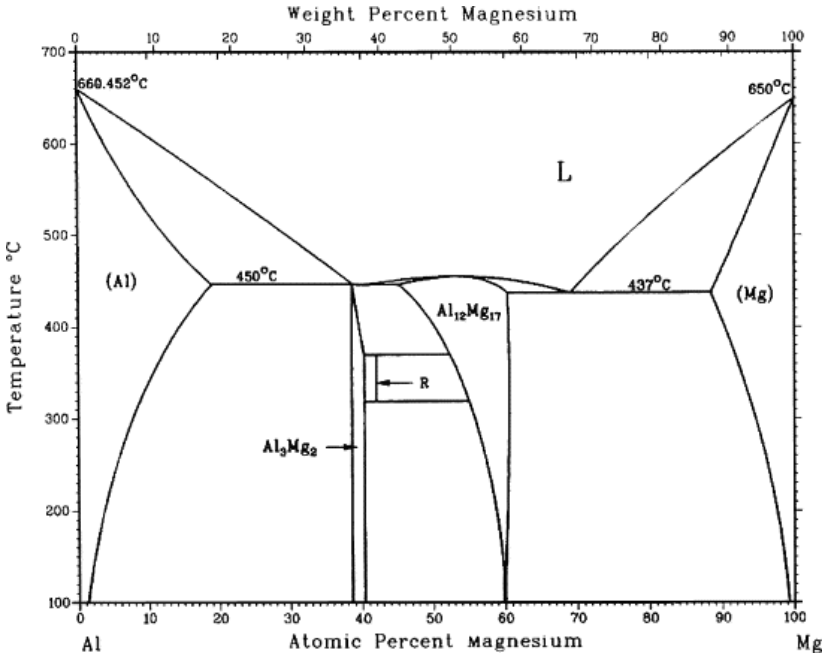

Figure 2.14 A typical Al-Mg binary phase diagram [152]

The addition of solute elements such as Mg reduces the formation of cell structures in Al. A study on deformation of Al-Mg alloys showed that formation of the cell structure is suppressed during tensile testing upon increasing addition of Mg, and cells completely disappear for an Al-7 wt% Mg alloy [157]. Transmission electron microscopy (TEM) studies on an Al-5.5 wt% Mg alloy showed that in non-cell forming metals and alloys, the microstructure evolution is characterized by a combination of three dimensional Taylor lattices (TLs), microbands and domain boundaries (DMBs) [141].

The Taylor lattice is a low energy incidental dislocation structure formed by rearrangement of by mutual trapping of dislocations, both mobile and stored, in order to reduce the energy per unit length of the dislocation lines. Figure 2.15 shows a schematic representation of such a situation. DMBs are boundaries formed between the TLs by GNBs in order to accommodate strain at minimum possible energy.

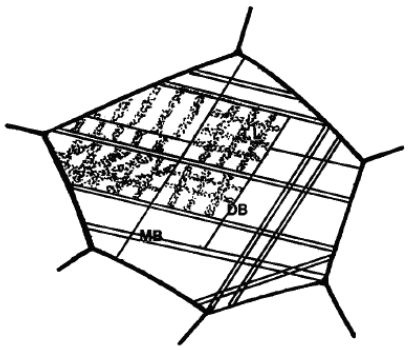

Figure 2.15. Schematic drawing of the subdivision of a grain in Taylor lattice forming metals. The dotted regions represent the Taylor lattice. DB in the picture refers to domain boundaries (DMBs) and MB= microbands [141].

Although, this theory explains well the evolution of microstructures by conventional deformation techniques, microstructure evolution of such materials by SPD is less understood. ECAP of solid solution Al alloys with higher quantities of solutes are difficult to process for large number of passes owing to significant solute interactions with dislocations and strain localization leading to fracture.

ECAP of high solute Al-Mg alloys at higher temperatures have been reported to undergo some localized static recrystallization in conjunction with increasing misorientations of the sub-structure, hence forming HAGBs with subsequent passes [158]. Dilute or low alloying content alloys are reported to evolve similar structures as in pure Al where the sub-structure forms initially and on repeated pressing increases the misorientations into HAGBs. The only difference is that the cell size in dilute Al-Mg alloys is much smaller than those observed in pure Al [18, 105, 159].

Furthermore, processing of heat treatable alloys has primarily been attributed to efforts to maximize strength by altering precipitation kinetics and at the same time refining the grains. The general idea is that during SPD processing, the precipitates may either break down into finer constituents thus effectively pinning the dislocations or dissolve into the matrix.

Al-Mg- Si alloys and Al-Mg-Sc alloys are the most studied heat treatable Al alloys by ECAP. These are difficult to process to large strains at room temperature and higher temperatures are employed. Investigations on an Al-Mg-Sc alloy deformed at 300°C revealed that the microstructure evolved by continuous dynamic recrystallization (CDRX) in conjunction with static recrystallization in between the passes [160]. Also, the driving force for static recrystallization has been attributed to high dislocation density sub-structures suppressing recovery.

Another study on the 6082 Al alloy showed that while recrystallization can be observed in the reference alloy at 315 °C, addition of Sc retained the ultra-fine structure up to 450°C [117]. An interesting report on the microstructure evolution of Zr and Zr+Sc dispersoids in a 6082 Al alloy [161], showed that $Al_3(Sc_{1-x},Zr_x)$ were highly coherent with the matrix and hindered the formation of HAGBs. The dispersoids also pinned dislocation tangles, thereby generating large fraction of free dislocations. Further, β-Mg_2Si particles were fragmented and became finer thus pinning the dislocations. However, Si particles dissolved during SPD processing.

2.3 ECAP of magnesium and its alloys

Magnesium and its alloys are very much preferred in automobile industry, aerospace industry and defence sector over a large variety of other materials. This is primarily due to their low density, corrosion resistance and good damping capacity. Unlike Al alloys, which contain a vast range of alloying elements, the alloying in Mg is restricted to Al, Zn and rare earths for most of the commercial applications. Both Zn and Al increase the strength by solid solution strengthening. Zn has an enhanced effect on strengthening compared to Al [162] as seen in Fig 2.16. However, addition of Al to Mg increases the castability of Mg and hence preferred over Zn.

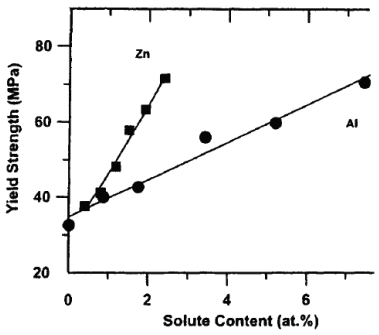

Figure 2.16. Effect of Zn and Al on the yield strength of Mg [162].

A number of reports have been published on ECAP of pure magnesium [42, 82, 163-175]. However, most of the results indicate inability of significant grain refinement in pure Mg as compared to FCC materials and Mg alloys. The need for a high processing temperature, cracking due to twinning and presence of shear localization due to anisotropy, are reasons why the ECAP process is ineffective. However, with the application of back pressure, grain size can be refined to ~1 μm at room temperature without any premature cracking [167]. Similarly, ECAP of Mg alloys is very difficult at room temperature owing to the hexagonal close packed (HCP) structure making it brittle at RT. Hence, plastic deformation of Mg alloys is limited to high temperature processing.

However, recently a number of reports have been published on the microstructure evolution and properties of Mg alloys after ECAP [176-197]. It has so far been believed that grain refinement in Mg and its alloys by ECAP is difficult, primarily due to the HCP crystal structure and the high processing temperature involved [82]. Figueiredo and Langdon [198, 199] laid down certain principles for processing Mg alloys. By extruding prior to ECAP, grain refinement in the ultra-fine regime is possible [200-204]. Alternatively, the usage of back pressure to prevent premature cracking was suggested [205]. Also increasing the channel angle Φ and successive reductions in processing temperatures [206, 207] were suggested to refine grains in Mg alloys by ECAP.

Within the grain refinement studies, authors propose a grain refinement mechanism where the new grains nucleate at the grain boundaries due to stress concentrations at boundaries along with subsequent activation of both basal and non-basal slip processes. This leads to an initial bimodal grain size distribution and with an increase in the number of ECAP passes, a more homogenized grain structure evolves. This is in contrast to a previously proposed refinement mechanism based on shear bands and dislocation entanglements within a grain [208].

Another important aspect of processing Mg alloys by ECAP is the superplastic characteristics. Early works on the AZ91 alloy by Mabuchi et al. [209] showed that elongation up to 661% can be obtained by ECAP processing at 473 K. Viscous glide of dislocations has been attributed to such low temperature superplasticity. Another study by the same group on an AZ91 alloy showed that the existence of non-equilibrium boundaries exhibited lower superplasticity than with equilibrium boundaries [210]. Here, the effect of long range stresses associated with non-equilibrium boundaries hindering grain boundary sliding are used as an explanation.

Further, processing of a commercial ZK60 Mg alloy showed a record tensile ductility of about 2040% at 220°C at 4 x 10^{-4} s^{-1} [211]. Also, a combination of extrusion and ECAP for a Mg-9 wt% Al alloy revealed low temperature and high strain rate superplastic properties even after 2 ECAP passes along with a significant grain refinement [201]. In the latter case, the alloy deformed up to

270% at 473 K at a strain rate of 10^{-2} s^{-1} under tension. Another study compared the extruded AZ61 alloy and ECAP'ed AZ61 alloy and showed that the ECAP'ed alloy exhibited an extraordinary elongation of 1320% at 473 K at a strain rate of 3.3 x 10^{-4} s^{-1} while the extruded counterpart elongated only 70% under identical conditions [212]. Also, a number of other papers reporting tensile elongations greater than 500% in Mg alloys have been published in the recent years [213-215].

The texture evolution in Mg during ECAP is not yet clearly understood. Texture studies performed on magnesium single crystals processed by ECAP at 503K for one pass were compared to the simulations using the VPSC model [216]. It was found that the orientation of the [001] and <100> axes with regard to the die channel was very important as it influenced the activation of different deformation modes during the initial stages of deformation. They also found that with the [001] axis parallel to the TD, activation of non-basal slip systems (both pyramidal and prismatic) occurred which prevented cracking. Absence of such a texture resulted in cracking along with the formation of shear bands. Beausir et al. [217] provided the ideal orientations for Mg by simple shear as shown in Table 2.2 and in Fig 2.17.

Table 2.2. Ideal orientation fibres for HCP materials processed by ECAP [217].

Fibre	Φ1°	Φ°	Φ2°
B	45	90	0-60
P	45	0-90	30
Y	45	30	0-60
C1	105	90	0-60
C2	165	90	0-60

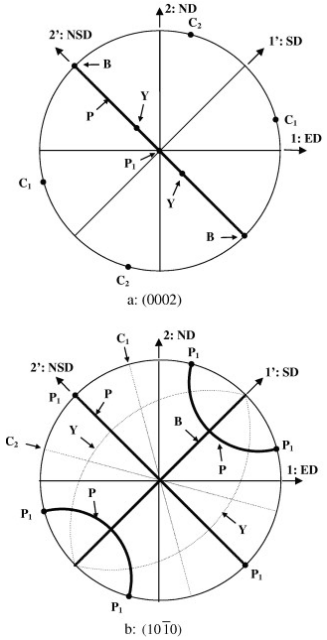

Figure 2.17. The locations of the ideal fibers for ECAP textures of magnesium under simple shear loading : (a) (0 0 0 2) and (b) (10-10) pole figures. The main fibres are identified with thick thick lines are further identified in Table 2.2[213].

Further, Beausir et al. showed that textures contained *c*-type fibres with their axis of rotation parallel to the *c*-axis, whereas the nucleation of grains during dynamic recrystallization (DRX) took place in positions rotated around the *c*-axis. They also found that while large lattice rotations take place in route A and route C around the TD axis, the textures rotated little and also not around TD in route Bc. Li [218] also studied the texture evolution of HCP materials and found that the stable orientations for ECAP involve characteristic alignments of the <a> axis or <c> axis with respect to the macroscopic deformation axes. Another study by Al-Maharbi et al. [219] on AZ31B, with two different initial textures revealed that there was a significant influence of the initial texture to the final texture. They found that the activity of prismatic slip reduced the amount of DRX occurring during ECAP of this alloy. Also the anisotropy increased when the initial texture had basal poles parallel to ED, while basal poles parallel to TD led to a relatively more random texture.

2.4 ECAP of bi-metals

Bi-metals are materials that consist of two dissimilar metals joined together at an interface. The interface can be either a single interface or multiple interfaces. Bi-metals are widely used for industrial applications that either demands a combination of characteristics that would be difficult to achieve if a single material is used. For instance, hack-saw blades have teeth made of martensitic steels joined to high carbon steel base using laser beam or electron beam welding to provide harder teeth with a soft base, i.e. being strong and less brittle respectively. In the present context, bi-metals can provide a similar combination of properties. Fabrication of Al/Mg bi-metal by SPD is particularly interesting due to the possible high strength to weight ratio as Mg is lighter than Al [220-222]. This also serves for the ease of processing Mg, which is difficult by conventional deformation methods and by SPD methods when treated separately [82, 223].

Severe plastic deformation is well preferred and also suitable for producing bi-metals, e.g. primarily due to the enhanced diffusion rates occurring during SPD. The existence of non-equilibrium boundaries, microcracks, dislocations and high densities of grain boundaries lead to ultrafast diffusion and is not possible by conventional materials [224]. Fujita et al. [171] showed that coupled Al-Mg diffusion has much lower activation energy than that is required for diffusion of Mg into Al in a fine grained state. Other important perspective here is the high strain involved such as in ECAP. High strain can assist bonding even at low temperatures and simultaneously reduce mean grain size. A detailed report by Paramsothy et al. [225] on Al/Mg bi-metal processed by disintegrated melt deposition (DMD) showed that addition of Al in Mg can lead to enhanced toughness. The mechanism involves mechanical interlocking, e.g. not only arresting of crack front by the Al region but also crack-tip blunting in the Mg region. This is believed to be a very unique feature of the bi-metal configuration. Also, beneficial high compressive strains can be obtained by encasing a Mg core within aluminium in a bi-metal configuration [226].

Of all the current SPD processes, accumulative roll bonding (ARB) is the most widely used technique for processing Al based bi-metals [46, 227-231]. Brokmeier et al. [228] observed the formation of $Mg_{17}Al_{12}$ and Al_3Mg_2

intermetallics by rolling magnesium and aluminium to 50% reduction at 400°C followed by ARB. The texture in Mg was a typical basal plane texture and was stronger than in accompanying 5052 Al alloy. ARB of 99.5% pure Al/AZ31 yielded a reduction of the grain size to 0.5 μm and 1 μm in the Al and AZ31 region respectively [232]. A recent report on the microtexture of Al/Mg ARB sheets showed that the presence of shear bands changed the microtexture of Al and Mg layers [230]. Although ECAP has been used for producing metal matrix composites (MMC), see [222, 233-236], the application of ECAP for Al based bi-metals is much less studied [237, 238]. Narooi et al. [238] focussed on the strain field and extrusion loads in Al-Cu ECAP. They showed that by decreasing the outer corner angle, the extrusion load increased and the strain inhomogeneity decreased. In another study, Liu et al. [237] investigated the processing of Al/Mg laminates by ECAP and emphasized the annealing behaviour.

2.5 ECAP of metal matrix composites

The processing of metal matrix composites (MMCs) by ECAP has been of added interest in the recent past. Most of the MMC processing has been limited to Al matrix composites [220, 239-247] and magnesium based composites [235, 248-251].

Earlier works by Valiev et al. [79, 244] dealt with ECAP of a 6061 Al alloy reinforced with Al_2O_3 particles. Other work engaged on an alloy containing 10 vol% Al_2O_3 and showed that the microhardness increased by a factor of ~2 and the grain size was reduced to a 1 μm after processing at RT [240]. However, the Al_2O_3 particles did not refine as much as the microstructure. In another study on a 6061 Al alloy composite reinforced with 20% Al_2O_3, it was reported that a very homogeneous distribution of particles could be observed after ECAP [245].

Furthermore, studies on an Al-5 wt% TiB_2 composite showed that even though the particle size remained unchanged, the matrix grain size was refined to ~500 nm after 4 ECAP passes. Also TiB_2 distribution became homogeneous after 4 passes [243]. These results point to the advantages of using SPD for processing MMCs. It is very difficult to achieve a homogeneous distribution of the reinforcements by conventional fabrication methods such as casting [252, 253].

Processing of a 2009 Al alloy with 15 vol% SiC_w whiskers [239] reported on the feasibility of processing ultra-fine grained MMCs by SPD and demonstrated the possibility of superplasticity.

Magnesium based composites processed by ECAP have not been explored as much as Al based composites. A comparative study on the AZ31 alloy containing 2 wt% Al_2O_3 processed by ECAP and by conventional extrusion showed that the former obtained a significant grain refinement and more homogeneous distribution of particles as compared to the extruded state [249]. Also, nano-particles increased the texture intensity of the basal and prismatic planes in both extruded and ECAP'ed conditions. Another interesting study on carbon nanotubes (CNT) reinforced Mg deformed by ECAP showed that the microstructure development was slowing down during initial passes. However, in the later stages, an accelerated kinetics of the hydrogen adsorption/desorption kinetics was observed [251]. Fast diffusion through the cores of CNTs was attributed to such fast hydrogen adsorption/desorption kinetics. Effect of ECAP on Mg_2Si reinforced in- situ Mg composite showed that after 2 passes, grain refinement becomes difficult owing to the hard-to-deform Mg_2Si particles in the matrix [234]. However, high strength of the composite was obtained after ECAP. They also proposed effective use of Si to precipitate type II Mg_2Si particles which can be easily refined by ECAP as compared to type I Mg_2Si particles.

The literature background on ECAP principles, processing routes, different materials, mechanisms, properties etc. shows that there have been an increasing number of publications over the last decade on novel concepts and ideas. Although the works are both fundamental and application oriented, a clear understanding of certain concepts involved during ECAP is still lacking. For instance, the grain refinement mechanisms involved in Mg alloys, texture evolution of HCP materials, precipitation behaviour of Al alloys, studies on bi-metals, etc. There is also a demand for novel applications of ECAP such as hydrogen storage, scaling up etc. The present scenario thus provides a lot of motivation and future scope for processing materials by ECAP for advanced and novel applications.

Chapter 3 Experimental procedures

The present study focuses on the development of novel light bi-metals involving Mg and Al. The aim is to achieve high strength combined with reasonable ductility and that these materials can be processed relatively easy at low cost. However, before such materials can be processed, the behaviour of Al and Mg deformed under various experimental conditions and different temperatures should be understood. The corresponding interface properties and structures, mechanical properties and microstructure evolution were therefore carefully examined. The work has been divided into three sections reflecting various types of studies performed on the following materials:

- Commercially pure (CP) Aluminium (99.9%)
- Al/AZ31alloy bi-metals
- Al based sheet composites

The experimental procedures for each of these type of materials are explained in the following paragraphs.

3.1 CP Aluminium studies

Investigations carried out on CP Al is regarded as a preparation part of the study that involves the co-deformation of CP Al and an AZ31 Mg alloy by equal channel angular pressing (ECAP) explained in section 3.2.A literature survey on the processing of Mg and its alloys showed that a high processing temperature is necessary in order to avoid any premature cracking during ECAP [82, 199]. On the other hand, studies reported on the processing of pure Al by ECAP showed a significant effect of temperature on the grain refinement mechanisms [6, 18]. By lowering the processing temperature, the recovery rate of Al decreases, thus resulting in a much finer mean grain size. Processing a combination of Al and Mg in bulk form is thus paradoxical and hence a detailed study was conducted on CP Al samples at different temperatures spanning from RT to 350°C in order to reveal the grain refinement characteristics with regard to processing temperature. The aim was to achieve both a reasonable refinement of grains in Al as well as high enough

temperature in co-deformation to achieve a successful and a strong dissimilar metal bonding between aluminium and magnesium when processing the Al/AZ31 alloy bi-metal system.

3.1.1 Composition

The composition of pure Al used in the present studies is shown in Table 3.1. The raw material was a cast billet obtained from Hydro Aluminium AS, Norway. The as-received billet was cut into a number of 19.8 x 19.8 x 100 mm^3 bars at the NTNU workshop. All samples were then homogenized at a temperature of 400ºC for 4 hours in a Scandia TC 901 induction furnace and then cooled in open air before processing.

Table 3.1. Composition of CP Al used in the present investigations.

Element	Al	Si	Fe	Mn	Mg
Wt %	99.9	0.033	0.059	0.0006	0.0004

3.1.2 Processing

Prior to the ECAP experiments, the specimens were cleaned with acetone, dried and then preheated at the processing temperature for about 30 minutes in a SCANDIA TC 901 furnace.

ECAP of all samples was performed in an in-house designed right angled ECAP die [21] with a channel cross section of 19.8 x 19.8 mm^2, channel angle 90º and ψ =20.6º giving an equivalent strain of about ~1 per pass [8]. The sample surfaces and the bottom and the sides of the punch tool were coated with OMEGA99® lubricant (based on petroleum and graphite) to minimize friction. A semi-continuous ECAP processing method was used where one sample was used to push another sample [254]. The samples were pressed at a speed of 2mm/s and were rotated by 90° in the counter clockwise direction (CCW) after each pass (route Bc) and processed to 1, 2, 4, 6 and 8 passes at RT, 150°C, 250°C and 350°C. After required number of passes, the samples were quenched in cold water. Figure

3.1 shows an overview of the various processing steps involved in the CP Al studies.

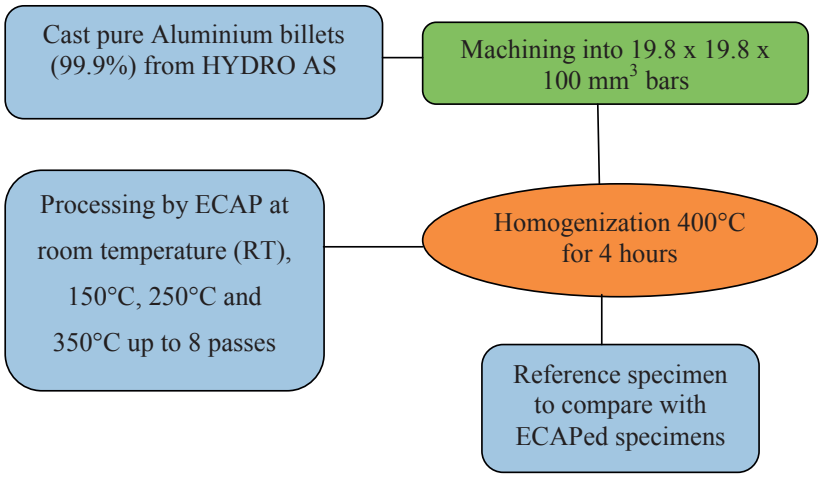

Figure 3.1. Process flowchart for processing CP Al by ECAP.

3.2 Al/Mg bi-metals

A successful fabrication of bi-metal by ECAP requires that two different materials are processed together and that a well bonded interface is achieved between the two metals. Based on the investigations carried out for CP Al, 250°C and 350°C were chosen to process the Al/AZ31 alloy bi-metals. Experimental investigations on Al/AZ31 alloy bi-metals were carried out on two different specimen geometries and techniques viz. (i) Rod type bi-metal structure and (ii) A macrocomposite type bi-metal structure. The rod type structure was investigated for the interface and mechanical properties, and served as a preliminary study to lead into the fabrication of a successful high strength macrocomposite. Investigations on the macrocomposite type bi-metal were aiming to understand the underlying mechanisms involved in the achieved mechanical properties. The processing methods for the two types differ significantly and are explained in the following sections.

3.2.1 Rod type bi-metal

As mentioned, the rod type structure was studied as a preliminary investigation in order to understand the interface structure during processing of Al/Mg bi-metal by ECAP.

Composition

Pure Al was obtained from the same billet and prepared similar to as described in Section 3.1.1. However, the pure Al bars were machined to dimensions shown in Fig 3.3. Further, AZ31 bars of 20 x 20 x 100 mm^3 obtained from Shanghai-Jiaotong University (SJTU) with a composition as shown in Table 3.2, were machined to dimensions given in Fig 3.3. The AZ31 rods were used as reinforcement and processed in the as-cast condition.

Table 3.2. Composition of the AZ31 Mg alloy used in the investigations of bi-metal processed by ECAP.

Element	Mg	Al	Zn	Mn	Fe
Wt %	Bal	~3.09	~1.02	~0.42	~0.001

Processing

Figure 3.2 shows an illustration overview of the process involved. The as received billets were machined to dimensions as shown. After machining, the samples were cleaned in acetone and dried in air. The CP Al specimens were then homogenized for 4 hours at 400°C and the AZ31 alloy rods were used in the as-cast condition.

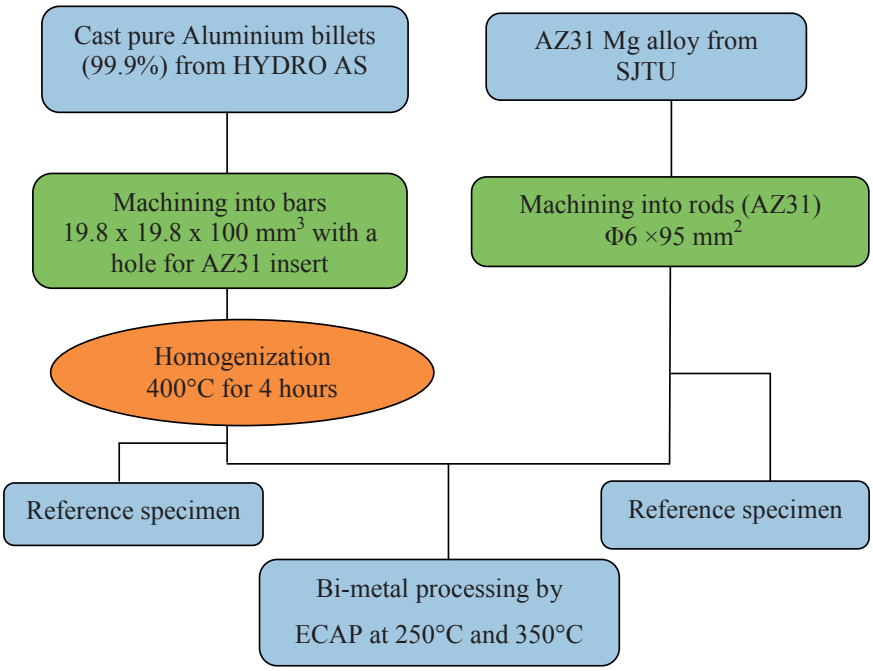

Figure 3.2. Process flowchart for processing the rod type Al/AZ31 Mg alloy reinforced bi-metal by ECAP.

The rod type AZ31 Mg alloy was placed in a hollow block of the CP Al specimen. A schematic representation of the processing is showed in Fig 3.3. Prior to ECAP, the outer surface of the AZ31 rod and the inner surface of the hollow block were cleaned by acetone in an ultrasonic cleaner and left to dry for a whole day to get rid of any lube oil or coolant remains from machining. The outer surface of the AZ31 rod and the inner surface of the hollow block were then roughened using SiC grit 80 emery sheets in order to increase friction. They were once again cleaned in acetone and dried to remove the remaining SiC particles. The AZ31 rods were then inserted into the Al blocks applying gentle hammering. After inserting the AZ31 rods, the bi-metal configuration was preheated for 30 minutes in the induction furnace at the required processing temperature prior to ECAP.

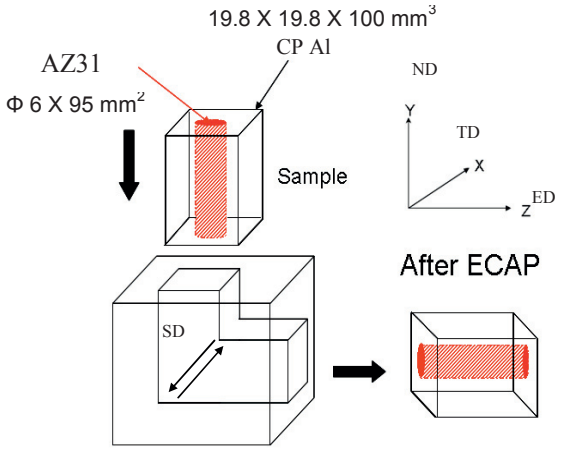

Figure 3.3. Schematic representation of the ECAP process for the rod type Al/AZ31 bi-metal.

ECAP was performed in the above mentioned in-house designed right angled ECAP die [21] at a speed of 2 mm/s. OMEGA99® lubricant (based on petroleum and graphite) was used to minimize friction. The lubricant was applied only on the sides of the punch tool and on the outer surface of the samples. In other words, no lubricant was applied to the bottom of the punch tool or at the top and bottom sides of the samples in order to prevent any contamination on the interface that would be detrimental to the interface evolution and the bonding of the materials. Here, a semi-continuous ECAP processing method was used where one sample was used to push the other sample through the die [254]. The samples were processed by route Bc to 1, 2, 4 and 6 passes at 350°C and to only 1 pass at 250°C.

3.2.2 Macrocomposite type bi-metal

The primary aim of the investigations on CP Al and rod type bi-metal was to assist and analyse the necessary criteria required to fabricate an Al and Mg based composite having high strength and low weight. The macrocomposite processing can be regarded as a result of the investigations made on CP Al and rod type bi-metal.

Composition

The macrocomposite bi-metal configuration was made of two different metals. One is CP Al and the other is an AZ31 Mg alloy. The composition of CP Al was exactly the same as shown in Table 3.1 and the composition of AZ31 alloy used was the same as described in Table 3.2. The content of the Mg alloy constituted 5% by weight and it was present in the form of meso-sized particles embedded in the aluminium matrix.

Processing

An illustration of the process flow of the macrocomposite processing is shown in Fig 3.4 below.

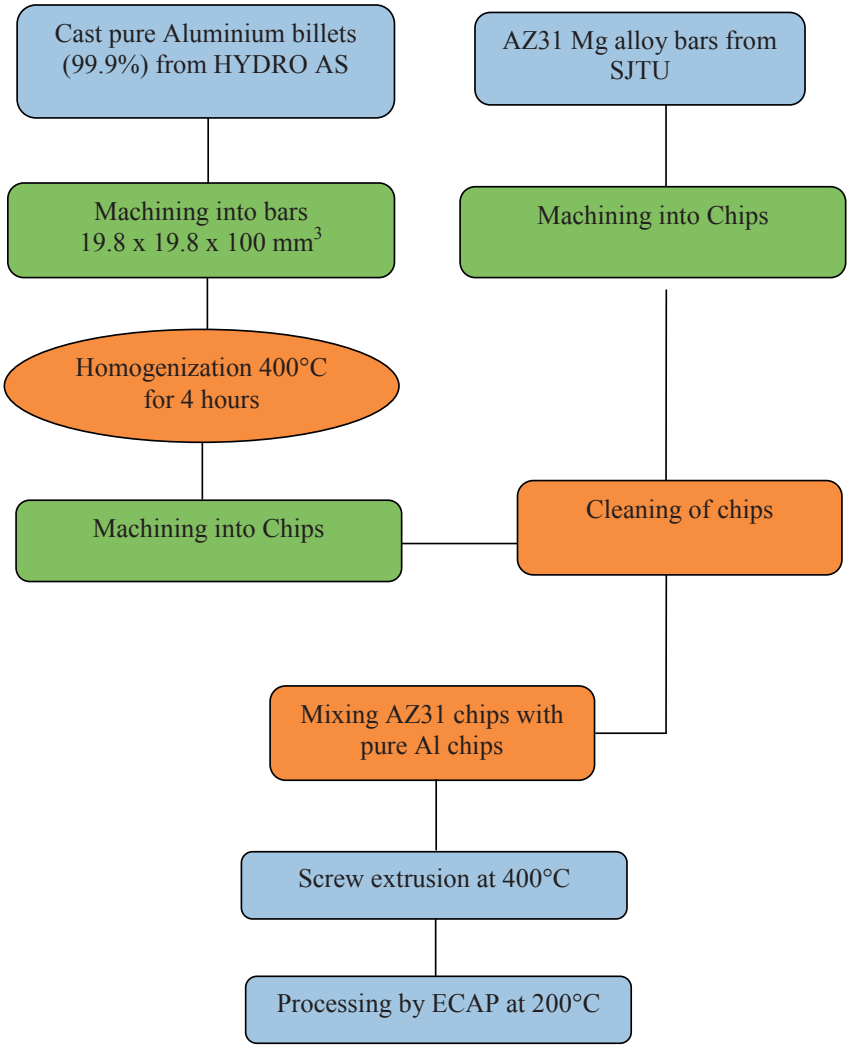

Figure 3.4. Process flowchart for processing the macrocomposite type Al/AZ31 Mg alloy bi-metal by ECAP.

The ECAP processing was a two-step procedure where the input material for ECAP is an already processed rod by screw extrusion. Therefore, the actual procedure for processing the macrocomposite can be divided into three stages, namely, *fabrication of chips, screw extrusion* and *ECAP processing.*

Fabrication of chips involved treating of the two raw materials as an input to the screw extrusion process and was the initial processing step. The homogenized aluminium bars were first machined to chips having average dimensions of 25 × 4 × 0.5 mm^3. The AZ31 bars were directly machined to chips with similar dimensions. The chips were machined using a clean tooling to avoid contamination with other materials. Then the chips were separately cleaned in acetone in an ultrasonic cleaner and completely dried to get rid of any oil/grease residue. Finally, about 5 wt% of AZ31 chips were then mixed with pure Al chips in an intended homogeneous manner.

The next stage was the *screw extrusion process*. The mixture containing 5wt% AZ31 chips was then fed to the screw extrusion setup and extruded at 400°C. The schematic representation of the screw extruder is shown in Fig 3.5. The mixture of Al and 5 wt% AZ31 chips was fed to the screw through the feeding hole. As the gear motor rotated, the chips were compacted on their way through the screw channel into the extrusion chamber and were finally extruded to a solid rod.

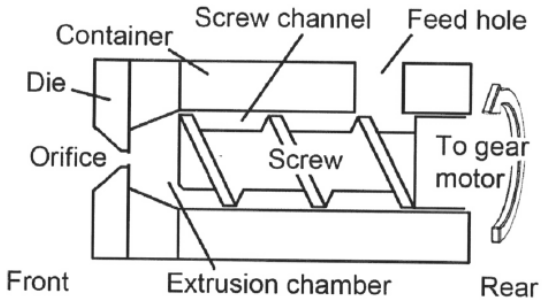

Figure 3.5. A schematic representation of the metal screw extruder [255].

A more detailed description and analysis of the present screw extrusion process can be found elsewhere [255].

The screw extruded bi-metal was then used for the *ECAP processing*, which was the last stage of the procedure. The extruded rods (15 mm in diameter) from the screw process were machined into Φ 9.8 mm cylinders of length 80 mm before processing by ECAP. The samples were firstly cleaned in acetone, dried and preheated in an induction furnace for 15 minutes at 200°C. The ECAP die and the processing method is similar to the procedure explained in Section 3.2.1. although the die had a new insert channel of 9.8 mm diameter. Finally, the samples were processed at 200°C for only one pass.

3.3 Al based sheet composites

The Al based sheet composites were investigated to understand the bonding criteria and associated mechanisms when two materials are jointly processed by ECAP. The investigations on these sheet composites could therefore throw light upon on how to achieve a good bonding. Also, sheets are easier to understand, as to the slipping behaviour of the mating surfaces, compared to that of the bi-metal configuration of the Al/AZ31 rod type structure and the macrocomposite type structure. Another advantage of the sheets is their stacking possibilities. The simple one-over-another stacking can reveal the relative flow of the sheets during the ECAP process itself; say by the internal contours. The sheet composite studies were divided into two categories, (i) Al/Al composite and (ii) Al/3103 composite in order to reveal different aspects of the bonding achieved.

3.3.1 Al/Al composite

The Al/Al sheet composite involved processing of different CP Al sheets stacked together and processed by ECAP. The primary goal was to optimise and identify the best experimental parameters for a good interface bonding.

Composition

Only one material, CP Al was involved in fabricating the Al/Al composite. The composition of the raw material is the same as shown in Table 3.1. The as

received billet was cut into two sets of plates. One set of plates (A) were machined to a rectangular cross section of 19.8 × 7.9 mm^2 and the other set (B) were machined to 19.8 × 4 mm^2. The length of the samples was varied in order to study the effect of the specimen length on the interface bonding. Table 3.3 summarizes the various process parameters used. All samples irrespective of the type and dimensions, were cleaned in acetone, dried in air and then homogenized at 400°C for 4 hours before processing.

Table 3.3. Various processing parameters for pure Al/pure Al sheet composites. Here L is the length of the ECAP samples in mm, S is the pressing speed in mm/s. Note that all samples were processed to only 1pass.

S / L	SiC paper								Wire brushing								Machine brushing							
	BP				NO BP				BP				NO BP				BP				NO BP			
	1	2	4	5	1	2	4	5	1	2	4	5	1	2	4	5	1	2	4	5	1	2	4	5
100		x		x		x		x		x		x		x		x		x				x		x
80		x		x		x		x		x		x		x		x		x	x	x		x		x
70									x	x	x	x		x		x	x	x	x	x	x	x	x	x
60										x		x						x		x				
50										x		x						x		x				

Processing

Once the samples were completely cleaned, the freshly cleaned surfaces were roughened using different techniques such as roughening by rubbing the surface with SiC grit 80, wire brushing using a steel brush and machine brushing at high speed (Table 3.3). Type A plates were roughened on one side while type B plates were roughened on both sides. A sandwich was then prepared by placing a B type plate in between two A type plates and then inserted into the ECAP die.

Here, each press series is divided into 5 columns representing the various pressing speeds marked as S, i.e. 1, 2, 4 and 5 mm/s. The five rows represent the various specimen lengths (L in mm). Further, cells marked with 'x' mean that a sample with the particular length was processed under the given conditions. Cells left blank indicate that samples under these particular conditions were not processed.

Since large numbers of samples were involved, the nomenclature of these Al/Al sheet composites needs further explanation: Samples are referred to as "XYZP", where X is the length in mm, Y the pressing speed (S) mm/s, Z designates the surface treatment method (where Z is denoted as S for SiC paper roughening, W for wire brushing, and M for machine brushing). P refers to the back pressure, where P is denoted either as B or N. B is used when samples are pressed with back pressure (fixed at 100 KN) and N for samples processed without back pressure. For example, 1002WB refers to a wire brushed sample having a length of 100 mm pressed at a speed of 2mm/s using a back pressure of 100 KN.

Figure 3.6 shows an illustration of the process flow, i.e. a complete overview of the various steps involved. The stacking sequence showed here means that the interface normal is parallel to the extrusion direction (PRE). Since the bonding between two surfaces depends on the amount of surface contamination, the sheets were immediately processed to maintain new and fresh surfaces.

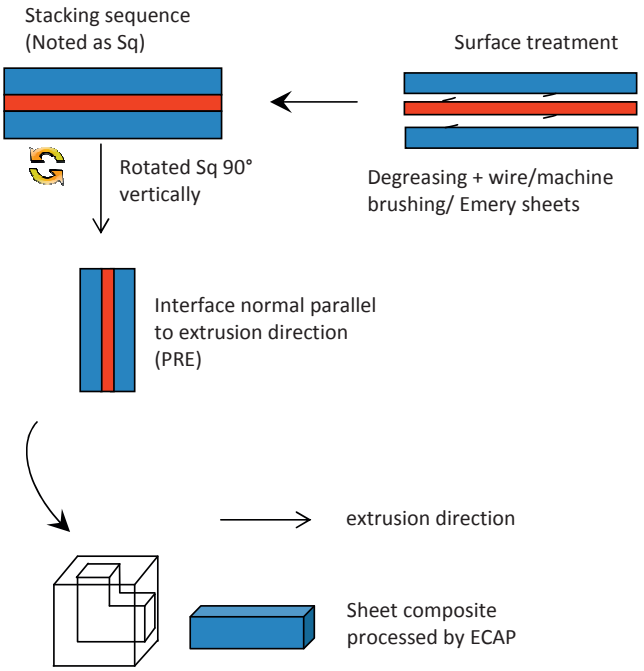

Figure 3.6. A schematic representation of the processing of sheet composites by ECAP.

A sandwich structure was made by stacking the sheets one over another along their length. The whole setup was then rotated 90° in the counter clock wise direction (CCW) along the axis perpendicular to the plane of the paper so that the length of the sheets was along the pressing direction. The interfaces were placed in such a way that the interface normal was perpendicular to the pressing direction as shown in Fig 3.6. This sandwich structure was then ECAP'ed using the back pressure (BP) ECAP die, as explained above.

The ECAP die used for the processing of Al based (both Al/Al and Al/3103, described below) composites, was an in-house designed back pressure ECAP (BP-ECAP) die. Figure 3.7 shows a photograph of this BP-ECAP die with various sections marked.

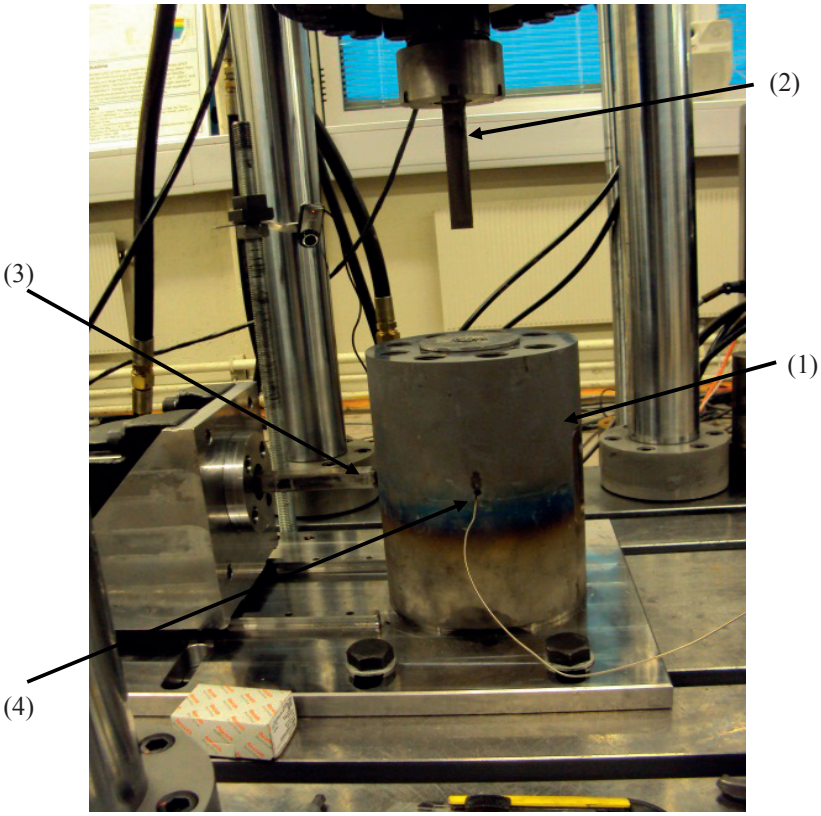

Figure 3.7. A photograph of the ECAP-BP die showing (1) Die with exit channel to the left, (2) pressing tool, (3) BP unit, (4) thermocouple at the intersection to measure the temperature rise.

The BP-ECAP die was similar to the die explained in Section 3.1.2, except that a back pressure unit was placed at the exit channel to guide and pressurize the sample during pressing. Irrespective of the type, dimensions and pressing speed, all samples processed with the presence of back pressure (BP) were processed at 100 KN BP force. As mentioned, Table 3.3 shows columns with the different applied roughening techniques. These columns are divided into two; BP and NO BP where, BP means samples were processed with a BP of 100 KN and no BP means that no BP has been used. To be noted, all these samples were processed at RT.

3.3.2 Al/3103 composite

Having established valid bonding criteria using Al/Al sheets, it was necessary to understand theMetall.l fundamentals involved for any given satisfactory bonding conditions. Therefore, the processing of the Al/AA3103 composite was aimed to understand the bonding fundamentals when two different materials were processed by ECAP. The Al/3103 composite involved the processing of a sandwich consisting of an AA3103 aluminium alloy placed in-between two pure Al sheets.

Composition

The Al/3103 composite was made of two different materials, CP Al and an AA3103 Aluminium alloy. The composition of CP Al was the same as explained in Section 3.1.1 and the composition of the AA3103 alloy is shown in Table 3.4.

Table 3.4. Composition of the AA3103 aluminium alloy used during ECAP processing of the Al/3103 composite.

Element	Al	Si	Fe	Mn	Mg
Wt %	Bal	~0.5	~0.7	~1	~0.3

All specimens were machined to a length of 70 mm, irrespective of whether type A or type B and the cross section being the same as for that of Al/Al composite described in Section 3.3.1. The sample preparation was similar to that explained above, except that type A plates were only machined from CP Al and type B plates were only machined from the AA3103 aluminium alloy.

Processing

The processing was very similar to that explained in Section 3.3.1. Moreover, the aim of the investigations was to understand the material behaviour during ECAP. Hence, all samples were processed with fixed parameters. They were processed with a length of 70 mm, back pressure 100 KN and with a pressing speed of 5 mm/s at room temperature. Figure 3.6 shows the corresponding process flow for these sheet composites. The applied ECAP set-up is shown in Fig 3.7 and

experimental procedures were the same as explained for the Al/Al composite in Section 3.3.1, except that type 'B' plates were replaced with the 3103 Al alloy.

3.4 Microstructure and texture

The obtained microstructures were analysed using optical microscopy and electron backscattered diffraction (EBSD). Optical microscopy on CP Al was carried out after anodising treatment ,where CP Al samples were first ground using 1200 and 2400 SiC emery sheets with water as a lubricant and then polished in a Struers DP- NAP applying 3 μm and 1 μm sheets, and a Struers blue lubricant. The samples were then anodised at 20 V for 90 s in a solution containing 5% HBF_4, then washed with water and ethanol before being analysed under polarized light in an optical microscope. For the AZ31 magnesium alloy, optical microscopy was carried out after grinding to 1200 and 2400 grit size using water as a lubricant, and then polished with 3 μm and 1 μm Struers DP-NAP cloths applying the Struers red lubricant. Finally, the samples were etched in a freshly prepared solution containing 1 ml HNO_3, 1 ml acetic acid, 1g oxalic acid and 150 ml water for 10s and subsequently examined under the light microscope.

EBSD was carried out in a FEGSEM Zeiss Ultra for the CP Al samples and a Hitachi SU6600 FE-SEM for the Al/AZ31 bi-metals and sheet composites. Both SEMs were equipped with an ultra-fast Nordif EBSD detector and TSM OIM EBSD software. The obtained data were then analysed using the TSL OIM analysis 6.0 software. Samples for EBSD (Al sheet composites and samples for CP Al studies) were polished using 1200, 2400 SiC emery sheets and then polished with Struers DP- NAP 3 μm and 1 μm sheets using a Struers blue lubricant. After mechanical polishing, electropolishing was carried out at –25ºC at 20 V for 12 s in a solution containing 80% ethanol and 20% perchloric acid. Samples containing Mg, i.e. the Al/AZ31 samples, were mechanically polished to 1micron and then subjected to milling in a Hitachi IM3000 flat milling system for 45 min at 3.5 KV, 80º inclination and rotated 360° CCW. The EBSD parameters used for scanning and analysis are listed in appendix A.

The macrotexture of CP Al samples was analysed using a Siemens D5000 X-ray diffractometer. Here, the samples were cut into 14 x 19.8 mm^2 blocks along

the ED-ND direction as shown in Fig 3.8 and subsequently polished using a 2400 SiC grit paper and finally etched with the Alubeis solution (10-20% NaOH + 1 tea spoon sugar) for 10 min followed by 25 s etching in a 20% HNO_3 solution.

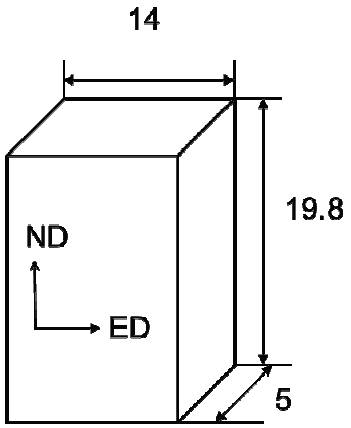

Figure 3.8. Schematic representation of the sample used for texture characterisation in the X-ray diffractometer.

Transmission electron microscopy (TEM) was also applied in order to study in-depth details of the microstructure. Samples for TEM were ground to about 100 microns thickness, then cut into discs of 3 mm diameter before electropolishing using a Struers Tenupol twin jet polishing machine at –30ºC, 20 V and an electrolytic solution containing 66% methanol and 34% HNO_3.

3.5 Interface studies

Examinations of the obtained inner interfaces were carried out on Al/Mg bi-metals in order to characterize the evolution and upon ECAP, the corresponding properties. To study their specific composition, energy dispersive spectrometry (EDS) and electron probe micro analysis (EPMA) were applied. The latter was carried out using a JEOL JXA-8500F microprobe equipped with 5 wavelength dispersive spectrometers. EDS analysis was performed using a Hitachi SU-6600

FESEM equipped with an EDAX system and analysed using the Siemens Espirit Quantax software. In addition, TEM and EBSD were used to characterize the interfaces. Here, a JEOL 2010 TEM and an EBSD system mounted on a Hitachi SU6600 FESEM having an ultrafast Nordif offline system, were used for the interfacial characterization. The EBSD data acquisition and analysis were carried out using the TSL OIM 6.0 software package.

3.6 Tensile tests

Tensile tests of Al/AZ31 bi-metals were performed at room temperature in a 100 KN servo hydraulic MTS 810 test machine, at constant cross head speed of about 2 mm/min. Elongation was recorded using a standard MTS extensometer with a gauge length of 25 mm. For rod type bi-metals, round tensile specimens were machined to dimensions as shown in Fig 3.9. The samples were machined such that the length of the tensile sample was along the extrusion direction (ED) and the width was along the normal direction (ND). However, for the macrocomposite, round specimens with dimensions shown in Fig 3.10 were used. The tensile tests were performed to compare the tensile properties of the as-received material with that of the ECAP'ed condition.

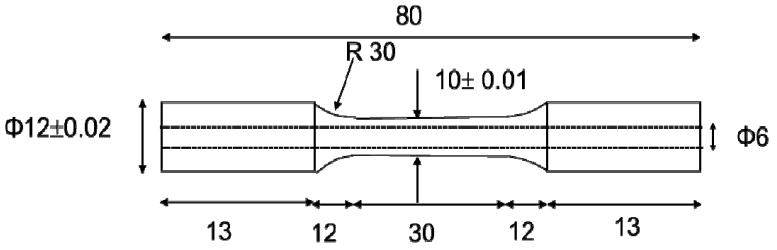

Figure 3.9. Dimensions of sample for tensile testing of Al/AZ31 bi-metal (rod type). The dotted line represents the AZ31 rod.

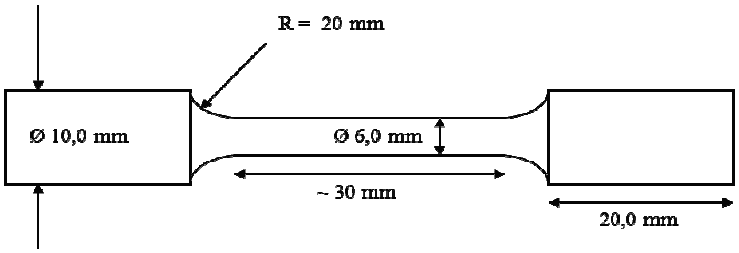

Figure 3.10. Dimensions of sample for tensile testing of Al/AZ31 bi-metal (macrocomposite type).

3.7 Microhardness

Microhardness measurements were carried out on all the various samples (CP Al, Al/AZ31 bi-metals and composites) using a Leica LVMH MOT microhardness tester. Here, a load of 100 grams was imposed for a time of 15 seconds. A minimum of four readings were taken to obtain the mean microhardness. In order to keep acceptable accuracy, the difference in indentation diagonals for valid measurements was less than 5%. Special attention was on the interface regions, but general (matrix) hardness was also measured.

Chapter 4 Experimental results

4.1 Introduction

The present chapter deals with the various experimental results oriented towards the development of high strength, low weight Al-Mg based materials for automotive and advanced structural applications. As mentioned in Chapter 3, the development of such advanced materials requires knowledge of various fundamental underlying issues. In order to understand the involved mechanisms, sequential preliminary investigations had to be carried out on different involved materials. The goal was to study different variables that can lead to promising development of bi-metal Al/Mg composites that have high strength and reasonable ductility and can be processed at a competitive cost.

The proceeding experimental results follow the chronological order of how these experiments were conducted. First, CP Al was investigated for the high temperature behaviour including grain refinement and texture evolution. The present literature study shows that successful processing of Mg and its alloys by ECAP should involve high temperature. Hence, successful co-deformation of CP Al along with Mg also relies on a proper understanding of the behaviour of CP Al at high temperatures. Secondly, Al/Mg bi-metal samples were prepared as a rod type structure set-up and processed according to the findings on high temperature behaviour of CP Al. The selected processing temperature had, of obvious reasons, to be high enough for the difficult-to-deform Mg. The results obtained on this Al/Mg bi-metal system were then analysed. The ambition was to obtain an Al/Mg bi-metal macrocomposite that can exhibit high strength as compared to its Al-Mg binary alloy counterparts. Thirdly, the optimization of such a macrocomposite was carried out by studying the interface bonding criteria and related mechanisms by employing both Al/Al and Al/AA3103 sheets for ECAP processing. One of the reasons for also using the latter configuration is that the stacked sheets have a simple geometry as compared to the present macrocomposite configuration. Hence the interface study became easier. Also, CP Al is soft, easy to process without cracking and a high processing pressure can be avoided. Al/Al sheets were used to

study experimental parameters and Al/AA3103 alloy sheets were employed to study bonding mechanisms. The various experimental results are explained in detail in the following.

4.2 CP Al studies

The behaviour that CP Al exhibited under a combination of high strain and high temperature was an important aspect in regard to find a balance between grain refinement and ease of processing the bi-metal involving CP Al and the AZ31 Mg alloy, as explained in Chapter 3. Most of the previous studies on CP Al have been focused on the microstructure evolution and the smallest mean grain size that can be achieved by ECAP at room temperature. Early works by Iwahashi et al. [13] and [101] showed that pure Al can be refined to 1 μm after 4 passes at RT and attributed the grain refinement to sub-grain evolution into high angle grain boundaries. Saravanan et al. [96] made a comparison of the various results published on the grain refinement of Al by ECAP. It was inferred that pure Al (99.99% pure) could not be refined less than ~1 μm after 8 passes at RT, while addition of small amount of impurities could lead to a drastic reduction in grain size. To the latter, 99.5% pure Al showed a grain size of 600 nm after 8 passes at RT. Even though several publications have been reported on RT processing of pure Al [13, 96, 101, 256-258], there have been very limited information on the microstructure evolution of pure Al by ECAP at high temperatures. The first article by Chakkingal et al. [259] showed that pure Al did not refine at all after ECAP at 500°C. Wang et al. [260] reported the evolution of the sub-grain size at various temperatures (298 K to 523 K) by transmission electron microscopy (TEM), but did not explain in detail the microstructure evolution in pure Al under severe plastic strains combined with high processing temperatures. Therefore, a clear understanding of the mechanisms that pure Al undergoes at high temperatures during ECAP is lacking and hence, the present study is important per se, but specifically for revealing the behaviour of CP Al upon co-deformation with the AZ31 Mg alloy.

It is to be noted that in the following orientation imaging microscopy (OIM) maps, a ‘grain’ refers to an entity with a boundary misorientation $\geq 15°$ and

any boundary with a a misorientation $\geq 15^{o}$ is considered to be a high angle grain boundary (HAGB) and all black lines in the OIM maps are high angle grain boundaries (HAGBs). Shear direction corresponds to the die intersection channel where the material deforms by simple shear, in this case, 45º to the extrusion direction, where extrusion direction corresponds to the direction of the push out of the sample.

The colours represent the orientation of the grains and sub-grains. This colour coding is similar for all CP Al studies and is explained in Fig 4.1, together with the sample directions relative to ECAP set-up. The general sample directions for all samples used in the EBSD analyses are as shown in Fig 4.1, unless otherwise specified in case to case.

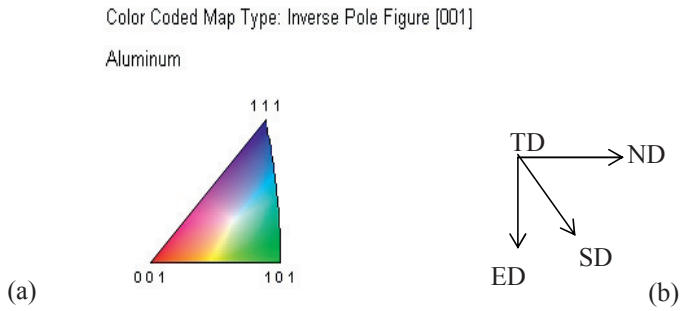

Figure 4.1. (a) The colour coding used to represent the orientations of different grains in CP Al. Here, [001] represents that the respective plane normal being parallel to the plane normal of paper surface; (b) The geometrical sample directions used in EBSD analysis unless specified otherwise. SD indicates shear direction.

4.2.1 As-received material

The as–received and subsequently homogenised material was analysed with respect to the initial grain size, texture and microhardness. Figure 4.2 shows a representative EBSD OIM image of the as received sample. The mean grain size was large and calculated to be ~1.2 mm and the average microhardness was 22±2 HV. As mentioned in Chapter 3, initial texture was determined using a four circle diffractometer, see Section 4.2.5.

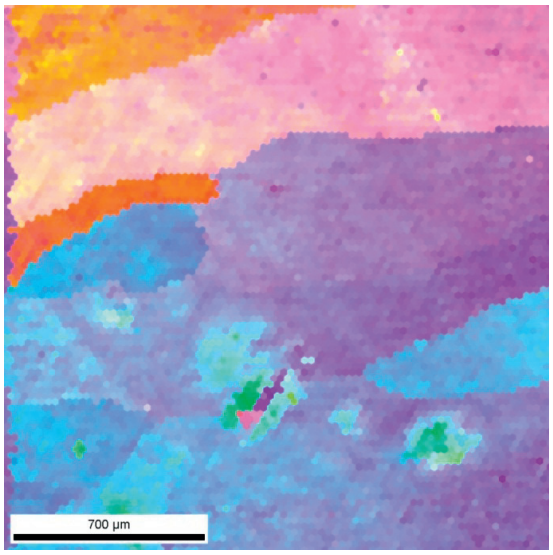

Figure 4.2. An EBSD OIM map of the as-received, homogenized CP Al sample showing a typical coarse grain structure (D≈1.2 mm).

4.2.2 Grain structure evolution

Grain morphology

The obtained inverse pole figure (IPF) maps of samples processed by ECAP for 1 pass at different temperatures are shown in Fig 4.3. It can be seen that during the first pass, microstructures of all samples look very similar and at all processing temperatures. Long band like structures or deformation bands, DBs (marked in black arrows in Fig 4.3) were formed. However, the thickness of the DBs increased with increasing deformation temperature. Also, a cell structure was developed at all processing temperatures. The direction of the deformed grains was along the shear direction (45° to the ED) for samples processed at RT and 150°C. However, for samples processed at 250°C and 350°C, the grains are oriented ~20° to the ED. Also, DBs were observed to originate along the grain boundaries for all samples. Another feature that could be observed was that at 350°C, a fraction of sub-grains had already started to form even after 1 pass. It is to be noted that in the present investigations, a "cell" represents a microstructural entity that has a

dislocation cell boundary and occurs in the initial stages of deformation. Such cells were also characterized by an increasing misorientation from the centre to the boundary. On the other hand, “Sub-grains” appeared to be similar to cells but they had well defined and sharp boundaries as they evolved by recovery of the dislocation networks. Also, unlike the cells, each sub-grain had a constant misorientation within itself. Normally the sub-grains were established during the later stages of deformation.

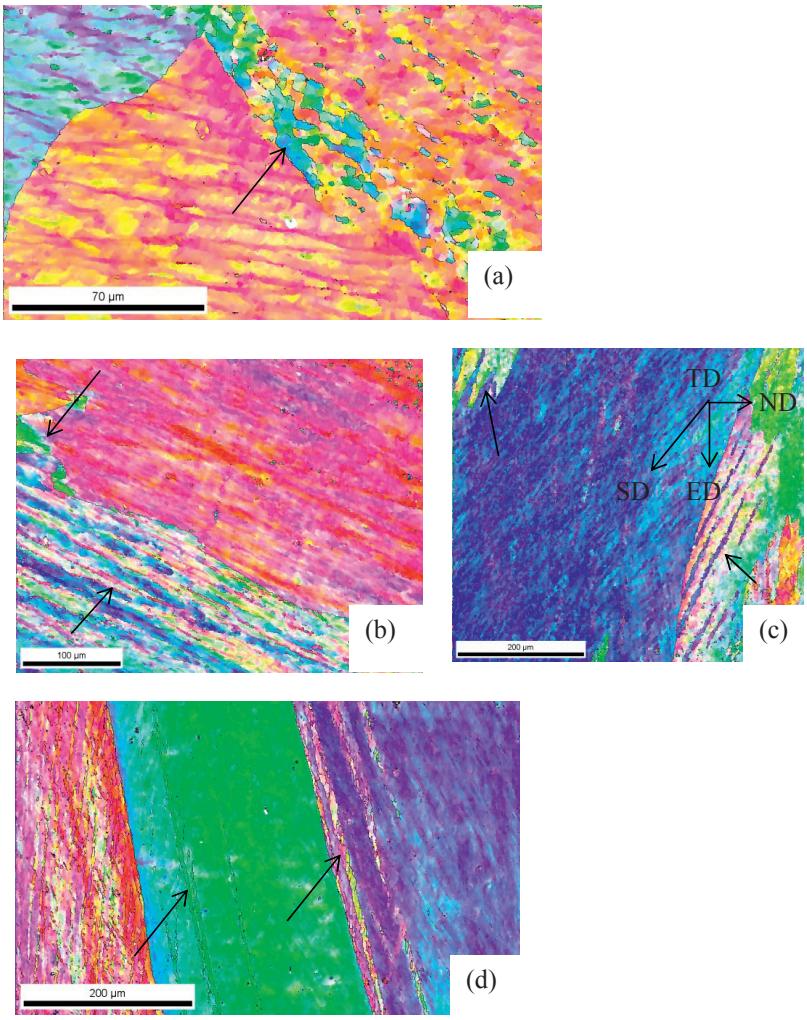

Figure 4.3. OIM maps representing the microstructure of CP Al after 1 pass ECAP at different temperatures. (a) RT, (b) 150°C, (c) 250°C, (d) 350°C. Black arrows point at deformation bands. ED: Extrusion direction.

Correspondingly, Figure 4.4 shows the IPF maps of samples processed for 2 passes at the same temperatures. The microstructures of all samples were inhomogeneous, with some grains obviously undergoing severe deformation. Also,

more deformation inhomogeneties such as microbands, incomplete HAGBs etc. were formed, e.g., see the black arrows in Fig 4.4 indicating such inhomogeneties.

Qualitatively, RT and 150°C samples showed similar IPF maps. Also 250°C and 350°C samples show similar IPF maps. Another feature was the microstructure development from 1 to 2 passes. Samples processed at RT and 150°C had a fraction of grains which were randomly elongated after two passes, while most of the microstructure was aligned along the shear direction. The thickness of the DBs decreased and their density was increased. Going from 1 to 2 passes, samples processed at 250°C and 350 °C showed an increasing density of GNBs and the grains were oriented ~23° to the ED. Further, samples processed at 250°C showed DBs comparable to those formed at 150°C, but the samples processed at 350°C had extremely large DBs around ~150 μm in thickness. However, a large fraction of small DBs were observed. For samples processed at 350°C, no microstructure development was seen between pass 1 and 2 as observed for the other temperatures. In other words, the DBs formed in the previous pass were replaced by new DBs formed in the current pass. Although 250°C samples show existence of previously formed DBs, the fraction was relatively low compared to that of samples processed at RT and 150°C.

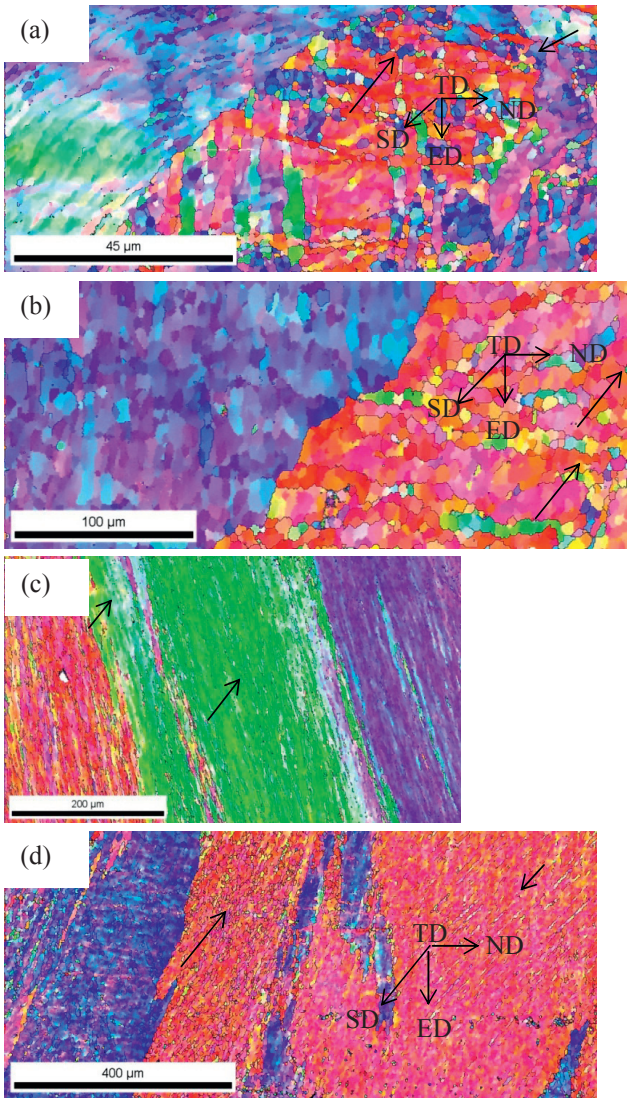

Figure 4.4. OIM maps representing the microstructure of CP Al after 2 pass ECAP at different temperatures. (a) RT, (b) 150°C, (c) 250°C, (d) 350°C.

Further extending the deformation to 4 passes (Fig 4.5), the entire microstructure was made up of long and thin DBs. The microstructures obtained at all temperatures showed a dominating number of DBs, microbands and incomplete HAGBs in different proportions and in general, gave an inhomogeneous impression.

The IPF maps for RT samples had a complex microstructure due to route Bc and fractions of fragmented small grains could be observed. The orientations of grains varied due to the retaining of previously formed microstructure constituents. However, new DBs did form and the grains developed during the fourth pass were oriented along the shear direction.

Samples deformed at 150°C showed a similar microstructure but at a larger scale, while at 350°C, the microstructure was developed during the latest pass. However, at 250°C, the samples showed a fraction of DBs oriented in a slightly different direction owing to the previously formed bands. One could maintain that samples processed at RT and 150°C showed almost a complete breakdown of the initial structure into DBs and fine grains and the DBs were only one cell diameter in thickness. On the contrary, grains in 250°C and 350°C samples were not completely broken down into DBs and fragments of fine grains existed, but the density of DBs increased. Also for samples deformed at 250°C, most of the DBs were thinned down to one or two cells in thickness. It seemed clear that 350°C samples were the least refined as compared to the samples deformed at lower temperatures. Although the frequency of DBs increased, they were thicker at 350°C and did not break down the uniformly large grains into DBs. It could be added here that RT samples had a relatively larger fraction of fine grains as compared to other samples deformed at higher temperatures.

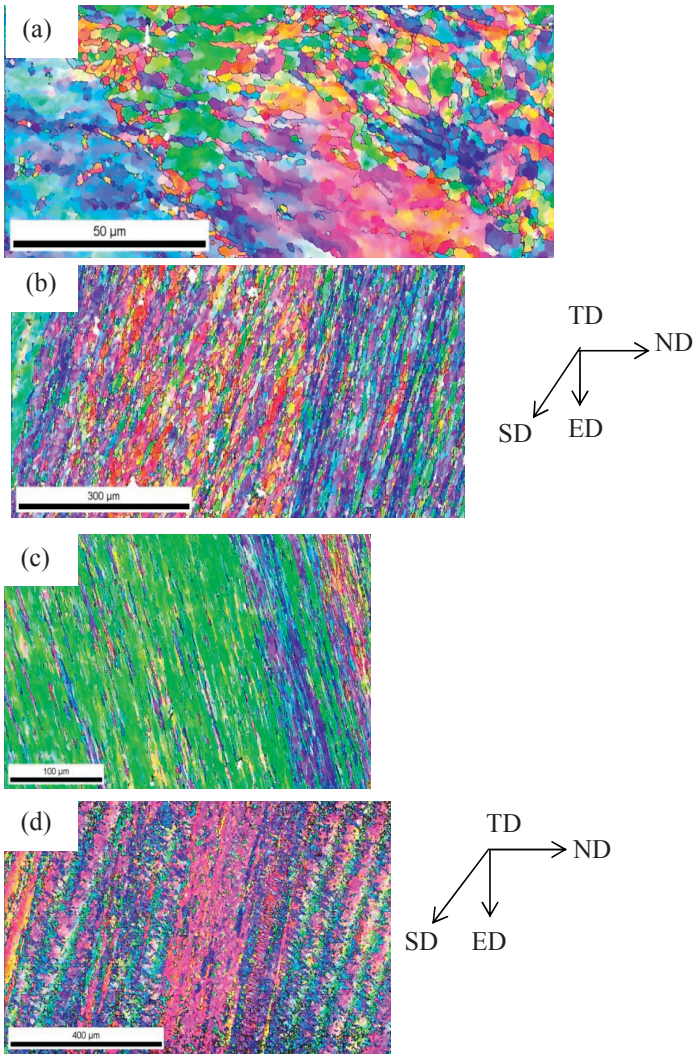

Figure 4.5. OIM maps representing the microstructure of CP Al after 4 pass ECAP at different temperatures. (a) RT, (b) 150°C, (c) 250°C, (d) 350°C.

Figure 4.6 shows the microstructures obtained after 6 passes. It can be seen that deformation at 250°C introduced a relatively homogeneous recovered microstructure as compared to all the other samples after 6 passes. A well-defined structure with sub-grains was the dominating feature. Samples processed at RT and 150°C showed similar microstructures and were relatively homogenous compared

to the 4 pass counterpart specimens. A mixture of undeformed regions and a set of fine grains could still be observed, while some grains were still evolving into fine grains, fine grains already formed recovered and had a constant misorientation within each grain.

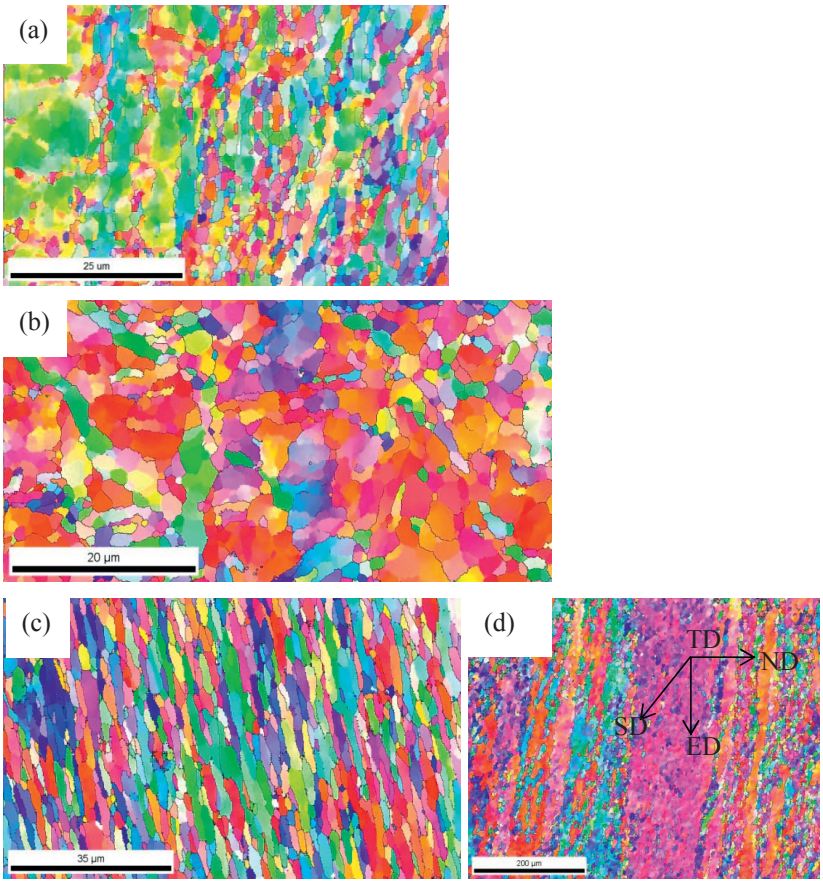

Figure 4.6. OIM maps representing the microstructure of CP Al after 6 passes ECAP at different temperatures. (a) RT, (b) 150°C, (c) 250°C, (d) 350°C.

Samples processed at 350°C showed a similar microstructure as to that of 4 passes ECAP, but now the structure was more recovered with sub-grains. The

incomplete boundaries and other deformation inhomogeneties such as microbands observed after 4 passes, were not seen for 250°C and 350°C samples while, such inhomogeneties were reduced in quantity for RT and 150°C samples.

Finally, the microstructures after 8 passes at different temperatures are shown in Fig 4.7. The microstructures obtained at RT, 150°C and 250°C contained uniform equiaxed fine grains and were quite similar in general. However, after processing at 350°C, the grains became elongated even after 8 passes, and were not broken down completely into equiaxed grains. It should be noted that the deformation inhomogeneties observed up to 6 passes were not observed after 8 passes. Also, for samples processed up to 250°C, it was difficult to distinguish the newly formed grains and the grains formed in the previous passes.

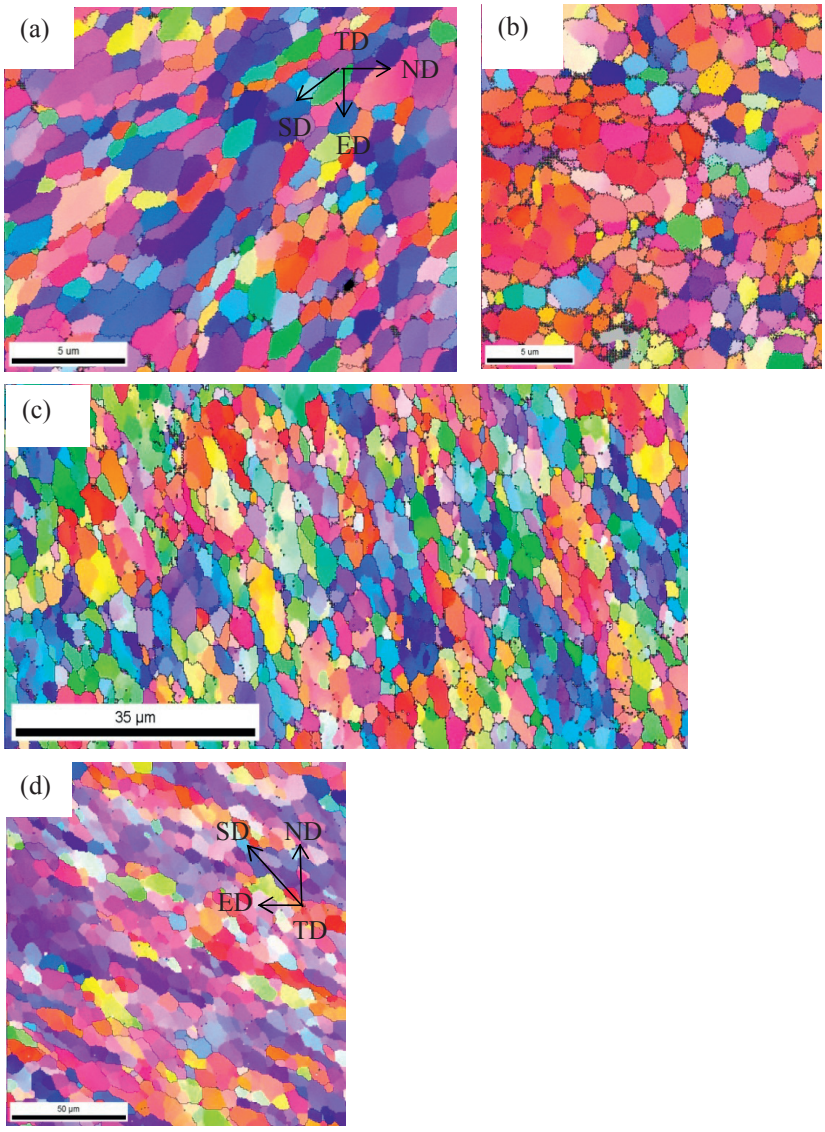

Figure 4.7. OIM maps representing the microstructure of CP Al after 8 passes ECAP at different temperatures. (a) RT, (b) 150°C, (c) 250°C, (d) 350°C.

Grain refinement

An overview of the mean grain size as a function of ECAP pass number at different temperatures is shown in Fig 4.8. Inhomogeneity plays a major role during intitial passes and hence non uniform grain refinement was expected. Accordingly, EBSD scans were taken in large areas and different regions. The homogenization with increasing number of passes is also discussed in Chapter 5.

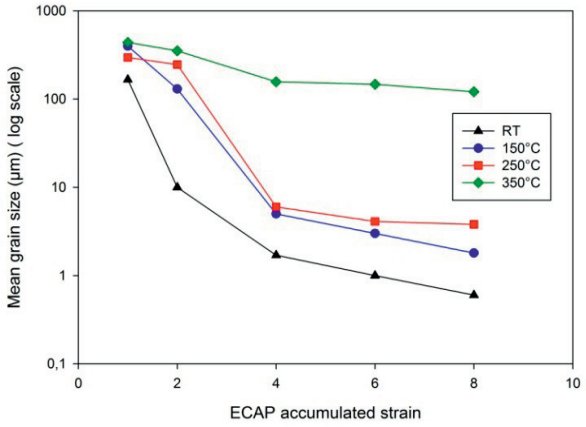

Figure 4.8. Mean grain size at different temperatures as a function of accumulated strain.

The average grain size decreased with increasing strain and decreasing temperature. It can be seen that samples processed at RT and 150°C showed a similar trend in mean grain size with increasing strain. The 250°C and 350°C samples exhibited a similar grain size up to 2 passes. With further straining, 250°C samples followed a similar trend as that of RT and 150°C samples. Samples processed at 350°C did not refine as significantly as that of the counterparts at lower deformation temperatures, even after 8 passes. It should be noted that the y-axis is in a log scale and hence, in general there was a significant grain refinement at all temperatures. While RT and 150°C samples showed a continuous decrease with increasing strain, the 250°C and 350°C samples showed very little refinement on a logarithmic scale beyond 4 passes.

In summary, the grains were refined and obtained their smallest size after 8 passes at all processing temperatures. The average grain size decreased to ~0.7 μm after eight passes at RT, and refined to ~4 μm and ~1.8 μm for the samples processed at 250°C and 150°C respectively. Although the samples processed at 350°C showed grain refinement (~120 μm), this was not as significant as for the lower deformation temperatures.

Grain boundary character

The distribution of HAGB fraction vs. accumulated strain has been plotted in Fig 4.9. The HAGB fraction increased continuously only for ECAP at RT and remained constant after 4 passes at 150 °C. Further, the HAGB fraction increased up to 6 passes and then remained constant at 250°C and 350°C. Also, the first 2 passes had similar HAGB fractions for all processing temperatures. After 4 passes, samples processed at 150°C and 250°C exhibited a higher fraction of HAGBs relative to ECAP at 350°C and RT samples. However, after 8 passes, RT samples showed a high fraction of HAGBs compared to samples processed at 150°C. It should be remarked that samples processed at 250°C showed the highest HAGB fraction after 8 passes. In summary, RT ECAP showed a continuous increase in the HAGB fraction, whereas 150°C and 250°C samples showed stagnation after 6 passes, and at 350°C, a decreasing fraction was present after 6 passes.

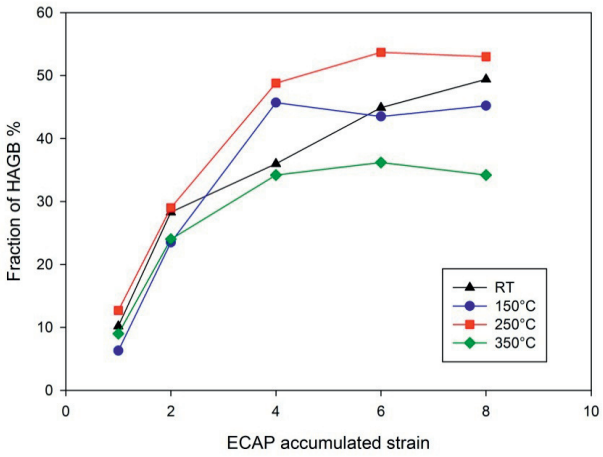

Figure 4.9. Fraction of HAGBs after processing at different temperatures as a function of ECAP accumulated strain.

4.2.3 Stored energy calculations

The stored energy after various passes at the given deformation temperatures was calculated using the results obtained from EBSD. Here, the stored energy can be calculated by the formula [32],

$$E_d = \frac{3\gamma_s}{d_{ecd}} \tag{4.1}$$

$$\gamma_s = \sum_{1.5}^{65} \gamma(\theta) f(\theta) \tag{4.2}$$

$$\gamma(\theta) = \gamma_m \left(\frac{\theta}{\theta_m}\right)\left(1 - \ln\left(\frac{\theta}{\theta_m}\right)\right) if\, \theta < \theta_m \tag{4.3}$$

$$\gamma = \gamma_m \;\; if\, \theta > \theta_m \tag{4.4}$$

where E_d is the stored energy inside the material, γ_s is the grain boundary energy for the entire grain structure, θ is the misorientation angle, f (θ) is the volume

fraction, γ_m is the high angle grain boundary energy (angle > 15°) taken as 0.324 Jm^{-2} for aluminium [261], θ_m is taken as 15° and d_{ecd} is the average equivalent circle diameter of the measured grains. Correspondingly, Figure 4.10 shows the estimated stored energy plotted as a function of accumulated strain at different temperatures, (Please note that the scale of the y-axis is logarithmic). As expected, the estimated stored energy was the highest for samples processed at RT and declined for samples processed at 150°C and 250°C for obvious reasons. Surprisingly, the energies at 150°C and 250°C were not very different, although being somewhat lower at 250°C than at 150°C. However, at 350°C, the energy was roughly two orders of magnitude lower. Generally speaking, the stored energy increased continuously with increasing number of passes for samples processed at RT and 150°C. For the samples processed at 250°C and 350°C, the energy increased up to 4 passes and then remained almost constant. Another general feature for the samples deformed at RT and 150°C was that, the stored energy increased rapidly up to 4 passes and then more gradually up to 8 passes.

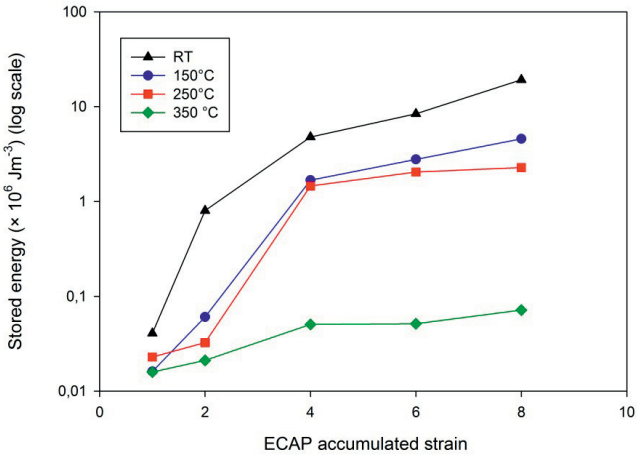

Figure 4.10. Predicted stored energy of samples processed at different temperatures as a function of ECAP accumulated strain. Please note: y-axis is logarithmic.

4.2.4 Microhardness evolution

The measured microhardness values are plotted as a function of ECAP strain in Fig 4.11. The hardness increased with increasing strain and by decreasing the deformation temperature. After 4 passes, the microhardness remained almost constant, actually with a very small slope for samples pressed at RT and 150°C. Samples processed at 250°C and 350°C showed a decreasing trend at high number of passes after reaching the maximum hardness. Samples processed at 250°C obtained maximum hardness after 6 passes, however the maximum occurred after just 4 passes for samples pressed at 350°C. At the latter temperature, there was also a small drop when moving from 1 to 2 passes.

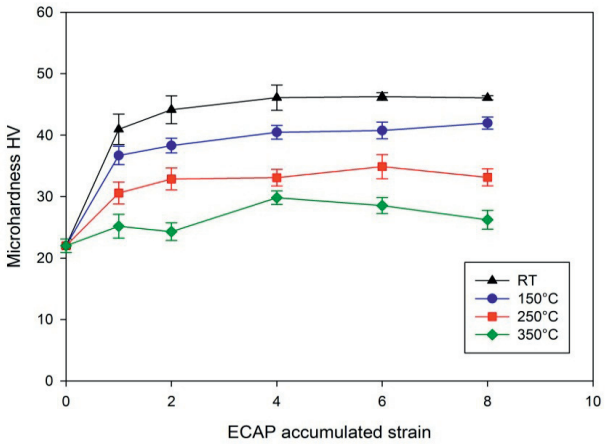

Figure 4.11. Mean microhardness of samples processed at different temperatures as a function of ECAP accumulated strain.

4.2.5 Crystallographic Texture

The initial texture of the as-received CP Al sample presented as a (111) pole figure is shown in Fig 4.12. The colour codes for the respective intensities in Fig 4.12c represent the scale for all macro textures obtained for CP Al throughout the thesis. It should be noted that this scale is used throughout the investigations on CP Al. From Fig 4.12, the initial texture of the as-received material could be characterized as random. The first pole (Fig.4.12a) represents the

raw figure as obtained from the XRD goniometry, whereas Figure 4.12b is the corresponding calculated pole figure, adjusted for sample symmetry and other characteristics such as x-ray absorption, sample height displacement. The calculations included texture using harmonic function iterations. The following (111) pole figures for various experimental conditions are calculated, and the texture evolution can be interpreted using the (111) ideal orientations for ECAP established by Li et al. [54], for e.g. see Chapter 2. Accordingly, one can see by comparing the 'B', 'C' and 'A' type texture components that, 'B' type variants and the 'A' type textures are getting more prominent at high temperatures.

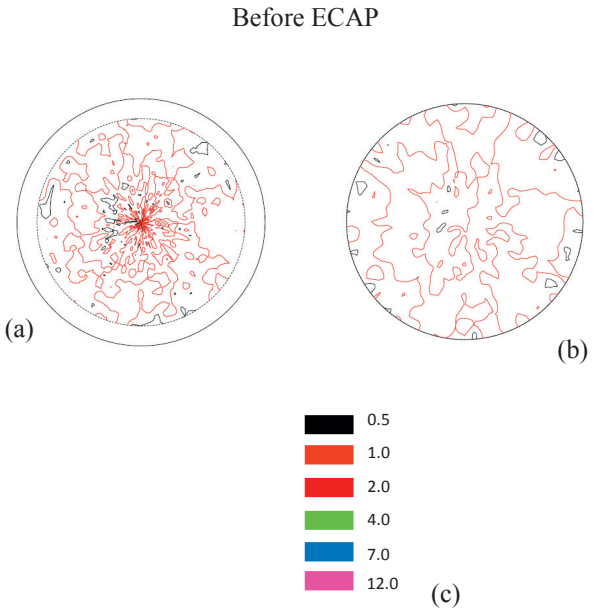

Figure 4.12. Obtained (111) pole figures of the as-received CP Al measured by X-ray goniometry; (a) measured, (b) calculated, (c) the corresponding intensity scale used for all x-ray (111) pole figures obtained for various conditions of CP Al.

Furthermore, Figure 4.13 depicts the calculated (111) pole figures for samples processed to 1 pass at different processing temperatures. It can be seen that

the textures are more spread at RT (Fig 4.13a) and become sharper with increasing temperature. While A and B components are prominent at all temperatures, samples at elevated temperatures (Figs 4.13b–4.13d) show non-uniform texture components. Also, the RT sample shows the C component. It can be generally inferred that the intensity of texture components increases with increasing deformation temperature.

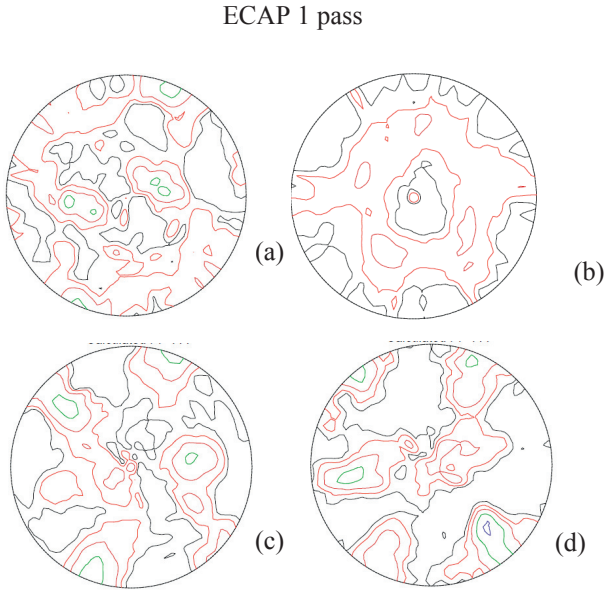

Figure 4.13. The obtained texture of CP Al after 1 pass ECAP measured by X-ray goniometry expressed as (111) pole figures; (a) RT, (b) 150°C, (c) 250°C, (d) 350°C.

Furthermore, the calculated (111) pole figures after 2 passes (Fig 4.14) for samples processed at RT, 150°C, 250°C and 350°C show that RT samples (Fig 4.14a) develop clear ECAP textures except that they are slightly misoriented from their ideal orientations. Also, the texture intensity for RT increased significantly for the B component. Samples processed at 150°C and 250°C (Figs 4.14b and 4.14c)

follow a similar trend, developing more ideal ECAP textures. However, they were not as complete and strong for RT samples. At 350°C, some ECAP components were developed, primarily B_0 and $-B_0$ and they were sharp but not fully established (Fig 4.14d).

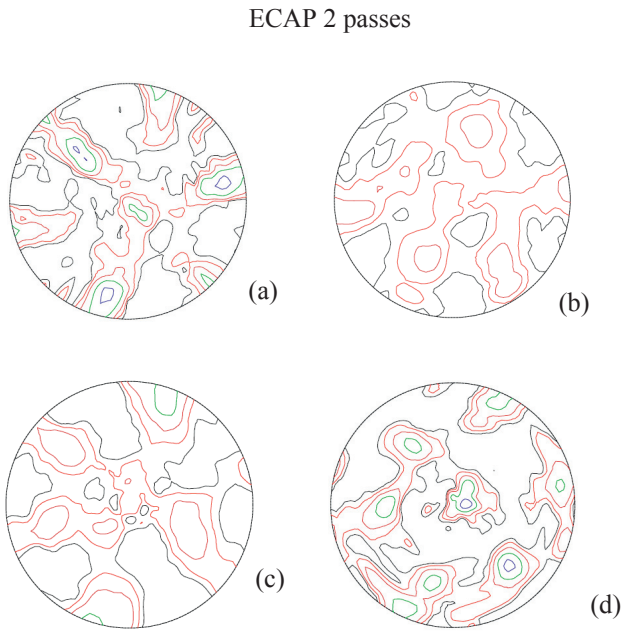

Figure 4.14. The obtained texture of CP Al after 2 passes ECAP measured by X-ray goniometry expressed as (111) pole figures; (a) RT, (b) 150°C, (c) 250°C, (d) 350°C.

The corresponding (111) calculated pole figures for samples processed to 4 passes are shown in Fig 4.15. The samples processed at RT, 150°C and 250°C (Figs 4.15a–4.15c) show fully developed ECAP orientations and they are relatively ideally oriented. 350°C samples (Fig 4.15d) had a more fibrous development of the A and the B components. Also, a weak C component was seen for the three lowest temperatures.

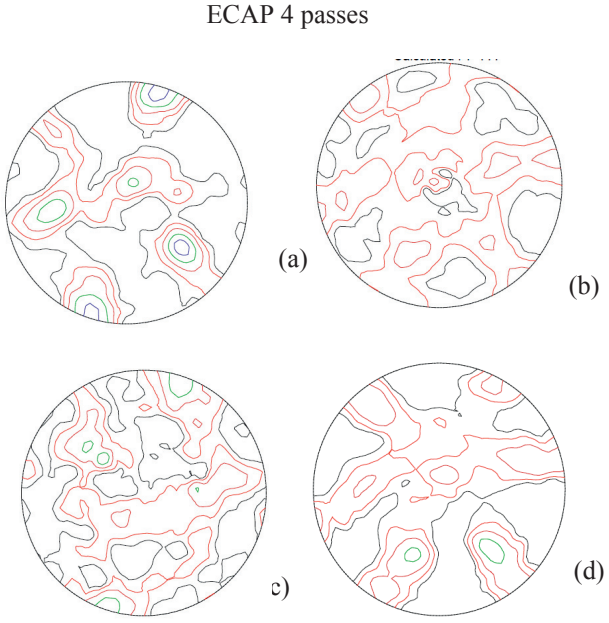

Figure 4.15. The obtained texture of CP Al after 4 passes ECAP measured by X-ray goniometry expressed as (111) pole figures; (a) RT, (b) 150°C, (c) 250°C, (d) 350°C.

After 6 passes, samples processed at RT, 150°C and 250°C (Figs 4.16a–4.16c) had more fibrous textures. In other words, ECAP shear textures developed instead of sharp components and the components became more uniform. Also, RT samples exhibited a weakening of the C component. Samples processed to 350°C developed more complete textures than those observed at 150°C and 250°C after 2 or 4 passes, i.e. without a significant C component. Also, the sharp B and A components finally became fibrous, i.e. typical to shear textures, at 350°C and 6 passes.

ECAP 6 passes

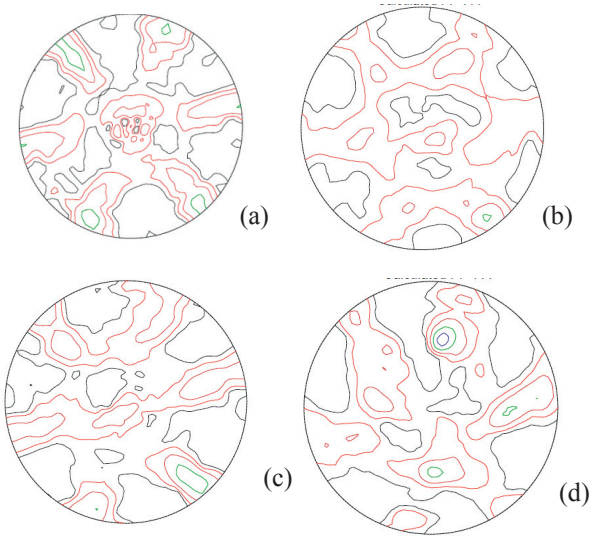

Figure 4.16. The obtained texture of CP Al after 6 passes ECAP measure by X-ray goniometry expressed as (111) pole figures; (a) RT, (b) 150°C, (c) 250°C, (d) 350°C.

Figure 4.17 shows the corresponding pole figures after 8 passes. While RT samples (Fig 4.17a) show a slight drop in intensity, all other samples (Figs 4.17b–4.17d) develop more shear type ECAP textures. In other words, the components became less sharp and more fibrous.

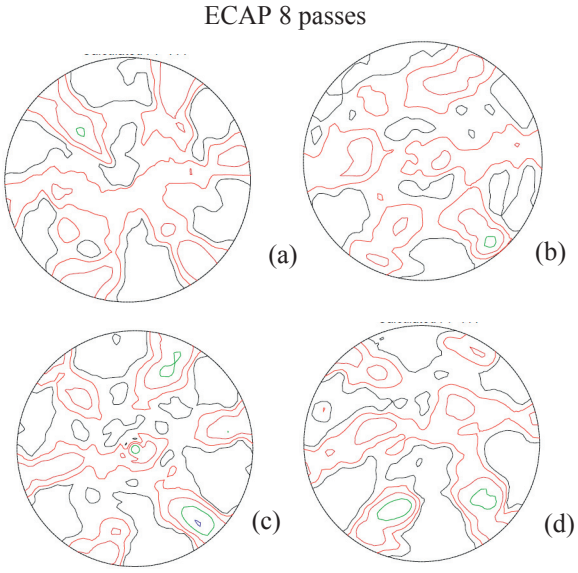

Figure 4.17. The obtained texture of CP Al after 6 passes ECAP measured by X-ray goniometry expressed as (111) pole figures ; (a) RT, (b) 150°C, (c) 250°C, (d) 350°C.

For a better understanding and to quantitatively analyse the textures, constant Φ2=45° ODF sections for the range Φ1= 0° to 360°, Φ = 0° to 90° are presented in Figs 4.18–4.21. The corresponding colour codes for the various intensities are given in Fig 4.22. Here, the A, B and C components are marked in the ODF plots. Samples processed at all given temperatures developed typical ECAP textures after 8 passes as have been reported in previous studies [52, 262]. For samples processed at RT, the A, B and C components were initially formed. In the first pass, the A type component appeared and after 2 passes, the B and C components were clearly identified. In addition, the intensity of the C component increased (Fig 4.18b). Hence, with increasing strain up to 4, the textures were concentrated around the C component (Fig 4.18c). With further increase in strain, i.e. after 6 and 8 passes as shown in Figs 4.18d–4.18e respectively, the textures reduced their intensity and approached more random orientations.

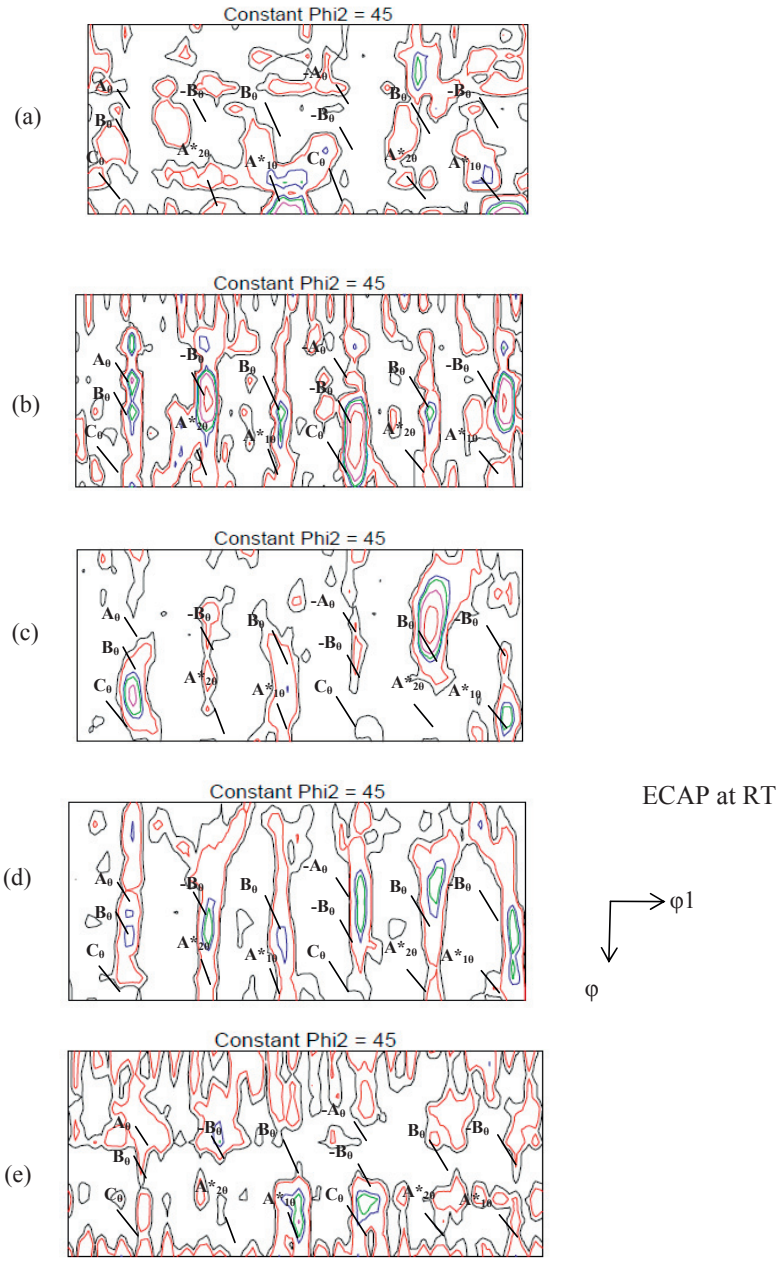

Figure 4.18. Constant φ2=45° ODF sections for (a) 1 pass, (b) 2 passes, (c) 4 passes, (d) 6 passes and (e) 8 passes ECAP of pure Al by route Bc at RT. Intensity colour code; refer to Fig 4.22.

Furthermore, samples processed at 150°C (Fig 4.19), exhibited a (111) fibre parallel to ND during the first pass along with the A and B components. However, the intensity of the obtained textures was not as strong as for RT. With increasing strain, A and B components manifested but the C component became weaker than that observed at RT after 4 passes. With further increase in strain, the C component decreased further in intensity, but other orientations (A and B type) did not change significantly.

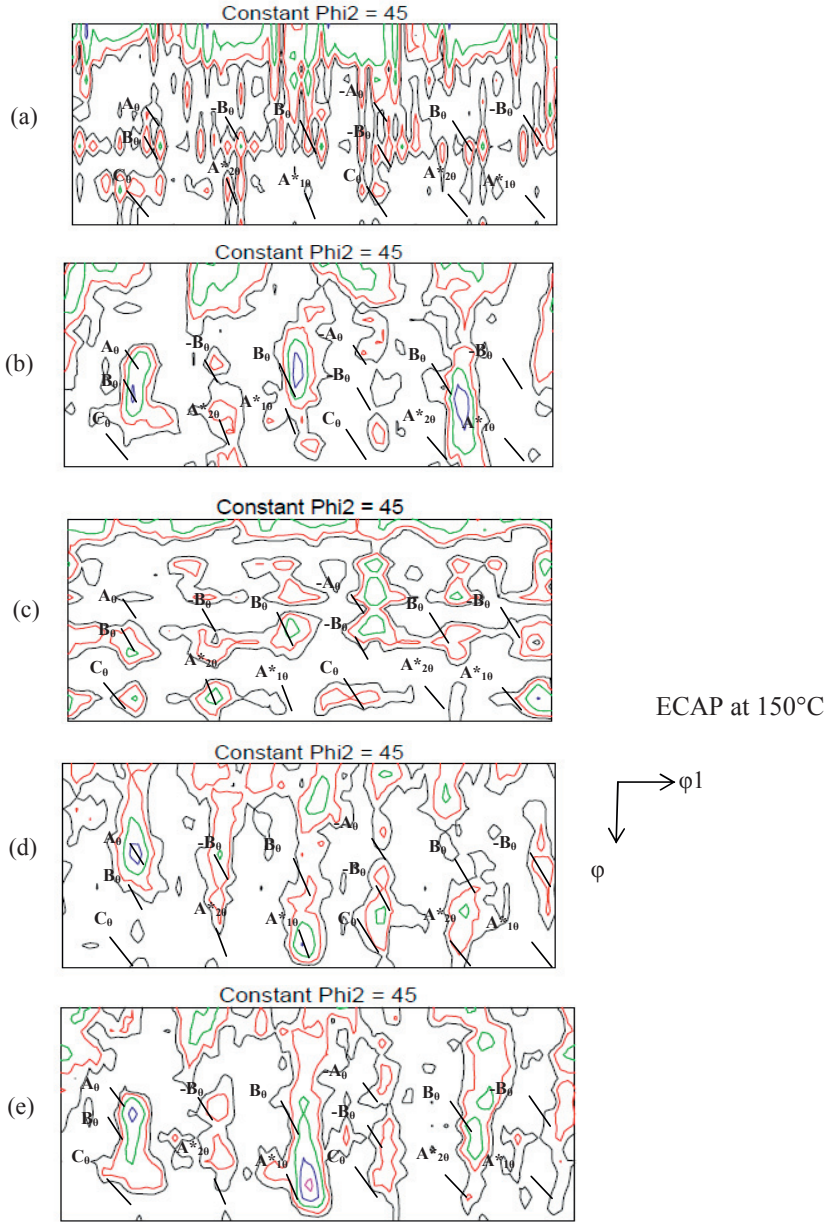

Figure 4.19. Constant φ2=45° ODF sections for (a) 1 pass, (b) 2 passes, (c) 4 passes, (d) 6 passes and (e) 8 passes ECAP of pure Al by route Bc at 150°C. Intensity colour code; refer to Fig 4.22.

The results obtained for samples processed at 250°C (Fig 4.20), showed a similar evolution as at 150°C. But the initial (111) fibre parallel to ND observed at 150°C was absent. While the strongest texture observed at 150°C was the A type orientations, the B type orientations were more dominating at 250°C with increasing strain. Additionally, a very weak cube texture could be observed after 8 passes.

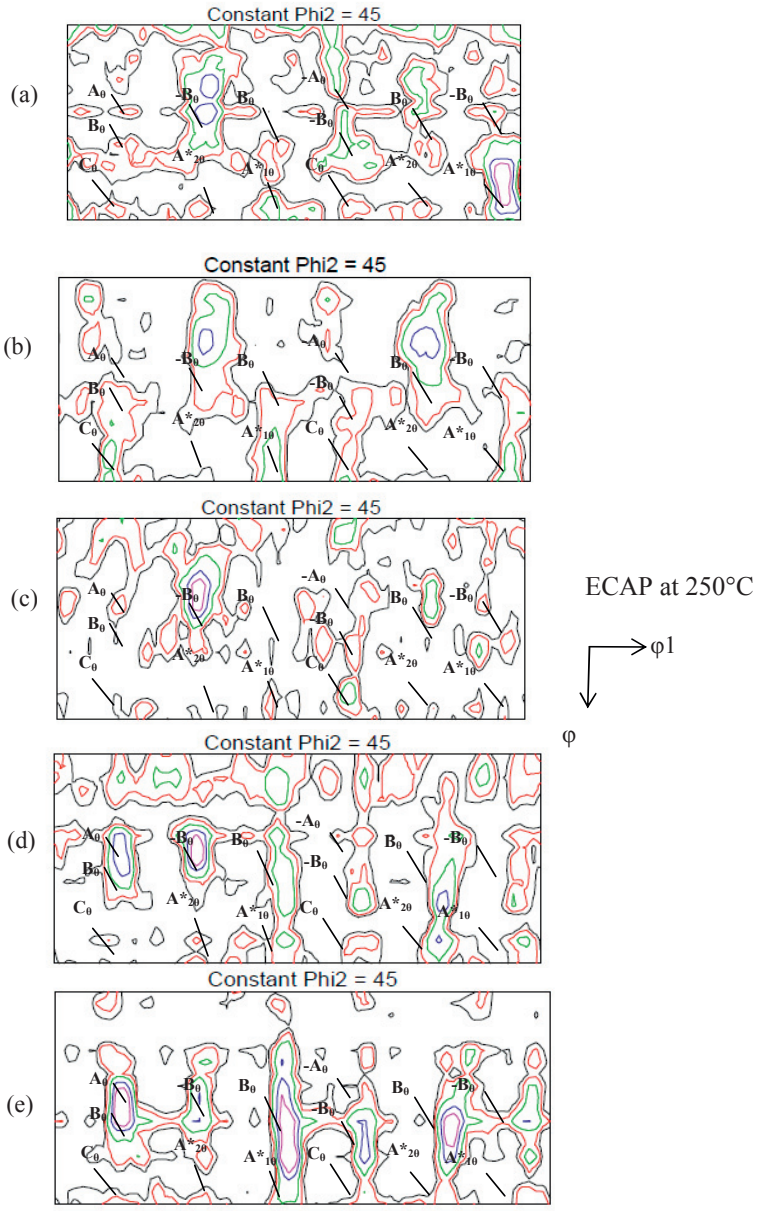

Figure 4.20. Constant φ2=45° ODF sections for (a) 1 pass, (b) 2 passes, (c) 4 passes, (d) 6 passes and (e) 8 passes ECAP of pure Al by route Bc at 250°C. Intensity colour code; refer to Fig 4.22.

For samples processed at 350°C (Fig 4.21), the textures became stronger compared to their counterparts deformed at lower temperatures. During the first four passes, A and B type components were developed with strong intensities. The C component started to develop only at 6 passes but disappeared again after 8 passes. Another feature that could be observed was the development of a rotated cube texture which progressively increased in intensity up to 6 passes and weakened after 8 passes.

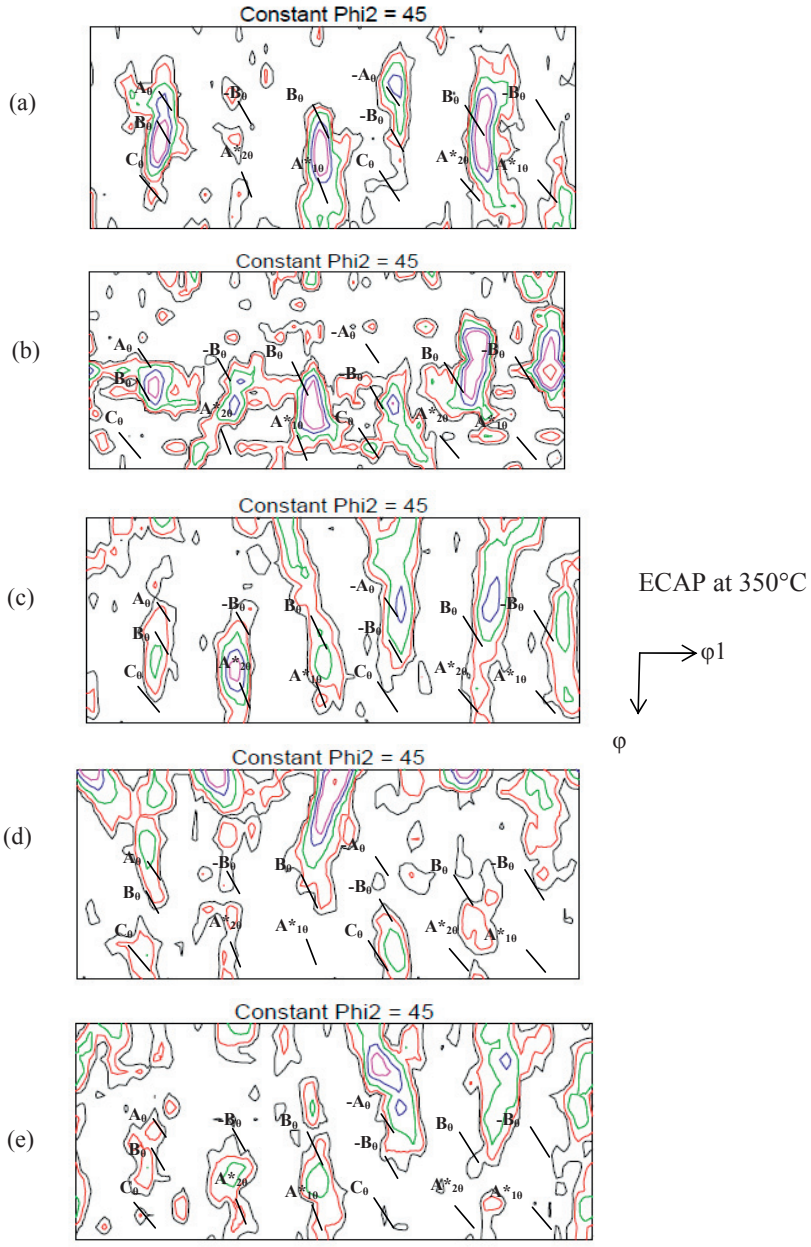

Figure 4.21. Constant φ2=45° ODF sections for (a) 1 pass, (b) 2 passes, (c) 4 passes, (d) 6 passes and (e) 8 passes ECAP of pure Al by route Bc at 350°C. Intensity colour code; refer to Fig 4.22.

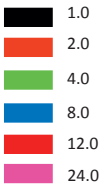

Figure 4.22. The scale used for all ODF intensities obtained for ECAP'ed CP Al for the constant ODF sections under various conditions.

A summary of three highest ODF texture components for the various deformation temperatures and respective pass numbers is collected in Table 4.1 below:

Table 4.1 Three highest intensities of the textures obtained from constant ODF sections of samples processed by ECAP for different passes at different processing temperatures.

ECAP passes	RT			150°C			250°C			350°C		
	Φ1	Φ	Φ2	Φ1	Φ	Φ2	Φ1	Φ	Φ2	Φ1	Φ	Φ2
1	164	86	45	10	3	45	346	70	45	346	70	45
	271	23	45	60	2	45	115	30	45	115	30	45
	20	54	45	30	54	45	278	25	45	278	25	45
2	294	60	45	294	60	45	113	30	45	349	45	45
	172	48	45	172	48	45	280	25	45	169	60	45
	52	60	45	52	60	45	38	80	45	294	35	45
4	231	33	45	231	33	45	110	30	45	111	40	45
	24	2	45	24	2	45	286	30	45	291	42	45
	166	49	45	166	49	45	224	72	45	229	44	45
6	56	45	45	56	45	45	107	40	45	184	8	45
	176	81	45	176	81	45	50	40	45	100	0	45
	114	40	45	114	40	45	288	70	45	229	80	45
8	170	70	45	174	77	45	170	70	45	209	18	45
	45	54	45	50	45	45	45	54	45	288	16	45
	286	59	45	291	63	45	286	59	45	353	21	45

From Table 4.1 and Figs 4.18–4.22, it can be seen that for all processing conditions, the textures were displaced ±20° from their ideal ECAP orientations. However, with increasing number of passes, the textures tend to orient themselves towards more stable ideal orientations. More details on the texture development during ECAP of CP Al with respect to deformation temperature and accumulated strain is discussed in Chapter 5.

4.3 Al/Mg bi-metals

As mentioned, the studies on Al/Mg bi-metals involved Al and Mg alloys processed by ECAP. The analysis of the rod type structure (Fig 3.2) led to a development of a macrocomposite that incorporated the deficiencies observed in this structure. The results obtained with these materials are explained below.

4.3.1 Rod type structure

The investigations on CP Al described above were performed to analyse the effect of deformation temperature on grain refinement in pure Al and simultaneously identify the optimized condition for co-deformation of CP Al and AZ31 materials. From the results shown in Section 4.1, it can be inferred that even at high temperature, CP Al can be refined significantly up to 250°C, i.e. exhibiting less than 5 μm mean grain size after 6 passes by ECAP route Bc. Hence, a minimum temperature of 250°C was selected to study the bonding and interfacial characteristics of co-deformed CP Al and AZ31 alloy bi-metal in the rod type structure set-up.

As-received materials

The microstructure of the as-received CP Al was shown above in Fig 4.2. The corresponding optical micrograph of the as-received AZ31 Mg alloy is shown in Fig 4.23. For the latter, the grain size distribution is bimodal having large and small grains. The initial mean grain size was found to be 46 μm for the AZ31 alloy and 1.2 mm for CP Al. Moreover, the microhardness values of the as-received CP Al and AZ31 alloy were 22±2 HV and 57±6 HV respectively.

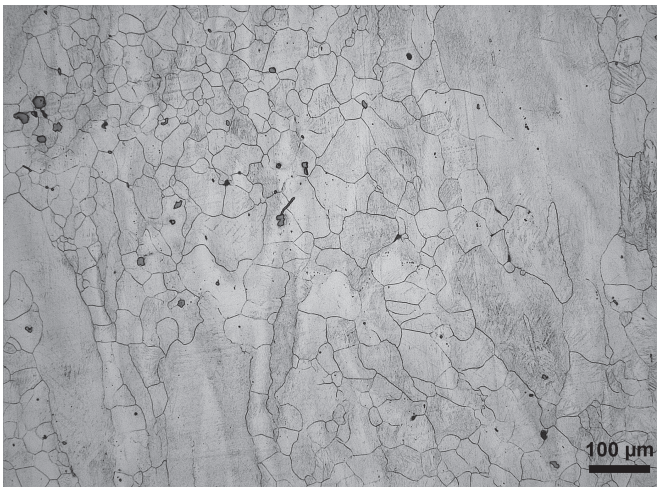

Figure 4.23. An optical micrograph of the as-received AZ31 Mg alloy used in the bi-metal studies.

ECAP processing

The CP Al/AZ31 Mg alloy bi-metal was processed by ECAP as a rod type structure at 250°C for one pass only. A macrograph of this sample is shown in Fig 4.24.

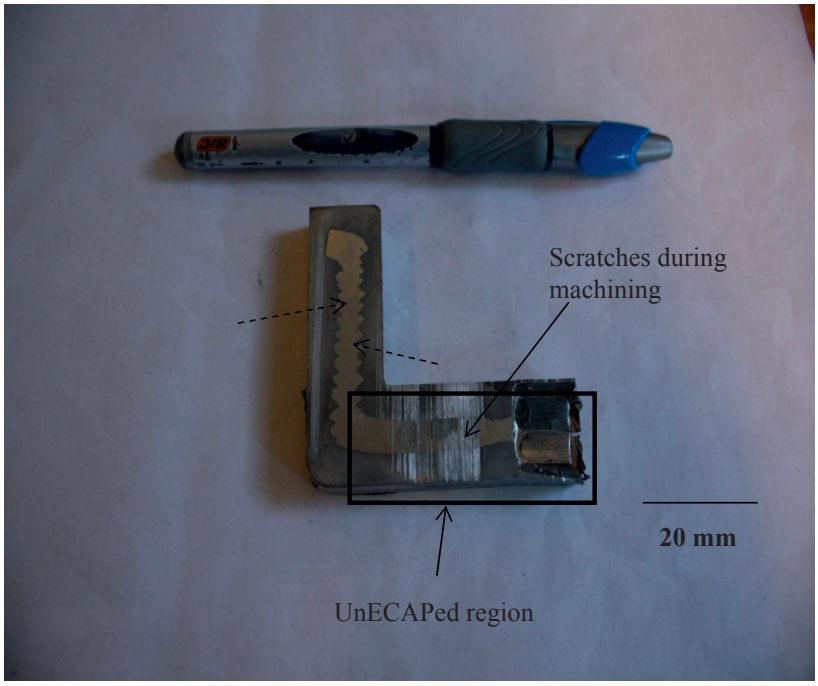

Figure 4.24. Overview of the Al-AZ31 rod type bi-metal sample processed by ECAP during 1 pass at 250°C. Dashed arrows indicate cracks in AZ31 core (associated with the zig-zag pattern). UnECAP'ed region and machining scratches are also marked for comparison.

Figure 4.24 depicts the unECAP'ed region in the lower right part, and a clear difference between scratches observed during machining and the zig-zag shaped cracked regions can be observed. A lot of cracks formed along the ECAP shear direction when observed in the ED-ND plane. Hence, it seemed difficult to process the bi-metal configuration with AZ31 in the core surrounded by CP Al at 250°C without any premature cracking. As a consequence, further ECAP processing trials were carried out at 350°C. The corresponding bi-metal processed at this temperature is shown in Fig 4.25.

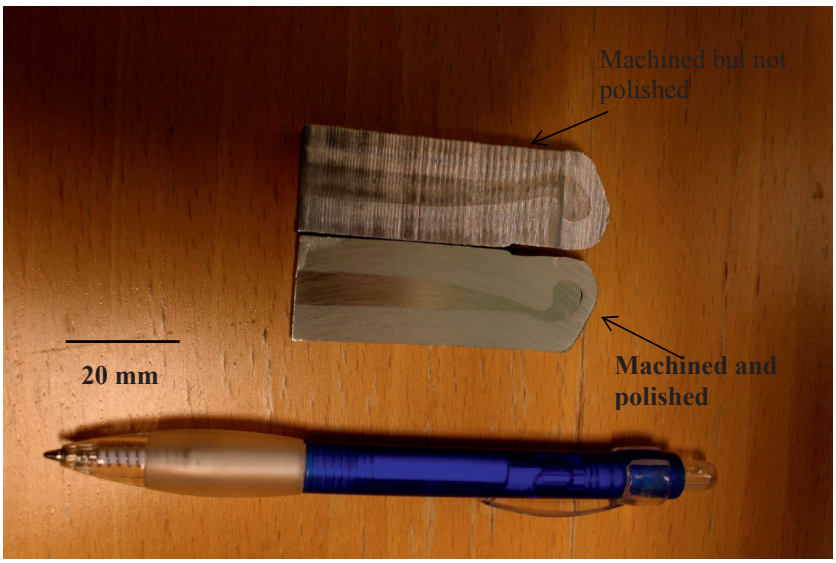

Figure 4.25. Macrograph of the Al-AZ31 rod type bi-metal sample processed by ECAP after 1 pass at 350°C.

The above figure shows one sample cut into two halves longitudinally, one having polished and the other, machined and not polished. The two conditions are shown for comparison. It can be seen that the typical zig-zag cracks shown in Fig 4.24 did not appear when processed at 350°C. Hence all subsequent samples were processed at 350°C and then up to 6 passes. It should be remarked that further investigations on microstructure evolution and mechanical properties were only carried out on samples successfully processed at 350°C, i.e. see the following results.

Interface studies

However, interface studies performed on the CP Al/AZ31 bi-metal were carried out on samples processed at both 250°C and 350°C using electron spectrometry techniques in combination with FEGSEM. Figure 4.26 shows a magnified SEM image of the interface in the sample processed at 350°C for 4 passes. Various regions were marked out and quantitative analysis was done by

EDS and EPMA. Figure 4.26 also shows EDS line scan (green line) and the corresponding concentration profile.

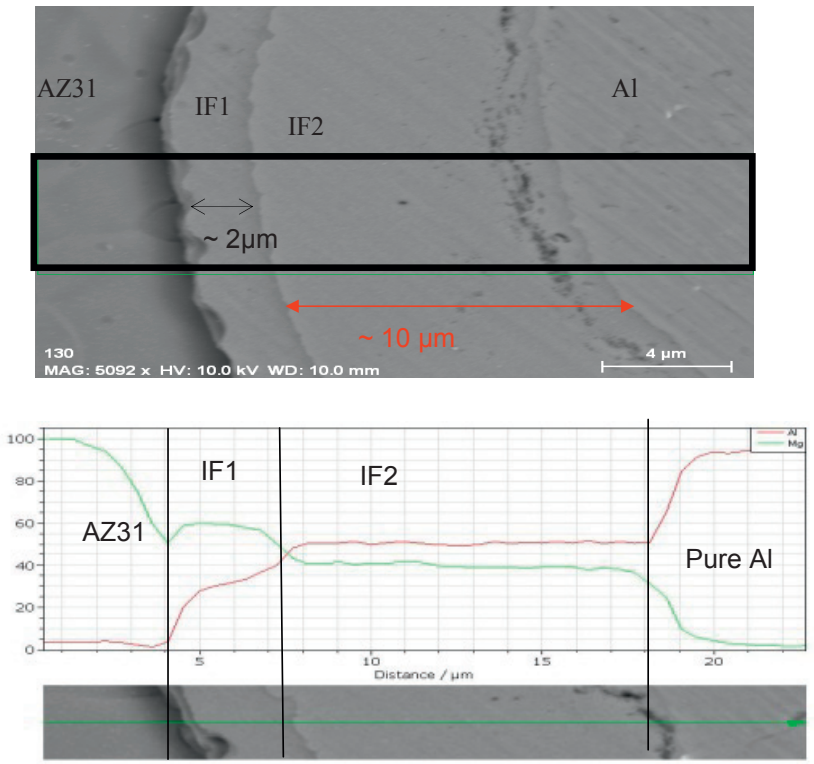

Figure 4.26.SEM micrograph of the cross-section of the bi-metal processed at 350°C to 4 passes. Two interface regions can be seen and their respective widths are marked as ~2 µm and ~10 µm. The black rectangle corresponds to the region shown in the lower part. Here the y-axis represents the composition in mass%. In this concentration profile, red curve corresponds to Al and the green curve represents the Mg content.

Further, Figure 4.27 shows the quantitative EPMA maps of Al, Mg and Zn for the sample processed at 250°C to 1 pass whereas Al, Mg and Mn maps for samples processed at 350°C to 1, 2, 4 and 6 passes are shown in Fig 4.28.

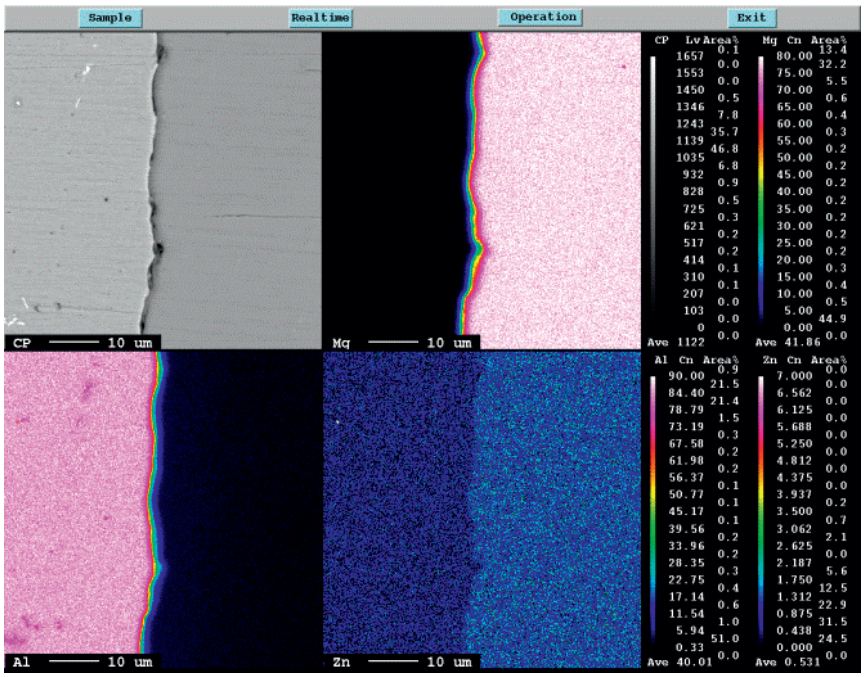

Figure 4.27. EPMA analysis of the interface in CP Al/AZ31 bi-metal processed by ECAP after 1 pass at 250°C.

ECAP 1 pass 350°C

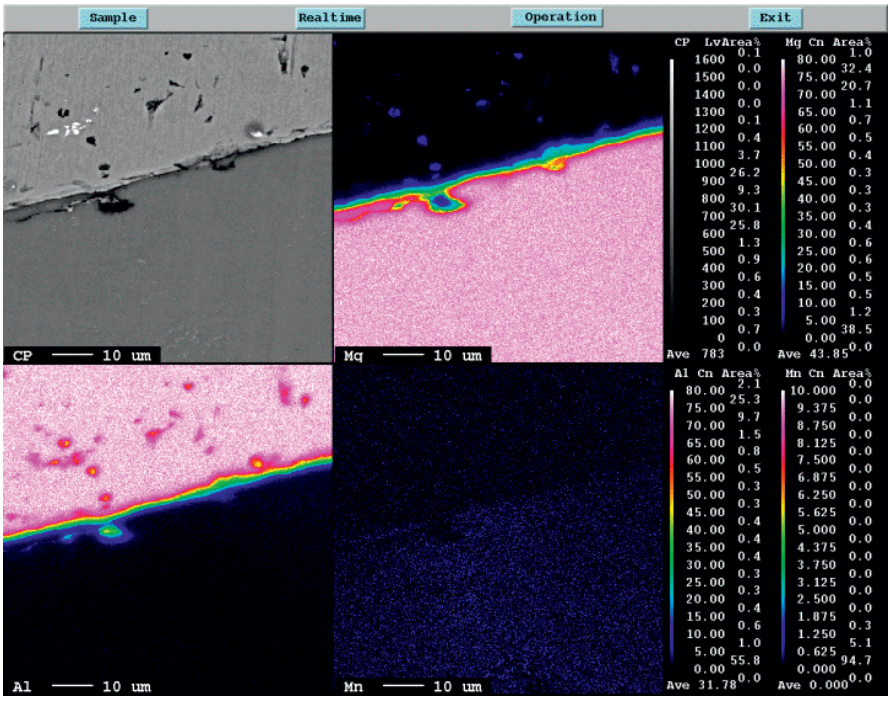

Figure 4.28a. EPMA mapping of the interface in CP Al/AZ31 bi-metal processed by ECAP at 350°C after 1 pass.

ECAP 2 passes 350°C

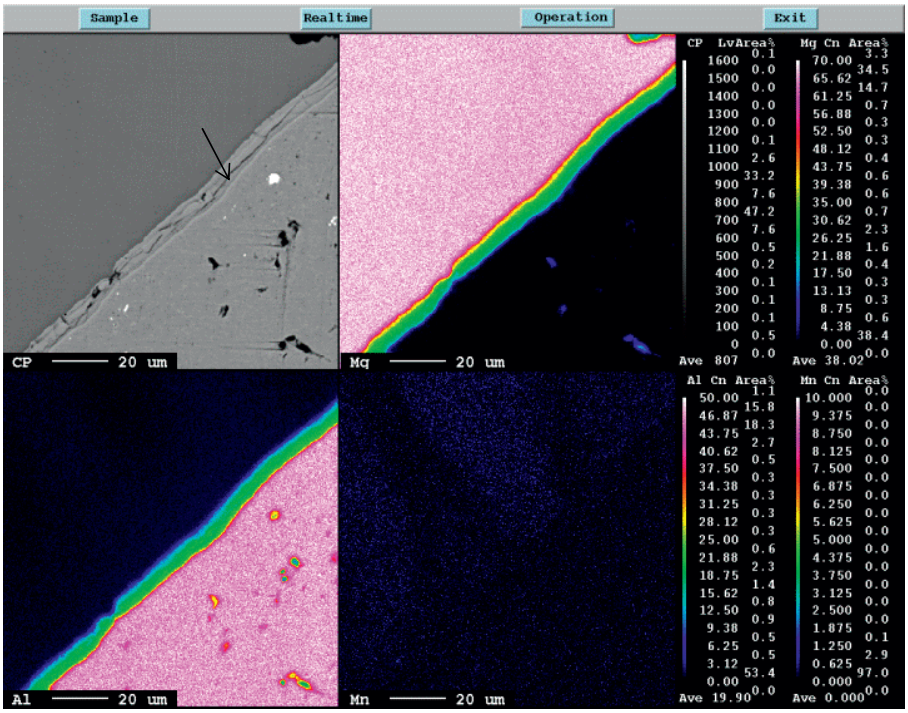

Figure 4.28b. EPMA mapping of the interface in CP Al/AZ31 bi-metal processed by ECAP at 350°C after 2 passes by route Bc. The black arrow represents type '1' cracks.

ECAP 4 passes 350°C

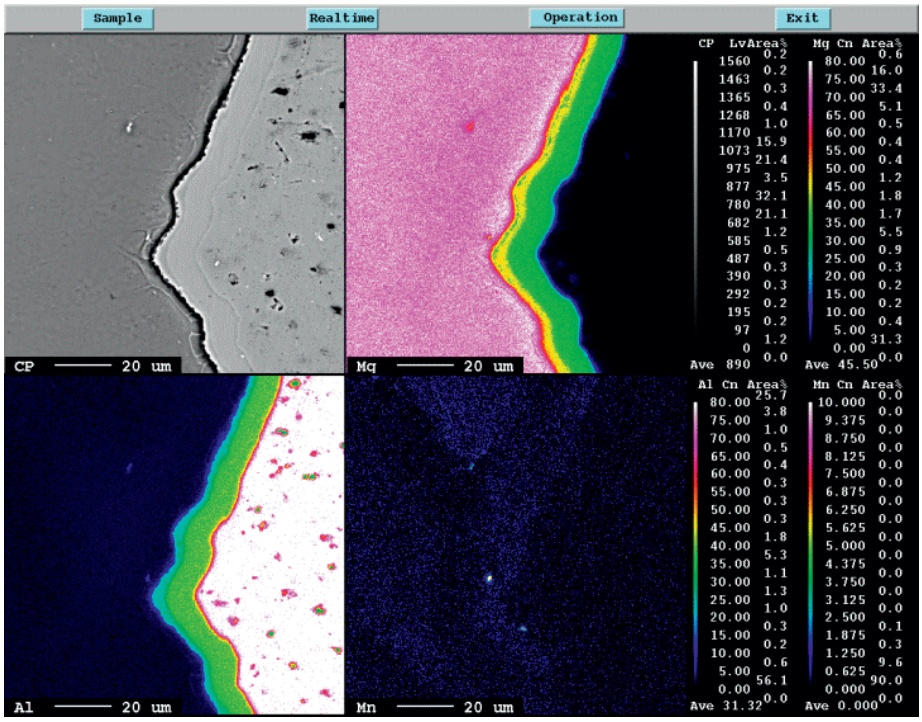

Figure 4.28c. EPMA mapping of the interface in CP Al/AZ31 bi-metal processed by ECAP at 350°C after 4 passes by route Bc.

ECAP 6 passes 350°C

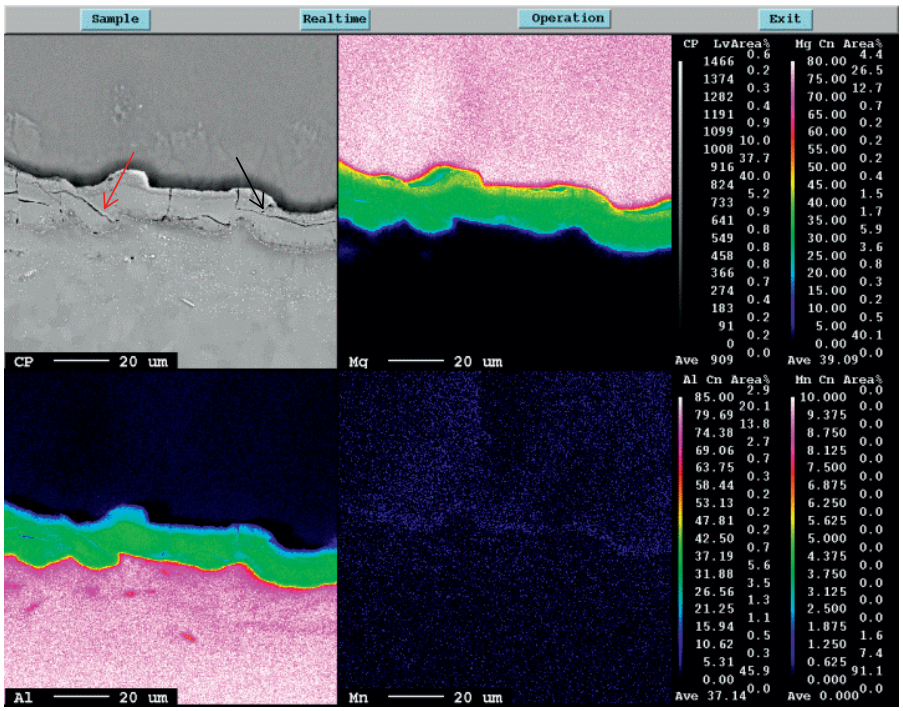

Figure 4.28 d. EPMA mapping of the interface in CP Al/AZ31 bi-metal processed by ECAP at 350°C after 6 passes by route Bc. The black arrow represents type '1' cracks and the red arrow represents type '2' cracks.

In other words, two distinct transition regions were observed in the interface area by quantitative EDS. IF1, the first region, close to the AZ31 alloy was identified as an $Mg_{17}Al_{12}$ intermetallic phase (yellow region in the Mg mapping). The second region (IF2) was identified as the Al_3Mg_2 intermetallic (shown as green in the Mg mapping in Fig 4.28) and was located close the pure Al region. Also, the various EPMA mappings showed that region IF2 was relatively uniform, continuous and increased in width with accumulated ECAP strain, whereas region IF1 was more localized (please refer to Figs 4.27–4.28).

Although bonding has been established by diffusion of Mg into the Al region, the interface consisted of a very thin region of intermetallics. With

increasing number of passes, the thickness (or the width) of the overall interface was increased. The variation in interface thickness with regard to the accumulated ECAP strain at 350°C can be imaged from Fig 4.28. Here, the increase in the region IF1 thickness was relatively small, whereas region IF2 showed a parabolic dependence with increasing strain. Another feature was that cracks formed in two different directions, as can be seen at the interface (red and black arrows in the Figs 4.28b and 4.28d). 'Type 1' cracks seemed to propagate along the circumference of the interface. However, some of the cracks propagated towards the Al region (Fig 4.28d) and are labelled 'Type 2' cracks.

Microstructure studies

The mean grain size in both Al and Mg rich regions decreased with increasing number of ECAP passes, i.e. see the plots in Fig 4.29.

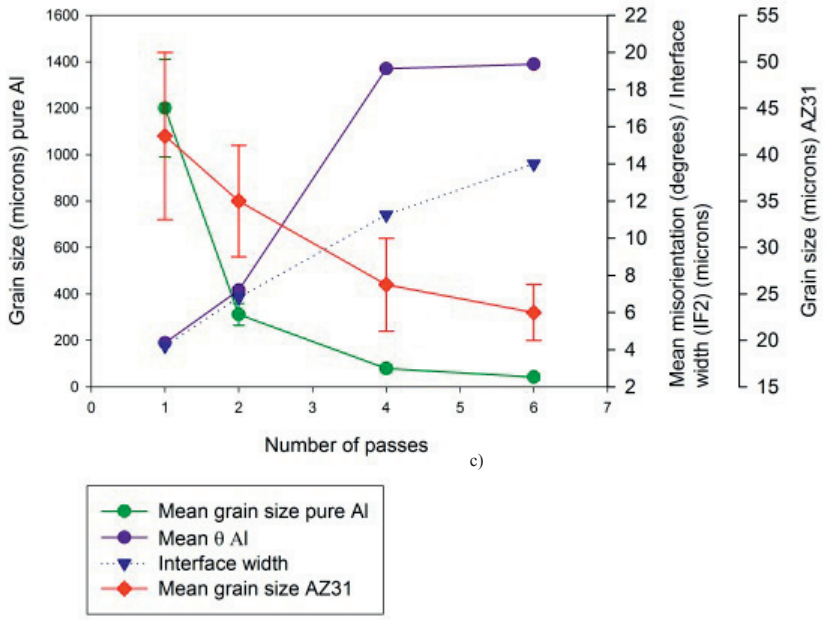

Figure 4.29. Mean grain size of Al and AZ31, width of the interface IF2 and average grain misorientation angle in Al as a function of ECAP passes.

Further, Fig 4.30 shows the corresponding OIM maps of CP Al in the ND-TD plane and one can see that the grain size decreased significantly. Here, the red arrows indicate the interface and the AZ31 alloy region. Some HAGBs were discontinuous, i.e. they stop at one of their ends (refer black arrows in Fig 4.30).

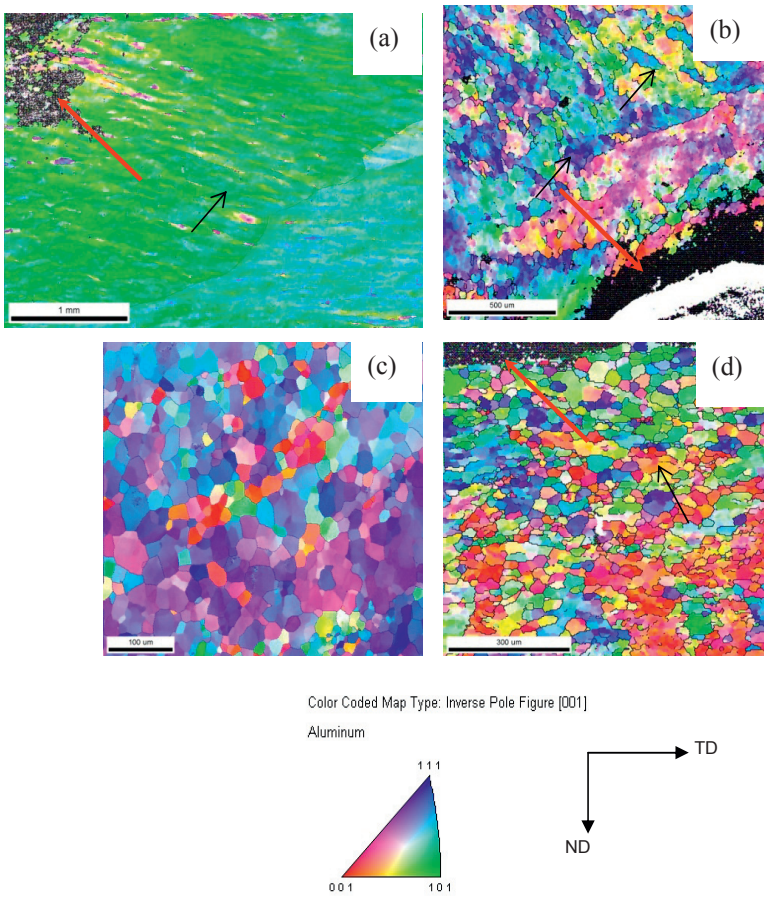

Figure 4.30. OIM maps of CP Al region in samples processed by ECAP at 350°C. (a) first pass; (b) two passes; (c) four passes; (d) six passes. The corresponding colour coding of the IPF maps is shown in the lower part. Note that the red arrow corresponds to the interface between AZ31 and Al regions. The black arrows show the discontinuous HAGBs with open ends.

Further, the OIM maps of the Mg rich AZ31 alloy region in the same plane are shown in Fig 4.31. It can be seen that the mean grain size did not refine as much as in CP Al. In order to reveal further quantitative details, curves containing various microstructural parameters were plotted against the accumulated strain, as shown above in Fig 4.29. The mean grain size in CP Al decreased significantly with increasing strain, e.g. from 1.2 mm to about 30 µm after 6 passes, whereas, the grain size in AZ31 decreased only slightly from ~46 µm to ~22 µm. By comparing the error bars in Fig 4.29 and the OIM maps in Fig 4.31, it can be inferred that the AZ31 region has a bimodal size distribution during the initial passes and the overall grain size became more homogeneous with increasing number of passes.

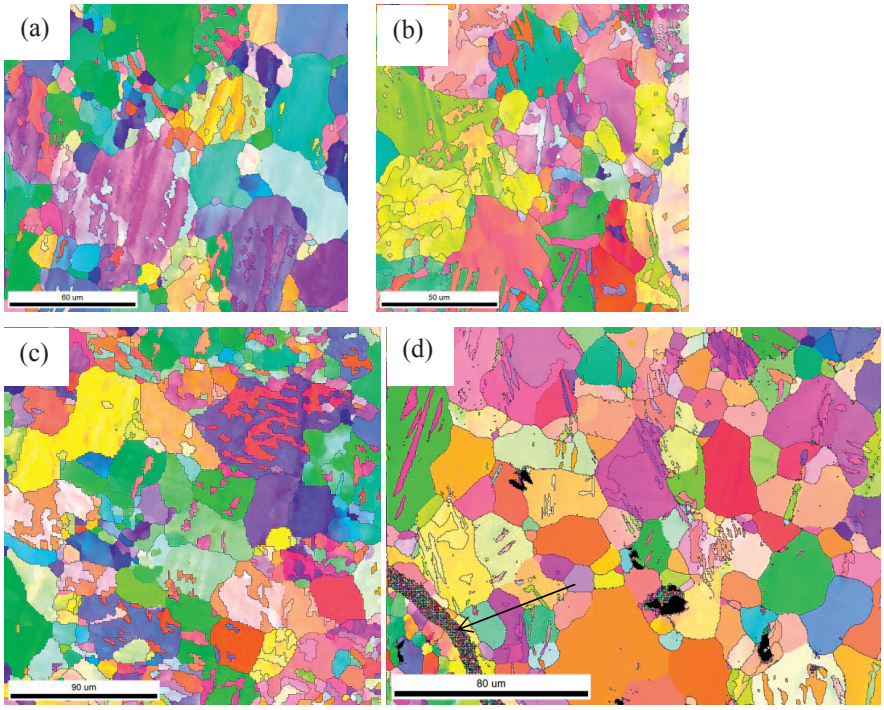

Figure 4.31. A series of OIM maps of the AZ31 region in samples processed by ECAP at 350°C. (a) first pass; (b) two passes; (c) four passes; (d) six passes. Note that the black arrow corresponds to the interface between the AZ31 and Al region.

The microhardness profile after various passes, plotted as a function of distance from the centre of the AZ31 region is shown in Fig 4.32. The hardness increased with increasing number of passes for both CP Al and Mg rich regions. The former increased from 22 HV to ~30 HV, whereas, AZ31 increased from 57 HV to ~66 HV after 6 passes. Another important feature was the reduction in hardness at the centre of the AZ31 region. However, the width of this reduction zone decreased with increasing number of passes.

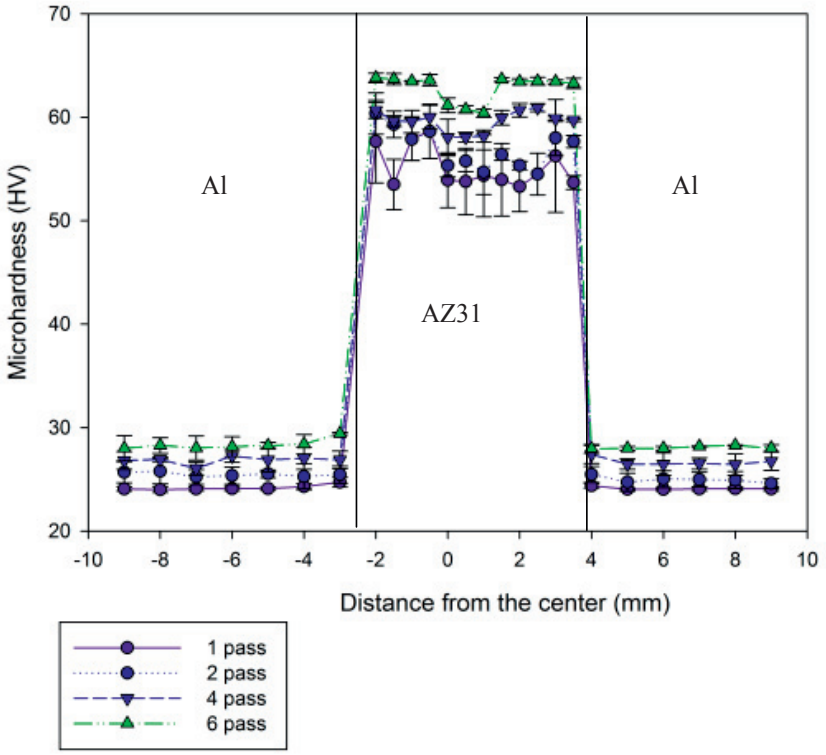

Figure 4.32. Microhardness profiles of samples processed by ECAP at 350°C for various passes plotted as a function of distance from the centre of the AZ31 region.

Tension tests and fracture studies

Tension tests were carried out at a ram speed of 2 mm/s for samples processed to 6 passes as explained in Section 3.7. Figure 4.33 shows a corresponding engineering stress-strain curve. The yield strength (YS) and the ultimate tensile strength (UTS) were 62 MPa and 136 MPa respectively, and the engineering strain at failure was ~15%.

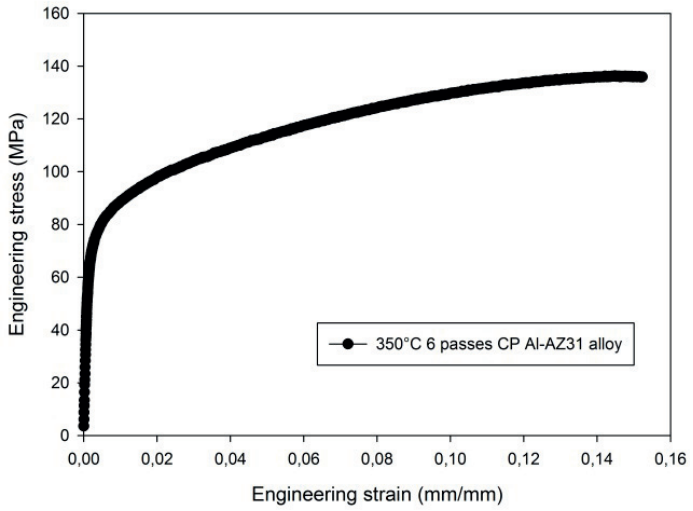

Figure 4.33. The engineering stress-strain curve of a CP Al-AZ31 bi-metal rod type sample processed to 6 passes ECAP at 350°C by route Bc.

The tested samples were investigated using SEM for fractography studies, i.e. Figure 4.34. Three distinct regions have been marked out. The region between the yellow and the green line represented by the yellow arrow, showed some AZ31 particles sticking to the surface of CP Al. The second region between the green and white line represented by a green arrow, failed in a ductile void coalescence manner and did not show any visible AZ31 particles on the aluminium surface. There were also a series of lines caused by sliding of the AZ31 rod which once probably was sticking to the CP Al surface. These lines represent a pull-out phenomenon.

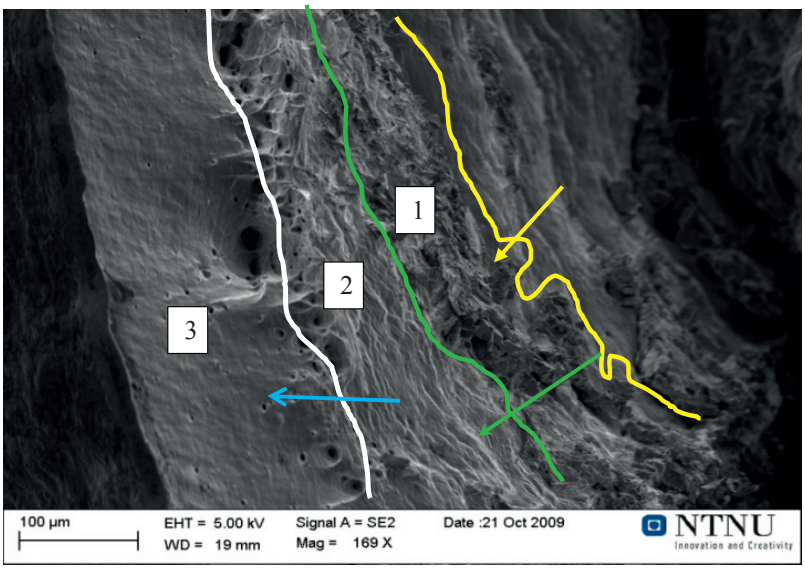

Figure 4.34 .SEM fractograph of a sample after six passes pulled in the uniaxial tensile test. Three distinct regions are marked accordingly; Yellow arrow indicates some AZ31 particles bonded to pure Al. Green arrow indicates inner region depicting delamination on application of stress. Region left of the white line represents the surface parallel to the plane of paper.

Furthermore, an EDS line scan was performed on the fracture surface in region 2 and region 3 to examine (along blue arrow in Fig 4.34) in order to confirm whether there was any presence of Mg on the surface of CP Al. Figure 4.35 reveals this EDS line scan of this blue arrow and in fact, revealed the presence of Mg on a local scale. This showed that there has been local bonding on the surface of Al before a pull-out occurred.

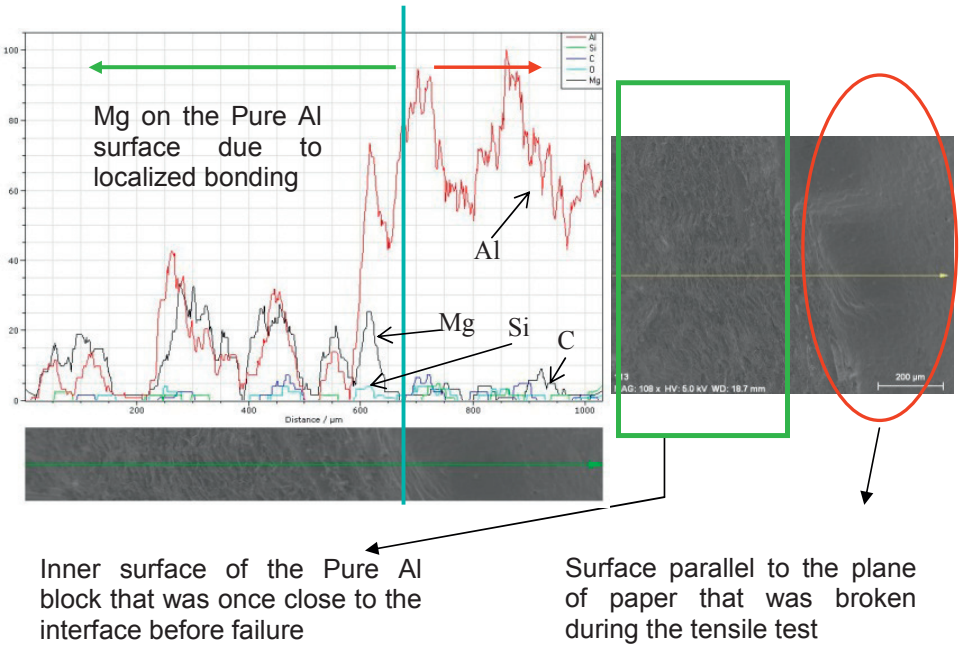

Figure 4.35. Fracture surface EDS line-scan analysis along the blue arrow in Fig 4.34. The localized Mg peaks in the failed region show that the bonding between Al and Mg was present. Y-axis represents the composition in mass% and the x-axis represents distance. Red and black lines correspond to Al and Mg respectively. Also, green, cyan and blue represent, Si, O and C respectively.

4.3.2 Macrocomposite type

As explained in Section 4.3.1, the rod type structure displayed a relatively well bonded interface between the Al block and the AZ31 core when processed at 350°C. The tensile strength of this dissimilar material configuration depended upon the weaker material, in this case CP Al. Also, the interface studies revealed the existence of intermetallics. It was then realised that the strength of an Al/Mg bi-metal can be improved by:

- Introduction of more interfaces with intermetallics .
- Alternate Al and AZ31 layers where the strength is less dependent on the weaker material.

- Increasing the specific surface area (surface area/volume) in order to promote diffusion of Mg.

These guidelines were incorporated in order to develop a higher strength material and led to the present macrocomposite bi-metal configuration. The various results obtained for the macrocomposite are explained in the following.

As-received materials

The as-received constituting materials were the same as those used for the rod type bi-metal structure. The CP Al and AZ31 Mg alloy had an initial mean grain size of 1.2 mm and 46 μm respectively before machining to chips.

Screw extruded macrocomposite

The initial screw extruded macrocomposite was examined by optical microscopy and SE microscopy for grain size and general microstructural analysis along the cross section. Figures 4.36 and 4.37 show the obtained polarized optical micrographs (POMs). Here, the bonding interfaces between various CP Al chips can be seen as black lines. However, the bonding of these chips was not perfect after screw extrusion as can be seen by the black arrows marked out in Fig 4.36. Also, the thick dark regions in the same figure correspond to the Mg rich regions, as indicated by the red arrows.

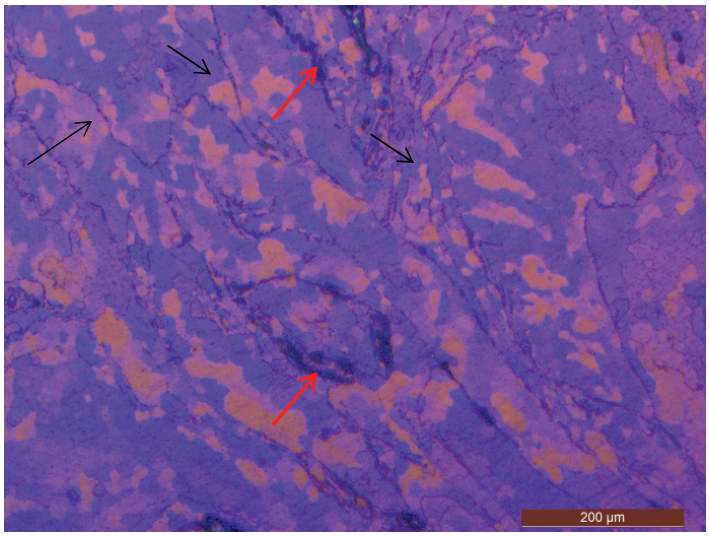

Figure 4.36. Polarized optical micrograph of the screw extruded macrocomposite. Red arrow indicates AZ31 islands and black arrows represent boundaries between bonded Al chips.

Interestingly, the initial as-received materials were subjected to significant grain refinement after machining to chips followed by screw extrusion and the overall mean grain size was found to be ~27±14 µm. Figure 4.37 shows the typical grain structure after screw extrusion as observed by polarized light (PO). CP Al grains are here in colours and AZ31 reinforcements appear as white islands, i.e. marked by black arrows. The overall average microhardness was 42±17 HV. The corresponding mean microhardness of Mg rich regions was 71±4 HV, whereas for the Al rich regions, it was 27±3 HV.

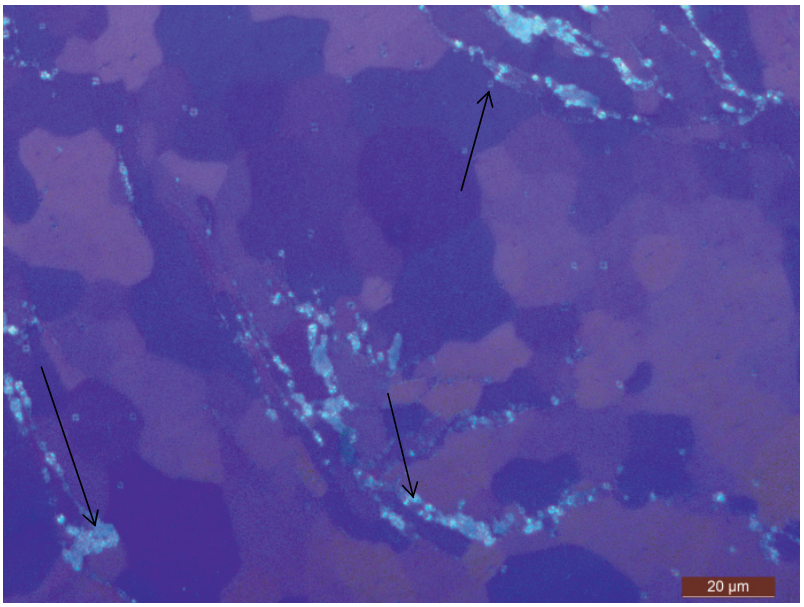

Figure 4.37. Polarized optical micrograph of the screw extruded macrocomposite at higher magnification. Black arrows indicate the AZ31 islands, whereas colored grains correspond to Al.

Further analyses were performed in an FEGSEM (see Fig 4.38). Islands of the AZ31 Mg can here be seen as darker areas and they were broken down into smaller dimensions during the screw extrusion process. The structure showed a more or less homogenized distribution of AZ31 chips along the cross section. However, the chips were broken down to smaller dimensions closer to the centre of the extruded rod. Along the edges of the cross-section, the AZ31 chips remained longer than those observed closer to the centre.

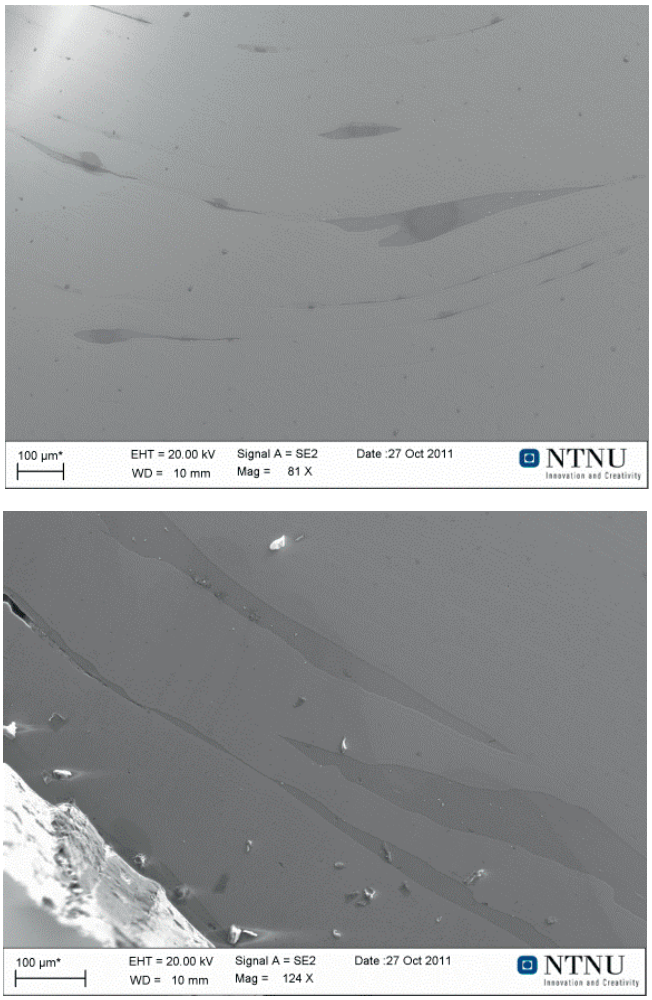

Figure 4.38. SEM micrographs of the screw extruded macrocomposite; (a) close to the center of the cross-section, (b) close to the end of the cross-section, i.e. the outer surface of the rod.

Furthermore, Figure 4.39 shows a magnified SE image of a typical AZ31 and CP Al interface. Two distinct transition regions on either side of the AZ31 island were observed. However, the interface structure and the composition remained similar to that observed in the Al/AZ31 rod type bi-metal configuration.

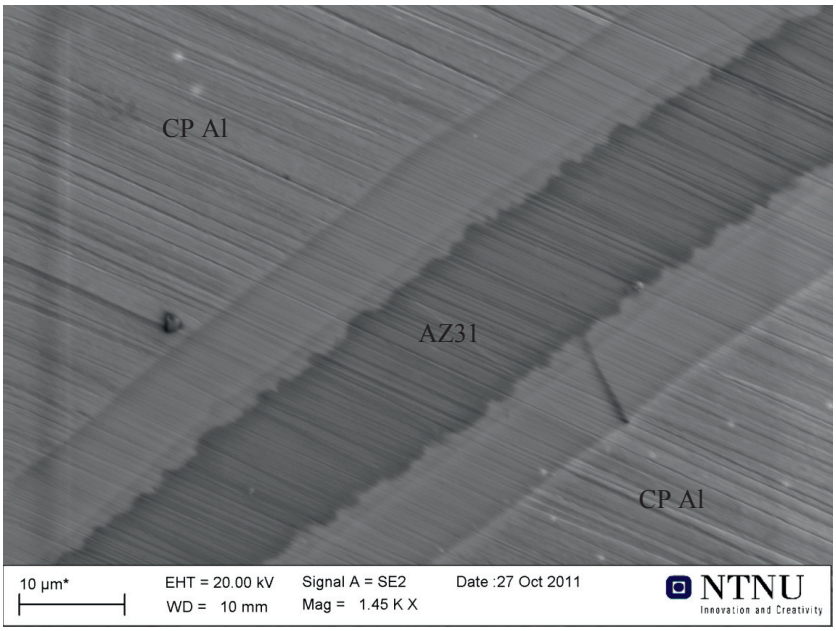

Figure 4.39. A high magnification SEM micrograph in the cross section of the screw extruded macrocomposite. The dark region is AZ31 and the symmetric transitions towards the aluminium are clearly exposed.

Also, EDS was carried out to collect more information on the interface structure. Figure 4.40 shows the characteristic results: Although most of the AZ31 constituents remained as such, i.e. showing little diffusion into Al, localized dissolution of Mg into Al regions occurred. Typically local dissolution occurred for islands where the thickness was quite small ≤ 1 µm.

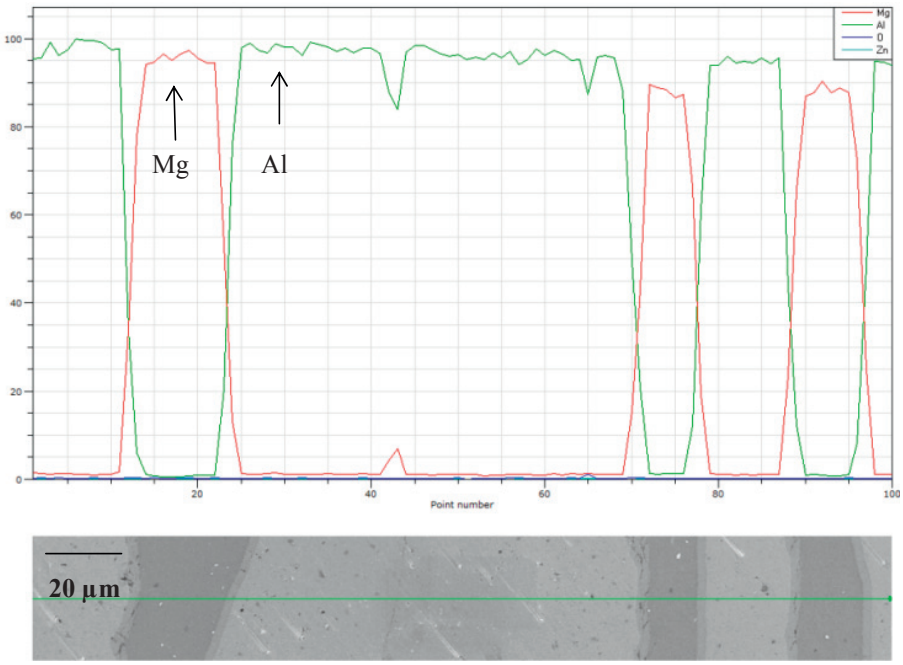

Figure 4.40. An EDS line scan across the Al/AZ31 interfaces in the cross section of the screw extruded macrocomposite. Y-axis represents the composition in mass% and the x-axis represents the distance. The red and green lines indicate Mg and Al respectively, while blue and cyan represent O and Zn.

Corresponding high magnification EDS results are shown in Fig 4.41. It can be seen that the composition of the interface regions consisted of two different interface transition regions, i.e. IF1 and IF2, similar to that explained in Chapter 4. Also, a similar observation as to the rod type bi-metal configuration was seen, i.e. cracks occurred in the interface transition regions (black arrows in Fig 4.41).

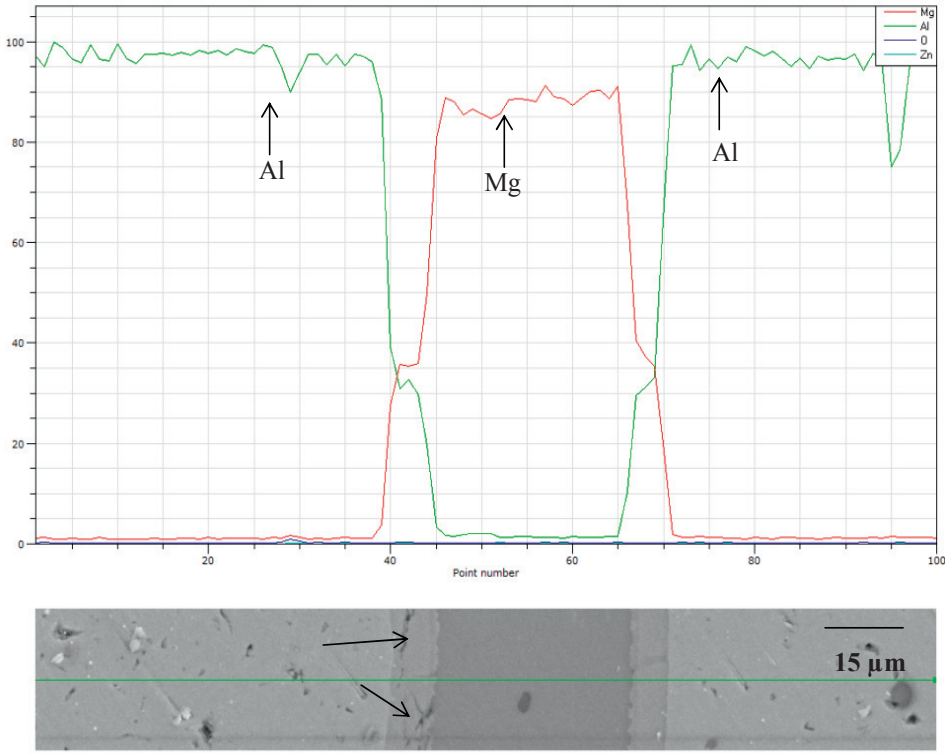

Figure 4.41. An EDS line scan of the Al/AZ31 interface in the cross section of the screw extruded macrocomposite but at a slightly higher magnification. Black arrows show cracks in the transition regions. Y-axis represents the composition in mass% and the x-axis represents the distance. The red and green lines indicate Mg and Al respectively, while blue and cyan represent O and Zn.

ECAP'ed macrocomposite

The ECAP'ed macrocomposite obtained from screw extrusion was analysed in a similar manner as the screw extruded condition itself. Figures 4.42–4.43 show some obtained polarized light micrographs, reflecting typical microscale characteristics.

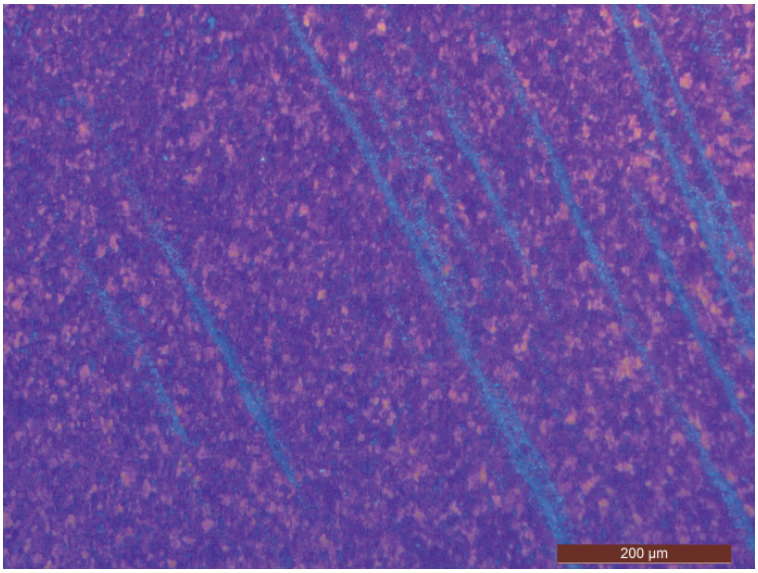

Figure 4.42. Polarized optical micrograph in the cross section view of ECAP'ed macrocomposite deformed at 200°C for 1 pass. The thin blue features are remains of AZ31 chips.

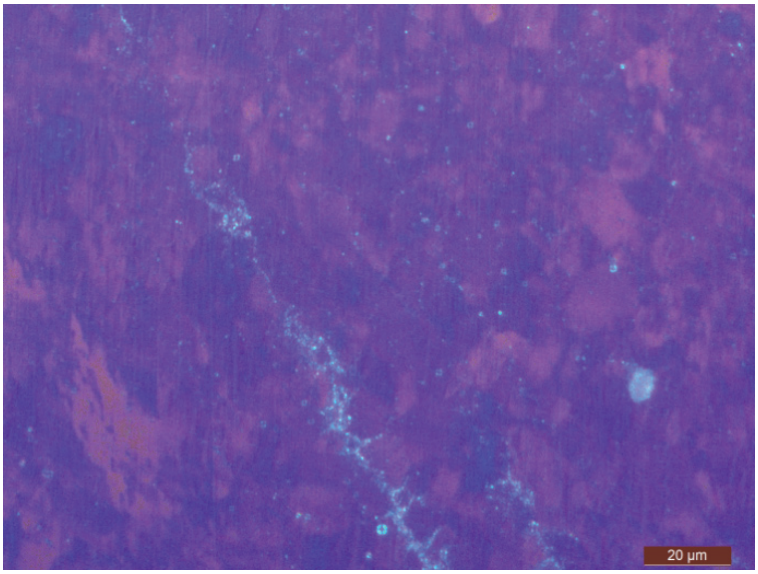

Figure 4.43. Polarized optical micrograph of the ECAP'ed macrocomposite at a higher magnification (T = 200°C, 1 pass).

Firstly, the optical microscopy revealed finer grains as compared to that of the as-screw material. Secondly, the bonding between CP Al chips and between CP Al and AZ31 constituents improved significantly, e.g. no interface boundaries between any two CP Al chips could be observed (contrary to those observed in Fig 4.36). Thirdly, the AZ31 islands observed in the form of thick constituents in the screw extruded samples were absent. Instead, thin and long plate-like morphologies were dominant. Also, the characteristic structure observed by polarized light microscopy (Fig 4.43), contained grains smaller than that observed after screw extrusion (ref. Fig 4.37). In fact, the overall grain structure was further refined from a mean grain size of ~27 μm (as-screw extruded) to a mean grain size of ~5 μm (after 1 pass ECAP at 200°C).

Furthermore, Figures 4.44–4.46 show the SEM (SE image) micrographs of the same ECAP'ed condition.

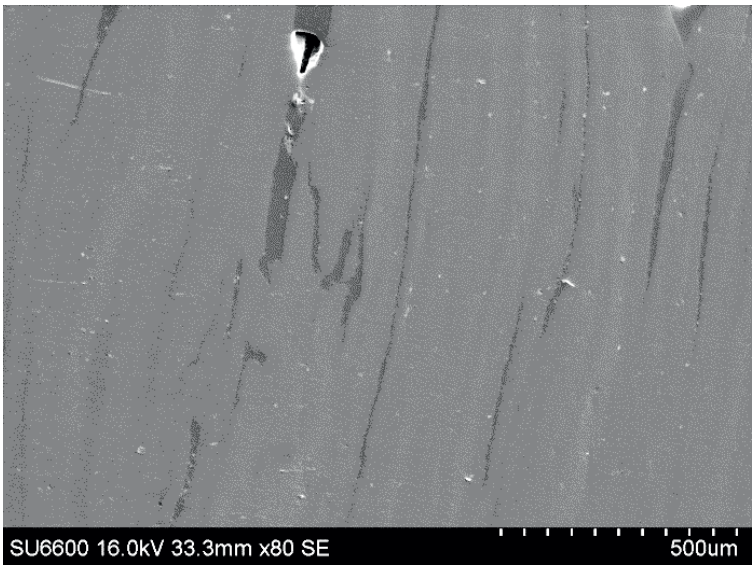

Figure 4.44. SEM micrograph in the cross-section view of the ECAP'ed macrocomposite (T= 200°C, 1 pass).

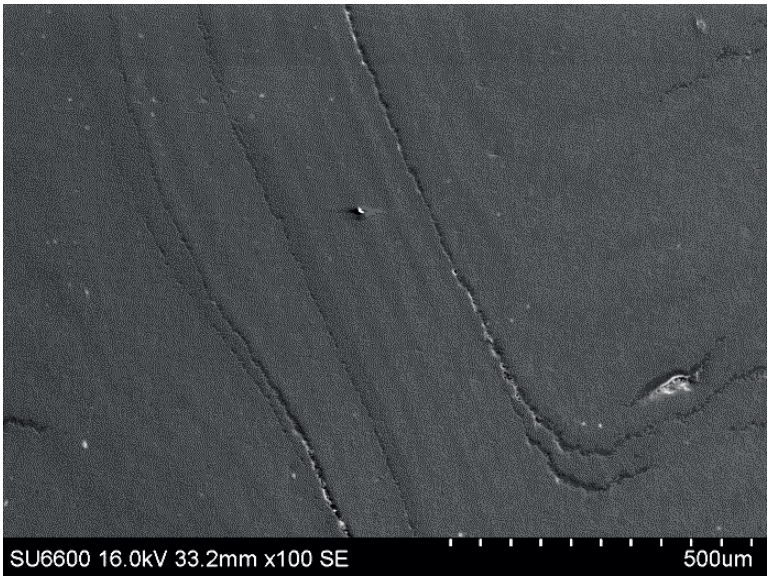

Figure 4.45. Another SEM micrograph in the cross-section view of the ECAP'ed macrocomposite but at a slightly higher magnification.

It can be seen that the Mg rich islands became smaller and thinner after ECAP. Another feature that can be seen from Figs 4.44–4.45 is the alternate bright and dark contrast, which represents the Al and Mg rich regions respectively. In fact most of the dissimilar material constituents were significantly thinned.

Furthermore, the interface observed after ECAP (Fig 4.46) was very different from that observed in the screw extruded macrocomposite. Firstly, the interface region did not show any transitional section. Secondly, no cracks were observed at the interface transition regions. In order to further investigate this interface structure and composition, EDS was also carried out in a FEGSEM.

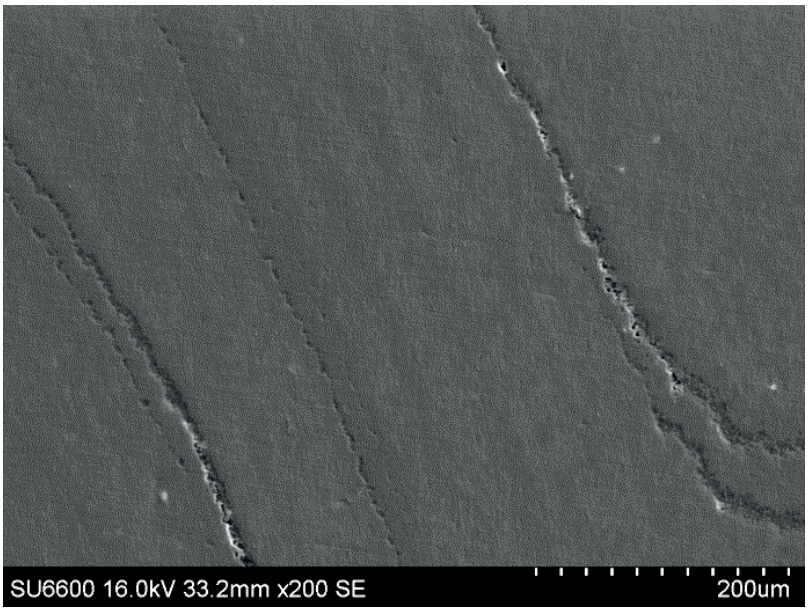

Figure 4.46. Another SEM micrograph of the cross-section view of the ECAP'ed The lighter bands consisted of dispersed Al-Mg intermetallics.

Figure 4.47 shows the EDS line analysis performed in a typical region of the ECAP'ed composite. This reveals that the composition of the Mg rich regions contained 65-80 wt% Mg and 16-25 wt% Al. However, it is important to note that the Mg rich islands did no longer exist as AZ31 Mg regions, but instead as an Mg-Al intermetallic dispersed in Al. Also, this figure reveals that Mg was uniformly dissolved into Al in solid solution and constituted about 3-5 wt%. This is very unlike the screw extruded condition where the latter exhibited a distinct distribution of Mg and Al rich constituents, and minor dissolution of Mg into Al occurred (refer Fig 4.40).

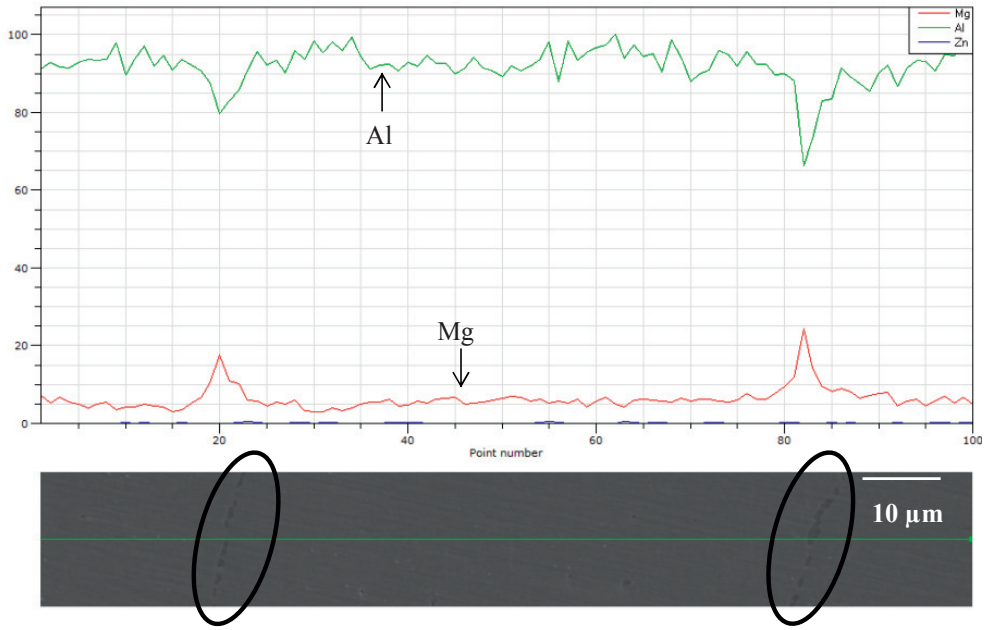

Figure 4.47. EDS line scan analysis of the cross-section view of ECAP'ed macrocomposite but at a slightly high magnification. Y-axis represents the composition in mass% and the x-axis represents the distance. The red and green lines indicate Mg and Al respectively, while blue represents Zn. Black ellipses indicate the interface structures.

EBSD analysis was also performed on the ECAP'ed macrocomposite in order to characterize the microstructure. Figures 4.48–4.49 show OIM maps taken in the ED-ND plane. The grains were refined significantly, i.e. to ~5 µm after ECAP. The noise in the OIM map shown in Fig 4.49 corresponds to poor patterns caused by high accumulated strains, combined with inherent poor indexing of the grain boundaries. In general, the grain size distribution was found to be homogeneous after ECAP.

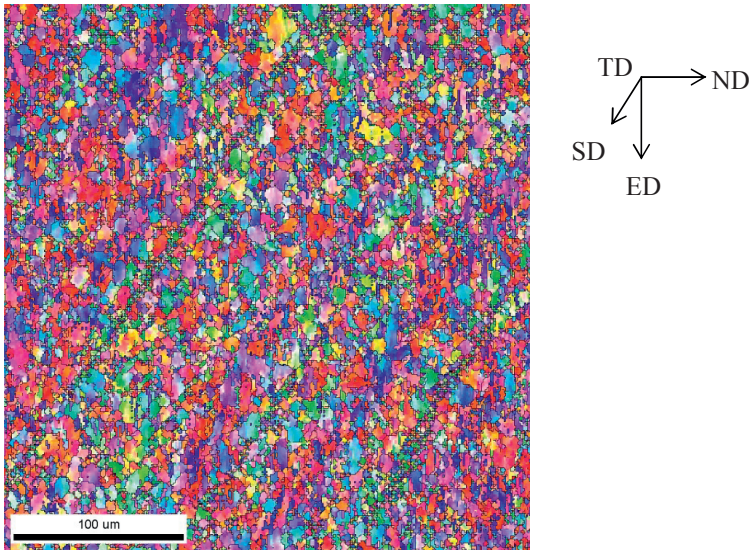

Figure 4.48. An OIM image of the macrocomposite after 1 pass ECAP at 200°C showing fine grains distributed in a homogeneous manner .

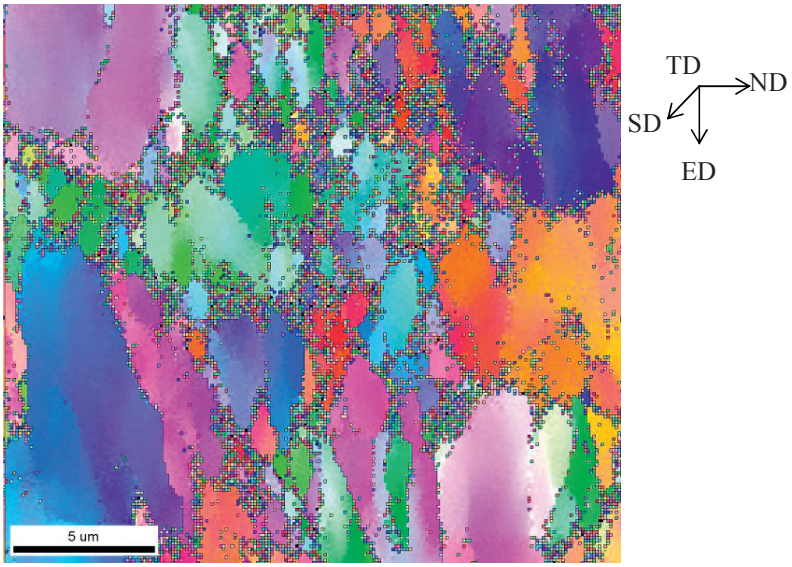

Figure 4.49. A corresponding high resolution OIM image. Some grains reveal misorientation gradients.

EDS mapping was also performed in random regions along the longitudinal ED-ND plane (Fig 4.50). It can be seen that a more significant diffusion of Mg into Al occurred as compared to that of the screw extruded counterpart. However, the width of Mg rich islands was not as thin as they were in the cross section. This could mean that diffusion of Mg into Al was more extensive along the ND and TD than in the ED. Here, green and red areas can be seen, representing alternate CP Al and Mg/Al intermetallics formed as a consequence of diffusion of Mg into aluminium.

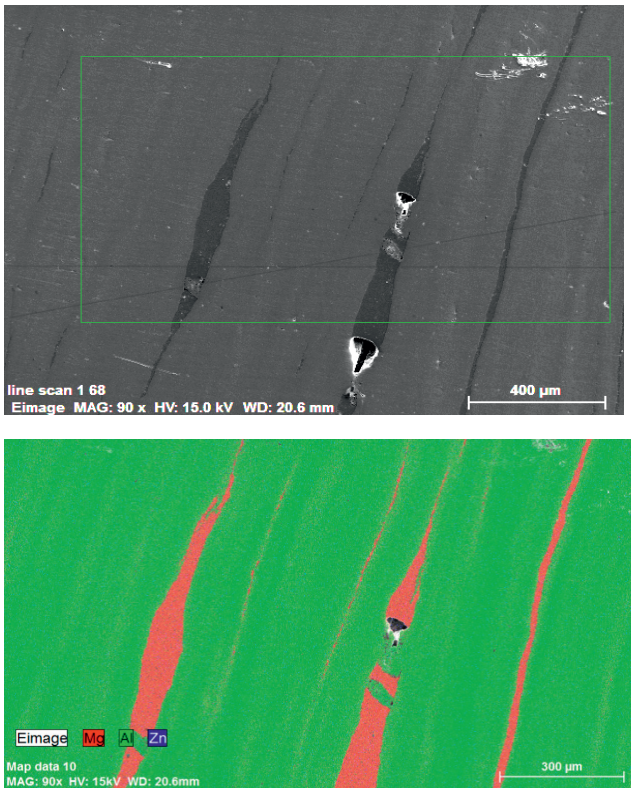

(a)

(b)

Figure 4.50. An EDS mapping of the ECAP'ed macrocomposite along the longitudinal ED-ND plane; (a) the SE image of the selected area. The mapped region is shown by the green rectangle. (b) EDS mapping of the selected region. Green color represents Al and the red colour represents Mg rich constituents.

Mechanical properties

Tensile tests were carried out to evaluate the strength of the material under uniaxial loading. To have a comparable set of data, tests were also performed on as-screw extruded specimens. Figure 4.51 shows the engineering stress strain curve for both screw extruded and subsequent ECAP'ed specimens. Table 4.2 gives the various properties calculated from these curves. It can be seen that both the yield strength and the UTS increased 1.5 times after ECAP. However, the strain to failure was reduced by ~50%. Another interesting feature that can be observed from these curves is the serrations.

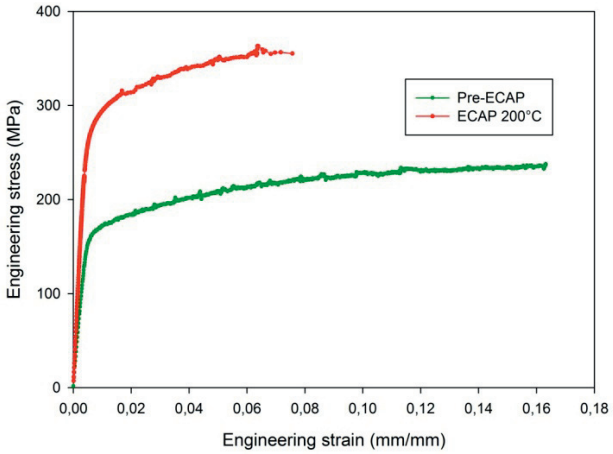

Figure 4.51. A comparison of engineering stress-strain curves of the screw extruded and the subsequent ECAP'ed macrocomposite.

Table 4.2 A comparison of the mechanical properties of the screw extruded macrocomposite and the ECAP'ed macrocomposite. The data is taken from a single test due to limited availability of material.

Sample	Yield strength (MPa)	UTS (MPa)	Elongation to failure (%)
Screw extruded macrocomposite	172	237	16.4
ECAP'ed macrocomposite	275	363	7.8

Fractography

The SEM fractographs of a failed as-screw extruded tensile sample is shown in Figs 4.52–4.53. This sample had undergone failure without undergoing necking and the sample surfaces appeared flat and bright. Several other features can also be observed from the fractographs. The black arrows represent cracks propagating through the AZ31 islands along their length. The red arrows represent a network of interconnecting voids. The screw extruded material failed in different ways in different regions. In general, AZ31 Mg alloy islands underwent brittle fracture at the interfaces and can be observed by the elliptic markings in Fig 4.52.

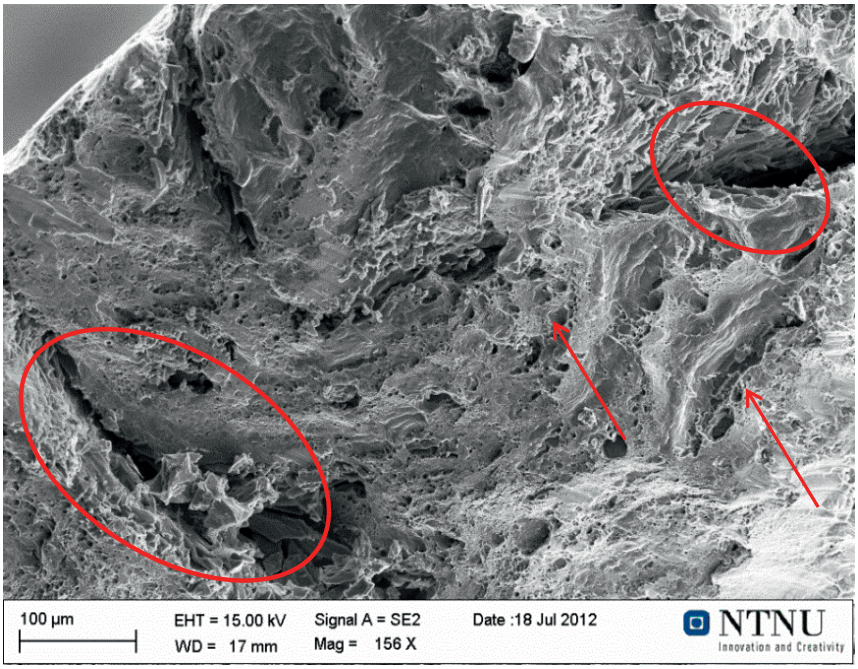

Figure 4.52. SEM fractograph from the as-screw extruded macrocomposite deformed in uniaxial tension. Red ellipses represent regions failed by brittle fracture (delamination) and the red arrows represent regions failed by ductile fracture (local dimple growth). Localization of slip was quite dominating as well, causing slip band decohesion. The upper left part shows a typical area where the latter mechanism is dominant.

The large secondary delamination cracks (red ellipses) correspond to brittle fracture at the interface where debonding of the AZ31 islands occurred. Smaller pores/dimples (red arrows) represent the cup and cone ductile fracture in Al and the size of these pores correlates with the dimensions of local AZ31 constituents. Also, the geometry of these pores is similar to the initial AZ31 alloy islands observed in the cross section, e.g. see Fig 4.37. In general, the CP Al matrix failed by ductile cup and cone fracture or slip decohesion. However, from the interconnected pores in Fig 4.53 (see the black arrows), it can be inferred that poor bonding between different chips had accelerated crack propagation through their boundaries.

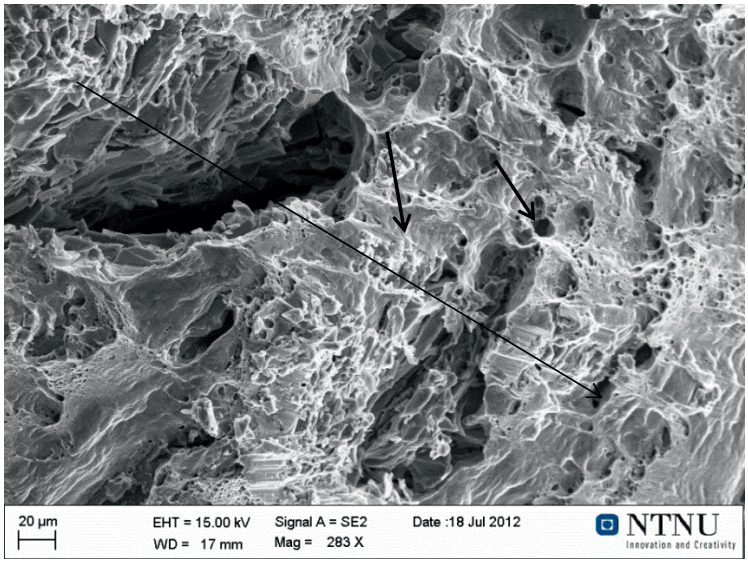

Figure 4.53. Another SEM fractograph of the failed screw extruded macrocomposite deformed in uniaxial tension. The black line represents the EDS scan used to identify the locations of Al and Mg alloy containing regions.

Also, an EDS line scan was performed along the line shown in Fig 4.53. The corresponding results shown in Fig 4.54 confirmed the discrete CP Al and AZ31 islands. It seems obvious from this plot that the CP Al regions contain some magnesium and the green peaks correspond to AZ31 islands embedded in the CP Al matrix.

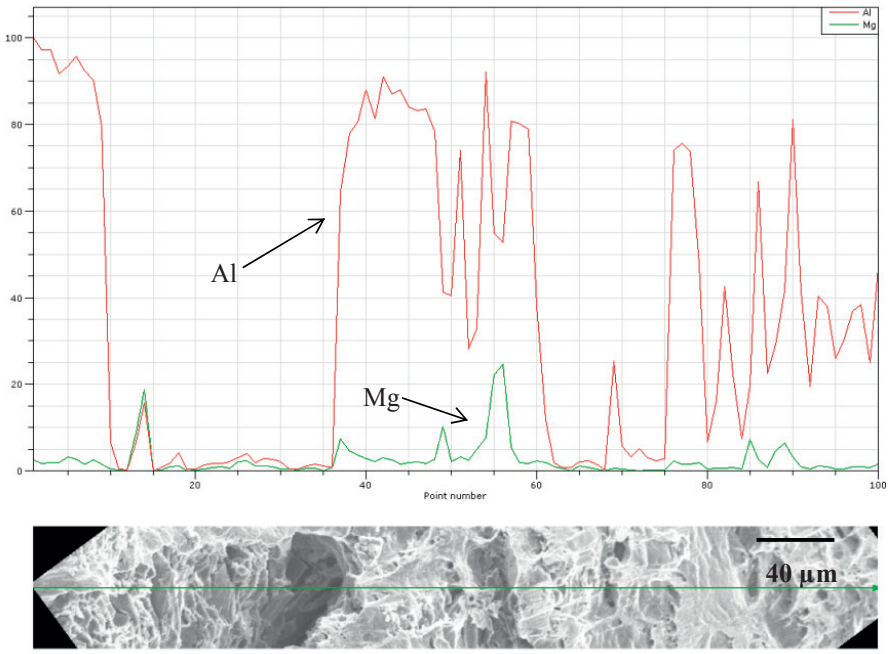

Figure 4.54. An EDS line scan of the screw extruded macrocomposite depicting Al and Mg composition along the line shown in Fig 4.53. Red line represents Al and the green line represents Mg rich constituents. The x-axis corresponds to the distance (point number) and the y-axis corresponds to composition in mass %.

Furthermore, Figures 4.55–4.57 show SEM fractographs of the subsequently ECAP'ed macrocomposite. The latter failed catastrophically without any visible necking. However, significant differences can be observed as compared to the screw extruded counterpart.

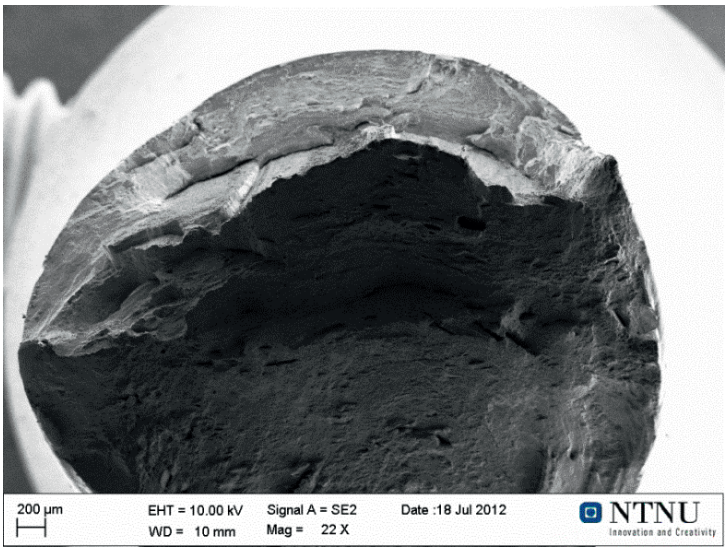

Figure 4.55. A low magnification SEM fractograph of the ECAP'ed macrocomposite pulled in uniaxial tension. A brittle fracture on a plane perpendicular to the cross-section can be observed.

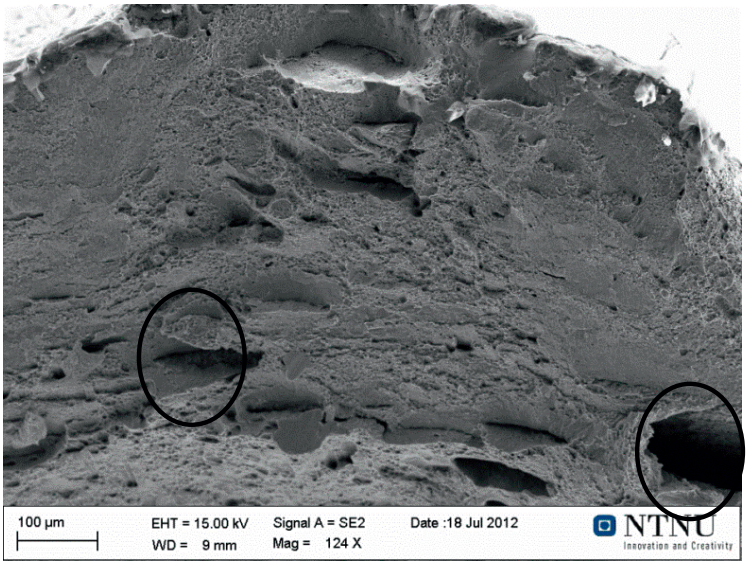

Figure 4.56. SEM fractograph showing a region failed predominantly by brittle fracture in the ED-ND plane of the ECAP'ed macrocomposite pulled in uniaxial tension. Black circles represent debonded regions at interfaces.

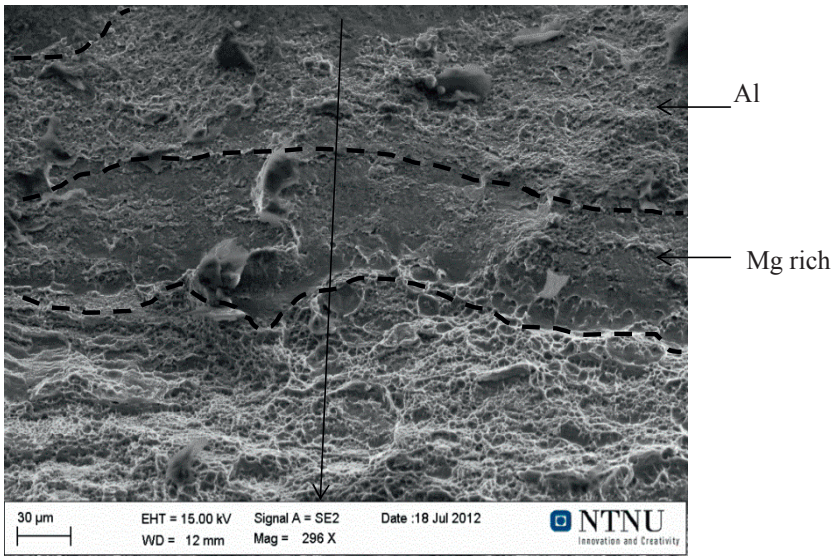

Figure 4.57. A high magnification SEM fractograph in the cross-section of the ECAP'ed condition. The black line illustrates the location of the EDS scan in Fig 4.58. Broken lines separate the regions of CP Al and the Mg rich constituents.

Firstly, the screw extruded macrocomposite showed flat bright surfaces typical for cleavage, whereas from Fig 4.55, a large brittle relief contour can be seen for the ECAP'ed macrocomposite. Figure 4.56 shows a magnified image of this contour. Here, the surface is smooth and some local ductile features appear due to presence of the CP Al matrix. However, the interfaces fractured in a brittle manner. Further, black circles depict large deep voids on the surface in Fig 4.56. The large voids represent the semi diffused AZ31 islands that once were aligned along the ED-ND plane prior to ECAP. A magnified image of the failed cross section is shown in Fig 4.57. Alternate ductile and brittle regions can be seen and are separated by dotted lines. These regions correspond to CP Al and Al-Mg intermetallics respectively, see Section 4.3.3. Further, an EDS line scan shows the existence of Mg within the alternate layers as shown in Fig 4.58 below and that Mg has been dissolved into CP Al to a large extent.

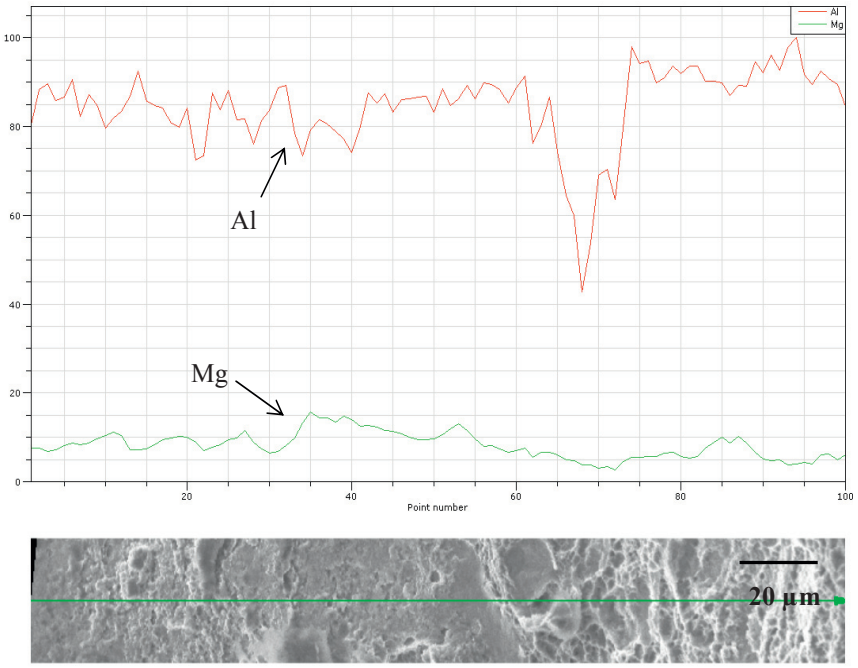

Figure 4.58. An EDS line scan of the screw extruded macrocomposite after ECAP depicting Al and Mg composition along the line in Fig 4.57. Red line and green line correspond to Al and Mg regions respectively. The x-axis corresponds to the distance (point number) and the y-axis corresponds to composition in mass %.

The CP Al matrix has a typical ductile cup and cone fracture and the dimples are relatively homogeneous corresponding to the homogeneous grain size observed.

The secondary cracks seemed to propagate along the length of the Mg/Al intermetallic interfaces. However, the presence of the surrounding CP Al matrix obstructed propagation, thus resisting any premature failure.

Microhardness

Microhardness measurements were made across the cross section in order to reflect the effect of Mg in the microstructure of the macrocomposite before ECAP and after being processed by ECAP. Figure 4.59 shows a comparative

microhardness plot of these two conditions against the distance along the cross-section. It is obvious that the ECAP'ed macrocomposite has a higher microhardness compared to screw extruded condition. Peaks in the as-screw extruded material represent the AZ31 islands. The difference in microhardness between the islands and the matrix is quite significant whereas for the ECAP'ed macrocomposite, the hardness of the matrix itself is high ~81±3 HV, which is approximately four times the value for the screw extruded sample. Secondly, the difference between the peaks and the matrix hardness in the ECAP'ed condition is relatively low and the peaks have similar values ~100-110 HV.

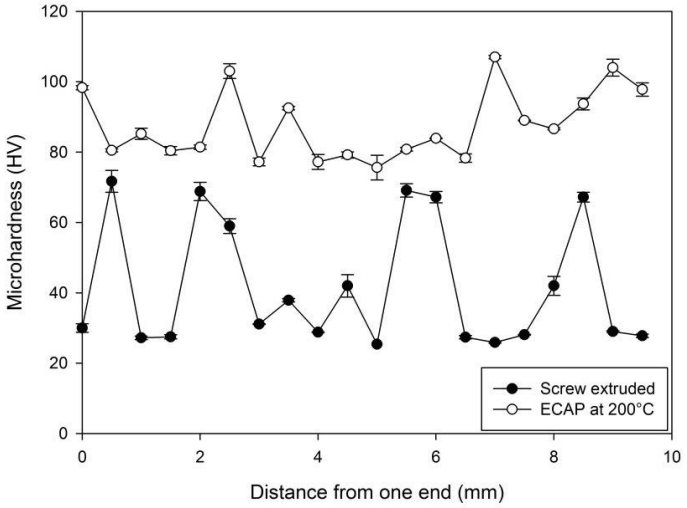

Figure 4.59. A comparison of the microhardness profiles of the as-screw extruded and the subsequent ECAP'ed macrocomposite over the cross-section.

4.4 Sheet composites

4.4.1 Al/Al composite

The Al/Al sheet composite is a sandwich structure containing three Al sheets stacked on top of each other and subsequently processed by ECAP. The presence of the exact same material at all interfaces makes interpretations of experimental results relatively straight forward. For example, the presence of the

same material means that the properties in adjacent sheets are equal, and the composite constituents are expected to behave similarly during ECAP. Secondly, since the chemical composition of the sheets is identical, different equilibrium and non-equilibrium phases are not expected at the interfaces. Finally, other effects such as additional strain hardening, solute strengthening or dynamic precipitation, are avoided by using this pure Al sheet configuration. Thus, any change in the sheet bonding characteristics would be originated from the ECAP processing conditions and relative parameters. In addition, pure Al is soft and the required pressure to process the Al/Al sheets composite is low. Also, the soft nature facilitates easy plastic flow in the sheet interface regions, thereby giving the necessary plasticity for mechanical bonding to occur under frictional conditions.

As-received material

The as-received material used for these particular investigations was the same as used for the CP Al studies described in Section 4.2. Figure 4.2 shows an OIM micrograph of the as-received structure and the initial mean grain size and microhardness were 1.2 mm and 22 ±2 HV respectively.

Investigations on the ECAP'ed material

As explained above, these investigations were aimed to identify the optimised experimental conditions for satisfactory bonding between the sheets. Therefore, the Al/Al sheets were processed by varying different ECAP parameters for, e.g.:

- Effect of sample length
- Effect of back pressure
- Effect of interface surface roughness
- Effect of pressing speed

Establishing bonding criteria

A detailed multi-parameter processing design was established in order to reduce the number of samples and experimental parameters. This procedure is described as follows:

Samples were first prepared to a length of 100 mm as this was the standard length for processing ECAP bars in the NANOSPD group at NTNU. The samples were then at first processed under the processing conditions normally conducted for Al based materials within this group. Three different sandwich structures having their sheet surfaces cleaned, dried and roughened using 80 grit SiC paper, then wire and machine brushed, were subjected to RT ECAP at 2 mm/s pressing speed without back pressure. However, none of the samples exhibited satisfactory bonding due to the slipping of sheets over each other. Therefore, another set was prepared and processed without back pressure at a higher speed, i.e. 5 mm/s. Still no bonding was obtained. Since all the samples failed to bond, a next set of similar samples were processed under identical conditions but with the introduction of ECAP back pressure of about 100 KN, at 2 mm/s. However, samples still failed to bond. New ECAP trials were then conducted at 5 mm/s with a BP of 100 KN. These samples were roughened similarly but did not bond. The sample that was machine brushed could not be processed completely, owing to the limited load-bearing capability of the punch-tool used for pressing (up to~600 KN). To summarize these initial investigations, a list of the trial samples are shown in Table 4.3, with the nomenclature explained in Section 3.3.1.

Table 4.3. Overview of the 100 mm long ECAP samples and their respective results.

Sample	(F)Failed/Bonded (BN)
1002SN	F
1002WN	F
1002MN	F
1005SN	F
1005WN	F
1005MN	F
1002SB	F
1002WB	F
1002MB	F
1005SB	F
1005WB	F
1005MB	Stopped due to pressure limit

Secondly, the length of the samples was varied as length could have an added effect to the operating ECAP conditions, since friction is significantly involved. Here, the length of all samples were reduced to 80 mm in order to facilitate more easy processing within the limits of the punch-tool especially for the machine brushed samples. In addition, a machine brushed sample was ECAP'ed at a speed of 4 mm/s (sample 804MB) as processing of the sheet composite at 5 mm/s having an 80 mm specimen length (805MB), reached the limit of the punch-tool, similar to the 1005MB sample. However, it was found that even the sample 804MB reached the limit for the punch-tool. A summary of these trials are shown in Table 4.4.

Table 4.4. Overview of the 80 mm long ECAP samples and their respective results.

Sample	(F)Failed/Bonded (BN)
802SN	F
802WN	F
802MN	F
805SN	F
805WN	F
805MN	F
802SB	F
802WB	F
802MB	F
805SB	F
805WB	F
805MB	Stopped due to pressure limit
804MB	Stopped due to pressure limit

Further, the same procedure was repeated for 70 mm length samples. Samples were also processed at 1 mm/s speed and then both with and without back pressure. The results are shown in Table 4.5. Interestingly, the sample 705MB bonded very well. However, samples 704MB, 701MB and 702MB did not show any bonding. As with the other samples, no bonding was obtained for specimens roughened with SiC paper and wire brushing.

Table 4.5. Overview of the 70 mm long ECAP samples and their respective results.

Sample	(F)Failed/Bonded (BN)
702SN	F
702WN	F
702MN	F
705SN	F
705WN	F
705MN	F
702SB	F
702WB	F
702MB	F
705SB	F
705WB	F
705MB	**BN**
704MB	F
704WB	F
704SB	F
701SN	F
701WN	F
701MN	F
701SB	F
701WB	F
701MB	F

After having observed successful bonding (705MB), it was necessary to further optimize the process. Therefore, the length of the samples and the pressing speed were varied systematically. From Tables 4.3–4.5, it can be seen that all samples failed to bond unless they were machine brushed. Hence, the new trials with sheet specimens were only processed at 5 mm/s and 2 mm/s using a back pressure of 100 KN for machine brushed samples. Disappointingly, all these

samples failed to bond. Table 4.6 shows a list of the samples processed with different lengths and pressing speeds and which were aimed at optimising the process.

Table 4.6. Overview of the 50 mm and 60 mm long ECAP samples and their respective results.

Sample	(F)Failed/Bonded (BN)
502WB	F
502MB	F
505WB	F
505MB	F
602WB	F
602MB	F
605WB	F
605MB	F

Analysis of ECAP'ed samples

Figure 4.60 shows a macro-photograph of some selected failed samples. The failed 100 mm sample (100WN) can be seen to the left. The middle sample shows a tailor-made 70 mm long sample that was used to investigate the severity of surface preparation. Here, the top sheet was wire brushed while the other two sheets were machine brushed. It can be seen that the bottom two sheets bonded very well while the top sheet remained un-bonded. The third sample to the right represents a machine brushed sample (605MB) that failed to bond.

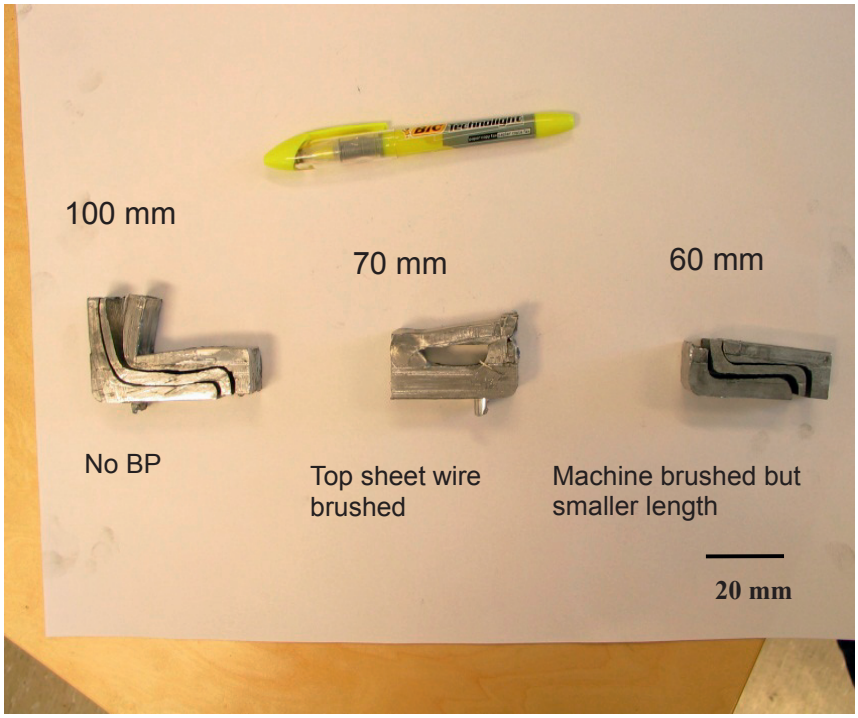

Figure 4.60. Macro-photographs showing examples of failed samples with respective various experimental conditions processed by ECAP at RT.

Microstructure analysis

Figure 4.61 shows an interesting macro-photograph of the well bonded sample (705MB) that has been sectioned along the longitudinal direction. The length shown in the picture is smaller than 70mm as the sample was previously cut for EBSD analysis and microhardness measurements before the photograph was taken.

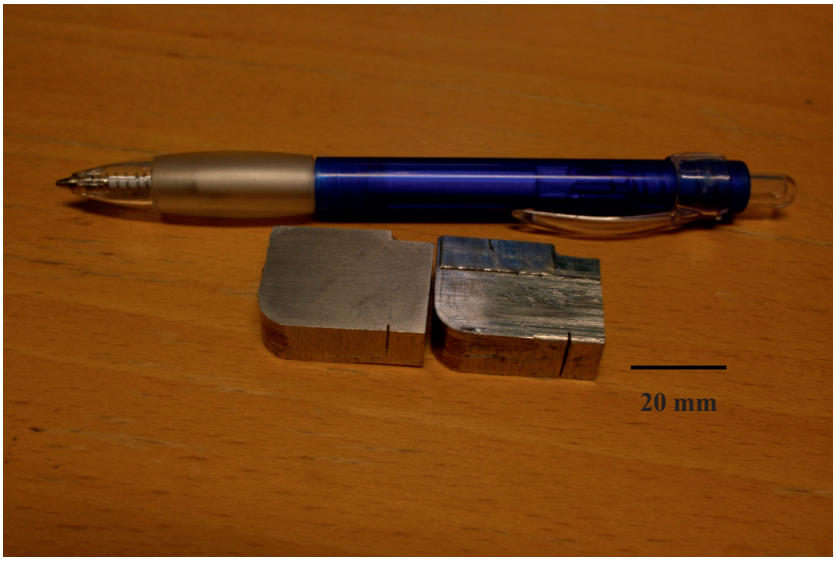

Figure 4.61. Overview of the successfully processed Al/Al sheet composite. (Sample 705MB). The right part depicts the outer surface and the left part shows the inner surface after ECAP.

A representative OIM map of the successfully processed Al/Al sheet composite along the ND-ED plane is shown in Fig 4.62. It is to be noted that interfaces were not observed even after careful SE and EBSD imaging in different regions. It can be seen that severe straining was introduced even after one pass. The grains were oriented along the shear direction and not the extrusion direction. A significant colour contrast can be seen within single grains, indicating obvious lattice rotations. Deformation bands are also observed (see black arrows in Fig 4.62). Interestingly, the grains were significantly refined from 1.2 mm to an average size of 400 μm after one pass ECAP. The average microhardness also increased from 22±2 HV in the as-received material, to 32±3 HV after one pass ECAP. In order to search for the interfaces and subsequently studying the possible effect of surface oxides on bonding, EPMA was conducted along the ED-ND plane.

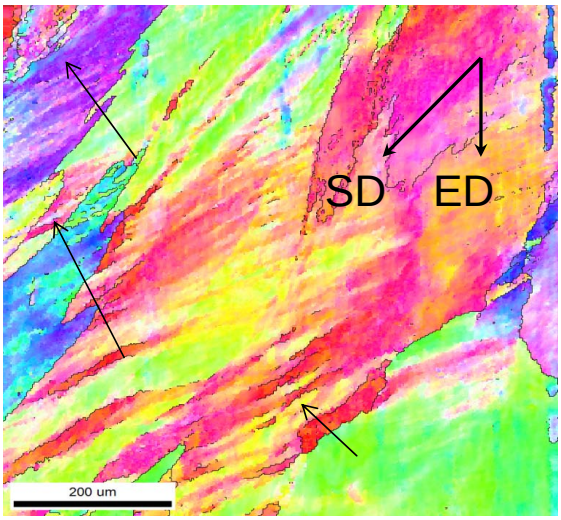

Figure 4.62. OIM map representing the microstructure of a successfully processed Al/Al composite by ECAP at RT. Sample id : 705MB. Black arrows indicate the deformation bands.

A corresponding EPMA quantitative map is shown in Fig 4.63. No oxides were observed at this resolution. In fact, it is quite obvious from the oxygen mapping that the existence of oxides could not be proven by the EPMA technique. However, some iron-rich particles were present. Also, the exact interface region was almost impossible to locate as there was complete plastic bonding of the sheets.

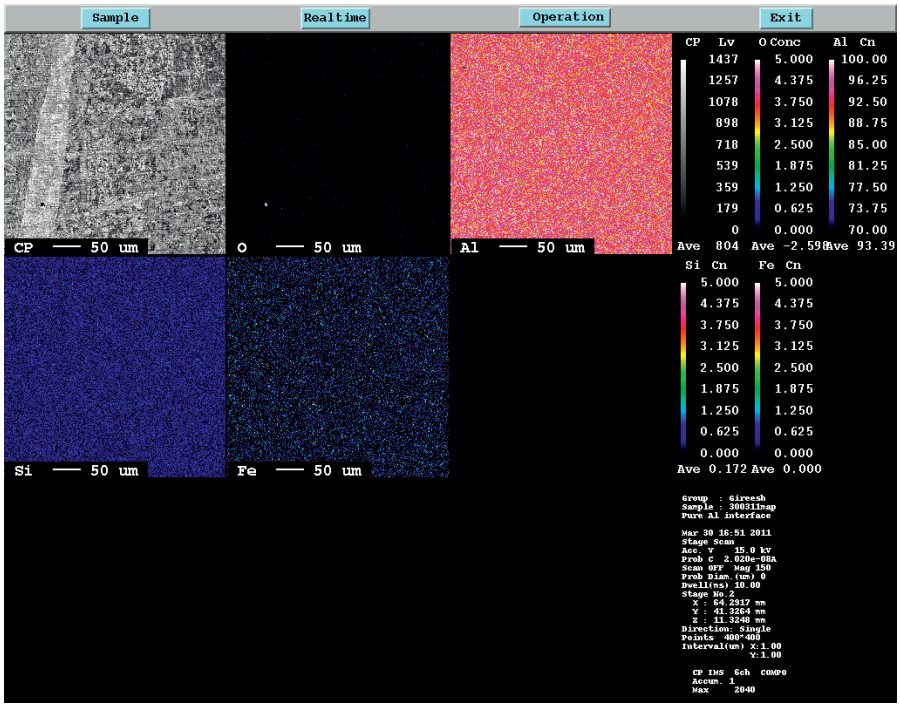

Figure 4.63. EPMA analyses of the successfully bonded Al/Al sheet composite processed by BP-ECAP at RT and 1 pass. The EPMA mapping depicts the composition of O, Al, Si and Fe contents. Sample id : 705MB.

4.4.2 Al/3103 composite

The above Al/Al composite was investigated for better understanding the effect of experimental parameters on bonding between two sheet surfaces processed by ECAP. From these results, it was found that bonding could be possible when a sample had its surfaces machine brushed and was processed by ECAP at RT at a speed of 5 mm/s with a BP of 100 KN. These conditions were therefore implemented to study the effect of material behaviour on the bonding characteristics when two different materials were used. In this case, CP Al and an AA3103 Al alloy were engaged, since both materials are relatively soft compared

to other Al alloys. Also the AA3103 alloy has different strain hardening characteristics as compared to CP Al. The obtained results for this configuration are presented in the following.

As-received material

The Al/AA3103 alloy sheet composite was made of two different materials, namely, CP Al and the alloy AA3103. The as-received CP Al is the same material used for the CP Al studies presented in in Section 4.1, e.g. Fig 4.2 showing a representative OIM map.

The corresponding OIM map of the as-received AA3103 alloy after homogenization is showed in Fig 4.64. The initial mean grain size was here ~80 µm and the average microhardness value 34±4 HV. The microstructure consisted of equiaxed grains having a more or less homogeneous distribution. Also, the grains contained sub-structures with various misorientations.

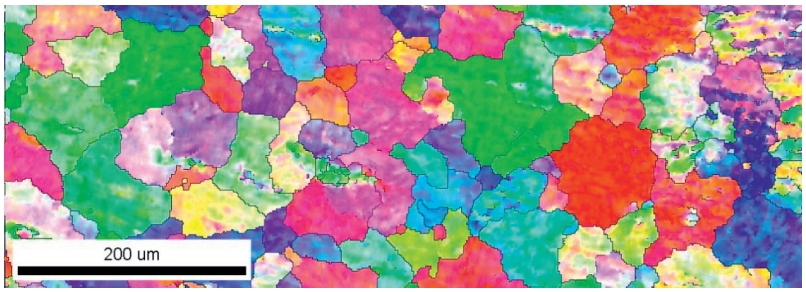

Figure 4.64. OIM map representing the microstructure of the as-received AA3103 Al alloy.

ECAP'ed Composite

Figure 4.65 shows the Al/3103 alloy composite specimen in the ND-TD and ED-ND planes respectively. It can be seen that the sample is well bonded after one pass and it is difficult to visually observe the bonding line between the two sheets.

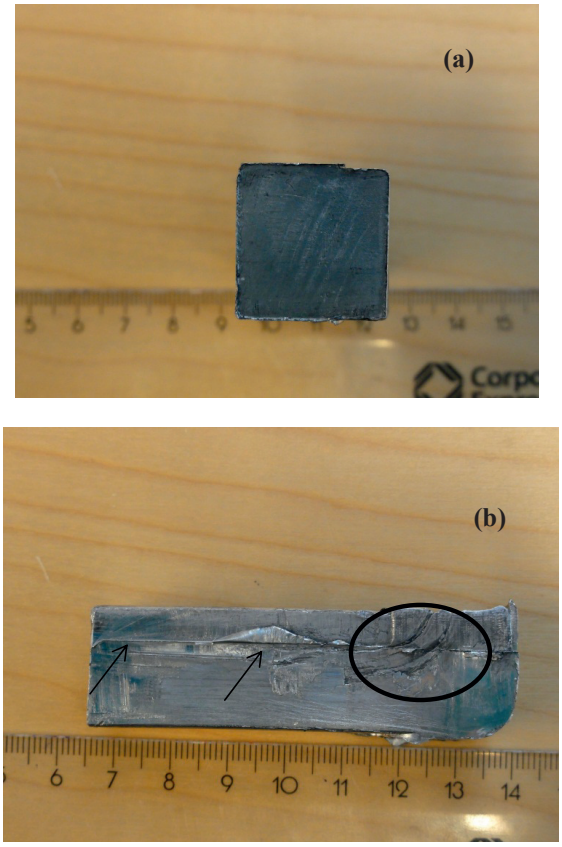

Figure 4.65. Photograph of a successfully processed Al/AA3103 sheet composite after 1 pass BP-ECAP at RT. (a) cross-section; (b) side view. The encircled area is commented in the text below.

The distinct sheets observed at the right corner, represented by a black circle in Fig 4.65b, correspond to the area that has not finished the ECAP flow path. The other artifacts shown by black arrows are due to the friction conditions towards the die wall and they are only few hundreds of microns thick. For instance, these are removed when grounding using a 1200 SiC grit paper.

The microstructure after ECAP processing was studied employing EBSD mounted to an FEGSEM. Figure 4.66 shows a representative raw (unprocessed) OIM map along with interface details.

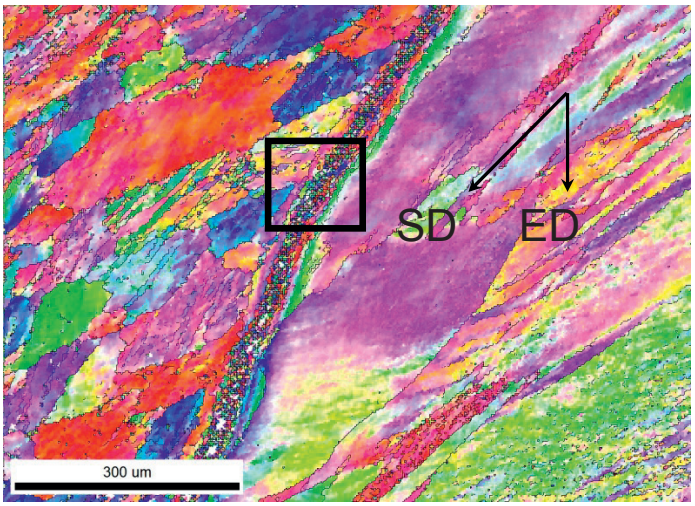

Figure 4.66. OIM map representing the microstructure of a successfully processed Al/AA3103 composite by BP-ECAP at RT. Left part: Alloy 3103 and right part: CP Al. The square marking identifies the area subjected to higher magnification inspections.

The two materials can easily be distinguished by the general microstructural features and grain size. It can be inferred from this figure that the mean grain size in CP Al decreased significantly, to a mean size of ~400 μm. However, there was only a slight decrease in the corresponding AA3103 region, i.e. to 56±12 μm. Interestingly, the interface region was constituted by a zone of very fine grains (see the black square in Fig 4.66). Since the step size is relatively large and the magnification is low for this actual image, high resolution (HR) OIM maps were made to resolve the interface details.

Figure 4.67 shows the corresponding raw map of the region marked with a black square in Fig 4.66. Similarly, Figure 4.68 is the high resolution map of the region marked in the red square in Fig 4.67. From the latter two figures, it seems that the interface region had been highly strained during ECAP and hence it was

difficult to index patterns exactly at the interface. However, regions very close to the interface, i.e. within ~5 µm distance, were indexed fairly well and a fine grain structure containing sub-micron units could be observed. Also, another important result could be noted from the HR OIM maps. In fact, the grains were refined gradually when approaching towards the interface. In other words, grains were much more refined at short distances to the border between the two materials.

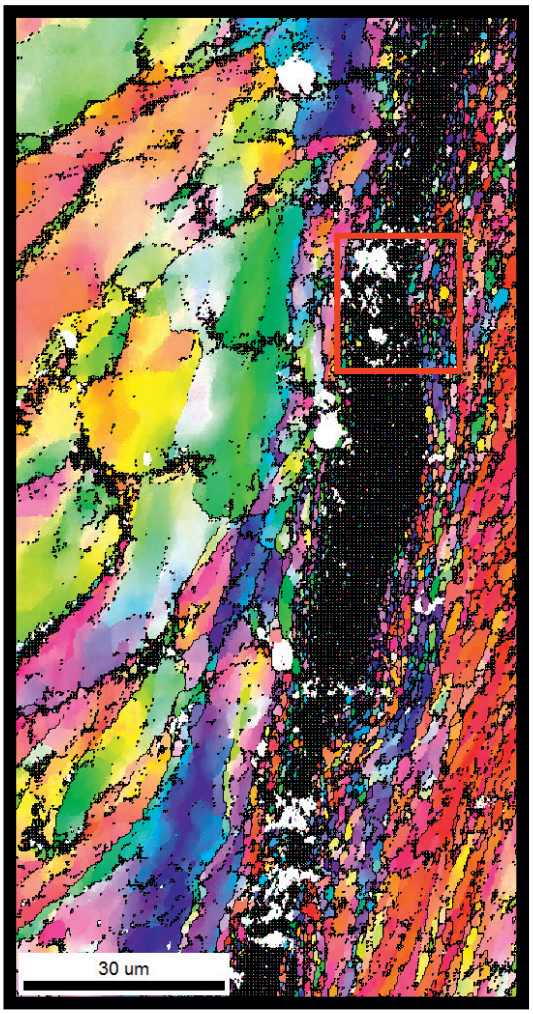

Figure 4.67. High resolution OIM map representing the microstructure in the interface region of a successfully processed Al/AA3103 sheet composite, i.e. by BP-ECAP at RT. The investigated area represents the black square in Fig 4.66. Left: CP Al, Right : Alloy 3103.

Figure 4.68. Close-up OIM map of the microstructure at the interface marked out as a red square in Fig 4.67. Left: CP Al, Right : Alloy 3103.

Furthermore, in order to analyze the grain size quantitatively, the average distance between the HAGBs was measured as a function of distance from the interface. Figure 4.69 shows the corresponding average distances, i.e. the mean grain size development in this region.

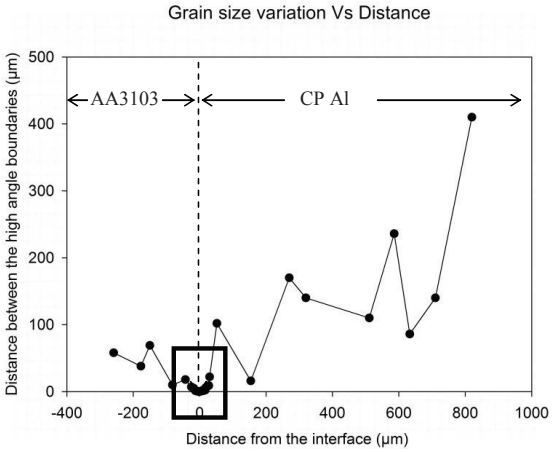

Figure 4.69. Mean grain size of the Al/AA3103 sheet composite plotted as a function of distance from the interface. Left part: Alloy 3103 and right part: CP Al.

A close-up graph was made in addition to improve the readability at the small distances from the interface (Fig 4.70). The curve shows a contour indicating a parabolic dependence. Also, the symmetry of refinement on either side of the curve was quite similar. The grains were in fact refined to less than 1 µm on both sides of the interface up to a ~10 µm distance. Further, grains ~300 nm in size were present very close to the interface along the Al rich region. Actually, within a distance of 5 µm, the grains were as small as 300 nm on either side. However at about ~17 µm from the interface on the 3103 alloy side and ~20 µm on the CP Al side, the grain size approached the representative values of the adjacent bulk materials.

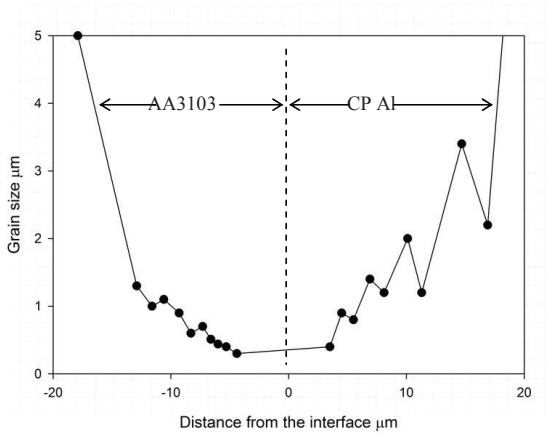

Figure 4.70. Close-up of measurements within the black square in Fig 4.69 representing the mean grain size of the Al/3103 composite plotted as a function of distance from the interface. Left part: Alloy 3103 and right part: CP Al.

Since the grains at the interface were not indexed properly, on either side closer than ~5 μm, SE microscopy was carried out to identify the physical width of the interface. Hence, Figure 4.71 shows an SEM micrograph of the interface viewed in the ED-ND plane. The width of this particular physical interface was ~70 nm. The black dashed lines represent the location of the interface.

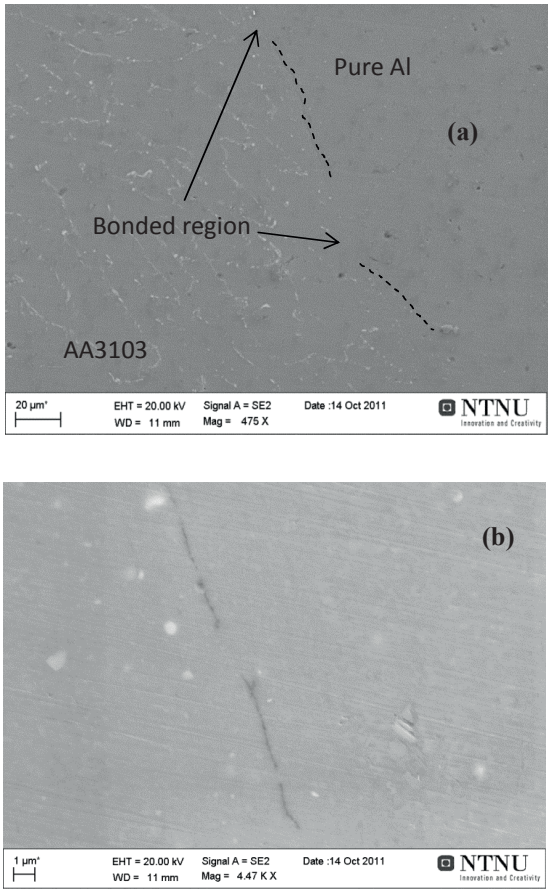

Figure 4.71. SEM micrographs showing the interface region in a successfully processed Al/3103 composite. (a) Low magnification, (b) high magnification. The dashed line in (a) indicates the physical interface.

TEM was also performed to investigate the grain size close to the interface. Figure 4.72 presents a micrograph showing small grains close to 200 nm in size and these grains had sharp boundaries. However, it is to be noted that although the existence of such small grains could be observed by TEM, the precise location of these grains with respect to the distance from the interface could not be truly identified owing to the experimental difficulties.

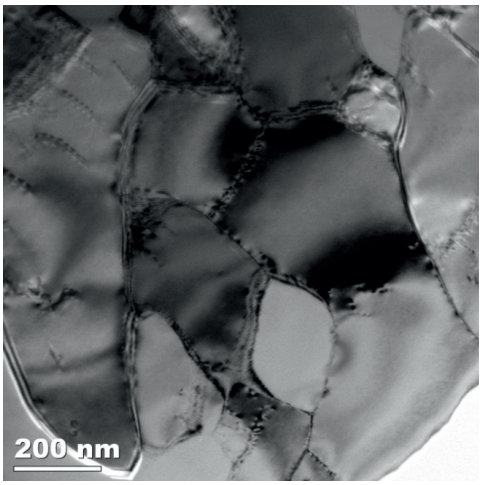

Figure 4.72. TEM micrograph showing very small grains close to the interface region in a successfully processed Al/3103 composite.

Mechanical properties

Bending tests were considered appropriate when evaluating the properties of this sheet composite. This mode of deformation depicts useful information since both compressive and tensile stresses are involved across the thickness. Consequently, a three point bending test was performed in an MTS 810 testing machine using a rectangular specimen with dimensions 3 x 3 x 28 mm^3. The span of the supporting rolls was 20.36 mm. It turned out that the interfaces were intact without failure until about 157° bending and simultaneously withstood a load of about 300 N. The flexural stress could then be calculated using the formula,

$$\sigma_f = \frac{3PL}{2bd^2} \tag{4.5}$$

where, σ_f is the flexural stress in MPa, P is the maximum load [N], L is the span of the support [mm], b is the width of the rectangular beam in [m] and d is the

thickness of the beam [mm]. The flexural strength thus calculated corresponded to 170 MPa. This result shows that the bonding at the interface was quite significant.

The sample was then examined in SEM after the bending test. A resulting micrograph is shown in Fig 4.73. It can be seen that the interface (red arrow in Fig 4.73) was intact even after 157° bending. Due to the plastic deformation introduced by the test, some areas developed roughness contours (black arrows).

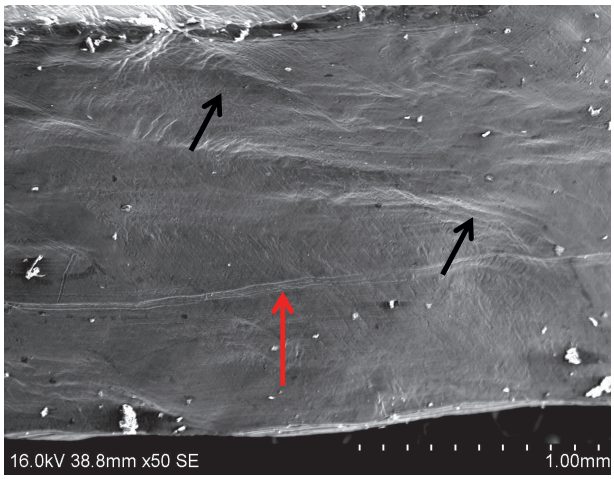

Figure 4.73. Side-view SEM micrograph (SE image) of a successfully processed Al/3103 composite sample subjected to three point bending showing physical interface (red arrow) and surface roughening (black arrows).

Chapter 5: Discussion

5.1 Introduction

Chapter 4 depicted the experimental results obtained during the present work aiming to develop a novel Al/Mg macrocomposite with relative high strength. In order to tailor the properties of such composites for high strength and ductility, it is necessary to understand the various parameters governing the structural evolution and which aid the strengthening mechanisms. Therefore the following discussion will analyse further the experiments and most important results. One also aims to clarify the various steps that led to the current Al/Mg macrocomposite.

5.2 CP Al studies

5.2.1 Grain alignment in the shear zone

The investigations on CP Al represent a hierarchical study on the effect of ECAP temperature on the various microstructural aspects. The OIM maps shown in Figs 4.3–4.7 illustrate the microstructure evolution with respect to strain and temperature. Further, Figure 5.1 shows the orientation of grains with respect to the ED up to 6 passes at different processing temperatures. Since route Bc was used for processing, distinct alignment of the grains with respect to the ED was difficult after 8 passes for RT, 150°C and 250°C samples, as various colonies of grains were differently aligned owing to the activation of many successively activated shear planes combined with the presence of fine equiaxed grains.

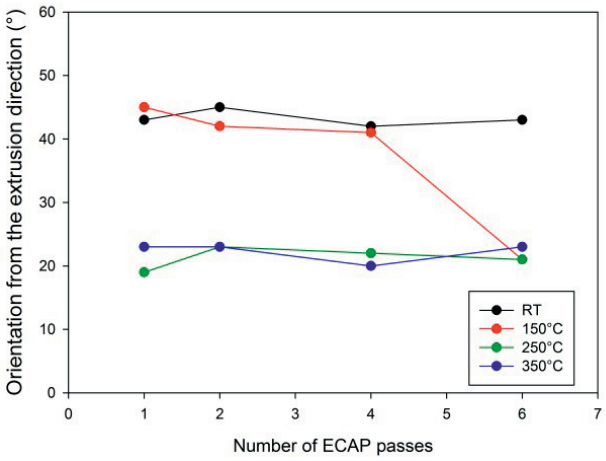

Figure 5.1. Orientation of grains with regard to the ECAP extrusion direction plotted as a function of number of passes for various processing temperatures.

Samples processed at RT showed almost constant orientation along the shear direction (45° to ED) even after 6 passes, but samples processed at 150°C were oriented along the shear direction up to 4 passes and aligned at ~23° for the subsequent passes. For the samples processed at 250°C and 350°C, the orientation of the grains was constant around 23° to the ED. It can be inferred that samples processed at RT undergo more severe strain along the shear direction than with the samples processed at high temperatures. Also, the orientation of ~23° is similar to the amount of deviation from the ideal shear direction due to the arc of curvature of the die i.e. 45°±20.6°. This deviation could be a result of the fan shaped deformation zone in a rounded die corner [36]. A deviation has also been reported by others with a rounded corner ECAP die having an arc of curvature [21, 263, 264]. While such a deviation have been observed during RT ECAP [21], the deviation in the present case is present only at elevated temperatures, as the RT processed samples showed orientation of grains along the shear direction. The reasons for not observing such deviations in the present experiments could be directly attributed to the experimental conditions involved, such as pressure of the

punch, friction between the sample and the walls of the die, type of processing, i.e. pressing a sample while the other samples is still in the channel. For instance, from the results of Mazurina et al. [265], the grains were oriented ~15°to the ED even though the ECAP die had no arc of curvature, while this was not observed by Chang et al. [266]. Therefore, it is difficult to generalize deformation of CP Al by ECAP and the experimental conditions determine the deformation of sample on a macro scale. However, it can be proposed that the deviation around the ED at elevated temperatures could be due to thermal effects of plasticity. Pure aluminium has a low melting point and hence the homologous temperature (T/Tm) is quite high even at RT (T/Tm~0.3). Therefore it is reasonable to assume that the high angle grain boundaries (HAGBs) are relatively mobile. Also, the material is softer at high temperature and yields at relatively low stress. As a sample is pressed through the channel at higher temperature, the highly mobile grain boundaries move dynamically and the grains assume the orientation of the latest deformation direction. This can be supported by the fact that at 150°C, the grains are initially oriented along the shear direction, however, with increase in strain, the grain boundary energy increases and the mean grain size decreases, hence making the HAGBs more mobile, thus rotating towards the extrusion direction.

5.2.2 Grain refinement studies

Figure 4.8 shows the mean grain size as a function of increasing strain and temperature. It is clear that the mean grain size decreases with increasing number of passes at all the processing temperatures, i.e. RT to 350°C. However, the amount of grain refinement is different at different temperatures. The smallest mean grain size was obtained for samples processed at RT after 8 passes (~700 nm) and the largest for samples processed at 350°C (~120 μm). It can be seen (Fig 4.8) that while grain refinement at 250°C and 350°C had reached stagnation after 8 passes, samples processed at RT and 150°C may still refine after 8 passes. Since the present investigation was focussed on the mechanisms operating during processing of Al/Mg bi-metal, no further ECAP processing beyond 6 passes was carried out. All samples, except those processed at 350°C, showed a similar trend up to 4 passes. Grain refinement was confined to the evolution of geometrically necessary

boundaries (GNBs) during intense straining. Several works on ECAP of pure Al at RT [8, 13, 92, 96, 101], showed that aluminium can be refined to 1 μm after 4 passes and this was attributed to sub-grain evolution into high angle grain boundaries. Zhilyaev et al. [264] reported a detailed microstructure evolution of pure Al by repetitive ECAP and found that during initial passes up to 4 by route Bc, the grain structure evolved heterogeneously due to the formation of a high density of deformation bands. The bands subsequently undergo homogenization, fragmentation and rotation into fine HAGB grains. Cabbibo et al. [92], also showed that ECAP of pure Al at RT resulted in a reduction of both cell/sub-grain and grain size with increasing number of passes. Hence, the present observations are fully in correspondence to the previous works on RT processing.

To better understand the present mean cell/sub-grain size evolution with increasing deformation temperature, EBSD data are plotted against accumulated ECAP strain for different temperatures (Fig 5.2).

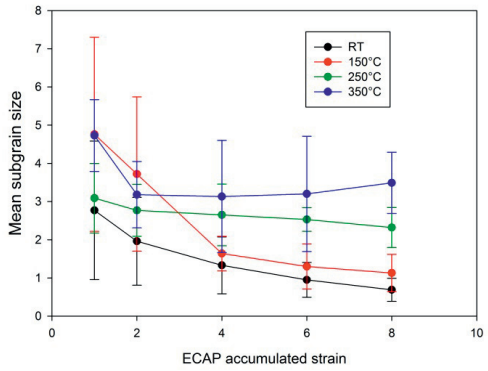

Figure 5.2. Mean cell/sub-grain size plotted as a function of ECAP accumulated strain.

Firstly, the mean sub-grain size increased with increasing ECAP temperature. The thermal exposure allows for microstructure coarsening and increases the mean free path of dislocations. Also, dislocations become more mobile as other temperature dependent mechanisms such as climb, vacancy

diffusion and cross slip are more prone to be activated. This results in a larger equilibrium distance of boundaries after recovery. For samples processed at RT and 150°C, the cell/sub-grain size decreased with increasing number of passes. However, at high temperatures (250°C and 350°C), the cell/sub-grain size was reduced only in the first two passes and then declined more slowly. According to [18], the smallest grain size that can be obtained in pure Al depends on the refinement of the cells during consecutive passes. However, by reducing the mean free path of statistically stored dislocations (SSDs), it is possible to get even finer grains [6, 18]. Since recovery is a thermally dependent process, further reduction of the mean grain size with increasing strain is difficult at high temperature [19, 259, 267, 268].

Introduction of small amounts of impurities can also retard the annihilation and rearrangement of dislocations, thereby reducing the grain size. As explained in Chapter 4, a comparative study by Saravanan et al. [96] showed that it was possible to obtain a 600 nm grain size for 99.5% pure Al whereas high purity Al obtained a mean grain size of ~1 μm at RT. Also, Mazurina et al. [265] investigated the microstructure evolution of a 2219 Al-Cu alloy at 523 K by ECAP and reported microstructure evolution with a mean grain size of ~1 μm after 8 passes. However, the recovery in alloy 2219 during the initial passes was limited as compared to the present study on pure Al, owing to the effect of precipitates and dispersoids retarding or preventing any strain relaxation inside the grains.

Similar studies were reported by Gao et al. [121, 269] on the microstructure evolution of spray cast aluminium alloys 7034 and 2024. It was found that in heat treatable Al alloys, where precipitation is the dominant strengthening mechanism, ECAP introduced a large number of dislocations inside grains and which later became potential sites for precipitate nucleation. While the strength of the as-received alloy was higher than ECAP processed material during the initial passes up to 473K, at higher temperatures, ECAP introduced an increased hardness. Here, the hardness in the as-received material was dominated by precipitation and dissolution mechanisms occurring at the operating temperatures, while a fine grain structure and high dislocation densities were

predominant for samples processed by ECAP. This in turn was due to retardation of recovery controlled by the presence of precipitates.

It can be seen from the error bars in Fig 5.2 that initially large deviations in the size of sub-grains were present. However, upon further processing, the error bars diminished and the microstructure was more homogeneous containing equiaxed sub-grains. Hence the recovery kinetics seems to govern the grain structure evolution in Al during high temperature ECAP.

It is also clear that quantitative grain refinement depends on the processing temperature. In other words, recovery and recrystallization phenomena determine the final grain size. Hence, grains can be refined significantly by controlling recovery and recrystallization processes. In the present case, recovery was the only thermally active and dominant mechanism retarding grain refinement. An introduction of small amounts of solute elements however, should retard any annihilation and rearrangement by preventing dislocation motions. Addition of non-soluble elements in pure Al would lead to retardation of recovery kinetics; however recrystallization might be activated and thus preventing a fine grain structure to develop. In order to obtain very fine grains, large amounts of small precipitates or particles would be needed, i.e. not pure Al anymore.

5.2.3 Microstructure evolution

From the literature study in Chapter 2 and the grain refinement studies explained above, it can be noted that the introduction of ECAP predominantly affects properties through the evolution of high densities of dislocations. In Chapter 2, it was shown that there are two types of dislocations that can evolve, i.e. (1) geometrically necessary dislocations (GNDs) that give rise to geometrically necessary boundaries (GNBs) and (2) statistically stored dislocations (SSDs). Based on these two types, the entire microstructural evolution at all the given temperatures can be divided into two regimes (please refer to the curves in Figs 4.8–4.9). In order to support this hypothesis, Figure 4.10 showing the estimated stored energy as function of increasing strain and temperature, should be considered.

The first regime, Regime I, comprises the initial parts of the curves in Figs 4.8–4.10 where an abrupt change in various parameters is observed with respect to increasing strain. The stored energy plot (Fig 4.10) also shows that for the samples subjected to different processing temperatures up to 250°C, a significant increase is observed during the first 4 passes, i.e. constituting an order of a magnitude rise. This corresponds to the evolution of high densities of GNBs and that this evolution is an effect of a large initial mean grain size. These grains are unable to deform uniformly, leading to the evolution of inhomogeneties usually referred to as deformation bands (DBs) and microbands [143, 150, 270]. In other words, such inhomogeneties are formed as a result of inherent inability of the initially large grains to deform under severe strain. This can also be confirmed by the HAGB fractions shown in Fig 4.9. It is interesting to note that the HAGB fractions during the first two passes remained very similar at all processing temperatures. This means that the initial grain size has a large effect during the initial deformation stages [143, 270, 271]. It also indicates that most of the strain was accommodated by GNBs. Hence, behaviour at different temperatures corresponds to the density of the evolved GNBs evolved. The effect of temperature in this regime is limited to a qualitative effect and does not alter the general microstructure evolution.

The second regime, Regime II, exhibits a slope change in the stored energy plot for all the deformation temperatures after 4 passes. This regime is dominated by subsequent dislocation accumulation and/or recovery. This can be explained by the differences observed in HAGB fractions and the estimated stored energy. For example, Figure 4.9 shows the evolution of HAGBs as function of accumulated ECAP strain. By comparing Figs 4.8–4.10 and 5.1, it can be deduced that although the evolution of GNBs can be assumed to develop continuously even after 4 passes, their dominance is not significant. If GNBs were as dominant as in Regime I, the HAGB fraction would continue to increase linearly after 4 passes. However, the drop in the HAGB fraction could mean that a high density of low angle grain boundaries (LAGBs) has been formed instead, which actually is supported by the results given in Fig 4.10. This comprises the formation of either SSDs or recovery facilitating the enhancement of LAGB fractions.

Samples processed at RT and 150°C showed an increase in stored energy while samples processed at 250°C and 350°C had almost constant values after 4 passes. While SSDs probably increase their density at RT and 150°C, 250°C and 350°C, samples attain a balance between dislocation accumulation (induced strain) and recovery. Further, samples processed at 250°C contain the highest HAGB fraction. This could mean that samples processed at RT and 150°C undergo a predominant accumulation of SSDs and with relatively less recovery along with an increase in GNBs. In the samples processed at 250°C, the role of SSDs in the microstructure evolution might be less significant due to the on-going dynamic recovery being a consequence of an increase in the homologous temperature (T/Tm~0.6). Furthermore, samples processed at 350°C (T/Tm~0.7) contain the lowest HAGB fraction among all present ECAP conditions. At such a high processing temperature, grain boundary sliding (GBS) and grain boundary migration (GBM) are common mechanisms resulting in less grain refinement compared to low temperature processing [140, 259, 272-274].

The above mentioned regimes at different processing temperatures are schematically illustrated in Fig 5.3. The two regimes are operating within different strain and processing temperatures. It is suggested that Regime I exists until 4 passes at all processing temperatures.

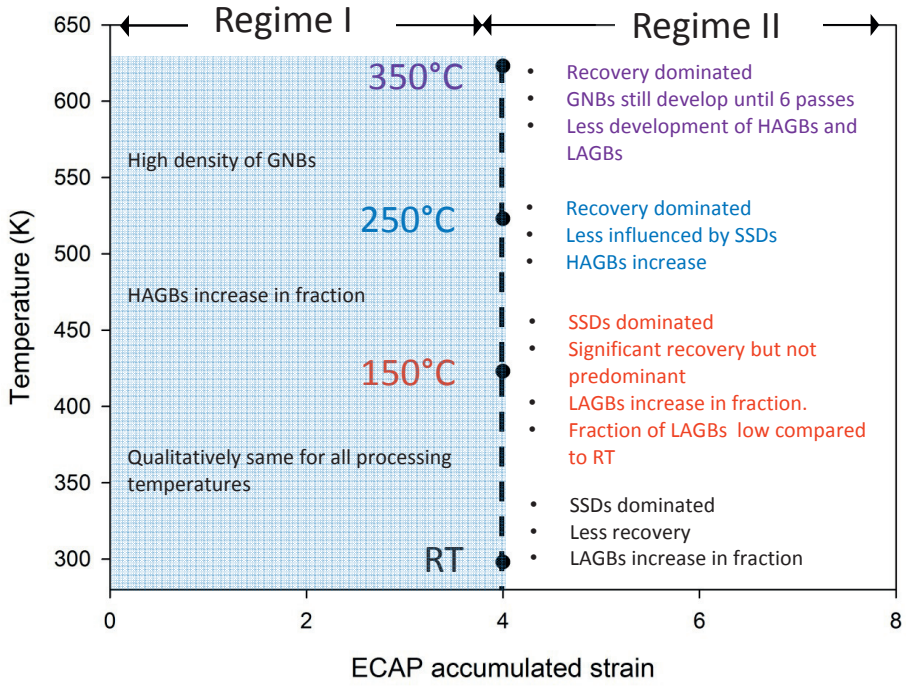

Figure 5.3. A schematic representation of the two regimes and related microstructure characteristics observed in CP Al investigations subjected to ECAP at various strains and processing temperatures.

The density of evolved GNBs depends on the physical accommodation of excessive strain to maintain contiguity [140, 150, 270, 275]. The most likely occurrence of GBS and GBM, reduces the strain imparted by ECAP, hence resulting in a low density of GNBs. In other words, Regime II is dominated by SSDs for samples processed at RT and 150°C, but recovery prevails in this regime during ECAP at 250°C and 350°C.

5.2.4 Evolution mechanisms

The stored energy, the accumulated ECAP strain and the processing temperature together determine the microstructure evolution. As a

general view, DBs are formed initially and then there is an onset of recovery after four passes for all processing temperatures used. The cells formed initially may either evolve continuously to sub-grains/grains after subsequent passes by dislocation accumulation, or they evolve into HAGBs due to the mutual interaction of inhomogeneties. However, to clearly summarize the microstructure evolution, each deformation temperature is dealt with separately and then compared in the following paragraphs.

Firstly, RT ECAP processing is considered. During the first ECAP pass, a strain of ~1 is introduced in each pass resulting in the formation of DBs and other inhomogeneties such as microbands and incomplete HAGBs. The microstructure also contains cells and deformation inhomogeneties, hence reducing the free energy of the structure according to the LEDS theory [146, 148-150].

After 2 passes, a high density of inhomogeneties is formed. The DBs established in the first pass simultaneously reduce their thickness. Now, the DBs occur frequently and they are part of the further evolving microstructure. It is to be noted that route Bc is involved and every time the sample is rotated by 90°, new shear planes are activated and hence new DBs are evolving. As a result, the microstructure observed after two passes, see Fig 4.4a, is complex and sub-grains orient at another angle relative to the ED. Sub-grains are formed as a result of intersecting DBs but also other inhomogeneties, as shown in Fig 5.4.

Figure 5.4 schematically explains the formation of a new small sub-grain/grain by the intersection of two inhomogeneties at different shear planes. It can be seen that two different bands formed in different shear planes with increasing passes, undergo mutual interaction by intersecting each other and hence resulting in a fine grain within the intersecting boundaries.

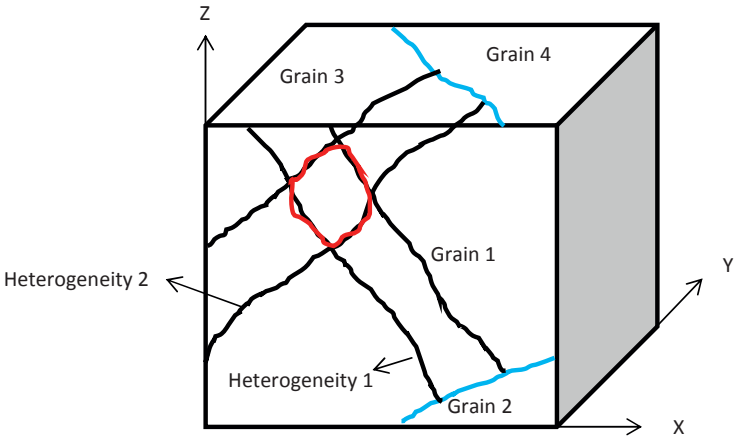

Figure 5.4. HAGBs formed at the intersection of two subsequently formed bands in two different shear planes, creating a small grain due to significant lattice rotation. Blue lines represent the grain boundaries of the initial grains and the red lines represent the HAGBs of the newly formed grain.

As the deformation progresses to 4 passes, the evolution becomes even more complex and involves various mechanisms occurring simultaneously. First, new DBs are formed and DBs formed in the previous pass are thinned. Also, the latter interact with the newly formed DBs. DBs that have reached the thickness of a cell or two, pinch off to form fragments of grains. This leads to the formation of a fraction of fine grains even after 4 passes. With subsequent passes up to 6, the evolution of DBs and other GNBs decreases and formation of SSDs dominate. The initially large grains have now broken down to smaller segments by the intersecting DBs, hence forming smaller grains. However, recovery also occurs resulting in the formation of sub-grains, reducing the ability of further noticeable refinement.

After 8 passes, no new DBs are formed. This is possibly due to the significant break-down of a high fraction of grains into smaller segments. Hence any further strain accommodation may rely on the formation of SSDs. Also dynamic recovery increases with increasing grain boundary energy as grains become finer.

For samples processed at 350°C, the evolution of GNBs is retarded during the initial passes, as the excessive strain is accommodated by high temperature processes such as GBS, GBM and other stress relaxation mechanisms [140, 272, 274]. Hence the density of DBs and other inhomogeneties are low. Secondly, the number of active slip systems within each grain increases as a result of thermal activation, resulting in relatively more homogeneous accommodation of strain as compared to the lower deformation temperatures. This also reduces the density of GNBs. Thirdly, the high homologous temperature promotes recovery resulting in formation of clear sub-grains even after 1 pass. This is in contrast to RT deformation where initial cells subsequently form sub-grains and grains. However, there is some refinement of the grains at 350°C, solely due to the formation of DBs inside large initial grains. This leads to the evolution of a moderate grain refinement. Hence, the grain size obtained even after 8 passes is relatively coarse and exhibits a non-equiaxed structure. However, it would be interesting to investigate the microstructure evolution of CP Al at high temperature separately with an initial fine grain structure as the heterogeneity of strain accommodation inherent to large grain deformation would be absent.

The microstructure evolution at different strains and temperatures is somewhat complex and a schematic summary of the microstructure evolution for different temperatures and strains is therefore shown below (Fig 5.5). This figure depicts the density, or the relative amount (qualitatively), of different entities (GNBs, SSDs, cells and sub-grains). Solid lines indicate that there was a significant evolution of given entities, while dotted lines represent less density or a weak presence.

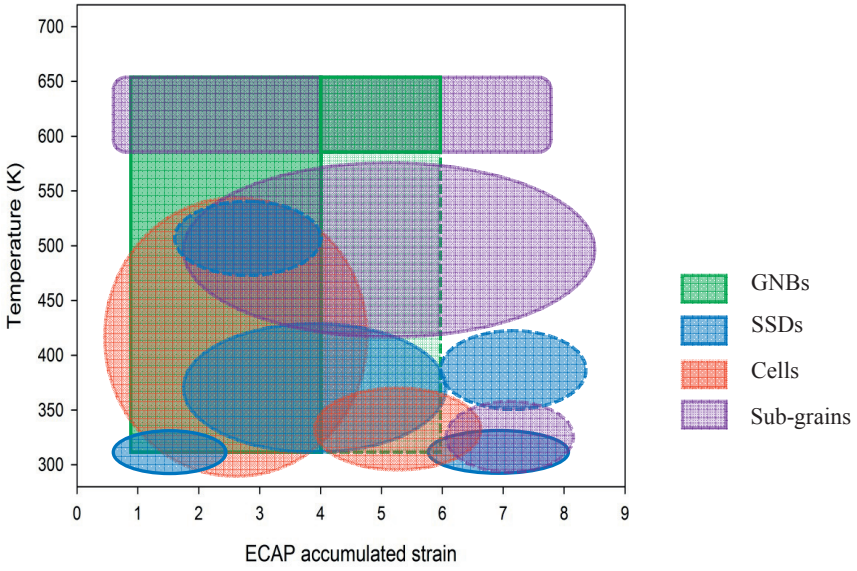

Figure 5.5. A schematic map depicting different entities in the microstructure evolution as function of strain and temperature. The solid lines indicate significant evolution of the entity and dotted lines indicate the weak presence.

For samples processed at the intermediate temperatures, i.e. 150°C and 250°C, the evolution mechanisms were intermediate to what prevailed at RT and 350°C (refer Fig 5.5). Samples at 250°C underwent a similar microstructural evolution as at RT during the first two passes, i.e. the grains were split into smaller segments and they further developed into fine grains. However, the density of DBs was less at 250°C than at room temperature due to recovery. Another feature during the first four passes at 250°C was that the history of deformation was lost, i.e. the evidence of previously formed DBs and other microstructural entities were replaced after each pass. However, after 6 passes, interactions between the previously formed and the new DBs could be observed. This was probably due to the fact that deformation bands became close to the size of a cell and hence any further deformation would lead to a collapse of the structure into colonies of fine grains. Hence, fine grains start to appear after 6 passes at 250°C. Also, due to

recovery more uniform sub-grains appear. Further, the intensity of recovery increased with increasing temperature and hence, deformation at 250°C showed more uniform sub-grains as compared to 150°C. After 8 passes, as in RT samples, no new DBs were formed at intermediate temperatures and only further interaction of already formed DBs took place producing fine equiaxed grains along with an increased tendency of recovery. For samples processed at 150°C, the evolution of DBs and inhomogeneties was similar to RT, but was not equivalent. In other words, the evolution at 150°C was qualitatively the same as that of RT samples, but there were quantitative differences. Also, after 6 passes, the amount of accumulation of SSDs is less since recovery at 150°C is more pronounced than at RT. After 8 passes, the grains were refined in a similar manner as that of RT but had a larger size close to ~1.8 μm.

In an effort to document recovery inside grains, Figure 5.6 exhibits the point-to-origin misorientation along the length direction of grains for samples processed to 1 pass at different temperatures.

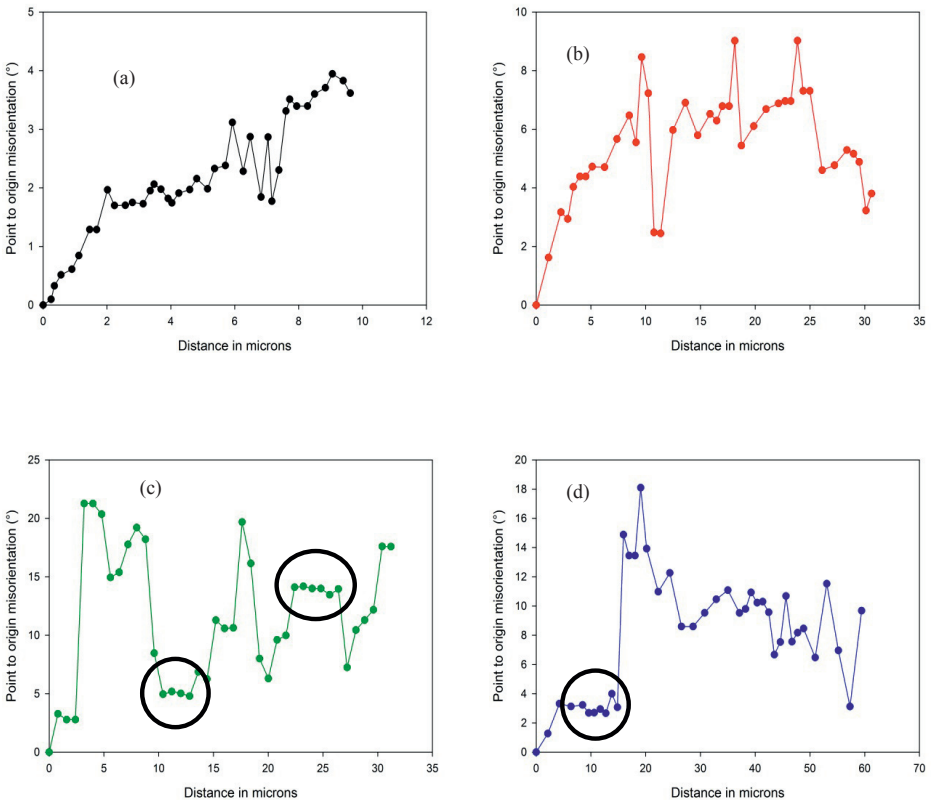

Figure 5.6. Point-to-origin misorientation plotted as a function of distance after 1 pass ECAP at different processing temperatures. (a) RT, (b) 150°C (c) 250°C, (d) 350°C . Black circles represent fully recovered regions.

It can be seen that while samples processed at RT and 150°C have an increasing misorientation along the direction of grains, deformation at 250°C and 350°C introduces recovered regions represented by drops in misorientation (see circles in Fig 5.6).

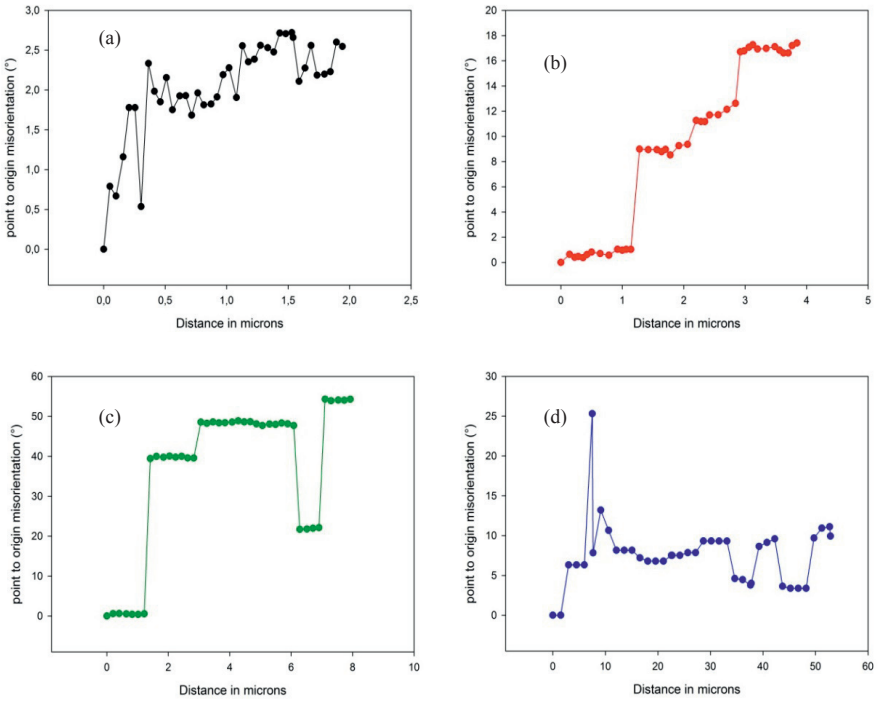

Figure 5.7. Point-to-origin misorientation plotted as a function of distance after 6 passes ECAP at different processing temperatures. (a) RT, (b) 150°C (c) 250°C, (d) 350°C .

Further, Figure 5.7 shows the corresponding point-to-origin misorientation after 6 passes at different temperatures. It can be seen that deformation at RT leads to a continuous evolution by dislocation accumulation, while deformation at the other temperatures shows simultaneous recovery. Interestingly, samples processed at 150°C have some regions with increasing misorientation. This clearly illustrates the effect of temperature on the onset of recovery. While, the samples processed at RT are evolving continuously by the accumulation of SSDs and increase their misorientation rotation of boundaries into HAGBs, the onset of recovery sets up for 150°C after 6 passes. Furthermore, 250°C and 350°C samples are completely recovered after 6 passes and the onset of recovery starts locally in some grains even at 1 pass (see Fig 5.6).

Figure 5.8 shows similar plots, but for RT samples and 8 passes. It can be seen that the local line-scan for the RT sample evolves continuously even after 8 passes. It is important that the validity of the present observation is to be made statistically. The average grain size obtained after 8 passes at RT is 700 nm. However, the present scan represents a large grain around 1.7 μm, twice as big as the mean grain size. Hence it is reasonable to assume that this particular grain has recovered. However, the observations show otherwise. Also, misorientation plots in other regions (refer appendix B) reveal a similar increase in misorientation. Thus, Figure 5.8 represents a typical behaviour of grains in CP Al after 8 passes. It is to be noted that some grains show almost no change in the misorientation gradient (see appendix B), meaning that recovery does in fact occur in some of the regions.

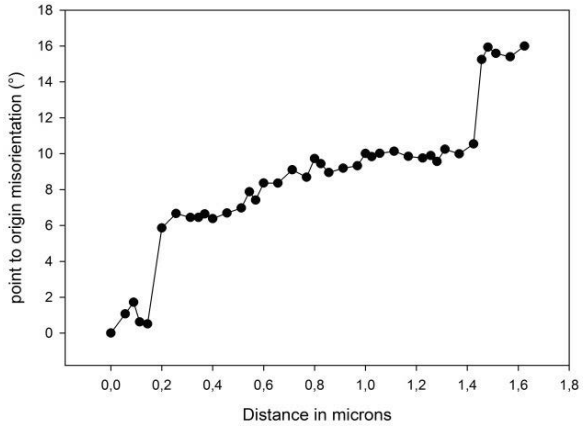

Figure 5.8. Point-to-origin misorientation plotted as a function of distance after 8 passes ECAP at RT.

5.2.5 Comparison with existing literature

A comparison of the present grain refinement observations with respect to literature has already been treated in Section 5.2.2. However, some additional comments could be made. The sub-grain size evolution with increasing temperature reported by Wang et al. [260], involved smaller sizes than that observed in the present study. This could be attributed to the present chemical

composition and the initial coarse grain size. While, CP Al in the work of Wang et al. had a composition of ~99.6% purity, the present CP Al was ~99.9% pure. Also the initial grain size reported (~330 μm) was a magnitude smaller than in the present study (~1.2 mm). Skrotzki et al. [102] reported the occurrence of discontinuous dynamic recrystallization (DDRX) in 99.999% pure Al deformed by ECAP at RT. A similar DDRX mechanism was observed in the same Al material deformed by torsion at cryogenic temperature [276]. The presence of impurities in pure Al change the deformation mode by hindering the motion of dislocations resulting in a smaller cell size and which further develop into small grains [6]. Interestingly, at 523 K, after a strain of ~8, the current work shows a similar sub-grain size as reported by Wang et al. [260].

The final grain size obtained also depends on the processing route [20]. The rotation of samples between each pass (route Bc) changes the planes undergoing simple shear at the die intersection. This change in the deformation mode would result in a different mean grain size after SPD due to changes in the operating mechanisms. Thus, for different ECAP processing routes [13], and similarly for HPT (cyclic HPT and monotonic HPT) [277], a different mean grain size can be obtained after the same amount of accumulated strain. However, the present microstructure evolution is based on route Bc which is believed to be the most efficient ECAP processing route for significant grain refinement in metals [6, 13].

Although it is interesting to compare the ECAP microstructure evolution of CP Al at elevated temperatures with literature observations, no detailed reports have been reported so far. The evolution of grains reported by Mazurina et al. [265] in a 2219 Al alloy can be compared to the present study and to the grain refinement mechanisms discussed above. The general microstructure evolution is not significantly different for the two materials. However, there are certain discrepancies. For instance, the HAGB fraction obtained with increasing strain is relatively higher for the Al alloy than for the present CP Al. This is probably due to additional dislocation pinning at precipitates in the 2219 alloy. A similarity can also be seen regarding an Al-Mg-Sc alloy deformed at 450°C [160]. The latter evolution involved initial formation of DBs which upon further strain underwent

mutual crossing of bands to finally develop fragments of small grains. However, quantitatively, the occurrence of the various mechanisms is differing, owing to the effect of different compositions and therefore the involved precipitates in case of the 2219 and the Al-Mg-Sc alloys.

To summarize the present microstructure evolution, it can be concluded that deformation at RT initially results in a very high density of GNBs, DBs and other inhomogeneties along the shear direction, i.e. due to heterogeneous strain accommodation for initially large grains up to 4 passes (see Figs 4.3–4.5). Upon further ECAP passes, these microstructure entities undergo severe deformation up to 8 passes and evolve continuously by rotation of boundaries aided by dislocation accumulation into HAGBs, thus forming fine grains (Figs 5.6–5.8). Some recovery may still occur.

Deformation at 150°C during the initial 4 passes results in the evolution of DBs and inhomogeneties (see Figs 4.3–4.5, 5.3). After 4 passes, the microstructure is dominated by the evolution of SSDs up to 6 passes, and recovery sets up after 6 passes (refer Figs 5.4 and 5.6). The grains are initially refined by the formation of GNBs up to 4 passes, then dominated by accumulation of SSDs up to 6 passes and finally refined by the mutually interacting (i.e. intersecting) GNBs formed on different shear planes as the specimen is rotated between passes. This refinement comes along with a reduction of excess energy (Fig 4.10).

Samples processed at 250°C undergo grain refinement by a predominant evolution of GNBs up to 4 passes (see Figs 4.3–4.5), although the onset of local recovery occurs even after just 1 pass (Fig 5.6). With increasing strain, the microstructure undergoes recovery and finally refine by the interacting GNBs similar to the situation seen at 150°C.

Deformation at 350°C results in severe recovery and therefore the refinement is limited (Figs 4.3–4.9). However, grain refinement is carried out by the formation of GNBs during all passes and the microstructure is even inhomogeneous after 8 passes.

5.2.6 Microhardness

The microhardness values obtained at the present processing temperatures (see Fig 4.11) correspond to the microstructure evolution just explained. There is a significant increase in hardness during the first two passes (exception: 350°C), due to a significant increase in the density of GNBs. With further increase in strain, the hardness change is limited due to a small increase in the number and density of GNBs. After four passes, SSDs dominate the evolution, leading to more or less constant values. For samples processed at 250°C, there is a hardness drop after 6 passes. This can be attributed to increased recovery combined with a negligible evolution of new DBs as mentioned above. However for 350°C, the hardness remains constant during the first two passes, and the evolution of GNBs becomes significant only after 4 passes, i.e. reflected by a small hardness increase. With further passes, recovery of the already formed DBs occurs resulting in a lower hardness, see Fig 4.11.

5.2.7 Crystallographic texture

The evolution of crystallographic texture in CP Al with increasing strain and temperature are represented by their respective (111) pole figures and ODFs in Euler angles in Figs 4.13–4.22. In addition, Table 4.1 described the three highest intensities for the various passes and corresponding processing temperatures.

Deformation at RT

It can be inferred that samples deformed at RT show a similar texture evolution as explained by other researchers [31, 54, 55, 218]. The first pass texture shows strong $A_{1\theta}$ along with weak C_{θ} and B_{θ} components. A weak texture distribution of other orientations can also be seen in the first pass (arbitrary texture intensity <2). This could be an effect of the relative initial coarse grain size. The initial large randomly oriented grains tend to rotate towards stable ECAP orientations, i.e. see the slight displacement of the $-B_{\theta}$ components from ideal positions (see Fig 4.18).

After 2 passes, stronger and typical ECAP components are developed due to the increasing strain. The $-B_{\theta}$ components developed in the first pass now rotate

and move towards the stable ECAP orientation. Further, C_θ components are non-uniform but develop strongly after 2 passes. This can possibly be due to the effect of the processing route, which is route Bc in the present case. The A_θ components were absent in the first pass, but show up in the second pass. However, the $A^*_{2\theta}$ components do not increase in intensity as much as other intensities.

With increasing strain up to 4, the textures become sharper and the previous texture established during pass 1 and 2 evolve and the grains seem to orient towards the more stable ECAP textures. The initially strong B_θ and C_θ components are displaced from the ideal positions along the Φ direction. This could be an effect of the fan shaped deformation zone, i.e. due to the presence of an arc of curvature [36, 40, 54] .

After 6 passes, orientations that were strong and non-uniform in the previous passes become more fibrous and CDRX occurs more predominantly. In this process, sub-grains and cells evolve into grains having gradual increasing misorientations and rotate towards the nearest stable ECAP orientation. The fibres were very similar to those reported by Li et al. [31]. It can be seen from Fig 4.18 that the f1 fibre consisting of only $A^*_{1\theta}$ - A_θ - $A_{2\theta}$ is similar to that observed in pure Al during deformation at RT [54]. Similarly, the f2 fibre that includes the C_θ - B_θ - A_θ components concentrated around C orientations along $<110>_\theta$ when deformed at RT, is also complete in the present case (Fig 4.18). Also, the f3 fibre shows a similar trend. However after 8 passes, the A, B and C components decrease their intensities and the ODF reveals a random texture with weak A, B and C components. This is in agreement to the observation of El-Danaf during ECAP of commercially purity aluminium at RT [55]. The weakening of texture could possibly be due to onset of recovery combined with establishment of more fine grains, i.e. resulting in crystallographic randomization.

In a nutshell, the texture evolution complements the microstructure evolution explained above. Initially large grains resist deforming homogeneously, hence forming DBs and causing changes in crystallographic orientations. With increasing strain, more stable ECAP textures are formed. The textures are initially sharp and non-uniform but on further increasing strain up to 6, they become more fibrous as more grains tend to adapt A/B type fibres along with C type orientations,

which are equivalent to the shear type textures observed during torsion [278]. After 8 passes, the grains become fine and equiaxed as a result of boundary rotation into HAGBs, i.e. no significant texture [55, 279].

Deformation at 150°C

ODF plots obtained for samples processed at 150°C are shown in Fig 4.19 and the three highest intensity textures are shown in Table 4.1. In general, the ODF plots show less strong and sharp textures as obtained at RT. While B and A components are the strongest, the C component is weaker as compared to RT samples. Also, during the initial passes the textures are not in ideal positions and on further processing, become more stable ECAP shear orientations [31, 36, 264]. This can be attributed to the deformation through the fan shaped deformation zone due to the arc of curvature [36], as explained for deformation at RT.

During the first pass, a (111) fibre along ND can be observed along with the evolving ECAP shear texture components (see Fig 4.19). By increasing ECAP deformation, the texture weakens. Hence, this could again be an effect of the initial coarse grain structure. Similar to the RT samples, initially strong B textures are obtained and with increasing strain, A components start developing. Also, the shear textures are not developed completely. However the f1 fibre is complete and contains A components, but f2 and f3 fibres are only partially stabilized having a small contribution from the C component. This is possibly due to the elevated temperature stimulating thermal activation of dislocations. The reduction of the C component at elevated temperature could be an effect of temperature on deformation mechanisms itself. Engler et al. [280] showed that in an Al-1.8% Cu alloy having a dominant {112}<111> orientation, regions adjacent to shear bands rotated towards {001}<110> orientations (equivalent to the C orientations in ECAP [31]) and the rotation was highest at the matrix-shear band interface. They attributed this observation to the high energy of the shear band boundaries having high dislocation densities. Similarly, a low intensity C component observed during high temperature ECAP in the present case could probably be due to an absence of high energy boundaries, as observed during RT ECAP of Cu and Al [6] exhibiting shear bands, non-equilibrium boundaries etc. The present CP Al deformed at

150°C does not tend to rotate towards random orientations as was observed for the counterpart RT samples [55]. Instead, the textures depict more ideal ECAP orientations after 8 passes.

Deformation at 250°C

The texture evolution at 250°C shown in Fig 4.20 exhibits a similar evolution as that of 150°C ECAP. However, the intensity of the individual components is now stronger than at 150°C. Also, the textures are rotated towards even more stable orientations. As explained for deformation at 150°C, a low degree of deformation might lead to a weak C component. Both 150°C and 250°C samples show qualitatively equivalent textures with the exception of the C component.

Deformation at 350°C

At 350°C (see Fig 4.21), ODF plots show a similar texture evolution as explained for 150°C and 250°C up to 4 passes. However, upon increasing strain to 6 passes, a strong cube texture oriented along the shear direction is observed. This is a noticeable observation and indicates that processing at 350°C initiates recrystallization. This means that the constant misorientation of grains and sub-grains observed in Figs 5.6–5.7 is not a result of recovery, but rather more extensive recrystallization. Here, recrystallized cube grains form at the expense of remaining unstable orientations [140]. Furthermore, with an increase up to 8 passes, the intensity of the cube texture decreases and the ECAP textures reappear as the most dominant.

Since a semi-continuous processing has been utilized (see Chapter 3), there exists a hold time between passes where the sample is experiencing a high temperature without being strained while the other sample is being pressed. Most probably, recrystallization takes place during this hold. As 350°C represents a quite high processing temperature (T/Tm~0.7), static recrystallization can occur. If the material were to recrystallize dynamically, the cube orientation along the shear direction should have increased in intensity. However, the textures presented in Fig 4.21 do not exhibit increasing cube intensity. Hence, samples processed at 350°C up to 6 passes most probably undergo static recrystallization. Further, since static

recrystallization is temperature and time dependent, the amount of recrystallized grains vary for each pass and could possibly be the reason for less strong textures observed after 8 passes.

A summary of the texture evolution with increasing strain and temperature is shown in Fig 5.9. It can be concluded that samples semi-continuously processed at 350°C undergo static recrystallization after 6 passes. Secondly, RT processing of CP Al undergoes rotation of boundaries into HAGBs resulting in the formation of new grains and hence the texture evolution tends toward random orientations [55]. Samples deformed at 150°C and 250°C undergo recovery and retain the ECAP shear textures. It can also be mentioned that during the evolution of DBs, and hereby the initial formation of GNBs, the texture components alternate between the A and B type orientations. This is probably due to the alignment of volume elements into the nearest possible slip system within grains. For CP Al (FCC structure), this introduces an evolution of A components and the {111} planes of the material align to the apparent ECAP shear plane. On the other hand, the presence of the <110> direction close to the shear direction would lead to the evolution of the B component [281]. A similar development has been observed by Zhilyaev et al. [264] during the ECAP of pure aluminium at RT up to 12 passes at RT. However, B type orientations can mostly be associated with the evolution of GNBs due to their twin-symmetric orientations that can occur in Al during the evolution of alternate DBs when processed by ECAP [282].

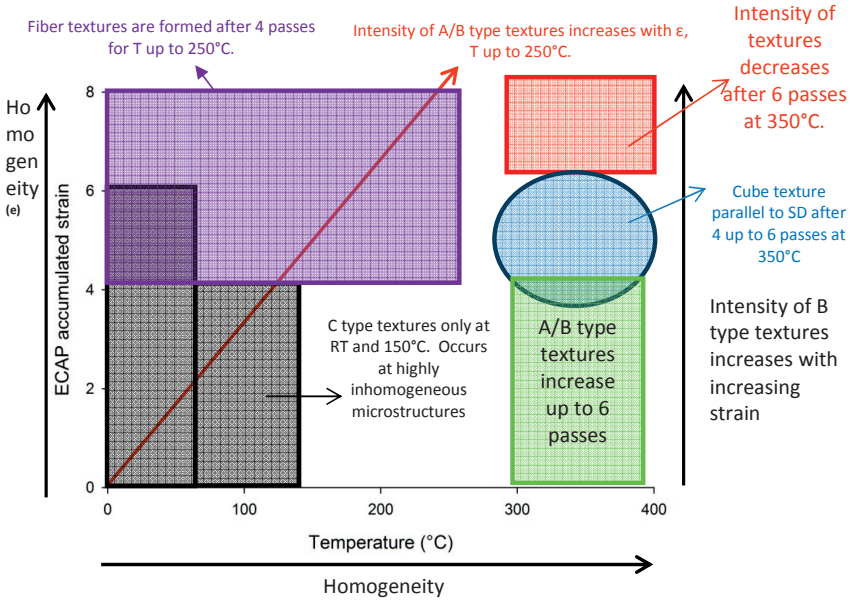

Figure 5.9. A schematic illustration of the texture evolution with respect to strain and temperature.

In addition, with increasing temperature, the evolution of strong A/B orientations can be related to dynamic recovery as observed in hot torsion experiments [278, 281] at intermediate temperatures and high strains, while with a high temperature (350°C), the intensity of both the A and B type textures drops [281] as in the present study. Also, the A/B type components evolve into more fibre textures as compared to the individual asymmetric components observed in the initial passes. Thus, the development of the A/B type fibres corresponds to an evolution of fine grains, strain homogenization and recovery. On the other hand, deformation inhomogeneity has a greater influence on the evolution of the C component and therefore this is weakened at higher temperatures. There is also an effect of strain inhomogeneity at low temperature [280] coupled with the evolution of non-self-symmetric textures due to intrinsic geometric considerations in Al [278].

5.3 Al/Mg bi-metal studies

5.3.1 Al/AZ31 bi-metal (rod type structure)

General overview

The microstructure evolution in CP Al showed that a homogeneous structure having a grain size of around ~5 μm can be obtained after 6 passes at 250°C. The grain structure can also be somewhat even at 350°C. This is important knowledge to bring into the study on Al/Mg bi-metal where the necessary processing temperature for good bonding is about 250°C.

As has been explained in Chapter 2, the processing of Mg based materials by ECAP is challenging and normally requires pre-processing in order to avoid cracks and to obtain grain refinement. However, the present investigations on the rod structure were focussing on the bi-metal interface and hence pre-processing was not carried out. The results on Al/AZ31 bi-metal deformed at 250°C (Fig 4.24), showed that the AZ31 rods cracked during ECAP at 250°C even after 1 pass. The temperature 250°C was also chosen in correspondence to various results published on ECAP of this alloy. While some works [199, 283, 284] reported crack free samples at 200°C, Agnew et al. [285] found that there was severe cracking when AZ31 was processed by ECAP at 200°C, but they obtained successful fabrication at 300°C. Hence, a temperature of 250°C was firstly chosen as this seemed to be a compromise. However, cracking still occurred at 250°C and it was decided to increase the pressing temperature to 350°C. The cracking behaviour of AZ31 has been analysed in the literature, e.g., by Kang et al. [286]. They found that fracture was controlled by flow localization and they developed processing windows for strain rate vs. temperature. Their analysis included a quantity called 'flow localization', denoted α, which is defined as the ratio of flow hardening or flow softening rate (γ') to the strain rate sensitivity of the material (m):

$$\alpha = -\frac{\gamma'}{m} \tag{5.1}$$

They showed that flow localization and cracking occurred, when $\alpha > 0$. Hence, it can be interpreted that even at low temperatures; a crack free surface can

be fabricated by varying the strain rate, or in practical terms, the pressing speed of the ECAP process. Although the above explanation is believed to be plausible, no present systematic experiments were conducted to reveal such flow localization analysis. One of the reasons is that the presence of Al changes the flow behaviour of the AZ31 alloy during ECAP. Anyway, samples were ECAP'ed at 350°C and no extensive cracking occurred (see Fig 4.25). Further processing of the bi-metal was carried out up to only 6 passes as CP Al showed recrystallization behaviour after 6 passes.

Interface studies

The interface studies were conducted in the cross section of samples and not in the ED-ND plane as for the CP Al studies. This was due to the fact that the Al/AZ31 rod type bi-metal investigations were focussing on the interface characteristics rather than the microstructure evolution itself. As a consequence, the microstructure evolution was also investigated in the cross-section area. The strain at the interface was higher than strain induced in the ED-ND plane due to the circular geometry of the AZ31 rod, i.e. see further below. Figure 4.26 and the EPMA maps in Figs 4.27–4.28 clearly show two distinct transition regions at the interface and they were identified by quantitative EDS and EPMA. IF1, the first region, close to the AZ31 alloy was identified as an $Mg_{17}Al_{12}$ intermetallic phase (region close to the Mg in yellow colour of the Mg mapping). The second region (IF2) was identified as Al_3Mg_2, in green in the Mg mapping in Fig 4.28b, and lies close the CP Al region. These observations are consistent with those made by Dietrich et al. [287].

The mean grain size is plotted against the number of passes in Fig 4.29. This trend shows that the mean grain size of AZ31 is not significantly reduced even after six passes. The lack of a substantial refinement can be attributed to two phenomena apart from the fact that grain refinement in Mg (hexagonal close packed) alloys is less prone to occur than in face centred cubic materials and body centred cubic materials [223]. First, the high processing temperature may play a vital role in grain refinement [82]. Second, and the more significant, is the effect of the interfacial shear stress (ISS) on grain refinement. During ECAP, volume

elements undergo shear at the intersecting die channels. However, in this case, the presence of an interface between the two metals introduces another stress component which is tangential to the cross-section of the interface, e.g. owing to the circular cross section of the interface combined with friction between the materials. This shear stress has its maximum at the edges and minimum at the centre of the AZ31 core. However with the increase in ECAP passes, the ISS increases resulting in a slight grain refinement. Comparing the error bars in Fig 4.29 and the OIM maps in Fig 4.30, it can be inferred that there exists a bimodal size distribution of grains during the initial passes. This is probably due to the onset of dynamic recrystallization (DRX) in AZ31. With increasing number of passes, the recrystallized grains increase in fraction thus increasing homogeneity. This is consistent with the belief that DRX contributes to grain refinement at the AZ31 core [82].

Diffusion is caused by a combined effect of deformation and high temperature. The bonding thus obtained, depends on interdiffusion and void closure mechanisms [288] . Mg diffuses faster in Al than vice versa and hence the diffusion kinetics depends on Mg interdiffusion into Al. Assuming an activation energy (Qc) of 130 $KJmol^{-1}$ for diffusion of Mg in coarse grained Al [289], D_0 = 1.24 x 10^{-4} m^2s^{-1} [289] , T= 623K and using R = gas constant, one can calculate the diffusivity D from:

$$D = D_o \, . \, e^{-\left(\frac{Q}{RT}\right)} \qquad (5.2)$$

The thickness of the interface (x) is then calculated from the formula, x= $2\sqrt{Dt_d}$, where t_d is the time for diffusion. It is here reasonable to assume the entire ECAP process as the maximum time for diffusion (t_d). For one pass ECAP, $t_d \approx 50$ s, which yields a value of x = 0.48 µm. However, this is a magnitude lower than the observed value ~5 µm (IF1+IF2). Back calculations show that the activation energy is 108 $KJmol^{-1}$, which is much less than Qc , but close to the activation energy for diffusion of Mg in fine grained Al (98 $KJmol^{-1}$) [171], even though the grains are quite large (Fig 4.29). This means that interface (IF1+IF2) is severely

deformed due to a combination of ECAP shear and ISS, thus having a lower Q value than expected. This is consistent with the fact that enhanced diffusion occurs in severely deformed materials and is contributed by extensive dislocation glide and the characteristic ultrafast transport channels [224].

Microhardness evolution

The microhardness profile after various passes, plotted as a function of distance from the centre, is shown in Fig 4.32. The microhardness increases with increasing number of passes. The increase after each pass is due to the increasing incremental strain imparted into the material during processing. An important feature that can be observed is the dip in the hardness profile at the centre of the AZ31 core. This is due to the effect of ISS. The strain that is imposed on the material is not efficiently transferred to the centre of the AZ31 core because ISS has a maximum at the edges and a minimum at the centre. As can be seen from the profiles, the width of this dip-zone decreases with increasing number of passes. This is probably due to an increase in ISS with increasing passes. Furthermore, Figure 4.28d shows some microcracks at the interface. These are believed to be formed due to the effect of ISS on the brittle nature of present intermetallics. The microcracks seem to propagate towards the softer CP Al region and hence may increase the total ductility and toughness of the bi-metal, e.g. due to mechanical interlocking and pinning of the crack front by ductile Al [225].

Microstructure evolution

Figure 4.30 shows the inverse pole figure maps (IPF) of the Al region close to the interface. Here, the Mg/Al interface is emphasized by red arrows. Interestingly, a significant grain size reduction to 30 μm after six passes in CP Al is observed. Figures 4.30b and 4.30c reveal a change in the colour contrast within a grain. Also, the average misorientation of the microstructure has been plotted as a function of number of passes (Fig 4.29) and there is a clear increase with increasing strain. However, the increase after four passes is reduced and remains almost constant, thus indicating onset of recovery. Recent reports show that sub-grain rotation by incremental strain can result in grain refinement by continuous

dynamic recrystallization (CDRX) at high temperatures [160, 290, 291]. In fact, the presence of incomplete high angle grain boundaries (HAGB) (black arrows in Fig 4.30) and the progressive misorientation within the grain shown by the change in colour contrast, indicate that the material has undergone grain refinement by CDRX [292].

Tension test and fracture studies

The tension test results show that the yield strength (YS) of the CP Al/AZ31 bi-metal rod type structure depends on the weaker material, in this case CP Al. However, the YS and UTS have both increased as compared to CP Al [293]. Also, the ductility of the bi-metal is ~15% which means that the ductility has increased relative to the as-cast AZ31. The EDS line scan performed in the delaminated region shows the presence of Mg on a localized scale (Fig 4.35). Fractography investigations confirm that the bi-metal remained completely bonded until fracture, even though there were localized pull-out regions.

Figure 4.34 shows three different regions on the uniaxial tension fracture surface. The region between the yellow and the green line corresponds to localized fracture of AZ31 at the interface due to stress concentration on the well bonded regions. Hence, broken AZ31 particles were found sticking to the CP Al surface in this region. Some of these brittle constituents lead to crack propagation and final fracture of the AZ31 alloy itself upon further tension. Also, any un-bonded or weakly bonded regions result in delamination of the interface. The presence of brittle intermetallics may also lead to fracture of the interface, hence resulting in further delamination. This transforms to the formation of the second region (area between the green and the white line in Fig 4.34). On further deformation by tension, CP Al undergoes ductile fracture as depicted in the white region, e.g. due to necking and void coalescence. Additionally, Figure 4.35 shows that even the delamination region (or the second region), contains Mg rich areas on the surface of CP Al. This means that even though delamination has occurred at the AZ31/CP Al surface, some Mg still remains bonded to CP Al. Alternately, some intermetallic particles may also remain stuck to the surface. Either way, this confirms the reasonable good bonding between CP Al and the AZ31 rod after ECAP.

The presence of intermetallics at the interface increase ductility of the AZ31 alloy by encasing CP Al around the AZ31 rod. Simultaneously, the yield strength of CP Al increases significantly having the reinforcing AZ31 rod at the core. However, the bi-metal combination did not as such behave uniquely as a single composite material, instead both CP Al and AZ31 behaved relatively independently during the deformation, except for the role of the interface regions. The SEM fractograph shown in Fig 4.34 explains the role of the interface on the mechanical properties. The contrast from the lines indicating yielding of CP Al in delaminated region two (II) along with the evidence of Mg in this region (Fig 4.35), show that the yield strength of CP Al was increased due to the resistance offered by the intermetallic Al_3Mg_2 (IF2) region. Stress introduced during the tension test seems to be transferred to the strong and brittle IF2 that is well bonded to CP Al. Hence, an additional stress is required for yielding CP Al than that would be required otherwise. With increasing stress, cracks formed are propagating towards the CP Al region. The latter has sufficient ductility to accommodate the crack, i.e. extending the ductility.

The microcracks seen in Fig 4.28 are evidence of crack propagation towards the CP Al region along the circumference of the interface. This is because, IF1 is stronger than IF2 and hence cracks are more prone to form in the IF2 region. Accordingly, this results in an increased ductility. However, further increase in stress level leads to cracks in the IF1 region and which result in breaking-off the interface bonding. If the bonding is strong, this may lead to the crack propagation in AZ31 resulting in brittle fracture of the latter and in turn causing total failure of the bi-metal.

In summary, a strongly bonded interface in Al/AZ31 bi-metal has been successfully fabricated by ECAP. Deformation at 250°C was not sufficient to produce sound bonding and hence samples had to be processed at 350°C. The strain during the first pass was utilised to establish bonding between the two materials. An interfacial shear stress was introduced in addition to ECAP shear due to the circular cross section of the interface. CP Al showed a significant grain refinement after six passes but AZ31 was less refined. The interfacial shear stress is very important for microstructure evolution of the AZ31 region and the ECAP

shear was more predominant in the Al region. This was also indicated by the microhardness profile along the cross section. Two intermetallics were formed at the interface and fractography showed that the material failed differently in various regions.

5.3.2 Al/AZ31 macrocomposite

The part above, regarding fabrication of a rod type bi-metal showed that processing of Al/Mg resulted in an interface with two different transition regions containing $Mg_{17}Al_{12}$ and Al_3Mg_2 intermetallics. As discussed, the presence of intermetallics enhances strength and partly ductility of the bi-metal. The results also showed, that upon increasing tensile strain the area of the interface regions increased. Although interface transition regions containing intermetallics could enhance mechanical properties, a wide interface that is several hundreds of microns thick would probably make the bi-metal configuration weak and susceptible to cracking, owing to the brittle phases. In order to overcome such a situation, fabrication of a bi-metal composite containing a large fraction of dispersed interfaces was undertaken. This led to a new type of Al/AZ31 macrocomposite. The related results thus obtained are discussed in the following paragraphs.

Bonding characteristics

Optical micrographs of the as-prepared composite (Figs 4.36–4.37) and the subsequently ECAP'ed material are shown (Figs 4.42–4.43). These micrographs reveal the bonding between mono-material chips and between CP Al and AZ31 islands. The width of the AZ31 chips observed in as-prepared screw extruded and in the ECAP'ed condition, show that ECAP introduced thinning of the AZ31 islands both in the cross section and along the longitudinal direction.

The as-screw extruded composite shows poor bonding characteristics and clustering of the AZ31 chips relative to the subsequently processed ECAP'ed condition. The introduction of ECAP, although conducted at high temperature (200°C), shows excellent bonding characteristics. This is due to the effect of high strain and moderate pressure imparted in ECAP. Also, the AZ31 islands which originally were clustered in the as-screw extruded condition were thinned and

elongated along the ECAP shear direction. The introduction of ECAP might also have resulted in dissolution of Mg into Al, thus contributing to a reduced width of the AZ31 chips. In order to confirm dissolution of Mg into CP Al, EDS line scan analyses of Al and Mg concentrations across the interface of pre- and post ECAP'ed material were obtained (see Figs 4.39–4.41 and Fig 4.47 respectively). The nature of different interface structures due to the imposed ECAP strain could be observed. While, the screw extruded composite showed an interface with transition regions similar to what was observed for the Al/AZ31 rod type composite, the ECAP'ed macrocomposite exhibited a single transition region (IF3) containing around 80 wt% Al and 20 wt% Mg. This composition corresponds to a mixture containing Al and Al_3Mg_2 intermetallic phases in agreement to the equilibrium phase diagram for the Al-Mg binary system.

Interface studies

Based on the SEM and EDS analysis, a phenomenological evolution of the interface bonding mechanism can be developed. Figure 5.10 illustrates the various stages of the interface intermetallic layers during screw extrusion. The same explanation can also be used for the interface structure developed during Al/AZ31 alloy bi-metal rod type structure since a similar interface can be observed for the latter.

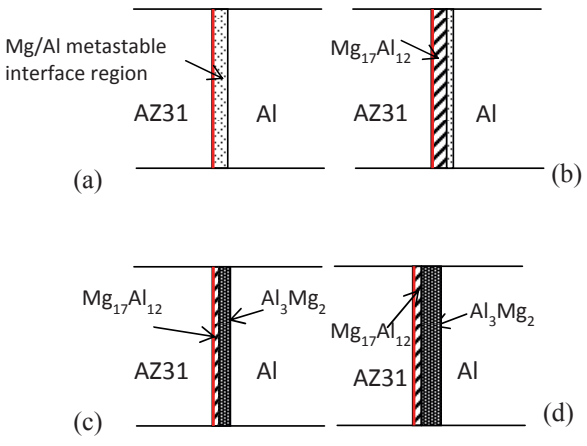

Figure 5.10. A schematic representation of the formation of intermetallic layers in an Al/Mg alloy bi-metal fabricated by screw extrusion; (a) first stage, (b) second stage, (c) third stage, (d) fourth stage. The red line represents the physical interface between Al and Mg.

During high temperature screw extrusion of the composite, diffusion of Mg into Al occurred, forming a temporary Mg/Al metastable transition region (see Fig 5.10a). Upon further time exposure, this developed into $Mg_{17}Al_{12}$ due to thermodynamic reasons (see Fig 5.10b). The introduction of ECAP strain might increase the stored energy of the material, resulting in diffusion through short circuit paths, i.e. including pipe diffusion and grain boundary diffusion, both having a low activation energy [294]. In addition, the interface experienced higher strain as compared to the bulk, hence more dislocations were activated here.

Wang et al. [295] studied the diffusion activation of energy of Mg and Al in an intermetallic Mg/Al joint and reported that the lowest activation energy (16.33 $KJmol^{-1}$) for diffusion of Mg in Al occurred in the $Mg_{17}Al_{12}$ intermetallic (IF1). This would have resulted in diffusion of Mg into Al from IF1 into IF2. This, in turn might have resulted in formation of the Al rich Al_3Mg_2 intermetallic (IF2) as shown in Fig 5.10c. It was reported that the diffusion activation energy of Al is lower than for Mg in Al_3Mg_2, i.e. 22.6 $KJmol^{-1}$ and 33.72 $KJmol^{-1}$ for Al and Mg respectively. Hence, simultaneous diffusion of Al into IF2 occurred as well. This might have led to the formation of a thicker IF2 as compared to IF1. Therefore, a two layered transition region could be observed at the interface in the present Al/AZ31 alloy bi-metal having a thick IF2 and a thin IF1 region as can be seen from Fig 5.10d. These characteristics of diffusion kinetics may also explain why the IF1 is thinner than IF2, both for the rod type structure and the screw extruded macrocomposite.

After screw extrusion, an interface structure similar to that observed in the rod type bi-metal was developed, see Fig 5.10d. With subsequent ECAP strain performed at relatively lower temperature than in the screw extrusion, different activation energies of Mg and Al in different phases lead to the three consequential processes illustrated in Fig 5.11.

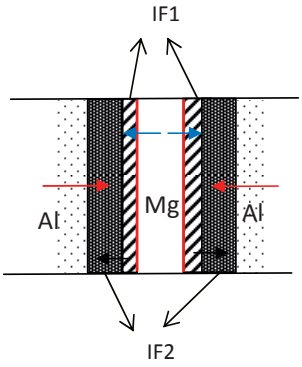

Figure 5.11. A schematic illustration of the diffusion processes involved during ECAP of the screw extruded bi-metal macrocomposite at 200°C.

Firstly, Al diffuses into the Al_3Mg_2 intermetallic phase as diffusion of Al is higher than Mg in this intermetallic (red arrows in Fig 5.11). This leads to a decrease in the concentration of Mg in IF2, thus resulting in higher diffusion of Mg from IF1 into IF2 to compensate for the decreasing Mg concentration (black arrows in Fig 5.11). Also, Mg from the AZ31 region diffuses into IF1 (blue arrows in Fig 5.11). As the deformation progresses, dissolution of Mg into Al occurs due to the diffusion of Al in IF2. Further, the AZ31 region and the interface IF1 collapse as a result of decreasing Mg content and Al and interface region IF2 combine to form a new single interface region as shown in Fig 5.12.

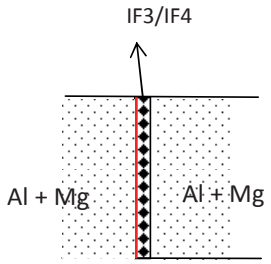

Figure 5.12. A representation of the final interface structure observed after ECAP at 200°C of screw extruded bi-metal macrocomposite. The red line represents the physical interface between Al and Mg.

In other words, the dissolution of Al into IF2 containing Al_3Mg_2 combined with the dissolution of Mg into IF2 from IF1 results in a new interface structure not present in the as-screw extruded condition. The width of the new interface (IF3) was narrow and ≤ 1 µm. However, some thicker regions were also observed (Fig 4.50) and illustrated by Fig 5.13 below. The regions between the white dotted lines in the lower part of Fig 5.13 are thick areas with a different contrast.

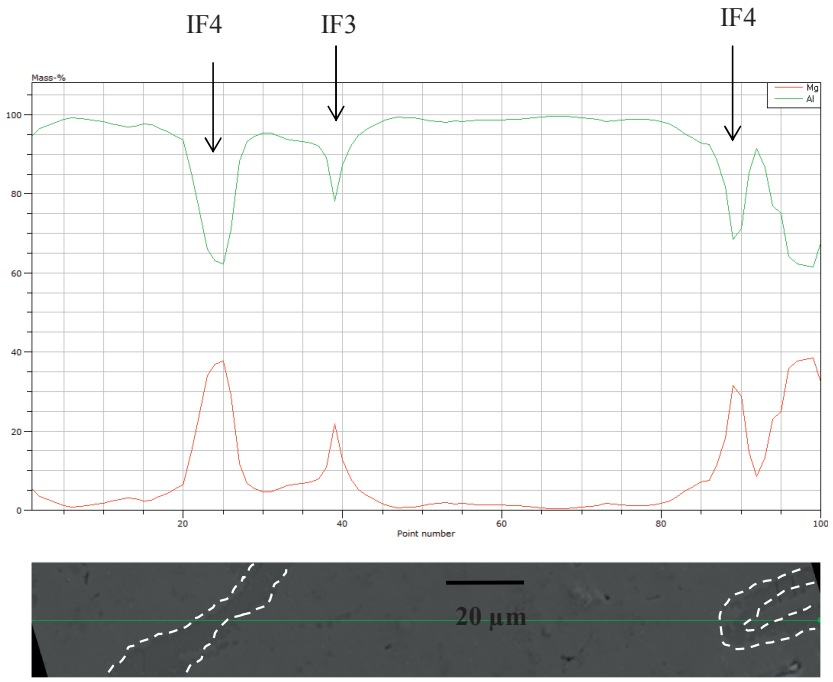

Figure 5.13. EDS line scan analysis of ECAP'ed macrocomposite depicting composition of Al and Mg along the green line in the lower illustration. The red curve depicts Mg and green represent Al. The y-axis is concentration in mass%.

The regions inside the black dotted lines correspond to AZ31 chips that are less deformed during screw extrusion than the majority of theAZ31 chips. This is possible, as the screw extrusion introduced bonding of CP Al and AZ31 chips due to high temperature and intensive shear straining. The width of these regions was

too large for dissolution of Mg and hence, Mg was not completely dissolved into Al. Instead, Al dissolved into Al_3Mg_2 intermetallics. Also, Mg from the AZ31 matrix dissolved into $Mg_{17}Al_{12}$ intermetallics and then from IF1 into IF2 (Al_3Mg_2). As mentioned above, the diffusion of Mg from AZ31 into IF1 and IF2 is faster than diffusion of Al into IF2. This results in a collapse of the Mg rich AZ31 regions into a transition region containing 60 wt% Al and 40 wt% Mg (IF4) as shown in Fig 5.13. This corresponds to a region containing almost a single phase Al_3Mg_2 intermetallic in accordance to the equilibrium phase diagram. However, since Al and Mg are light elements and next to each other in periodic table, accuracy of the EDS analysis is reduced [296]. This means that the IF4 region may not contain a single phase Al_3Mg_2 intermetallic but rather exist as a mixture of Al_3Mg_2 + Al or Al_3Mg_2 + $Mg_{17}Al_{12}$.

Furthermore, Figure 5.13 shows that identified IF4 regions are wide apart. Also, the CP Al matrix between such regions contains very little Mg (almost without Mg). This supports the above mentioned mechanism involving dissolution of Al into the Al_3Mg_2 intermetallic. In other words, the closer the AZ31 islands are spaced, the more homogeneous is the dissolution of Mg in Al. On the other hand, if the AZ31 islands are wide apart, the dissolution of Mg is restricted to the regions close to the AZ31 islands, thus leaving large regions of pure Al.

In summary, mechanisms responsible for the evolution of interface structures during screw extrusion and after subsequent ECAP have been explained. These interface structures look similar as to what was observed for the rod type bi-metal after ECAP. They contained two transition regions, IF1 and IF2 which were primarily made up of $Mg_{17}Al_{12}$ and Al_3Mg_2 intermetallics. After ECAP, the interface structure of the macrocomposite was transformed into a single transition region. The composition of this region was determined by the thickness of the AZ31 islands initially present before ECAP. For thin regions, thickness $\leq$ 2 μm after ECAP, the interface structure consisted of Al and the Al_3Mg_2 intermetallic (IF3), while interfaces with thickness larger than 2 μm consisted of regions with Al_3Mg_2 intermetallics (IF4). These transformations have been attributed to the differences in the diffusion activation energies of Mg and Al in different regions such as Al, AZ31, IF1 and IF2 interface regions.

Grain size studies

From the polarized optical micrographs (POMs) in Figs 4.36–4.37, 4.42–4.43 and the IPF map in Fig 4.48, it can be seen that the grain structure was significantly refined, i.e. from an average of ~27 μm after screw extrusion to ~5 μm after ECAP at 200°C. This significant grain refinement could also be attributed to the ECAP process itself, but was aided by the dissolution of Mg in aluminium. The refinement mechanism is believed to be similar to that observed in Al-Mg solid solution alloys [106, 111, 297]. The IPF map in Fig 4.48 shows that, unlike CP Al undergoing ECAP where a cell structure was predominant even at RT (see Figs 4.3–4.7), a non-cellular microstructure develops even at 200°C ECAP (see Figs 4.48 and 4.49). This is probably due to the effect of Mg in solid solution reducing dislocation mobility due to solute drag effects. Interestingly, a similar structure has been observed for an Al- 3Mg alloy during ECAP processed at RT [298].

Additionally, the presence of intermetallics results in the formation of small grains close to them. Chen et al. [297] investigated the microstructure evolution of various Al-Mg alloys by ECAP and found that fine grains, i.e. finer than that achieved in the bulk material, were present around Fe rich impurities. It was reported that the hard particles stimulate an increase in local misorientation. Also, large particles produced higher misorientations along the HAGBs as compared to smaller particles [297]. Apps et al. [299] reported similar deformation zones around second phase particles. Hence, in the present macrocomposite the interface regions (IF3 and IF4) correspondingly assist grain refinement, especially in their nearest neighbourhoods. Since these interfaces are long, streaks of small grains are formed in the vicinity of interface regions decorated with intermetallics (see in Fig 4.48).

Tension tests and fractography

Tension tests showed that high strength can be achieved for the macrocomposite. From Figure 4.51 and Table 4.1, one can conclude that the yield strength increases by a factor of 2 after ECAP. In spite of this increase, the ductility remained quite reasonable. The relative high strength is believed to be achieved by

the presence of alternate layers of IF3 and IF4 containing intermetallics. Unlike the screw extruded macrocomposite containing AZ31 islands surrounded by aluminium and separated by interfaces containing two transition regions, the interface structure in the ECAP'ed macrocomposite appeared different. Also, the interface structure after ECAP is relatively thin as compared to that of the screw extruded composite. It seems likely from the above discussion on the interface structures that about ~3 wt% Mg is dissolved in aluminium. All these characteristics are believed to contribute to the high strength observed in the macrocomposite.

From the literature survey, serrations in the stress strain curve seemed to appear at particular deformation conditions promoting strain localization [300] and are quite commonly observed in Al-Mg alloys. Serrations obtained in these materials are commonly referred to as the "Portevin-Le Chatelier effect" (PLC effect) [301-304]. Serrations are believed to occur from dynamic strain ageing (DSA) due to the interaction between solute atoms and mobile dislocations where solid solution hardening is the primary strengthening mechanism [305-313]. Mobile dislocations are repeatedly locked and unlocked from to the solute atoms, hence resulting in the zigzag flow curves in the plastic region. For some precipitation alloys (e.g. Al-Mg-Zn, Al-Mg-Si etc.), the PLC effect is partly attributed to the shearing of the precipitates. Mobile dislocations accumulate around the precipitates and shear repeatedly, resulting in observable serrations [301, 310, 314-318]. Polycrystalline materials are found to exhibit three types of serrations, namely, A, B and C type serrations [319].

The present screw extruded composite shows serrations similar to type A (see Fig 4.51). However, they are not as periodic as typical type A serrations reported [308, 316, 319]. However, it is believed that the present serrations are a result of dynamic plastic events occurring at the interfaces and in the Al matrix respectively. When the present screw extruded composite is deformed under uniaxial tension, strain localization occurs due to non-uniform strain accommodation within different composite constituents. This strain localization may result in crack formation at the interfaces and is provoked by local stress. However with progressing deformation, there is sufficient plastic flow capability in

aluminium to continue deformation without substantial crack growth. These events are manifested by the jerky flow in the stress-strain curves.

In other words, the present jerky flow has partly a different origin than the classical PLC effect. Although one can confirm the presence of Mg in solid solution in Al rich areas, the effect of IF3, i.e. the Al_3Mg_2 intermetallic interface (but also the IF4) is quite significant compared to the Mg effect in Al. The reason for the increased effect is probably due to the more homogeneous distribution of long streaks of these interfaces within the composite. However, it is to be noted that, this possible mechanism is a conjecture. The scope of the present tensile testing is limited to demonstration of the relative high strength achieved. Hence, more work is needed in order to answer certain questions. For example, is there any real significance of the interfaces as compared to the classical solute effect in the macrocomposite? If so, can it be empirically or quantitatively explained? What is the relative effect of the two different interfaces as compared to that of solid solution?

Furthermore, Figures 4.52 and 4.53 show SEM fractographs of the screw extruded composite and the fractography reveals distinct features. First, small voids (V1) accompanied by some beach marks were observed (arrows in Fig 4.52). Second, large voids (V2) which were long and deep were observed. The small voids correspond to the ductile fracture occurring in Al rich areas. This means that, far from the AZ31 islands, ductile fracture due to void coalescence is the prevailing mechanism. The large voids (V2) are pull-outs where AZ31 islands disintegrate from the matrix at the interface. The brittle nature of the intermetallics (IF1 and IF2) could also lead to rapid crack propagation at the transition regions of the interfaces, thus delaminating from the bond between AZ31 and Al constituents. However, fracture of the AZ31 into smaller fragments is unlikely owing to the dimensions of these voids (V2) which were more or less similar to that of the AZ31 chips (see Section 4.3.5 in Chapter 4). Also, EDS line scan analysis (Fig 4.54) conducted on the fracture surface along the line shown in Fig 4.53 clearly depicts the interface and the CP Al matrix regions.

From the above interpretations, the failure of the composite material can be described as a two-step process. First, with increasing stress, AZ31 islands

delaminated from the CP Al matrix at the interface. The interfaces were of brittle nature and contained pre-existing cracks formed during screw extrusion and which propagated towards the ductile Al regions as explained by Paramsothy et al. [225]. The pull-out of the strong AZ31 islands from the Al matrix reduced the cross-section area, thus increasing the effective stress. With further tension, more pull outs occurred resulting in the final failure of the material, i.e. by fracture of the remaining Al matrix.

However, the fracture of the ECAP'ed macrocomposite was quite different from that of the screw extruded composite. While the screw extrusion composite failed in a ductile manner, the ECAP'ed macrocomposite appeared to be significantly less ductile. Interestingly, the sample failed along the tensile direction. Also, the fractured surface was quite irregular. Figure 4.56 showed that the fracture surface contained some large voids with smooth walls and there were also alternate ductile and brittle regions (see Section 4.3.5 and Fig 4.57). The irregular fracture surface along the tensile direction revealed that failure nucleated by the presence of interface intermetallics. Careful investigations of the fractured surface revealed that the large voids observed on the walls along the tensile direction were absent in the sample cross-section. In addition, several crack nucleation sites were visible as shown in Fig 5.14.

(a)

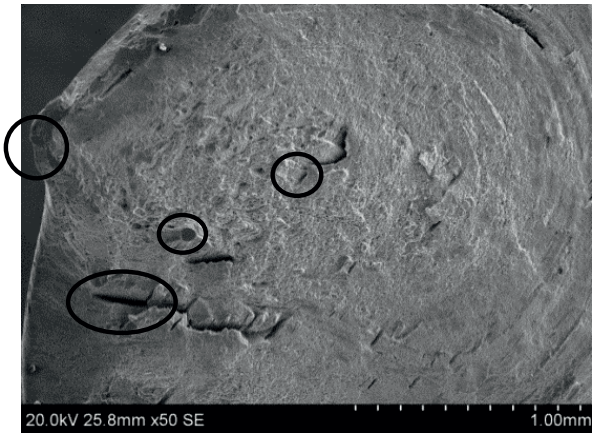

(b)

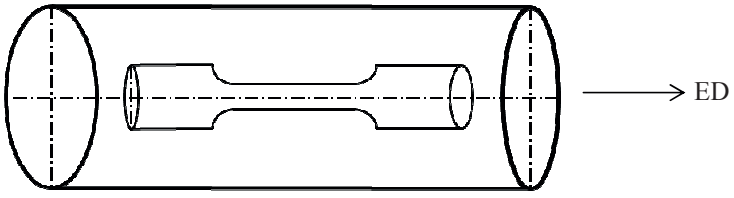

Figure 5.14. (a) SEM fractograph of the failed ECAP'ed macrocomposite. Some crack initiation sites are emphasized by the black circles, (b) Location of tensile sample in the ECAP'ed material.

It is here remarked that this sample had been screw extruded prior to ECAP and hence the AZ31 chips were shaped into concentric circles corresponding to the characteristic strain path [255]. Thus, crack initiation must have caused failure along the chip boundaries in a similar fashion. The morphology of the fracture surface in Fig 5.14a actually shows such concentric lines. As just mentioned, large voids observed on the walls perpendicular to the cross-section area were not visible in the cross-section. This could mean that while the fracture process developed in the cross-section, the interface regions (predominantly IF4 regions) delaminated from the Al matrix. The IF3 regions being very thin, most probably broke down discretely. Irregular, rugged boundaries in IF3 could here, aid

fracture along the interfaces. Furthermore, the smooth surface of these meso-sized voids actually supports the pull out mechanism described above. The investigations across the cross section area actually revealed that failure occurred both in Al matrix and through the interface regions. This resulted in the alternate ductile and brittle regions shown in Fig 4.57. Here, EDS analysis confirmed that this pull-out mechanism was very likely.

In summary, the screw extruded composite failed by ductile fracture of CP Al caused by a reduction of load bearing area. The latter occurred due to fracture of transition regions at the interfaces followed by pull-out of AZ31 islands from the matrix. The ECAP'ed macrocomposite, on the other hand, had failed by multiple crack initiations along chip interfaces. Crack propagation along the interfaces facilitated an easy pull-out of previous chip elements. Since the aluminium rich areas also contained dissolved Mg, the ductility was lowered and crack propagation accelerated towards final failure.

Comparison between ECAP'ed macrocomposite and Al alloys

The strength achieved in the ECAP'ed macrocomposite is relatively high as compared to pure Al or even AZ31 alloys after ECAP. In order to realise the potential of the macrocomposite, it is necessary to compare the properties with the characteristics of existing Al-Mg binary alloys and other Al alloys in the similar strength regime. Murashkin et al. [111] showed an extremely high ultimate tensile strength of about 950 MPa for a commercial 1570 alloy (Al - 5.7 wt% Mg - 0.32 wt% Sc - 0.4 wt% Mn) pressed in HPT by 20 turns at RT. Although the present macrocomposite does not show such a high strength, the strength can be compared to that of an annealed Al 1570 aerospace alloy (~376 MPa). It must be noted that the very high strength from such a heat treatable alloy comes from a combination of high solute content (Mg) and a large fraction of extremely small Al_3Sc precipitates in the matrix. Similarly, the strength from the present material originates from the interlayers of Al_3Mg_2 intermetallics combined with the diffusive dissolution of Mg into Al regions. Moreover, Furukawa et al. [320] studied the factors influencing flow and hardness of ultra-fine grained Al alloys. They examined an Al-3 wt% Mg alloy subjected to ECAP at room temperature for

4 passes and which was further annealed at different temperatures for one hour. The present macrocomposite processed by ECAP displayed a yield strength of 275 MPa which is lower than that observed for the Al-3Mg alloy after 4 passes ECAP at RT (~370 MPa) and it exhibited only half of the elongation to failure. Although the ductility and yield strength of the macrocomposite were lower than for the ECAP'ed Al-3Mg alloy, the UTS of the present macrocomposite was higher. Also, by comparing with a similar study on the improvement of mechanical properties of different Al alloys by Horita et al. [321], the present macrocomposite seemed to have a better combination of high yield strength and a good ductility as compared to the Al alloys 2024 and 5083.

Furthermore, in order to extend the strength of the ECAP'ed macrocomposite, it was cold-rolled from an initial thickness of 10mm to 1mm resulting in a von Mises strain of about ~2.7. Hence, Figure 5.15 shows a comparison of the screw extruded, ECAP'ed and the subsequently cold rolled samples subjected to tension testing.

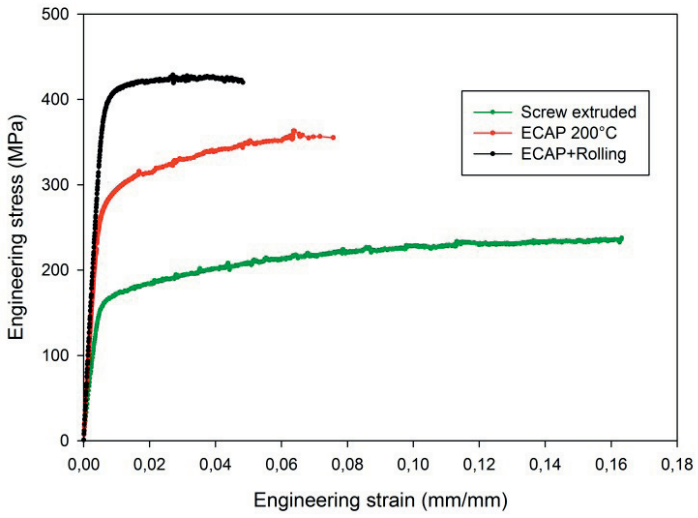

Figure 5.15. A comparison of engineering stress-strain curves of the as-screw extruded, ECAP'ed and ECAP + cold-rolled macrocomposite originated from screw extrusion.

It can be seen that there is a significant increase in yield stress after rolling, i.e. ~395 MPa. However, the ductility has decreased to about 4%. The high fracture strength (430 MPa) in the cold-rolled condition is similar to that observed for a 5083 Al-Mg alloy ECAP'ed to 4 passes although the ductility was lower for the rolled macrocomposite. The high strength obtained in the rolled condition is believed to be due to high densities of accumulated dislocations resulting from low dislocation mobility at RT caused by (i) dissolved Mg in Al together with, (ii) the presence of intermetallic particles which, (iii) might have been broken down into smaller fragments. The obtained mechanical properties are particularly interesting as the high strength reported for alloy 5083 was obtained by an ultra-fined grain size, while this was not a major characteristic of present macrocomposite after rolling. However, a mean grain size close to 1 μm assumed to be present in the latter case. EBSD scans were taken along the ED-TD plane to see if the grains were ultra-fine and Figure 5.16 shows a corresponding OIM image of the rolled sample.

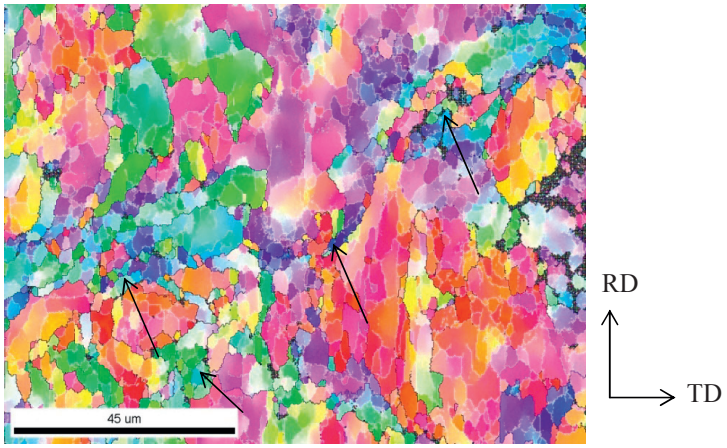

Figure 5.16. OIM map of the ECAP'ed macrocomposite, post processed by rolling at RT. Black lines indicate HAGBs and white lines indicate LAGBs.

It can be seen that a necklace of fine grains is observed in some regions (black arrows in Fig 5.16), while most of the matrix is constituted by a larger grain size. It should be added that this investigation was purely intended to demonstrate

high strength potentials of the Al/Mg macrocomposite originating from screw extrusion. Hence, further analysis, e.g. of the cold-rolled condition, was not performed.

Anyway, the present study clearly illustrates the potential of such a new genre of mechanically mixed Al/Mg materials containing interfacial intermetallics and an Al matrix strengthened by one or more constituents of Mg rich particles. In other words, the present study leaves big room for further investigations and developments.

Microhardness evolution

The microhardness values show that the ECAP'ed macrocomposite is harder and stronger than the screw extruded macrocomposite counterpart (refer Fig 4.59). It seems obvious that peaks correspond to interface regions in both the plots and the valleys represent the Al rich matrix. The hardness value of the latter for the screw extruded condition was on average ~27±3 HV. This value is very similar to the as received hardness of CP Al before processing. On the other hand, an average hardness of ~81±3 HV was observed for the Al matrix in the ECAP'ed material. A comparison of these values shows a significantly higher hardness for the ECAP'ed condition, i.e. three times higher than the screw extruded material. This difference indicates that Mg was dissolved into aluminium after ECAP, as discussed above.

The hardness ratio between the interface and the Al rich region for the screw extruded macrocomposite is ~3 whereas the ratio drops to ~1.25 for the ECAP'ed macrocomposite. This probably confirms the dissolution of Mg into Al during ECAP. From the investigations on alloy Al-3Mg and a commercial Al-Mg-Li-Mn alloy (CA) [320], it was found that the ECAP'ed Al-3Mg alloy showed a mean hardness of ~120 HV whereas the CA alloy had a value of ~118 HV. However, on annealing to 473 K, the observed hardness was ~100 HV for the CA alloy, i.e. similar to that observed for the average hardness of the macrocomposite processed by ECAP at 473 K (87±10 HV). To be mentioned, the average hardness of the CP Al constituents of the macrocomposite ~81 HV is quite similar to ~85 HV of the ECAP'ed Al-3Mg alloy annealed at 573 K.

The above results and discussion show that the present macrocomposite prepared from Al and AZ31 chips could be a new genre of ECAP'ed high strength Al/Mg based materials for novel structural applications. The untreated ECAP'ed macrocomposite processed at 473 K (200°C) is similar to ECAP'ed Al alloy 5083 after 4 passes at RT. However, if the macrocomposite is processed at RT, the latter material is believed to reach much higher strength levels.

5.4 Sheet composites

5.4.1 General overview

The Al/Mg macrocomposite processed by ECAP and the subsequent post processing by cold-rolling revealed a significant increase in the UTS and yield strength of the material. Although, fabrication of this novel material is encouraging, the process had to be optimised for both experimental and material conditions in order to achieve consistent and even more attractive results. Having said, it is practically difficult to optimise the macrocomposite owing to the complex interface structure and multiple processing steps. Hence, Al based sheet composites and rod shaped bi-metals were fabricated and subsequently studied to discover important characteristics that can be used for optimizing the experimental conditions and to better understand the material behaviour during ECAP of interfaced materials in general.

5.4.2 Al/Al composite

Effect of experimental parameters

As explained earlier (see Section 4.4.1), an Al/Al composite was designed to study the effects of experimental parameters on the bonding behaviour of similar sheets upon ECAP. Tables 4.1–4.4 show whether the sheets were bonded for various experimental conditions. Investigations on the Al/Al composites were divided into two broad categories, viz., samples processed without back pressure and samples processed with back pressure. Samples processed with back pressure were further subdivided into three categories, namely, (1) SiC brushed, (2) wire brushed and (3) machine brushed samples.

Figure 5.17 shows force vs. pressing speed plots for samples processed without back pressure for varying lengths and roughening techniques.

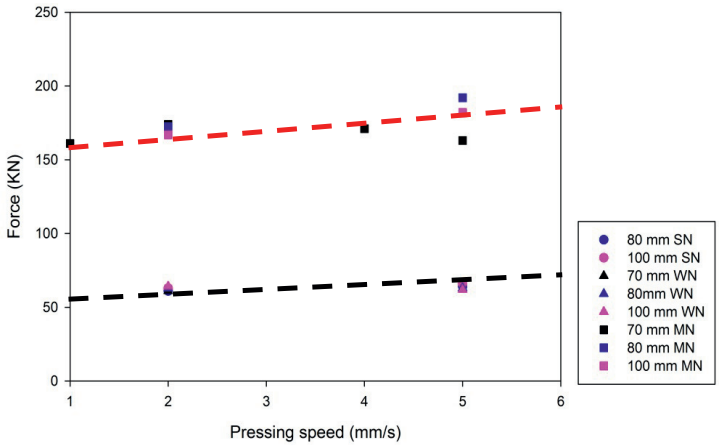

Figure 5.17. Force vs. pressing speed plots of samples processed without back pressure and with various lengths and roughening techniques. Black dotted line indicates the trend of samples roughened by SiC emery sheets and wire brush. Red dotted line represents the samples roughened by machine brushing.

It can be seen that the samples roughened by machine brushing require a significant higher pressing force than SiC sheets and wire brushed samples having the same length. This could be an effect of increased friction between the two sheets. In order to resolve the effect of friction, a CP Al block of length 100 mm and a cross section of 19.8 × 19.8 mm^2 was ECAP'ed at RT. A force of ~45 KN was required to ECAP such a material at 2 mm/s. Now, the total force (F_T) required to ECAP the present Al/Al sheets can be expressed as:

$$F_T = F_{ECAP} + 2 \cdot F_{fric} \qquad (5.1)$$

Here, F_{ECAP} is the force required to ECAP a bulk counterpart and F_{fric} is the additional frictional force between the sheets. This value is multiplied by 2 as there are two interfaces in the present configuration. Since the same Al material has been used, F_{ECAP} can be assumed to be 45 KN obtained from ECAP of the CP Al block.

It has already been discussed (see Chapter 2) that the effect of pressing speed does not have any significant influence on the microstructure evolution as long as recovery kinetics are not influenced, e.g. see [11]. Also, since a semi-continuous ECAP method (see Chapter 3) has been applied, the effect of specimen length on the processing force can be assumed to be negligible for pure materials [6]. Hence it is reasonable to assume a constant ECAP force of 45 KN in the present case. Now,

$$F_T = 45 + 2 \cdot F_{fric} \qquad (5.2)$$

Applying Equation 5.2 to the samples processed without back pressure, the frictional force (F_{fric}) was obtained to be ~3 KN for samples roughened by SiC grinding papers or wire brushing pressed at 1 mm/s, and F_{fric} ~7.5 KN for 5 mm/s pressing speed. However, for machine brushed samples, F_{fric} ~57 KN at 1 mm/s and F_{fric} ~65 KN at 5 mm/s. Hence, the machine brushed samples experience higher frictional forces at the interfaces as compared to that of the SiC roughened and wire brushed samples. It is to be noted that this is a simple derivation and assumes that the deformation at both interfaces is equivalent. However, in reality such a situation is probably unlikely. This is due to the inhomogeneity in the ECAP deformation process itself [21]. Also, the presence of the characteristic arc of curvature (ψ) in the ECAP tool has a significant effect on deformation homogeneity during ECAP [6]. In addition other factors such as lubrication and material characteristics, such as the presence of local impurities, may change the behaviour of the sheets and the interfaces. The two slopes of the plots in Fig 5.17 show a weak increasing tendency vs. pressing speed, e.g. higher slope for the machine brushed surfaces than for the other two roughening methods. The general positive slope probably corresponds to a positive strain rate sensitivity of the pure aluminium [322, 323]. Further, the higher friction between machine brushed surfaces could accelerate work hardening. This in turn, will increase the necessary pressing force. However, all samples processed without back pressure slipped on the sheet surfaces, thus preventing interface bonding since the hydrostatic pressure was too low.

Furthermore, Fig 5.18 shows the necessary ECAP force as function of pressing speed for wire brushed samples processed with a back pressure of 100 KN.

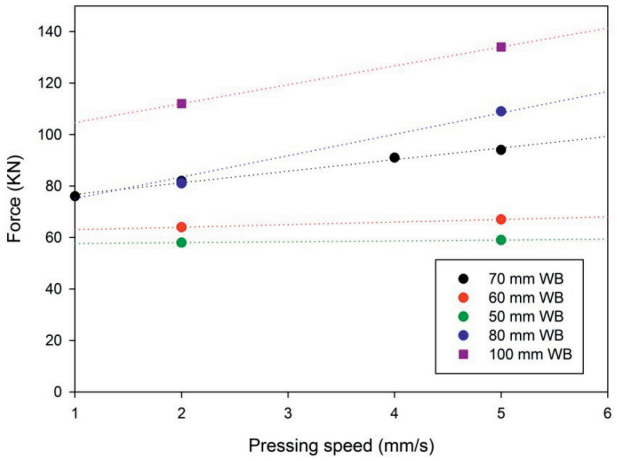

Figure 5.18. Force vs. pressing speed plots of wire brushed samples processed with an ECAP back pressure of 100 KN for various lengths.

Obviously samples longer than 60 mm show an increasing frictional force with increasing pressing speed, whereas samples shorter than 60 mm do not show such an obvious effect. The shortest specimens behave relatively similar to the samples processed without back pressure (Fig 5.17). This means that 70 mm is the threshold length. Above this value, the samples show increasing friction with increasing pressing speed when a back pressure is set at 100 KN.

This could be due to an effect of the deformation rate on friction [324-327]. Accordingly, it is a general notion that the increasing deformation rate increases friction of the interacting surfaces. Two different speeds are here considered to explain such an effect. At a pressing speed of 2 mm/s, it can be seen that the pressing force is proportional to the length of the samples (F~58 KN for 50 mm and F~116 KN for 100 mm wire brushed samples, i.e. doubled). Increasing pressing force means increasing hydrostatic pressure inside the channel. The probability of local interface bonding is therefore increased, decreasing the

tendency of slipping of the sheets. However, the bonding could not be established. A probable reason could be that the above local interface bonding might be a self-strengthening effect and since more massive or continuous plastic flow requires very high shear stress, the effect of such dependence might require higher order dependence than the present linear effect.

Effect of length on friction at higher pressing speeds can be explained by the dependence of deformation rate on flow stress, i.e. by increasing the deformation rate, this elevates the flow stress ($m > 0$), which in turn increases the hydrostatic pressure inside the channel. However, bonding did not occur even at higher speeds. This could be due to the limitation of surface roughness. Wire brushing could have produced too little roughness than required to hold the sheets together at the given hydrostatic pressure. The poor surface roughness might have resulted in little interlocking of sheets, causing interface sliding. As a result, subsequent bonding and debonding could occur at the interface as the sample is pressed through the channel. This local bonding and debonding due to interface sliding would increase the frictional force at the interface with increasing length. This is probably the additional force obtained at higher pressing speeds as compared to that at lower pressing speeds. For instance, at 5 mm/s pressing speed, the necessary force (F~134 KN) is higher for the 100 mm long sample than a 50 mm sample (F~62 KN). Considering a similar effect as obtained for 2 mm/s, there is an additional 10 KN ($134 – 2\times62$ KN) at 5 mm/s due to the interface sliding.

The resulting frictional force calculated for the samples plotted in Fig 5.18 is summarized in Table 5.1.

Table 5.1. Frictional force calculated for the wire brushed samples processed with a back pressure of 100 KN for different lengths.

Length (mm)	Pressing speed (mm/s)	F_{fric} (KN)
50	2	6.5
50	5	7
60	2	9.5
60	5	11
70	1	15.5
70	2	18.5
70	4	23
70	5	24.5
80	2	18
80	5	32
100	2	33.5
100	5	35.5

By comparing Fig 5.17 and Table 5.1, it can be proposed that the machine brushed condition processed without back pressure has a higher frictional force at the interface than the wire brushed samples processed with a back pressure of 100 KN. This means that surface preparation is critical for generating a high frictional force at the interface.

Figure 5.19 summarizes the force vs. pressing speed plots for machine brushed samples processed with different lengths and a back pressure of 100 KN.

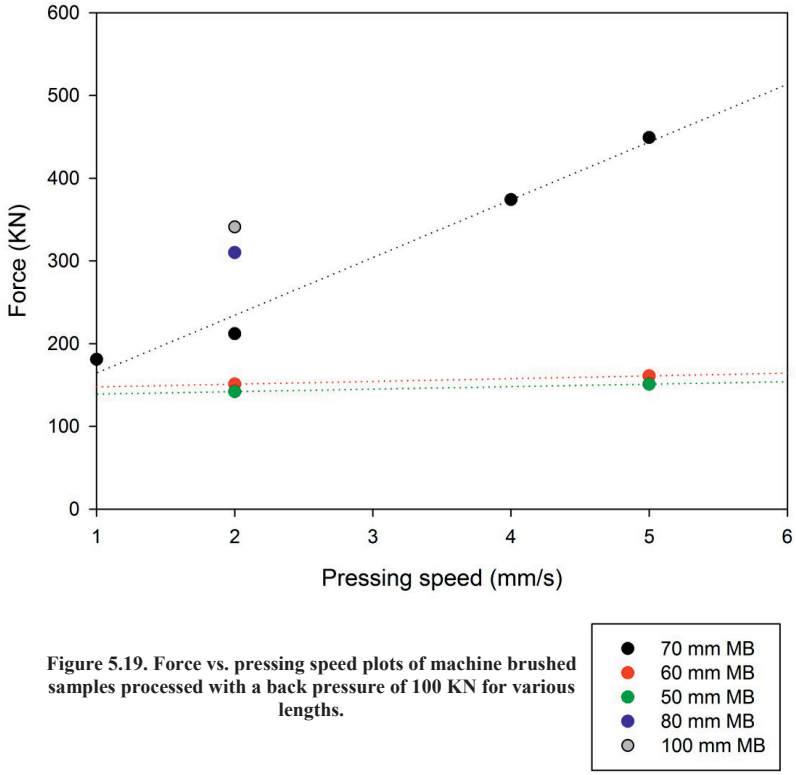

Figure 5.19. Force vs. pressing speed plots of machine brushed samples processed with a back pressure of 100 KN for various lengths.

By comparing the scale of the y-axis in Figs 5.18–5.19, it can be observed that wire brushed samples showed relatively less increase in the frictional force with increasing pressing speed as compared to machine brushed samples. This is clearly visualized by Fig 5.20 showing the frictional force of samples processed under different conditions.

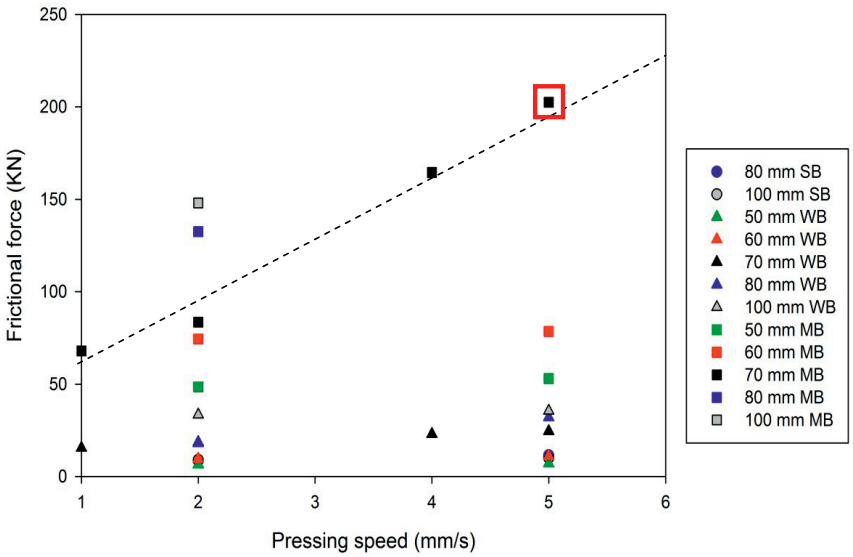

Figure 5.20. Frictional force as function of pressing speed for samples processed with a back pressure of 100 KN under various experimental conditions. Red box denotes the sample 705MB that achieved bonding.

It can be seen that samples processed with a length up to 60 mm do not show any significant increase in friction with increasing pressing speed. Also, of all samples, only those surfaces that are machine brushed with length greater than 60 mm show higher frictional force as compared to the force required to perform ECAP on a solid bar, i.e. $F_{fric} \geq 2 \cdot F_{ECAP}$. Secondly, the sample 705MB showed an excellent bonding between the two sheets without any interface, i.e. the sheets have been transformed into a bulk material after just 1 pass ECAP. From the above observations it can be proposed that for the current experimental setup, at least 200 KN of frictional force is required to achieve bonding between the sheets.

For the current conditions, the sample length must at least be 70 mm and processed with a back pressure of 100 KN. By comparing Figs 5.18 and 5.20, it can be proposed that for lengths greater than 70 mm, the change in the frictional force (F_{fric}) per mm per second, i.e. the slope of the line in Fig 5.20, increases with increasing length. However, physical evidence of the increasing slopes for lengths

greater than 70 mm could not established for BP-ECAP due to the limitations of the current die setup, which can withstand only 600 KN force.

Microstructure evolution

A typical OIM map of the sheets processed by ECAP was shown in Fig 4.62. As mentioned in Chapter 4, the processing of sample 705MB led to good bonding between the sheets and the specimen became fully consolidated upon ECAP deformation. It was also difficult to identify individual interfaces in the material after ECAP. Observations from the OIM investigations showed that grains were severely strained and numerous deformation bands were formed. Although the total force required to process the composite was high, no significant grain refinement was observed. The mean grain size observed in the current sheet composite was similar to that observed in a CP Al block processed to 1 pass by ECAP at RT in the present study (see Section 5.2).

Bonding mechanism

Bonding between sheets prepared by ECAP has to the present author's knowledge, not been published. However, a number of previous works focussed on the bonding mechanism involved during roll-bonding of sheets [1, 2, 47, 74, 78, 328]. For instance, Bay et al. [76] developed a general model and explained the bonding mechanism involved during rolling. According to these authors, initially, fracture of a contaminant film occurs followed by extrusion of material through the cracks and then finally, coalescing with the opposite surface by building the real contact bond. The model also proposed that a threshold surface expansion of the material had to be exceeded in order to achieve bonding. A similar work by Vaidyanath et al. [329] reported that surface deformation by scratch brushing removed layers of contaminant films and subsequent layers stuck to each other upon rolling. This led to unified break-up of layers, resulting in extrusion of a maximum area of virgin metal during the bonding process. Further, another report by the same group [330] showed that there was a remarkable time dependence on the initiation of bonding during rolling deformation.

A specific bonding mechanism can be proposed for ECAP of sheet composites based on the above literature studies. This mechanism is in general similar to that proposed by Bay et al. [76]. However, there are some differences. But first, Figure 5.21 shows a schematic illustration of the bonding mechanism explained by Bay et al. [76].

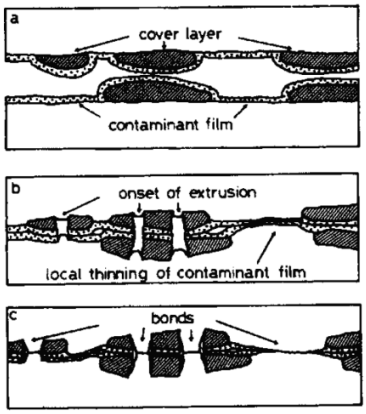

Figure 5.21. Schematic illustration of the bonding mechanism on a scratch brushed surface, (a) prior to deformation, (b) at small strains, (c) at large surface expansion [76].

In the present situation, the sample surface prior to the ECAP is heavily deformed and the surface is relatively rougher, due to machine brushing as compared to scratch brushing utilized in the roll-bonding study. The prepared surface is then immediately processed by ECAP, i.e. the surface is fresh and has a minimum of contaminant film. Hence, the surface is expected to have less contaminant film as compared to that of the roll bonded sample. As the sample is pressed through the die, bonding is initiated at the channel intersection shear zone. The presence of back pressure hinders recovery of stresses that may lead to debonding, once the sample has passed through the channel intersection.

A number of other observations were also made from the present results. Firstly, samples processed at pressing speeds lower than 5mm/s might have had enough time to undergo stress recovery, hence preventing any further bonding of the sheets. This idea is in correspondence to the theory for weld break-up driven by elastic recovery forces, see McFarlane and Tabor [331]. Also, samples having lengths shorter than 70 mm did not show the high frictional force required for the

extrusion of virgin material and hence, the surfaces remained unbonded. This could be an effect of the inherent nature of the ECAP process itself. Secondly, unlike roll-bonding, ECAP involves a constant cross section area and the material is subjected to severe shear only for a short time interval when passing through the channel intersection. At a pressing speed of 5 mm/s for a 70 mm long sample, the actual total sample deformation process lasts only 12 seconds. This could certainly limit diffusion. Thirdly, the frictional force at the sheet interfaces must be at least ~2 times higher than the force required for ECAP of a bulk specimen in order to achieve bonding.

Finally, EPMA was carried out to validate the bonding mechanism involving the break-up of contaminant film during bonding (see Fig 4.63). The results obtained on the well bonded specimen showed no physical evidence of local oxide particles. However, such identification is very difficult since oxides could be very small due to fragmentation and at the same time, the surrounding areas including the bond might be severely deformed. In addition, there is a practical limitation, i.e. the typical resolution limit of EPMA is ~1 μm.

In order to illustrate the bonding process explained above, a schematic illustration is shown in Fig 5.22. The schematic is divided into three, i.e. part (a), (b) and (c). Part (a) describes the macroscopic view of the sheets stacked upon each other along with the interface along the ED-ND plane. The red dashed line depicts the shear zone in the ECAP channel. Part (b) is a magnified illustration of part (a) and illustrates the microstructure evolution before and after ECAP as the sample passes through the shear zone. Part (c) is a magnified illustration of the interface structure before and after the shear zone.

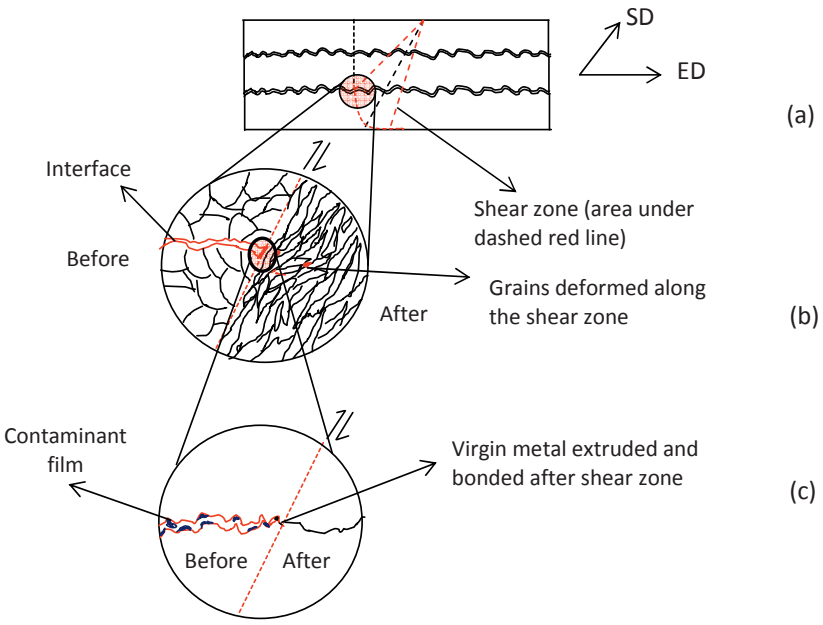

Figure 5.22. A schematic illustration of the proposed bonding mechanism operating during ECAP of multiple sheets. (a) macroscopic view of the sheets with interface and shear zone (red dashed line); (b) microstructure evolution before and after ECAP; (c) interface structure before and after passing through the shear zone depicting the virgin metal extrusion.

5.4.3 Al/3103 sheet composite

The purpose of studying the Al/3103 composite was to reveal the material behaviour during ECAP of dissimilar sheet composites. As discussed above (see Chapter 4), the Al/3103 composite was fabricated under constant conditions based on the Al/Al composite study (70 mm length, 100 KN BP, 5 mm/s pressing speed and machine brushed).

Figures 4.64–4.68 show the OIM micrographs of this composite after ECAP. It can be seen that the microstructure appeared somewhat different from the Al/Al composite. Although the grain refinement characteristics were similar, i.e. no significant grain refinement, the grain structure looked different. Firstly, the two materials underwent different amounts of grain refinement. This is probably due to an effect of the initial grain size. The initial grain size of CP Al was quite large as compared to the as-received grain size of the alloy 3103. In other words, large

grains have an inherent tendency for deformation heterogeneity leading to deformation bands and other inhomogeneties (see Section 5.2.2), while smaller grains deform more uniformly.

Secondly and most importantly, Figs 4.67–4.68 show very fine grains along the interface. While grains on either side of the interface had relatively less grain refinement, grains obtained at the interface were ultra-fine (see Fig 4.70). This is believed to be an effect of different flow stress and strain hardening properties of the two materials. Another difference between Al/Al and the current Al/3103 composite is that the former showed good bonding (under optimal conditions) resulting in almost no interface, while the latter composite had a discontinuous interface similar to that observed by Vaidyanath et al. in their study on rolling [253]. Also the latter authors attributed the appearance of a discontinuous interface to the difference in work hardening parameters. The characteristics of the brittle layer formed on top of the rough surface depend on the work hardened layer produce during surface preparation. Different work hardening behaviours could lead to varying layer properties, thus leaving local discontinuities after ECAP. In fact, this could be observed as some interface regions had local prevailing discontinuities (Fig 4.71).

These investigations were conducted to simplify the interface structure and to understand the interface evolution when two different materials were ECAP'ed under constant operating conditions. It is considered useful to correlate the interface evolution with regard to the macrocomposite. For instance, the interface characteristics of dissimilar sheets can be used for understanding the streak of fine grains observed in the ECAP'ed macrocomposite (see Fig 4.44). Two events might probably have occurred during ECAP. First, partial recrystallization could occur at the interface leading to a nucleation of fine grains. A similar mechanism has been observed by others [253, 332, 333]. Secondly, it is possible that different work hardening parameters can lead to break-up of brittle phases into fine fragments, as actually observed in the present Al/3103 sheet composite.

Also, the three point bending tests revealed that the interface of the Al/3103 composite withstood high stress (~170 MPa) at about 157° bending of the sample without failing. The black lines in Fig 4.73 indicate the effect of severe

compressive stresses being present during bending. This showed that the Al/3103 sheet composite could be fabricated with good bonds between the two different materials. In addition, the microhardness measurements show that the material became stronger after ECAP.

In summary, the primary aim of processing the Al/3103 composite was to reveal important effects of involving different materials, e.g. regarding the microstructural behaviour and the formation of fine grains at the interfacial regions.

Chapter 6: Future scope: Applications and Challenges

6.1 Introduction

The results and discussion of the different materials (CP Al, bi-metal and sheet composites) in the present study, not only demonstrate the potential application of the techniques and materials for various purposes, but also acknowledge the need for more investigations and understanding of underlying mechanisms that are necessary for processing more robust advanced Al/Mg bi-metal materials. Some of the possible applications and the challenges of the different materials and processes are treated in the following paragraphs.

6.2 ECAP of pure aluminium billets

Investigations on pure aluminium are directed towards understanding the behaviour of Al with regard to a combination of temperature and large strain deformation. Firstly, the discussion reveals that even though, pure Al is susceptible to significant thermal effects on plasticity during high temperature processing, it is possible to refine grains from the as-cast state significantly up to 250°C. The mechanisms in the microstructure evolution change significantly first at 350°C. This is an important observation as most of the ECAP processing involving Al alloys and Al based composites are carried out at RT. Hence, the present study indicates that high temperature processing up to 250°C can retain acceptable mechanical properties. Also, when processing alloys, the additional solute effect and precipitation could lead to even finer grains after ECAP at 250°C. Secondly, for the initial two ECAP passes, the effect of temperature on the microstructure is minimal, leading to the conclusion that Al based materials can be pre-treated with ECAP at a high temperature (T/Tm~0.7) before further processing. Finally, a good combination of strength and ductility can be achieved with high fractions of small equiaxed grains [6]. From the observations in this study, although the grain structure is much finer at RT, grains are relatively fine, more equiaxed and the fraction of HAGBs is high at 250°C as compared to RT processing. Hence, it is

suggested to firstly achieve fine grains at 250°C before processing at RT and thereby obtain better properties than that achieved by RT processing alone.

In order to understand the behaviour of pure Al at high temperatures with respect to strain and temperature, some further investigations are to be made. For example, the effect of temperature on the mechanical properties with increasing temperature and strain should be studied. As explained in Chapter 5, the effect of impurities on the microstructure evolution of pure Al with respect to strain and temperature is not fully understood. Also, in the present study, the effect of temperature on the microstructure has not been revealed for strains >8. It would be interesting to see whether the microstructure evolution saturates or changes after 8 passes and increasing temperature. Also, the effect of initial grain size upon increasing strain at different temperatures should be investigated as the initial large grains are influencing the initial microstructure evolution up to T = 350°C.

6.3 ECAP of Al/Mg bi-metal

The Al/AZ31 rod type bi-metal investigations reveal the potential for processing the hard-to-deform AZ31 material by encasing it with a more deformable material. Although a similar configuration has been demonstrated previously [226], ECAP processing of such a configuration can only lead to better properties if grain refinement is achieved. However, the present rod type reinforcement leads to interfacial shear displacements at the interface (see Chapter 5) and hence, a flat interface geometry is suggested for better properties since the interface deformation then would involve compressive stresses and reduce interface displacements.

Anyway, the Al/Mg macrocomposite is the most interesting of all the materials studied herein. A high strength along with reasonable ductility has been demonstrated (Chapter 5). In order to illustrate the potential of this new genre of materials, an empirical model based on the various material characteristics is put forth in the following.

The yield strength of the Al/Mg macrocomposite (σ_{MC}) can initially be expressed as,

$$\sigma_{MC} = V_{f(Al)} \cdot \sigma_{Al} + \Delta\sigma_{INT} \quad (6.1)$$

where, σ_{Al} and $V_{f(Al)}$ represent the yield stress and the volume fraction of pure Al respectively, and $\Delta\sigma_{INT}$ is the additional strengthening due to the interface effects. For the present case, $V_{f(Al)} \cong 0.97$ was obtained from volume fraction calculations by analysing area fractions in different planes and taking σ_{MC} = 275 MPa. Further, as explained before (Chapter 4), Al contains about 3 wt% of dissolved Mg (mean value) locally. Furukawa et al. [334] developed an equation for microhardness versus grain sizes for an Al-3Mg alloy processed by ECAP (HV = 46 + $35d^{-0.5}$), where d is the mean grain size. Accordingly, the yield strength of an Al-3Mg alloy after 1 pass at RT was ~240 MPa [329]. Substituting these values into equation (6.1), this gives $\Delta\sigma_{INT} \cong$ 35MPa. The $\Delta\sigma_{INT}$ value can be expressed as the sum of the effect of strengthening by the interface regions and can be expressed as follows:

$$\Delta\sigma_{INT} = (1 - V_{f(Al)}) \cdot K_{IF3+IF4} \quad (6.2)$$

Here, $K_{IF3+IF4}$ represents a combined strengthening effect of interfaces labelled, IF3 and IF4. Li et al. [335] studied the interface strengthening ability in Cu/Al multilayers and showed that an increasing lattice mismatch increased the interface strengthening ability (analogous to $K_{IF3+IF4}$). From their report, $K_{IF3+IF4}$ can be expressed as,

$$K_{IF3+IF4} = \kappa \cdot \lambda^{-\frac{1}{2}} \quad (6.3)$$

$$\kappa = \eta\mu\sqrt{b(\delta - \varepsilon)} \quad (6.4)$$

Here, λ is the interface layer thickness; η is a constant independent of the material, μ represents the shear modulus of the matrix and b, δ and ε represent the

Burger's vector, lattice misfit and misfit strain respectively. Hence, $\Delta\sigma_{INT}$ can be rewritten as,

$$\Delta\sigma_{INT} = (1 - V_{f(Al)}) \cdot \eta\mu\sqrt{b(\delta - \varepsilon)} \cdot \lambda^{-\frac{1}{2}} \quad (6.5)$$

The above equation shows that $\Delta\sigma_{INT} \propto \lambda^{-\frac{1}{2}}$. Hence, equation (6.1) can be written as,

$$\sigma_{MC} = V_{f(Al)} \cdot \sigma_{Al} + (1 - V_{f(Al)}) \cdot c \cdot \lambda^{-\frac{1}{2}} \quad (6.6)$$

Here, *c* is constant.

It is to be noted that the effect of interface regions observed in the finally processed macrocomposite is different from that obtained in the as-screw extruded composite. In the as-screw extruded condition, interface regions lead to a local strengthening lattice and an elastic mismatch, resulting in a change in the forces acting on the glissile dislocations in regions close to interfaces [336, 337]. The effect of such an interface configuration is explained above ($K_{IF3+IF4}$). However after ECAP, though these effects still remain in effect, the configuration of the interfaces is different from the as-screw extruded condition. In case of the ECAP'ed material, IF3 and IF4 are thin, long and discontinuous. This means that the presence of intermetallic interfaces act as reinforcements. Hence, $\Delta\sigma_{INT}$ can be modified to,

$$\Delta\sigma_{INT} = x \cdot c \cdot \lambda^{-\frac{1}{2}} + (1 - x) \cdot \Delta\sigma_{DH} \quad (6.7)$$

Here, $\Delta\sigma_{DH}$ corresponds to the effect of intermetallics acting as dispersoids and *x* represents the fraction of the interfaces that are continuous, i.e. planar and long interfaces. Strain accommodation by dislocation storage is believed to be accelerated due to the reinforcing effect of the intermetallic particles (i.e. discontinuous interfaces). This can be understood from the obtained yield strength of the cold-rolled ECAP sample (~400 MPa). The yield strength increases about 1.5 times for the ECAP + cold-rolled sample (CR) as compared to the ECAP'ed macrocomposite. This is believed to be due to the break-down of long streaks of interfaces into smaller dispersoids, thus resulting in a more homogeneous

distribution of intermetallics dispersed in the Al matrix containing dissolved magnesium. Hence, with increasing cold deformation, the first term in Eqn (6.7) disappears (assuming that almost all interface regions are broken down into tiny fragments) and the second term becomes more important. Hence Eqn (6.6) could be re-written for the final cold-rolled condition as,

$$\sigma_{MC\,CR} = V_{f(Al)} \cdot \sigma_{Al} + \Delta\sigma_{DH} \tag{6.8}$$

The CR sample exhibited a yield strength of about 395 MPa. Substituting $V_{f(Al)} \cong 0.97$, $\sigma_{MC\,CR}$ = 395 MPa, $\sigma_{Al} = 330$ MPa [329], this gives $\Delta\sigma_{DH}$ ~65 MPa. Now, $\Delta\sigma_{DH}$ is an effect of the small plate-like dispersoids. Hence, in order to achieve a strength of $\Delta\sigma_{DH} = 65$ MPa, and using Orowan's equation for dispersion hardening [338-340], the size of the intermetallic particles are ~20 nm for equiaxed particles.

However, it is logical to assume that although the intermetallic interfaces are broken down to fragments, reduction to a size of ~20 nm is probably difficult in this material. In addition, some POMs show that large particles as big as ~20 μm could be present. Also, some continuous sections still remained unbroken. The present structure cannot be assumed to be plate-like structures as the width of these particles would be very large (few hundreds of microns) as compared to the thickness (less than 1 μm). Hence, the additional stress ($\Delta\sigma_{DH}$) is believed to contain additional hardening contributions probably due to increased dislocation densities and grain boundary segregation of Mg. Several works have reported such strong segregation characteristics of Mg in Al alloys after ECAP along the non-equilibrium grain boundaries, e.g. changing the excess energy of the grain boundaries [330, 331, 336, 340-345]. This is in addition to the fact that Al alloys containing high Mg solute contents, show excess segregation along grain boundaries [346, 347]. As a result of segregation, dislocation mechanics is changed resulting in a high required stress for dislocations to go past the obstacles, thus increasing the yield strength.

In Al-Mg alloys solid solution and grain boundary strengthening are predominant mechanisms, while in the present macrocomposite additional hardening comes from the presence of interface intermetallics. If the interface structures are not completely broken down into tiny fragments, as is the case in the present material, further strengthening by resisting slip transmission across the interfaces occurs. Also, very fine grains formed at the interface boundaries contribute to the strengthening. Thus the additional stress components $(\Delta\sigma_{INT})$ and $(\Delta\sigma_{DH})$ can be replaced with a single term representing total additional stress $(\Delta\sigma_{tot})$:

$$(\Delta\sigma_{tot}) = x \cdot c \cdot \lambda^{-\frac{1}{2}} + (1-x) \cdot \Delta\sigma_{DH} + \Delta\sigma_{GB} + \Delta\sigma_{R} \qquad (6.9)$$

In Eqn (6.9), the first term refers to interface strengthening, the second term is strengthening due to the fragments of interfaces broken down to dispersoids during cold working, the third term $(\Delta\sigma_{GB})$ refers to strengthening by grain boundary segregation and the last term, $(\Delta\sigma_{R})$, represents strengthening by fine grains formed at the interface boundaries. With regard to Eqn (6.9), Eqn (6.6) can now be re-written as,

$$\sigma_{MC} = V_{f(Al)} \cdot \sigma_{Al} + x \cdot c \cdot \lambda^{-\frac{1}{2}} + (1-x) \cdot \Delta\sigma_{DH} + \Delta\sigma_{GB} + \Delta\sigma_{R} \qquad (6.10)$$

This equation represents the total strength achieved by the Al/Mg macrocomposite containing intermetallic interfaces. In order to validate the equation, more analysis of microstructures are required in order to identify different components and their contributions.

Figure 6.1 shows yield strength as function of strain. Data for other Al-Mg alloys were obtained from literature [169, 297, 320, 329]. It should be remarked that values obtained for the present macrocomposite are subject to discretion.

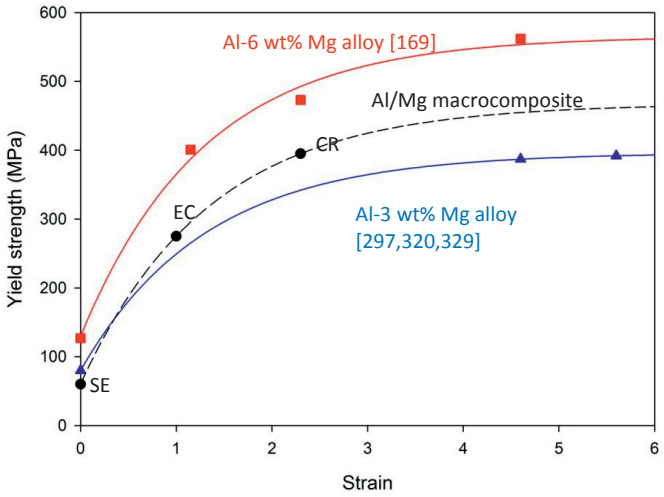

Figure 6.1. Yield strength as function of von Mises strain for different Al-Mg alloys compared to the present macrocomposite containing 5 wt% alloy AZ31.

The initial yield strength (marked SE in Fig 6.1) corresponds to the yield strength of the as-screw extruded condition, and EC refers to the yield strength of the ECAP'ed condition at 200°C and CR refers to the yield strength of the finally cold-rolled material at RT.

The strength of the present Al/Mg macrocomposite is most probably "underestimated" as the processing involved different temperatures, i.e. for screw extrusion, ECAP and cold-rolling. However, considering the negative effect of the elevated temperatures applied here, lower processing temperatures would probably increase the strength. For instance, ECAP could probably be conducted at a lower temperature. Also, it would be valuable to conduct separate ECAP experiments on the macrocomposite to different accumulated strains in order to understand the precise effect of strain on yield strength. However, the curve clearly shows that the macrocomposite has higher strength than the Al-Mg alloy counterparts with similar composition. Also, processing the Al/5 wt% Mg macrocomposite containing less than 5 wt% Mg content is easier than processing a conventional solid solution Al-5 wt% Mg alloy.

The above preliminary physical modelling shows that additional strengthening parameters, for e.g. dispersion hardening from intermetallic particles, possible grain boundary segregation of Mg, enhanced dislocation accumulation due to interactions with intermetallics and Mg solid solution strengthening are probably responsible for the high strength achieved.

Consequently, this new concept involving mechanical alloying may introduce a new avenue of interest in fabrication, analysis, modification and development of materials processed by severe deformation.

6.4 Sheet composites

The above discussion on the different sheet composites (Al/Al and Al/3103 composites) was focussed on understanding the experimental and material behaviour on the evolution of bonding during ECAP. Although, different experimental parameters were investigated in Al/Al sheet composites, the effect of stacking was lacking. In other words, the effect of different number of sheets stacked together and the direction in which they were stacked were not studied. Such kind of investigations could reveal important implications on strength and microstructure. For instance, layering sheets only a few microns thick would mean several thin sheets stacked on top of each other. Processing of such a configuration after, for instance anodising, would result in more oxides at the bonding surfaces, thus making the entire composite reinforced with alternate layers of alumina enhancing the mechanical properties. Similarly, using stronger material in-between alternate sheets would result in very fine grains at interfaces during deformation. For instance, replacing the AA3103 alloy with a relatively stronger light material such as Ti, would probably produce enhanced grain refinement at the Al/Ti interface along with a good bonding.

Some suggestions for future work have been given above. However, the present study being relatively new and novel, will have numerous additional opportunities to explore and the scope of such investigations is wide open owing to the very limited literature existing on such materials (Al/Mg bi-metals and Al based sheet composites) subjected to severe plastic deformation.

Chapter 7 Conclusions

The main conclusive comments from the present study can be summarized as follows:

- The effects of deformation temperature (RT, 150°C, 250°C and 350°C) and accumulated strain on the microstructure evolution of commercial pure aluminium (CP Al) processed up to 8 passes by ECAP route Bc were investigated. During the first two passes, there was no significant effect of temperature. With increasing strain, influence of recovery increased with increasing temperature.
- Microstructure evolution in CP Al was dominated by the formation of GNBs, accommodating a significant portion of the excess strain up to four passes at all processing temperatures. Further straining led to progressive dislocation accumulation and rotation of SSDs into HAGBs for samples deformed at RT, while recovery occurred at higher temperatures (up to 250°C). For samples deformed at 350°C, onset of recovery was triggered even during the initial passes. The microstructure evolved as a result of balancing GNB evolution and recovery.
- In CP Al, there was significant grain refinement in all samples at all processing temperatures. The mean grain size decreased with increasing strain but increased with increasing temperature. ECAP at RT showed the highest grain refinement, to ~700 nm, and processing at 350°C gave the least refinement, to ~120 μm after 8 passes. Also, samples processed up to 250°C showed a homogeneous grain structure but at 350°C the microstructure became very inhomogeneous. This was attributed to differences in their evolution mechanisms.
- For CP Al, stored energy calculations and texture analysis corresponded to the explanations discussed in regard to various microstructure evolutions with increasing strain and temperature. Interestingly, samples deformed at 350°C seemed to undergo static recrystallization after 6 passes ECAP.
- The CP Al investigations suggested that pure aluminium can be significantly refined, down to ~5 μm after 8 passes at 250°C. This gave insight into the

possibility of deforming at higher temperatures without compromising grain refinement and at the same time reducing the force required to press hard-to-deform bi-metals containing aluminium as a component.

- The studies on Al/AZ31 bi-metal were divided into two parts. The first part involved processing a rod type (core-shell) material, i.e. to understand the bonding characteristics of the Al/Mg combination. The second part dealt with fabrication trials of a high strength Al/AZ31 Mg alloy macrocomposite for structural applications.
- The investigations on Al/AZ31 bi-metal showed that it was difficult to ECAP the as-cast AZ31 Mg alloy at T<350°C due to premature cracking, even if encased with pure aluminium. However, the Al/AZ31 bi-metal was successfully fabricated at 350°C and was further investigated as to interface characteristics with increasing ECAP strain up to ~6 by route Bc.
- The interfaces formed in the Al/AZ31 bimetal consisted of two regions, namely, the IF1 made of a $Mg_{17}Al_{12}$ intermetallic and the IF2 constituted by an Al_3Mg_2 intermetallic.
- The tensile test results of the Al/AZ31 bi-metal showed that the yield strength was predominantly dependent on the weaker shell (pure Al). Hence, it was concluded that a single and thick brittle interface would be detrimental to the idea of achieving high strength and therefore a multi-interfaced structure was suggested to be more promising.
- An Al/Mg macrocomposite was then fabricated by a combination of hot screw extrusion and ECAP processing using pure Al chips and 5 wt% AZ31 alloy chips. The ECAP'ed material showed relatively high yield strength ~275 MPa. The high strength was attributed to the presence of a different interface-matrix configuration as compared to that of the initial material in the as-screw extruded condition. In addition, the dissolution of Mg in Al was also observed. A mechanism responsible for formation of the characteristic interface configuration was also discussed.
- The ECAP'ed macrocomposite was subsequently cold-rolled in order to demonstrate the potential of a new genre of Al/Mg composites prepared by

screw extrusion and ECAP. The yield strength of the cold-rolled material increased substantially (~400 MPa) as compared to the ECAP'ed condition. The high yield strength in the cold-rolled state was attributed to the role of interfaces, here acting as non-shearable particles after being broken down into smaller fragments, combined with other microstructural effects such as grain boundary segregation, solid solution strengthening and grain refinement. The strength was then compared to literature data on similar Al-Mg compositions. It was concluded that cold rolling after ECAP was superior to the corresponding conventional binary Al-Mg alloys as to mechanical strength.

- Finally, sheet composites were fabricated in order to simplify and understand the experimental and material characteristics of interfaces during ECAP. Here, Al/Al sheets were used to investigate the effect of experimental parameters. Effects of specimen length, back pressure, pressing speed and surface treatment on the interface characteristics were established.
- The ECAP'ed Al/Al sheet composite revealed that surface treatment of the sheets before ECAP was very critical and only machine brushed samples achieved satisfactory bonding. Also, back pressure was very vital to achieve bonding. It was further concluded that the specimen should be at least 70 mm long to achieve sufficient hydrostatic pressure for bonding. Pressing speeds less than 5 mm/s proved to be detrimental for bonding.
- Finally, investigations on an Al/AA3103 sheet composite showed that when materials with two different strain hardening behaviours were ECAP'ed, fine grains evolved at the interfaces.

References

[1] European Aluminium. Association (EAA), Aluminium in cars unlocking the light-weighting potential, Brussels, 2012.

[2] J. Cui, PhD thesis, Department of Materials Science and Engineering, Norwegian University of Science and Technology, Trondheim, 2011, pp.1- 208.

[3] R. Feynman, in: Annual meeting, American Physical Society, Caltech, "There is plenty of room at the bottom",December 29th 1959.

[4] V.M. Segal, V.I. Reznikov, A.E. Drobyshevskiy, V.I. Kopylov, Russ. Metall., (1981) 99-105.

[5] NanoSPD, www.nanospd.org, 2002.

[6] R.Z. Valiev, T.G. Langdon, Prog. Mater. Sci., 51 (2006) 881-981.

[7] M. Furukawa, Y. Iwahashi, Z. Horita, M. Nemoto, T.G. Langdon, Mater. Sci. Eng. A-Struct. Mater. Prop. Microstruct. Process., 257 (1998) 328-332.

[8] Y. Iwahashi, J.T. Wang, Z. Horita, M. Nemoto, T.G. Langdon, Scr. Mater., 35 (1996) 143-146.

[9] K. Furuno, H. Akamatsu, K. Oh-ishi, M. Furukawa, Z. Horita, T.G. Langdon, Acta Mater., 52 (2004) 2497-2507.

[10] D. Yamaguchi, Z. Horita, M. Nemoto, T.G. Langdon, Scr. Mater., 41 (1999) 791-796.

[11] P.B. Berbon, M. Furukawa, Z. Horita, M. Nemoto, T.G. Langdon, Metall. Mater. Trans. A, 30 (1999) 1989-1997.

[12] K. Nakashima, Z. Horita, M. Nemoto, T.G. Langdon, Mater. Sci. Eng. A-Struct. Mater. Prop. Microstruct. Process., 281 (2000) 82-87.

[13] Y. Iwahashi, Z. Horita, M. Nemoto, T.G. Langdon, Acta Mater., 46 (1998) 3317-3331.

[14] K. Xia, X. Wu, Scr. Mater., 53 (2005) 1225-1229.

[15] R.Z. Valiev, I.V. Alexandrov, Y.T. Zhu, T.C. Lowe, J. Mater. Res., 17 (2002) 5-8.

[16] P.W.J. McKenzie, R. Lapovok, Y. Estrin, Acta Mater., 55 (2007) 2985-2993.

[17] R. Lapovok, Y. Estrin, J. Mater. Sci., 40 (2005) 341-346.

[18] R.Z. Valiev, R.K. Islamgaliev, I.V. Alexandrov, Prog. Mater. Sci., 45 (2000) 103-189.
[19] Y. Iwahashi, Z. Horita, M. Nemoto, T.G. Langdon, Metall. Mater. Trans. A, 29 (1998) 2503-2510.
[20] U. Chakkingal, A.B. Suriadi, P.F. Thomson, Scr. Mater., 39 (1998) 677-684.
[21] J.C. Werenskiold, PhD Thesis, Department of Materials science and Engineering, Norwegian University of Science and Technology (NTNU), Trondheim, 2004, pp. 1-262.
[22] K. Neishi, Z. Horita, T.G. Langdon, Mater. Sci. Eng. A-Struct. Mater. Prop. Microstruct. Process., 325 (2002) 54-58.
[23] Y. Zhang, J.Q. Liu, J.T. Wang, Z.B. Wu, F. Liu, Microstructures and Mechanical Properties of fcc Pure Metals with Different Stacking Fault Energies by Equal Channel Angular Pressing, in: J.T. Wang (Ed.) Nanomaterials and Plastic Deformation, 2011, pp. 193-203.
[24] Y. Zhang, J.Q. Liu, J.T. Wang, Z.B. Wu, F. Liu, TMS annual meeting, Influence of Stacking Fault Energy on microstructures and mechanical properties of fcc pure metals by equal channel angular pressing, 2010.
[25] Z. Horita, T. Fujinami, M. Nemoto, T.G. Langdon, Metall. Mater. Trans. A, 31 (2000) 691-701.
[26] Y.M. Wang, M.W. Chen, F.H. Zhou, E. Ma, Nature, 419 (2002) 912-915.
[27] J.K. Kim, H.G. Jeong, S.I. Hong, Y.S. Kim, W.J. Kim, Scr. Mater., 45 (2001) 901-907.
[28] W.J. Kim, C.S. Chung, D.S. Ma, S.I. Hong, H.K. Kim, Scr. Mater., 49 (2003) 333-338.
[29] I.J. Beyerlein, S. Li, D.J. Alexander, C.T. Necker, C.N. Tome, M.A. Bourke, Heterogeneity in texture development in single pass equal channel angular extrusion in: Zhu, Y. T., Langdon, T. G., Valiev, R.Z. (Eds.) UFG Materials III Symposium, Charlotte, USA, 2004.
[30] A.A. Gazder, S. Li, F.H. Dalla Torre, I.J. Beyerlein, C.F. Gu, C.H.J. Davies, E.V. Pereloma, Mater. Sci. Eng. A-Struct. Mater. Prop. Microstruct. Process., 437 (2006) 259-267.

[31] S. Li, I.J. Beyerlein, M.A.M. Bourke, Mater. Sci. Eng. A-Struct. Mater. Prop. Microstruct. Process., 394 (2005) 66-77.
[32] W.T. Read, W. Shockley, Physical Review, 78 (1950) 275.
[33] W.Q. Cao, A. Godfrey, Q. Liu, Mater. Sci. Eng. A-Struct. Mater. Prop. Microstruct. Process., 361 (2003) 9-14.
[34] H.W. Hoppel, L. May, M. Prell, M. Goken, Int. J. Fatigue, 33 (2011) 10-18.
[35] V.M. Segal, Mater. Sci. Eng. A-Struct. Mater. Prop. Microstruct. Process., 197 (1995) 157-164.
[36] I.J. Beyerlein, L.S. Toth, Prog. Mater. Sci., 54 (2009) 427-510.
[37] A. Gholinia, P. Bate, P.B. Prangnell, Acta Mater., 50 (2002) 2121-2136.
[38] D.A. Hughes, R.A. Lebensohn, H.R. Wenk, A. Kumar, Proceedings of the Royal Society of London. Series A: Mathematical, Physical and Engineering Sciences, 456 (2000) 921-953.
[39] Q. Xue, I.J. Beyerlein, D.J. Alexander, G.T. Gray, Acta Mater., 55 (2007) 655-668.
[40] S. Li, Acta Mater., 56 (2008) 1031-1043.
[41] S.C. Vogel, D.J. Alexander, I.J. Beyerlein, M.A.M. Bourke, D.W. Brown, B. Clausen, C.N. Tome, R.B. Von Dreele, C. Xu, T.G. Langdon, Investigation of texture in ECAP materials using neutron diffraction, in: Chandra, T. Torralba J. M. Sakai T. (Ed.) Thermec'2003, Pts 1-5, 2003, pp. 2661-2666.
[42] G.G. Yapici, I. Karaman, Mater. Sci. Eng. A-Struct. Mater. Prop. Microstruct. Process., 503 (2009) 78-81.
[43] S.H. Yu, H.S. Ryoo, D.H. Shin, S.K. Hwang, Texture evolution in Zr grain-refined by equal channel angular pressing, in: R.B. Schwarz, G. Ceder, S.A. Ringel (Eds.), Materials for Energy Storage, Generation and Transport, 2002, pp. 143-148.
[44] S.R. Agnew, P. Mehrotra, T.M. Lillo, G.M. Stoica, P.K. Liaw, Acta Mater., 53 (2005) 3135-3146.
[45] W.J. Kim, S.I. Hong, Y.S. Kim, S.H. Min, H.T. Jeong, J.D. Lee, Acta Mater., 51 (2003) 3293-3307.
[46] T. Liu, Y.D. Wang, S.D. Wu, R. Lin Peng, C.X. Huang, C.B. Jiang, S.X. Li, Scr. Mater., 51 (2004) 1057-1061.

[47] S.R. Agnew, P. Mehrotra, T.M. Lillo, G.M. Stoica, P.K. Liaw, Mater. Sci. Eng. A-Struct. Mater. Prop. Microstruct. Process., , 408 (2005) 72-78.
[48] G.G. Yapici, I. Karaman, Z.-P. Luo, Acta Mater., 54 (2006) 3755-3771.
[49] D.H. Shin, I. Kim, J. Kim, Y.S. Kim, S.L. Semiatin, Acta Mater., 51 (2003) 983-996.
[50] G.C. Kaschner, C.N. Tomé, I.J. Beyerlein, S.C. Vogel, D.W. Brown, R.J. McCabe, Acta Mater., 54 (2006) 2887-2896.
[51] R. Lapovok, P.F. Thomson, R. Cottam, Y. Estrin, J. Mater. Sci., 40 (2005) 1699-1708.
[52] S.Y. Li, D.J. Alexander, I.J. Beyerlein, D.W. Brown, Texture ewvolution during multi-pass equal channel angular extrusion of beryllium in: A.D. Rollett (Ed.) Materials Processing and Texture, Amer Ceramic Soc, Westerville, 2009, pp. 563-569.
[53] I.J. Beyerlein, R.D. Field, K.T. Hartwig, C.T. Necker, J. Mater. Sci., 43 (2008) 7465-7473.
[54] S. Li, I.J. Beyerlein, D.J. Alexander, S.C. Vogel, Scr. Mater., 52 (2005) 1099-1104.
[55] E.A. El-Danaf, Mater. Sci. Eng. A-Struct. Mater. Prop. Microstruct. Process., 492 (2008) 141-152.
[56] T. Hanlon, Y.N. Kwon, S. Suresh, Scr. Mater., 49 (2003) 675-680.
[57] H. Mughrabi, H.W. Hoppel, M. Kautz, Scr. Mater., 51 (2004) 807-812.
[58] S.R. Agnew, J.R. Weertman, Mater. Sci. Eng. A-Struct. Mater. Prop. Microstruct. Process., 244 (1998) 145-153.
[59] A. Vinogradov, S. Hashimoto, Materials Transactions Jim, 42 (2001) 74-84.
[60] A.Y. Vinogradov, V.V. Stolyarov, S. Hashimoto, R.Z. Valiev, Mater. Sci. Eng. A-Struct. Mater. Prop. Microstruct. Process., 318 (2001) 163-173.
[61] S. Hashimoto, Y. Kaneko, K. Kitagawa, A. Vinogradov, R.Z. Valiev, Materials Science Forum, 312 (1999) 593-598.
[62] A. Vinogradov, S. Hashimoto, Advanced Engineering Materials, 5 (2003) 351-358.
[63] A. Vinogradov, Scr. Mater., 39 (1998) 797-805.

[64] H.W. Höppel, Z.M. Zhou, H. Mughrabi, R.Z. Valiev, Philosophical Magazine A, 82 (2002) 1781-1794.
[65] A. Vinogradov, S. Nagasaki, V. Patlan, K. Kitagawa, M. Kawazoe, Nanostructured Materials, 11 (1999) 925-934.
[66] C.H.M. Jenkins, Journal of Institute of Metals, 40 (1928).
[67] G. Davies, J. Edington, C. Cutler, K. Padmanabhan, J. Mater. Sci., 5 (1970) 1091-1102.
[68] D.H. Avery, W.A. Backofen, ASM Transactions Quarterly, 58 (1965) p. 551.
[69] D.H. Avery, W.A. Backofen, Journal of Metals, 17 (1965) p. 1017.
[70] S.W. Zehr, W.A. Backofen, ASM Transactions Quarterly, 61 (1968) p. 300.
[71] D.L. Holt, W.A. Backofen, ASM Transactions Quarterly, 59 (1966) p. 755.
[72] A.H. Chokshi, A.K. Mukherjee, T.G. Langdon, Materials Science and Engineering: R: Reports, 10 (1993) 237-274.
[73] T.G. Langdon, Acta Metall. et Materialia, 42 (1994) 2437-2443.
[74] T.G. Langdon, Mater. Sci. Eng. A-Struct. Mater. Prop. Microstruct. Process., 174 (1994) 225-230.
[75] R.B. Figueiredo, M. Kawasaki, T.G. Langdon, Developing Superplasticity in Metallic Alloys through the Application of Severe Plastic Deformation, in: M. Cabibbo, S. Spigarelli (Eds.) Recent Developments in the Processing and Applications of Structural Metals and Alloys, Materials Science Forum, 2009, pp. 97-111.
[76] N. Bay, Cold pressure welding – the mechanisms governing bonding, Journal of Engineering for Industry, Vol. 101, No. 2, 05.1979, p. 121-127.
[77] C. Xu, M. Furukawa, Z. Horita, T.G. Langdon, Developing a superplastic forming capability in nanometals, in: K.J. Kurzydlowski, Z. Pakiela (Eds.) Bulk and Graded Nanometals, 2005, pp. 23-30.
[78] R.Z. Valiev, A.V. Korznikov, R.R. Mulyukov, Mater. Sci. Eng. A-Struct. Mater. Prop. Microstruct. Process., 168 (1993) 141-148.
[79] R.Z. Valiev, D.A. Salimonenko, N.K. Tsenev, P.B. Berbon, T.G. Langdon, Scr. Mater., 37 (1997) 1945-1950.
[80] C. Xu, M. Furukawa, Z. Horita, T.G. Langdon, Acta Mater., 51 (2003) 6139-6149.

[81] R.K. Islamgaliev, N.F. Yunusova, R.Z. Valiev, N.K. Tsenev, V.N. Perevezentsev, T.G. Langdon, Scr. Mater., 49 (2003) 467-472.
[82] A. Yamashita, Z. Horita, T.G. Langdon, Mater. Sci. Eng. A-Struct. Mater. Prop. Microstruct. Process., 300 (2001) 142-147.
[83] Z. Horita, K. Matsubara, K. Makii, T.G. Langdon, Scr. Mater., 47 (2002) 255-260.
[84] M. Geetha, A.K. Singh, R. Asokamani, A.K. Gogia, Prog. Mater. Sci., 54 (2009) 397-425.
[85] J.-W. Park, Y.-J. Kim, C.H. Park, D.-H. Lee, Y.G. Ko, J.-H. Jang, C.S. Lee, Acta Biomaterialia, 5 (2009) 3272-3280.
[86] M. Nakai, M. Niinomi, X. Zhao, X. Zhao, Materials Letters, 65 (2011) 688-690.
[87] V.G. Pushin, D.V. Gunderov, N.I. Kourov, L.I. Yurchenko, E.A. Prokofiev, V.V. Stolyarov, Y.T. Zhu, R.Z. Valiev in: Zhu, Y. T., Langdon, T. G., Valiev, R.Z. (Eds.), UFG Materials III Symposium, Charlotte, USA, 2004, pp. 481-486.
[88] V.V. Stolyarov, E.A. Prokof'ev, S.D. Prokoshkin, S.B. Dobatkin, I.B. Trubitsyna, I.Y. Khmelevskaya, V.G. Pushin, R.Z. Valiev, Physics of Metals and Metallography, 100 (2005) 608-618.
[89] I. Tereshina, E. Tereshina, G. Burkhanov, S. Dobatkin, Hysteresis Magnetic Properties of Nd-Ho-Fe-Co-B Alloys after Intense Plastic Deformation, in: J.T. Wang, R.B. Figueiredo, T.G. Langdon (Eds.), Nanomaterials by Severe Plastic Deformation: Nanospd5, Parts 1 and 2, Materials Science Forum, 2011, pp. 1065-1070.
[90] K. Suehiro, S. Nishimura, Z. Horita, Mater. Trans., 49 (2008) 102-106.
[91] A. Cabibbo, E. Evangelista, C. Scalabroni, Micron, 36 (2005) 401-414.
[92] M. Cabibbo, W. Blum, E. Evangelista, M.E. Kassner, M.A. Meyers, Metall. Mater. Trans. A, 39A (2008) 181-189.
[93] M. Furukawa, Z. Horita, M. Nemoto, T.G. Langdon, Microstructural evolution in pure aluminum during equal-channel angular pressing in: Taleff, E. M., Mahidhara, R. K. (Eds.), Modeling the Mechanical Response of Structural Materials, 1998.

[94] M. Hoseini, M. Meratian, M.R. Toroghinejad, J.A. Szpunar, Materials Characterization, 61 (2010) 1371-1378.
[95] T.R. McNelley, D.L. Swisher, Z. Horita, T.G. Langdon, Influence of processing route on microstructure and grain boundary development during equal-channel angular pressing of pure aluminum in: Zhu, Y. T., Langdon, T. G., Mishra, R. S. et al. (Eds.), UFG Materials II Symposium, 2002.
[96] M. Saravanan, R.M. Pillai, B.C. Pai, M. Brahmakumar, K.R. Ravi, Bulletin of Materials Science, 29 (2006) 679-684.
[97] A.D. Shan, I.G. Moon, H.S. Ko, J.W. Park, Scr. Mater., 41 (1999) 353-357.
[98] C. Xu, M. Furukawa, Z. Horita, T.G. Langdon, The deformation characteristics of pure aluminum processed by equal-channel angular pressing in: Zhu, Y. T., Varyukhin, V.(Eds.) Nanostructured Materials by High-Pressure Severe Plastic Deformation, 2006.
[99] C. Xu, K. Xia, T.G. Langdon, Acta Mater., 55 (2007) 2351-2360.
[100] G. Zhao, S. Xu, Y. Luan, Y. Guan, N. Lun, X. Ren, Mater. Sci. Eng. A-Struct. Mater. Prop. Microstruct. Process., 437 (2006) 281-292.
[101] Y. Iwahashi, Z. Horita, M. Nemoto, T.G. Langdon, Acta Mater., 45 (1997) 4733-4741.
[102] W. Skrotzki, N. Scheerbaum, C.G. Oertel, H.G. Brokmeier, S. Suwas, L.S. Tóth, Acta Mater., 55 (2007) 2211-2218.
[103] Z. Horita, K. Kishikawa, K. Kimura, K. Tatsumi, T.G. Langdon, Grain refinement of high-purity FCC metals using equal-channel angular pressing, in: Kang, S. J. L. , M.Y. Huh, N.M. Hwang, H. Homma, K. Ushioda, Y. Ikuhara (Eds.), Recrystallization and Grain Growth III, Parts 1 and 2, Materials Science Forum, 2007, pp. 1273-1278.
[104] Y.J. Chen, Y.C. Chai, H.J. Roven, S.S. Gireesh, Y.D. Yu, J. Hjelen, Mater. Sci. Eng. A-Struct. Mater. Prop. Microstruct. Process., 545 (2012) 139-147.
[105] Y.J. Chen, H.J. Roven, S.S. Gireesh, P.C. Skaret, J. Hjelen, Materials Letters, 65 (2011) 3472-3475.
[106] M. Liu, H.J. Roven, X. Liu, M. Murashkin, R.Z. Valiev, T. Ungar, L. Balogh, J. Mater. Sci., 45 (2010) 4659-4664.

[107] M. Liu, H.J. Roven, M. Murashkin, R.Z. Valiev, Mater. Sci. Eng. A-Struct. Mater. Prop. Microstruct. Process., 503 (2009) 122-125.
[108] M.P. Liu, H.J. Roven, X.T. Liu, M. Murashkin, R.Z. Valiev, T. Ungar, L. Balogh, Transactions of Nonferrous Metals Society of China, 20 (2010) 2051-2056.
[109] R.Z. Valiev, I.V. Alexandrov, N.A. Enikeev, M.Y. Murashkin, I.P. Semenova, Reviews on Advanced Materials Science, 25 (2010) 1-10.
[110] R.Z. Valiev, On grain boundary engineering of UFG metals and alloys for enhancing their properties, in: Y. Estrin, M.H. J. (Eds.), Nanomaterials by Severe Plastic Deformation Iv, Parts 1 and 2, Materials Science Forum, 2008, pp. 22-28.
[111] M.Y. Murashkin, A.R. Kil'mametov, R.Z. Valiev, Physics of Metals and Metallography, 106 (2008) 90-96.
[112] D.R. Fang, Q.Q. Duan, N.Q. Zhao, J.J. Li, S.D. Wu, Z.F. Zhang, Mater. Sci. Eng. A-Struct. Mater. Prop. Microstruct. Process., 459 (2007) 137-144.
[113] Y.B. Lee, D.H. Shin, K.T. Park, W.J. Nam, Scr. Mater., 51 (2004) 355-359.
[114] J. Wang, Y. Iwahashi, Z. Horita, M. Furukawa, M. Nemoto, R.Z. Valiev, T.G. Langdon, Acta Mater., 44 (1996) 2973-2982.
[115] O. Nijs, B. Holmedal, J. Friis, E. Nes, Mater. Sci. Eng. A-Struct. Mater. Prop. Microstruct. Process., , 483–484 (2008) 51-53.
[116] R. Kapoor, J.K. Chakravartty, Acta Mater., 55 (2007) 5408-5418.
[117] G. Angella, P. Bassani, A. Tuissi, D. Ripamonti, M. Vedani, Microstructure evolution and aging kinetics of Al-Mg-Si and Al-Mg-Si-Sc alloys processed by ECAP, in: Z. Horita (Ed.) Nanomaterials by Severe Plastic Deformation, Trans Tech Publications Ltd, Zurich-Uetikon, 2006, pp. 493-498.
[118] M. Cabibbo, E. Evangelista, J. Mater. Sci., 41 (2006) 5329-5338.
[119] K.R. Cardoso, D.N. Travessa, W.J. Botta, A.M. Jorge, Jr., Mater. Sci. Eng. A-Struct. Mater. Prop. Microstruct. Process., 528 (2011) 5804-5811.
[120] S. Dadbakhsh, A.K. Taheri, C.W. Smith, Mater. Sci. Eng. A-Struct. Mater. Prop. Microstruct. Process., 527 (2010) 4758-4766.
[121] N. Gao, M.J. Starink, M. Furukawa, Z. Horita, C. Xu, T.G. Langdon, Evolution of microstructure and precipitation in heat-treatable aluminium alloys during ECA pressing and subsequent heat treatment, in: Z. Horita (Ed.)

Nanomaterials by Severe Plastic Deformation, Trans Tech Publications Ltd, Zurich-Uetikon, 2006, pp. 275-280.
[122] M. Gazizov, R. Kaibyshev, Journal of Alloys and Compounds, 527 (2012) 163-175.
[123] J. Gubicza, I. Schiller, N.Q. Chinh, J. Illy, Z. Horita, T.G. Langdon, Mater. Sci. Eng. A-Struct. Mater. Prop. Microstruct. Process., 460 (2007) 77-85.
[124] K. Hockauf, T. Halle, M. Hockauf, L.W. Meyer, M.F.X. Wagner, T. Lampke, Materialwissenschaft Und Werkstofftechnik, 41 (2010) 756-764.
[125] S.K. Panigrahi, R. Jayaganthan, Journal of Alloys and Compounds, 470 (2009) 285-288.
[126] T. Radetic, M. Popovic, E. Romhanji, B. Verlinden, Mater. Sci. Eng. A-Struct. Mater. Prop. Microstruct. Process., 527 (2010) 634-644.
[127] X. Sauvage, M.Y. Murashkin, R.Z. Valiev, Kovove Materialy-Metallic Materials, 49 (2011) 11-15.
[128] G. Sha, S.P. Ringer, Z.C. Duan, T.G. Langdon, Int. J. Mater. Res., 100 (2009) 1674-1678.
[129] G. Sha, Y.B. Wang, X.Z. Liao, Z.C. Duan, S.P. Ringer, T.G. Langdon, Acta Mater., 57 (2009) 3123-3132.
[130] G. Sha, L. Yao, X. Liao, S.P. Ringer, Z.C. Duan, T.G. Langdon, Ultramicroscopy, 111 (2011) 500-505.
[131] M. Vaseghi, A.K. Taheri, S.I. Hong, H.S. Kim, Materials Design., 31 (2010) 4076-4082.
[132] M. Vedani, G. Angella, P. Bassani, D. Ripamonti, A. Tuissi, Journal of Thermal Analysis and Calorimetry, 87 (2007) 277-284.
[133] V. Vidal, Z.R. Zhang, B. Verlinden, J. Mater. Sci., 43 (2008) 7418-7425.
[134] Y.H. Zhao, X.Z. Liao, Z. Jin, R.Z. Valiev, Y.T. Zhu, Acta Mater., 52 (2004) 4589-4599.
[135] H.J. Roven, M. Liu, J.C. Werenskiold, Mater. Sci. Eng. A-Struct. Mater. Prop. Microstruct. Process., 483-84 (2008) 54-58.
[136] M. Cabibbo, E. Evangelista, M. Vedani, Metall. Mater. Trans. A, 36A (2005) 1353-1364.

[137] Z.Y. Liu, S. Bai, X.W. Zhou, Y.X. Gu, Mater. Sci. Eng. A-Struct. Mater. Prop. Microstruct. Process., 528 (2011) 2217-2222.
[138] J. Mao, S.B. Kang, J.O. Park, Journal of Materials Processing Technology, 159 (2005) 314-320.
[139] N.M. Rosengaard, H.L. Skriver, Physical Review B, 47 (1993) 12865-12873.
[140] F.J. Humphreys, Recrystallization and Related Annealing Phenomena, Pergamon, 1996.
[141] D.A. Hughes, Acta Metall. Et Mater., 41 (1993) 1421-1430.
[142] B. Bay, N. Hansen, D. Kuhlmann-Wilsdorf, Mater. Sci. Eng. A-Struct. Mater. Prop. Microstruct. Process., 158 (1992) 139-146.
[143] C.S. Lee, B.J. Duggan, R.E. Smallman, Acta Metall. et Mater., 41 (1993) 2265-2270.
[144] B. Bay, N. Hansen, D. Kuhlmann-Wilsdorf, Mater. Sci. Eng. A-Struct. Mater. Prop. Microstruct. Process., 113 (1989) 385-397.
[145] N. Hansen, Scr. Metall. Mater., 27 (1992) 1447-1452.
[146] D. Kuhlmann-Wilsdorf, Mater. Sci. Eng. A-Struct. Mater. Prop. Microstruct. Process., 86 (1987) 53-66.
[147] D. Kuhlmann-Wilsdorf, Physica Status Solidi A, 149 (1995) 225-241.
[148] D. Kuhlmann-Wilsdorf, Scr. Mater., 34 (1996) 641-650.
[149] D. Kuhlmann-Wilsdorf, Scr. Mater., 36 (1997) 173-181.
[150] D. Kuhlmann-Wilsdorf, Acta Mater., 47 (1999) 1697-1712.
[151] D.A. Hughes, N. Hansen, Acta Mater., 48 (2000) 2985-3004.
[152] T.B. Massalski, H. Okamoto, P.R. Subramanian, L. Kacprzak, ASM International, Metals Park, OH. (1990) p170.
[153] A. Bochenek, K.N. Braszczyńska, Mater. Sci. Eng. A-Struct. Mater. Prop. Microstruct. Process., 290 (2000) 122-127.
[154] D.Y. Maeng, J.H. Lee, S.I. Hong, B.S. Chun, Mater. Sci. Eng. A-Struct. Mater. Prop. Microstruct. Process., 311 (2001) 128-134.
[155] S.G. Fries, T. Jantzen, Thermochimica Acta, 314 (1998) 23-33.
[156] S. Ignat, P. Sallamand, D. Grevey, M. Lambertin, Applied Surface Science, 225 (2004) 124-134.
[157] G.W.J. Waldron, Acta Metall., 13 (1965) p. 897.

[158] D.G. Morris, M.A. Munoz-Morris, Acta Mater., 50 (2002) 4047-4060.
[159] C. Xu, Z. Horita, T.G. Langdon, Mater. Sci. Eng. A-Struct. Mater. Prop. Microstruct. Process., 528 (2011) 6059-6065.
[160] O. Sitdikov, T. Sakai, E. Avtokratova, R. Kaibyshev, K. Tsuzaki, Y. Watanabe, Acta Mater., 56 (2008) 821-834.
[161] J. Gubicza, G. Krallics, I. Schiller, D. Malgin, Evolution of the microstructure of Al 6082 alloy during equal-channel angular pressing, in: J. Gyulai (Ed.) Materials Science, Testing and Informatics Ii, Trans Tech Publications Ltd, Stafa-Zurich, 2005, pp. 453-457.
[162] G.E. Totten, L. Xie, K. Funatani, Handbook of Mechanical Alloy Design, Marcel Dekker, 2004.
[163] E.J. Kwak, C.H. Bok, M.H. Seo, T.S. Kim, H.S. Kim, Mater. Trans., 49 (2008) 1006-1010.
[164] W.M. Gan, M.Y. Zheng, H. Chang, X.J. Wang, X.G. Qiao, K. Wu, B. Schwebke, H.G. Brokmeier, Journal of Alloys and Compounds, 470 (2009) 256-262.
[165] G.D. Fan, M.Y. Zheng, X.S. Hu, H. Chang, K. Wu, Int. J. Mod. Phys. B, 23 (2009) 1829-1834.
[166] N. Birbilis, K.D. Ralston, S. Virtanen, H.L. Fraser, C.H.J. Davies, Corros. Eng. Sci. Technol., 45 (2010) 224-230.
[167] J.Z. Li, W. Xu, X.L. Wu, H. Ding, K.N. Xia, Mater. Sci. Eng. A-Struct. Mater. Prop. Microstruct. Process., 528 (2011) 5993-5998.
[168] N.Q. Chinh, Z. Horita, T.G. Langdon, Work hardening in metals: Microscopic and macroscopic behavior through a wide range of strain, in: T. Chandra, J.M. Torralba, i.T. Saka (Eds.) Thermec'2003, Pts 1-5, 2003, pp. 453-458.
[169] N.Q. Chinh, J. Illy, Z. Kovacs, Z. Horita, T.G. Langdon, Effect of Mg additions on the work hardening behavior of aluminum over a wide range of strain, in: P.J. Gregson, S.J. Harris (Eds.) Aluminum Alloys 2002: Their Physical and Mechanical Properties Pts 1-3, 2002, pp. 1007-1012.
[170] W.S. Choi, H.S. Ryoo, S.K. Hwang, M.H. Kim, S.I. Kwun, S.W. Chae, Metall. Mater. Trans. A, 33 (2002) 973-980.

[171] T. Fujita, Z. Horita, T.G. Langdon, Philosophical Magazine A, 82 (2002) 2249-2262.
[172] A. Ostapovets, P. Seda, A. Jaeger, P. Lejcek, Scr. Mater., 64 (2011) 470-473.
[173] P. Seda, A. Jaeger, P. Lejcek, Microstructure and Texture of Magnesium Single Crystals Processed by ECAP, in: J.T. Wang, R.B. Figueiredo, T.G. Langdon (Eds.), Nanomaterials by Severe Plastic Deformation: Nanospd5, Parts 1 and 2, 2011, pp. 355-360.
[174] P. Seda, A. Jaeger, P. Lejcek, L. Tanger, Microstructure and texture evolution during ECAP processing of pure magnesium, Metal 2010: 19th InternationalMetall.l and Materials Conference.
[175] X. Wu, W. Xu, M. Kubota, K. Xia, Bulk Mg produced by back pressure equal channel angular consolidation (BP-ECAC), in: Y. Estrin, H.J. Maier (Eds.) Nanomaterials by Severe Plastic Deformation Iv, Pts 1 and 2, 2008, pp. 114-118.
[176] K.N. Braszczynska-Malik, Journal of Alloys and Compounds, 487 (2009) 263-268.
[177] R. Ding, C. Chung, Y. Chiu, P. Lyon, Mater. Sci. Eng. A-Struct. Mater. Prop. Microstruct. Process., 527 (2010) 3777-3784.
[178] R.B. Figueiredo, T.G. Langdon, J. Mater. Sci., 45 (2010) 4827-4836.
[179] R.B. Figueiredo, Z. Szaraz, Z. Trojanova, P. Lukac, T.G. Langdon, Scr. Mater., 63 (2010) 504-507.
[180] R.B. Figueiredo, S. Terzi, T.G. Langdon, Acta Mater., 58 (2010) 5737-5748.
[181] J. Gubicza, K. Mathis, Z. Hegedus, G. Ribarik, A.L. Toth, Journal of Alloys and Compounds, 492 (2010) 166-172.
[182] Y. He, Q. Pan, Y. Qin, X. Liu, W. Li, J. Mater. Sci., 45 (2010) 1655-1662.
[183] Y. He, Q. Pan, Y. Qin, X. Liu, W. Li, Y. Chiu, J.J.J. Chen, Journal of Alloys and Compounds, 492 (2010) 605-610.
[184] F. Kang, J.Q. Liu, J.T. Wang, X. Zhao, Advanced Engineering Materials, 12 (2010) 730-734.
[185] M. Krystian, M.J. Zehetbauer, H. Kropik, B. Mingler, G. Krexner, Journal of Alloys and Compounds, 509 (2011) S449-S455.
[186] J. Li, H. Ding, X. Wu, W. Xu, K. Xia, The Influence of Texture and Grain Size on Compressive Deformation Behavior of Pure Mg Through Equal-Channel

Angular Processing, in: J.T. Wang, R.B. Figueiredo, T.G. Langdon (Eds.) Nanomaterials by Severe Plastic Deformation: Nanospd5, Pts 1 and 2, 2011, pp. 385-390.

[187] J. Li, W. Xu, X. Wu, H. Ding, K. Xia, Mater. Sci. Eng. A-Struct. Mater. Prop. Microstruct. Process., 528 (2011) 5993-5998.

[188] A. Ma, J. Jiang, N. Saito, I. Shigematsu, Y. Yuan, D. Yang, Y. Nishida, Mater. Sci. Eng. A-Struct. Mater. Prop. Microstruct. Process., 513-14 (2009) 122-127.

[189] S.M. Masoudpanah, R. Mahmudi, Mater. Sci. Eng. A-Struct. Mater. Prop. Microstruct. Process., 526 (2009) 22-30.

[190] P. Seda, A. Ostapovets, A. Jaeger, P. Lejcek, Philosophical Magazine, 92 (2012) 1223-1237.

[191] G. Sha, J.H. Li, W. Xu, K. Xia, W.Q. Jie, S.P. Ringer, Mater. Sci. Eng. A-Struct. Mater. Prop. Microstruct. Process., 527 (2010) 5092-5099.

[192] D. Song, A.B. Ma, J.H. Jiang, P.H. Lin, D.H. Yang, J.F. Fan, Corrosion Science, 53 (2011) 362-373.

[193] L.B. Tong, M.Y. Zheng, H. Chang, X.S. Hu, K. Wu, S.W. Xu, S. Kamado, Y. Kojima, Mater. Sci. Eng. A-Struct. Mater. Prop. Microstruct. Process., 523 (2009) 289-294.

[194] H.J. Yang, X.H. An, X.H. Shao, X.M. Yang, S.X. Li, S.D. Wu, Z.F. Zhang, Mater. Sci. Eng. A-Struct. Mater. Prop. Microstruct. Process., 528 (2011) 4300-4311.

[195] D.L. Yin, X. Chen, J.T. Wang, Microstructure and Toughness of an AZ80 Mg Alloy Processed by ECAP and Ageing Treatment, in: J.T. Wang, R.B. Figueiredo, T.G. Langdon (Eds.) Nanomaterials by Severe Plastic Deformation: Nanospd5, Pts 1 and 2, 2011, pp. 475-480.

[196] D. Zhang, S. Li, Mater. Sci. Eng. A-Struct. Mater. Prop. Microstruct. Process., 528 (2011) 4982-4987.

[197] R. Zhu, Y.J. Wu, W.Q. Ji, J.T. Wang, Materials Letters, 65 (2011) 3593-3596.

[198] R.B. Figueiredo, T.G. Langdon, J. Mater. Sci., 44 (2009) 4758-4762.

[199] R.B. Figueiredo, T.G. Langdon, Mater. Sci. Eng. A-Struct. Mater. Prop. Microstruct. Process., 501 (2009) 105-114.
[200] H.K. Lin, J.C. Huang, T.G. Langdon, Mater. Sci. Eng. A-Struct. Mater. Prop. Microstruct. Process.,, 402 (2005) 250-257.
[201] K. Matsubara, Y. Miyahara, Z. Horita, T.G. Langdon, Acta Mater., 51 (2003) 3073-3084.
[202] K. Matsubara, Y. Miyahara, Z. Horita, T. Langdon,Metall.l and Materials Transactions A, 35 (2004) 1735-1744.
[203] R.B. Figueiredo, T.G. Langdon, Mater. Sci. Eng. A-Struct. Mater. Prop. Microstruct. Process.,, 430 (2006) 151-156.
[204] Y. Miyahara, Z. Horita, T.G. Langdon, Mater. Sci. Eng. A-Struct. Mater. Prop. Microstruct. Process.,, 420 (2006) 240-244.
[205] R. Lapovok, Y. Estrin, M.V. Popov, T.G. Langdon, Advanced Engineering Materials, 10 (2008) 429-433.
[206] R.B. Figueiredo, P.R. Cetlin, T.G. Langdon, Acta Mater., 55 (2007) 4769-4779.
[207] S.X. Ding, C.P. Chang, P.W. Kao,Metall.l and Materials Transactions A, 40 (2009) 415-425.
[208] C.W. Su, L. Lu, M.O. Lai, Mater. Sci. Eng. A-Struct. Mater. Prop. Microstruct. Process., 434 (2006) 227-236.
[209] M. Mabuchi, H. Iwasaki, K. Yanase, K. Higashi, Scr. Mater., 36 (1997) 681-686.
[210] M. Mabuchi, K. Ameyama, H. Iwasaki, K. Higashi, Acta Mater., 47 (1999) 2047-2057.
[211] R. Lapovok, R. Cottam, P. Thomson, Y. Estrin, J. Mater. Res., 20 (2005) 1375-1378.
[212] Y. Miyahara, Z. Horita, T.G. Langdon, Mater. Sci. Eng. A-Struct. Mater. Prop. Microstruct. Process., 420 (2006) 240-244.
[213] V.N. Chuvil'deev, T.G. Nieh, M.Y. Gryaznov, V.I. Kopylov, A.N. Sysoev, Journal of Alloys and Compounds, 378 (2004) 253-257.
[214] V.N. Chuvil'deev, T.G. Nieh, M.Y. Gryaznov, A.N. Sysoev, V.I. Kopylov, Scr. Mater., 50 (2004) 861-865.

[215] H. Watanabe, T. Mukai, K. Ishikawa, K. Higashi, Scr. Mater., 46 (2002) 851-856.
[216] P. Seda, A. Ostapovets, A. Jager, P. Lejcek, Philosophical Magazine A, 92 (2012) 1223-1237.
[217] B. Beausir, S. Suwas, L.S. Toth, K.W. Neale, J.J. Fundenberger, Acta Mater., 56 (2008) 200-214.
[218] S.Y. Li, Acta Mater., 56 (2008) 1031-1043.
[219] M. Al-Maharbi, I. Karaman, I.J. Beyerlein, D. Foley, K.T. Hartwig, L.J. Kecskes, S.N. Mathaudhu, Mater. Sci. Eng. A-Struct. Mater. Prop. Microstruct. Process., 528 (2011) 7616-7627.
[220] S. Goussous, W. Xu, K. Xia, Developing aluminum nanocomposites via severe plastic deformation, in: W. Skrotzki, C.G. Oertel, H. Biermann, M. Heilmaier (Eds.), 15th International Conference on the Strength of Materials, Journal of Physics Conference Series, 2010.
[221] H.S. Shahabi, M. Eizadjou, H.D. Manesh, Mater. Sci. Eng. A-Struct. Mater. Prop. Microstruct. Process., 527 (2010) 5790-5795.
[222] K. Xia, Advanced Engineering Materials, 12 (2010) 724-729.
[223] Y.J. Chen, Q.D. Wang, H.J. Roven, M. Karlsen, Y.D. Yu, M.P. Liu, J. Hjelen, Journal of Alloys and Compounds, 462 (2008) 192-200.
[224] S.V. Divinski, J. Ribbe, G. Reglitz, Y. Estrin, G. Wilde, J. Appl. Phys., 106 (2009) 063502-063508.
[225] M. Paramsothy, S.F. Hassan, N. Srikanth, M. Gupta, Journal of Physics D: Applied Physics, 41 (2008) 175402.
[226] A. Sankaran, S. Vadakke Madam, A. Nouri, M.R. Barnett, Scr. Mater., 66 (2012) 725-728.
[227] R.Z. Valiev, Advanced Engineering Materials, 5 (2003) 296-300.
[228] H.G. Brokmeier, H. Chang, W.M. Gan, M.Y. Zheng, K. Wu, Texture development of ARB processed Mg/Al multilayers, in: W. Skrotzki, C.G. Oertel, H. Biermann, M. Heilmaier (Eds.), 15th International Conference on the Strength of Materials, Journal of Physics Conference Series, 2010.

[229] K. Wu, H. Chang, E. Maawad, W.M. Gan, H.G. Brokmeier, M.Y. Zheng, Mater. Sci. Eng. A-Struct. Mater. Prop. Microstruct. Process., 527 (2010) 3073-3078.
[230] H. Chang, M.Y. Zheng, W.M. Gan, K. Wu, E. Maawad, H.G. Brokmeier, Scr. Mater., 61 (2009) 717-720.
[231] T. Hausoel, V. Maier, C.W. Schmidt, M. Winkler, H.W. Hoeppel, M. Goeken, Advanced Engineering Materials, 12 (2010) 740-746.
[232] H.S. Liu, B. Zhang, G.P. Zhang, Journal of Materials Science & Technology, 27 (2011) 15-21.
[233] W. Xu, X. Wu, T. Honma, S.P. Ringer, K. Xia, Acta Mater., 57 (2009) 4321-4330.
[234] W.M. Gan, K. Wu, M.Y. Zheng, X.J. Wang, H. Chang, H.G. Brokmeier, Mater. Sci. Eng. A-Struct. Mater. Prop. Microstruct. Process., 516 (2009) 283-289.
[235] G. Zhou, X. Zeng, Q. Xu, Microstructure Evolution and Mechanical Behavior of CNTs/AZ31 Magnesium Alloy Composites Processed by Equal Channel Angular Pressing, in: Jiang, Z. , C.L. Zhang (Eds.) Manufacturing Science and Engineering, Pts 1-5, 2010, pp. 1628-1632.
[236] L. Bian, W. Liang, G. Xie, W. Zhang, J. Xue, Mater. Sci. Eng. A-Struct. Mater. Prop. Microstruct. Process., 528 (2011) 3463-3467.
[237] X.B. Liu, R.S. Chen, E.H. Han, Journal of Materials Processing Technology, 209 (2009) 4675-4681.
[238] K. Narooei, A. Karimi Taheri, Applied Mathematical Modelling, 36 (2012) 2128-2141.
[239] R.S. Mishra, R.Z. Valiev, S.X. McFadden, R.K. Islamgaliev, A.K. Mukherjee, Scr. Mater., 40 (1999) 1151-1155.
[240] Y. Li, T.G. Langdon, J. Mater. Sci., 35 (2000) 1201-1204.
[241] F. Dobes, M. Besterci, B. Ballokova, K. Sulleiova, P. Dymacek, Mater. Sci. Eng. A-Struct. Mater. Prop. Microstruct. Process., 532 (2012) 567-572.
[242] G. Ramu, R. Bauri, Materials Design, 30 (2009) 3554-3559.
[243] K.R. Ravi, M. Saravanan, R.M. Pillai, A. Mandal, B.S. Murty, M. Chakraborty, B.C. Pai, Journal of Alloys and Compounds, 459 (2008) 239-243.

[244] R.Z. Valiev, R.K. Islamgaliev, N.F. Kuzmina, Y. Li, T.G. Langdon, Scr. Mater., 40 (1998) 117-122.
[245] I. Sabirov, O. Kolednik, R.Z. Valiev, R. Pippan, Acta Mater., 53 (2005) 4919-4930.
[246] B. Mani, M.H. Paydar, Journal of Alloys and Compounds, 492 (2010) 116-121.
[247] H. Mohseni, S. Keirs, S.L.I. Chan, M. Ferry, Mater. Sci.and Tech., 26 (2010) 597-603.
[248] J. Milligan, R. Vintila, M. Brochu, Mater. Sci. Eng. A-Struct. Mater. Prop. Microstruct. Process., 508 (2009) 43-49.
[249] Y. Radi, R. Mahmudi, Mater. Sci. Eng. A-Struct. Mater. Prop. Microstruct. Process., 527 (2010) 2764-2771.
[250] V.I. Semenov, Y.R. Jeng, S.J. Huang, Y.Z. Dao, S.J. Hwang, L.S. Shuster, S.V. Chertovskikh, P.C. Lin, Journal of Friction and Wear, 30 (2009) 194-198.
[251] V.M. Skripnyuk, E. Rabkin, L.A. Bendersky, A. Magrez, E. Carreno-Morelli, Y. Estrin, International Journal of Hydrogen Energy, 35 (2010) 5471-5478.
[252] J. Hashim, L. Looney, M.S.J. Hashmi, Journal of Materials Processing Technology, 123 (2002) 251-257.
[253] J. Hashim, L. Looney, M.S.J. Hashmi, Journal of Materials Processing Technology, 123 (2002) 258-263.
[254] Y.J. Chen, H.J. Roven, S.S. Gireesh, P.C. Skaret, J. Hjelen, Materials Letters, 65 (2011) 3472-3475.
[255] International world patent WO/2008/063076, "Screw extruder for continuous extrusion of materials with high viscosity", Inventors: J. C.Werenskiold, L. Auran, H J. Roven, N. Ryum, O. Reiso, published 29.05.2008.
[256] P.L. Sun, P.W. Kao, C.P. Chang, Scr. Mater., 51 (2004) 565-570.
[257] P.L. Sun, P.W. Kao, C.P. Chang, Metall. Mater. Trans. A, 35A (2004) 1359-1368.
[258] P.L. Sun, E.K. Cerreta, G.T. Gray, III, J.F. Bingert, Metall. Mater. Trans. A, 37A (2006) 2983-2994.
[259] U. Chakkingal, R.F. Thomson, Journal of Materials Processing Technology, 117 (2001) 169-177.

[260] Y.Y. Wang, P.L. Sun, P.W. Kao, C.P. Chang, Scr. Mater., 50 (2004) 613-617.
[261] L.E. Murr, Interfacial Phenomena in Metals and Alloys, Addison-Wesley, Reading, 1975.
[262] S.Y. Li, I.J. Beyerlein, D.J. Alexander, S.C. Vogel, Scr. Mater., 52 (2005) 1099-1104.
[263] S. Terhune, D. Swisher, K. Oh-Ishi, Z. Horita, T. Langdon, T. McNelley,Metall.l and Materials Transactions A, 33 (2002) 2173-2184.
[264] A.P. Zhilyaev, D.L. Swisher, K. Oh-ishi, T.G. Langdon, T.R. McNelley, Mater. Sci. Eng. A-Struct. Mater. Prop. Microstruct. Process., , 429 (2006) 137-148.
[265] I. Mazurina, T. Sakai, H. Miura, O. Sitdikov, R. Kaibyshev, Mater. Sci. Eng. A-Struct. Mater. Prop. Microstruct. Process., 473 (2008) 297-305.
[266] J.-Y. Chang, J.-S. Yoon, G.-H. Kim, Scr. Mater., 45 (2001) 347-354.
[267] P.J. Apps, M. Berta, P.B. Prangnell, Acta Mater., 53 (2005) 499-511.
[268] Y.C. Chen, Y.Y. Huang, C.P. Chang, P.W. Kao, Acta Mater., 51 (2003) 2005-2015.
[269] N. Gao, M.J. Starink, M. Furukawa, Z. Horita, C. Xu, T.G. Langdon, Mater. Sci. Eng. A-Struct. Mater. Prop. Microstruct. Process., , 410–411 (2005) 303-307.
[270] S.S. Kulkarni, E.A. Starke, D. Kuhlmann-Wilsdorf, Acta Mater., 46 (1998) 5283-5301.
[271] C.G. Lee, K.J. Kim, S. Lee, K.M. Cho, Metall. Mater. Trans. A, 29 (1998) 469-476.
[272] M. Abo-Elkhier, J. of Materi Eng and Perform, 13 (2004) 241-247.
[273] M. Kawasaki, I.J. Beyerlein, S.C. Vogel, T.G. Langdon, Acta Mater., 56 (2008) 2307-2317.
[274] F.R.N. Nabarro, Acta Mater., 54 (2006) 263-295.
[275] D. Kuhlmann-Wilsdorf, Mat Res Innovat, 1 (1998) 265-297.
[276] F. Haessner, The study of recrystallization by calorimetric methods, in: Recrystallization 90: International Conference on Recrystallization in Metallic Materials, 1990.

[277] J. Zhang, N. Gao, M.J. Starink, Mater. Sci. Eng. A-Struct. Mater. Prop. Microstruct. Process., 528 (2011) 2581-2591.
[278] G.R. Canova, U.F. Kocks, J.J. Jonas, Acta Metall., 32 (1984) 211-226.
[279] P. Venkatachalam, S. Roy, B. Ravisankar, V.T. Paul, M. Vijayalakshmi, S. Suwas, J. Mater. Sci., 46 (2011) 6518-6527.
[280] O. Engler, J. Hirsch, K. Lücke, Acta Metall. Et Mater., 43 (1995) 121-138.
[281] F. Montheillet, P. Gilormini, J.J. Jonas, Acta Metall., 33 (1985) 705-717.
[282] T.R. McNelley, S. Swarninathan, J.Q. Su, A.P. Zhilyaev, Texture and High-Angle Boundary Formation during Deformation Processing, in: M. Cabibbo, S. Spigarelli (Eds.), Recent Developments in the Processing and Applications of Structural Metals and Alloys, Materials Science Forum, 2009, pp. 251-258.
[283] S. Kamado, T. Ashie, H. Yamada, K. Sanbun, Y. Kojima, Materials Science Forum, 350 (2000) 65-72.
[284] H.K. Lin, J.C. Huang, T.G. Langdon, Materials Science and Engineering A, 402 (2005) 250-257.
[285] S.R. Agnew, T.M. Lillo, J. Macheret, G.M. Stoica, L. Chen, Y. Lu, D. Fielden, P.K. Liaw, 2001, pp. 243-247.
[286] F. Kang, J.T. Wang, Y. Peng, Mater. Sci. Eng. A-Struct. Mater. Prop. Microstruct. Process., , 487 (2008) 68-73.
[287] D. Dietrich, D. Nickel, M. Krause, T. Lampke, M. Coleman, V. Randle, J. Mater. Sci., 46 (2011) 357-364.
[288] A. Hill, E.R. Wallach, Acta Metall., 37 (1989) 2425-2437.
[289] W.D. Callister, Fundamentals of Materials Science and Engineering: An Integrated Approach, John Wiley & Sons, Incorporated, 2007.
[290] A. Goloborodko, O. Sitdikov, R. Kaibyshev, H. Miura, T. Sakai, Mater. Sci. Eng. A-Struct. Mater. Prop. Microstruct. Process., 381 (2004) 121-128.
[291] I. Mazurina, T. Sakai, H. Miura, O. Sitdikov, R. Kaibyshev, Materials Transactions, 50 (2009) 101-110.
[292] Y.J. Chen, Y.J. Li, J.C. Walmsley, S. Dumoulin, H.J. Roven, Metall. and Materials Transactions A, 41 (2010) 787-794.
[293] J.R. Davis, J.R. Davis, Associates, A.I.H. Committee, Aluminum and Aluminum Alloys, ASM International, 1993.

[294] R.E. Reed-Hill, Physical Metallurgy Principles, Van Nostrand, 1972.
[295] J. Wang, Y. Li, W. Huang, Reaction Kinetics and Catalysis Letters, 95 (2008) 71-79.
[296] D. Brandon, W.D. Kaplan, Microstructural Characterization of Materials, Wiley, 2008.
[297] Y.J. Chen, Y.C. Chai, H.J. Roven, S.S. Gireesh, Y.D. Yu, J. Hjelen, Mater. Sci. Eng. A-Struct. Mater. Prop. Microstruct. Process., , 545 (2012) 139-147.
[298] J. Gubicza, N.Q. Chinh, Z. Horita, T.G. Langdon, Mater. Sci. Eng. A-Struct. Mater. Prop. Microstruct. Process., 387 (2004) 55-59.
[299] P.J. Apps, J.R. Bowen, P.B. Prangnell, Acta Mater., 51 (2003) 2811-2822.
[300] Y. Estrin, L.P. Kubin, Acta Metall., 34 (1986) 2455-2464.
[301] R.A. Mulford,Metall.l Transactions A, 10 (1979) 1527-1532.
[302] L.P. Kubin, Y. Estrin, Journal De Physique, 47 (1986) 497-505.
[303] L.P. Kubin, Y. Estrin, Acta Metall. Et Mater., 38 (1990) 697-708.
[304] N. Louat, ScriptaMetall., 15 (1981) 1167-1170.
[305] P.G. McCormick, Acta Metall., 36 (1988) 3061-3067.
[306] E. Pink, A. Grinberg, Acta Metall., 30 (1982) 2153-2160.
[307] J. Guillot, J. Grilhe, Acta Metall., 20 (1972) p. 291.
[308] B.J. Brindley, Worthing.Pj, Acta Metall., 17 (1969) 1357-&.
[309] K. Matsuura, Nishiyam.T, S. Koda, Transactions of the Japan Institute of Metals, 10 (1969) 429-&.
[310] P. Hahner, Acta Mater., 45 (1997) 3695-3707.
[311] H. Halim, D.S. Wilkinson, M. Niewczas, Acta Mater., 55 (2007) 4151-4160.
[312] M. Lebyodkin, Y. Brechet, Y. Estrin, L. Kubin, Acta Mater., 44 (1996) 4531-4541.
[313] M.A. Lebyodkin, Y. Estrin, Acta Mater., 53 (2005) 3403-3413.
[314] Y. Brechet, Y. Estrin, Acta Metall. et Mater., 43 (1995) 955-963.
[315] Y. Brechet, F. Louchet, C. Marchionni, J.L. Vergergaugry, Philosophical Magazine A, 56 (1987) 353-366.
[316] E. Pink, Acta Metall., 37 (1989) 1773-1781.
[317] F.A. Mohamed, K.L. Murty, T.G. Langdon, Acta Metall., 22 (1974) 325-332.
[318] R.B. Schwarz, L.L. Funk, Acta Metall., 33 (1985) 295-307.

[319] B.J. Brindley, P.J. Worthington, International Materials Reviews, 15 (1970) 101-114.
[320] M. Furukawa, Z. Horita, M. Nemoto, R.Z. Valiev, T.G. Langdon, Philosophical Magazine A, 78 (1998) 203-216.
[321] Z. Horita, T. Fujinami, M. Nemoto, T.G. Langdon, Journal of Materials Processing Technology, 117 (2001) 288-292.
[322] E. Samuel, J. Jonas, F. Samuel,Metall.l and Materials Transactions A, 42 (2011) 1028-1037.
[323] J.R. Davis, A.I.H. Committee, Metals Handbook: Desk Edition, Taylor & Francis Group, 1998.
[324] B. Bernd-Arno, C. Hans, P. Pavel, Int J Mater Form, 2 (2009) 613-616.
[325] Y. Brechet, Y. Estrin, Scr. Metall. Mater., 30 (1994) 1449-1454.
[326] I. Flitta, T. Sheppard, Mater. Sci.and Tech., 19 (2003) 837-846.
[327] L. Wang, J. Zhou, J. Duszczyk, L. Katgerman, Tribology International, 56 (2012) 89-98.
[328] H.J. Roven, M. Liu, M. Murashkin, R.Z. Valiev, A.R. Kilmametov, T. Ungar, L. Balogh, Nanostructures and Microhardness in Al and Al-Mg Alloys Subjected to SPD, in: M. Cabibbo, S. Spigarelli (Eds.), Recent Developments in the Processing and Applications of Structural Metals and Alloys, Materials Science Forum, 2009, pp. 179-185.
[329] L.R. Vaidyanath, D.R. Milner, British Welding Journal, The Welding Institute, 1960.
[330] L.R. Vaidyanath, M.G. Nicholas, D.R. Milner, British Welding Journal, The Welding Institute, 1959.
[331] J.S. McFarlane, D. Tabor, Proceedings of the Royal Society of London Series a-Mathematical and Physical Sciences, 202 (1950) 224-243.
[332] P. Chekhonin, B. Beausir, J. Scharnweber, C.-G. Oertel, T. Hausöl, H.W. Höppel, H.-G. Brokmeier, W. Skrotzki, Acta Mater., 60 (2012) 4661-4671.
[333] S.C.V. Lim, A.D. Rollett, Mater. Sci. Eng. A-Struct. Mater. Prop. Microstruct. Process., , 520 (2009) 189-196.
[334] M. Furukawa, Z. Horita, M. Nemoto, R.Z. Valiev, T.G. Langdon, Acta Mater., 44 (1996) 4619-4629.

[335] Y.P. Li, G.P. Zhang, W. Wang, J. Tan, S.J. Zhu, Scr. Mater., 57 (2007) 117-120.
[336] R.G. Hoagland, T.E. Mitchell, J.P. Hirth, H. Kung, Philosophical Magazine A, 82 (2002) 643-664.
[337] A. Misra, H. Kung, Advanced Engineering Materials, 3 (2001) 217-222.
[338] C. Chi, H. Yu, J. Dong, X. Xie, Z. Cui, X. Chen, F. Lin, Acta Metall. Sinica-English Letters, 24 (2011) 141-147.
[339] A.W. Zhu, E.A. Starke Jr, Acta Mater., 47 (1999) 3263-3269.
[340] Y. Futamura, T. Tsuchiyama, S. Takaki, Effect of solute copper on grain growth of austenite in high chromium steels in: Gottstein, G., Molodov, D. A. (Eds.), Recrystallization and Grain Growth, Vols 1 and 2 2001.
[341] X. Sauvage, G. Wilde, S.V. Divinski, Z. Horita, R.Z. Valiev, Mater. Sci. Eng. A-Struct. Mater. Prop. Microstruct. Process., , 540 (2012) 1-12.
[342] G. Sha, L. Yao, X. Liao, S.P. Ringer, Z. Chao Duan, T.G. Langdon, Ultramicroscopy, 111 (2011) 500-505.
[343] R.Z. Valiev, I.M. Razumovskii, V.I. Sergeev, Physica Status Solidi A, 139 (1993) 321-335.
[344] R.Z. Valiev, R.S. Musalimov, N.K. Tsenev, Physica Status Solidi A [345] P.P.V. Liddicoat, X.Z. Liao, Y.H. Zhao, Y.T. Zhu, M.Y. Murashkin, E.J. Lavernia, R.Z. Valiev, S.P. Ringer, Nat. Commun., 1 (2010) 63.
[346] X.Y. Liu, J.B. Adams, Acta Mater., 46 (1998) 3467-3476.
[347] T. Malis, M.C. Chaturvedi, J. Mater. Sci., 17 (1982) 1479-1486.

Appendix A: Parameters for EBSD scan data

The EBSD scans for all materials studied (both pre-processed and processed) were performed in FEGSEM equipped with a NORDIF UF1000 detector. The patterns were indexed offline in the NORDIF OIM DC 1.4 indexing software and analysed using TSL OIM 6.0 EBSD software. The CP Al samples were investigated using a Zeiss Ultra FEGSEM and the other samples were investigated using a Hitachi SU6600 FE-SEM.

1. *Parameters for performing EBSD scans in the Zeiss Ultra FEGSEM*

Accelerating voltage: 20 KV
Working distance: 20 mm
Tilt angle: 70°
Aperture size: 300 µm
Acquisition settings: Frame rate: 300 frames per second (fps)
Resolution: 120 x 120 pixels (px)
Exposure time: 3283 µs
Calibration settings: Frame rate: 50 fps
Resolution: 480 x 480 px
Exposure time: 19950 µs

Gain for both acquisition and calibration was adjusted according to the brightness of the patterns, based on the binning and sample conditions. The minimum possible gain was used in order to reduce noise.

2. Parameters for performing EBSD scans in the Hitachi SU6600 FESEM

Accelerating voltage: 16 KV
Working distance: 24-29 mm
Tilt angle: 70°
Aperture size: Anode aperture 500 µm
Objective aperture 50 µm
Acquisition settings: Frame rate: 300 frames per second (fps)
Resolution: 120 x 120 pixels (px)
Exposure time: 3283 µs
Calibration settings: Frame rate: 50 fps
Resolution: 480 x 480 px
Exposure time: 19950 µs

Gain for both acquisition and calibration was adjusted according to the brightness of the patterns, based on the binning and sample conditions. Minimum possible gain was used in order to reduce noise (similar to Zeiss Ultra scans).

Other adjustments

The step-size for each scan was determined by the smallest grain/sub-grain size in the microstructure. An initial large step-size scan typically 1-5 µm was performed on a large area to obtain a rough estimate of the grain size. A subsequent scan, more precise, was performed such that the step size is 5 times smaller than the smallest rough grain/sub-grain size. Subsequently, the corresponding area was chosen.

Four corner points and a centre point were chosen to obtain sample EBSD spot patterns to calibrate the patterns. The four corners were chosen to take into account the shift in the pattern centre. In addition, one point was chosen inside the selected area as a sample acquisition pattern.

OIM analysis parameters

After indexing the data, the .osc file was analysed in a TSL OIM 6.0 package. The calculations for grain size was chosen such that the confidence index (CI) was at least 0.1. The clean-up process secured that the data was neither lost and no artefacts were added. Grain dilation was used carefully and for scans with small grain sizes, such as for ECAP at RT and 8 passes, neighbour CI correlation and CI standardisation cleaning techniques were used.

Appendix B: EBSD line scans on the CP Al samples

An OIM image of the CP Al sample processed at RT by ECAP route Bc up to 8 passes showing the location of line scans utilized (red lines):

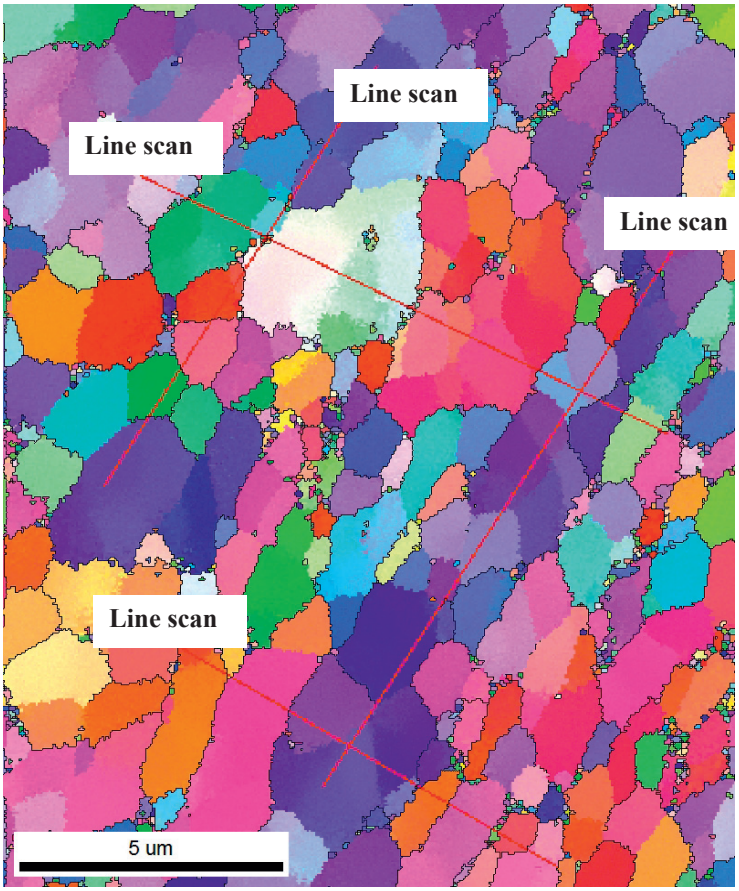

A series of misorientation profiles from the EBSD line scans of the sample processed by ECAP route Bc up to 8 passes at room temperature, were established. Line scans 2 and 3 were carried out along the shear direction, while line scans 1 and 4 were carried out along the extrusion direction. It can be seen that some

regions show misorientation build-up (black circles), some regions reveal the occurrence of recovery (i.e. no change in misorientation).

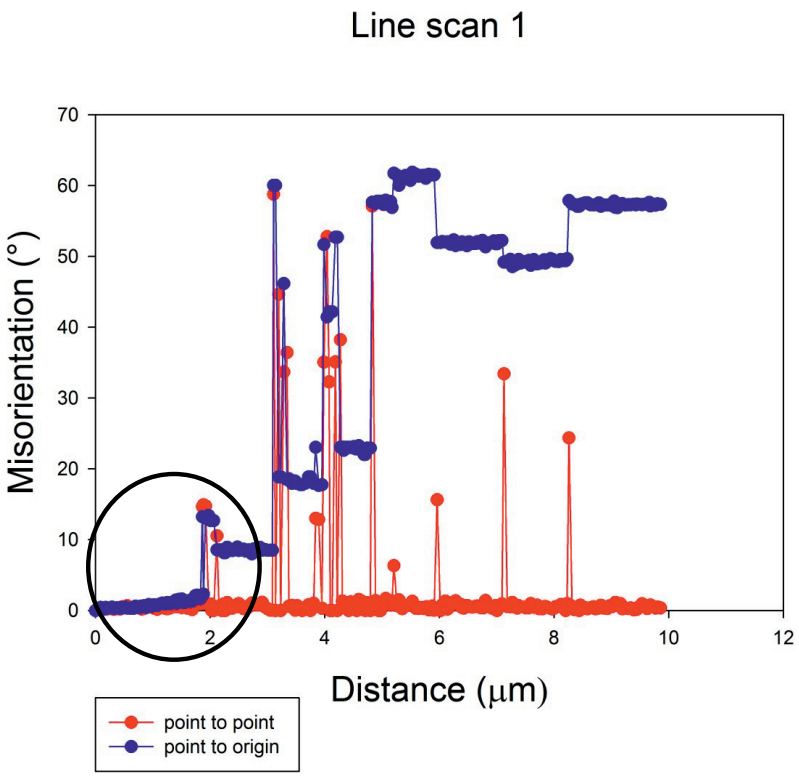

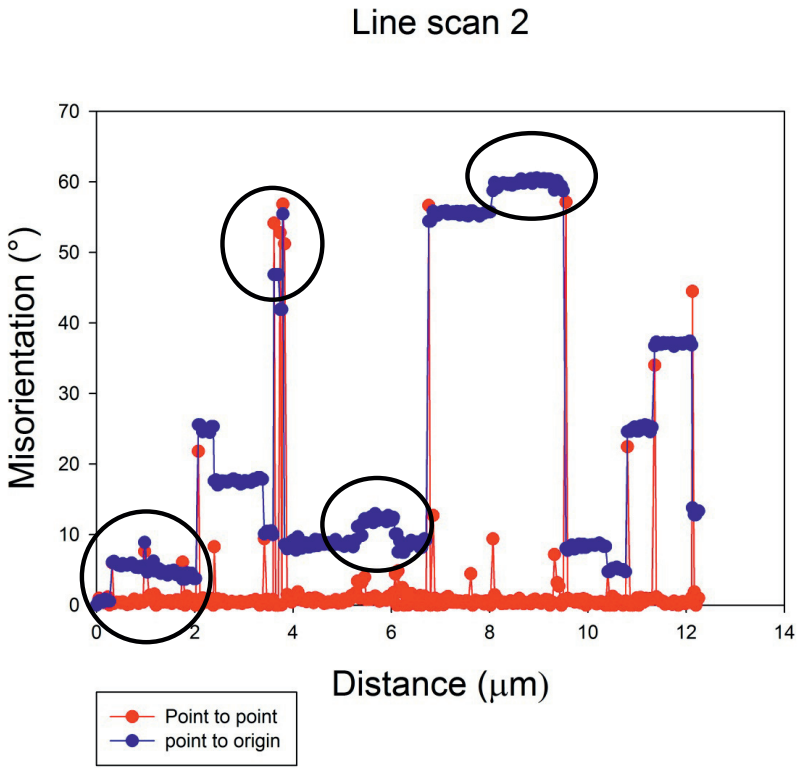
Line scan 2
Misorientation (°)
Distance (μm)
0
10
20
30
40
50
60
70
0
2
4
6
8
10
12
14
Point to point
point to origin

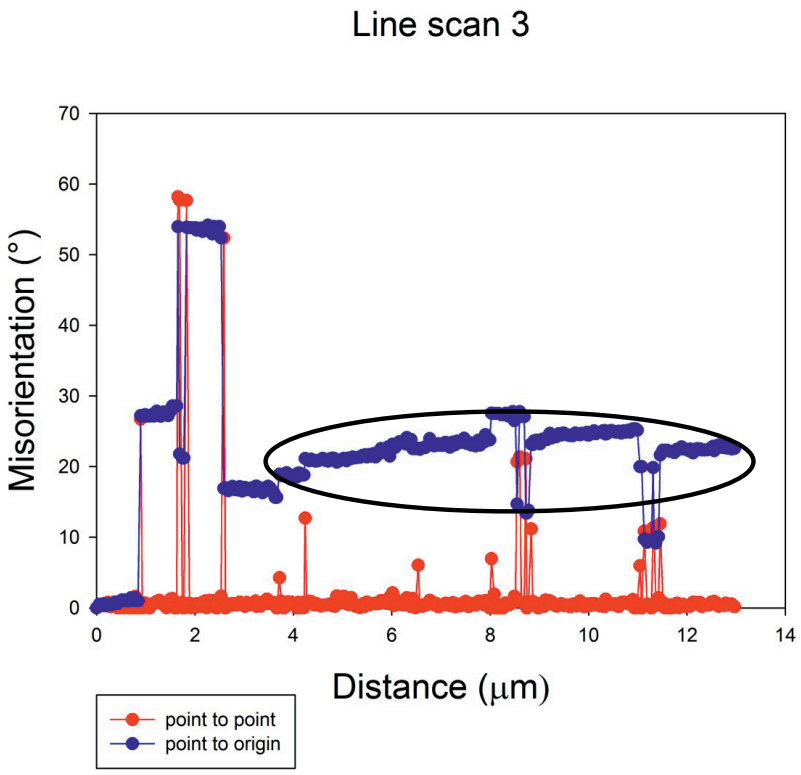
Line scan 3
Misorientation (°)
70
60
50
40
30
20
10
0
0
2
4
6
8
10
12
14
Distance (μm)
point to point
point to origin

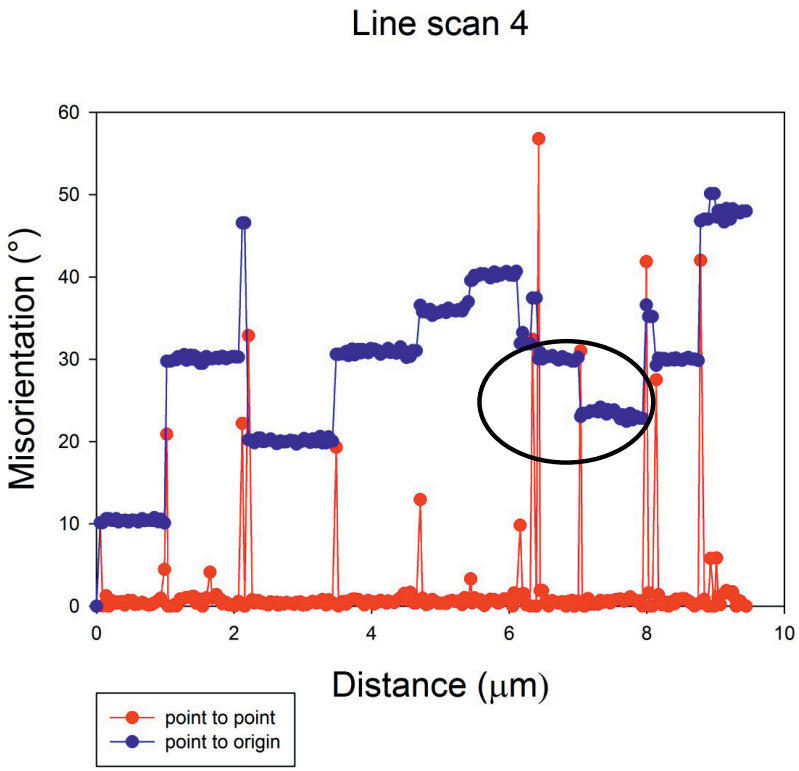
Line scan 4
Misorientation (°)
60
50
40
30
20
10
0
0
2
4
6
8
10
Distance (μm)
point to point
point to origin